

The Effects of a Planar Wall  
on the Low Reynolds Number Motion  
of Solid Particles, Drops and Bubbles

Thesis by  
Edward Paul Ascoli

in Partial Fulfillment of the Requirements  
for the Degree of  
Doctor of Philosophy

California Institute of Technology  
Pasadena, California

1988

(Submitted May 27, 1988)

## Acknowledgement

I would like to thank my research advisor Professor L. Gary Leal. His patience and his confidence in my abilities has been invaluable.

The members of the Leal, Herbolzheimer and Brady groups have been an invaluable source of information, comraderie and support. These and other friends have made the bad times bearable and the good times all the more enjoyable. Last, but certainly not least, very special thanks to Kathy Lewis.

## Abstract

This thesis focuses on the low Reynolds number interaction of solid particles, deformable drops and bubbles with a rigid plane boundary. In chapters I, II and III we use a numerical technique which employs a boundary integral equation reformulation of Stokes system. In particular, the kernels in the integral reformulation derive from the Green's function corresponding to a no-slip planar boundary. Motion is assumed axisymmetric about the line perpendicular to the plane and through the drop or particle center.

We consider the solid particle case in chapter I. Particle velocity is prescribed and the resultant hydrodynamic force on the particle calculated. The results are discussed in the context of near and far field asymptotic theories as well as existing numerical techniques.

In chapter II deformable drop motion via buoyancy is examined and the time evolution of drop shape is obtained. Interfacial tension is assumed constant. Emphasis is placed on the details of drop "dimpling". In particular, at the initial stages of dimpling, pressure variation normal to the wall is found to be significant in the film trapped between the drop and the wall. Thin-film analytic theories neglect this variation in pressure. The consequences of neglect of this pressure variation are discussed.

In the appendix to chapter II we develop a thin-film asymptotic theory for the buoyancy driven motion of a bubble toward a planar wall. The consequences of this theory are related to the results of chapter II. This work is still in progress, and for this reason it is relegated to an appendix.

Thermocapillarity provides the mechanism for drop motion and deformation in chapter III. Surface tension is allowed to vary with temperature and the drop is placed in a non-constant temperature field. The effects of physical parameters on drop evolution are discussed.

Chapter IV is a digression from low Reynolds number wall effects. Here we examine a numerical technique developed by Ryskin and Leal for generating

boundary-fitted orthogonal coordinate grids. Specifically, we present a proof of the existence of a boundary-fitted orthogonal grid for the case when the ratio of “scale factors” is of product form.

## Thesis Introduction

The bulk of this thesis focuses on the low Reynolds number interaction of solid particles, deformable drops and bubbles with a rigid plane boundary. In chapter I we consider the solid particle case. Particle velocity is prescribed and the resultant hydrodynamic force on the particle calculated. The results of chapter I are of importance in a wide variety of particle sedimentation processes. In particular, all real systems are externally bounded by rigid walls or free surfaces. When these external boundaries are located at finite distances from the particle, they can have significant effects on the particle motion.

In chapter II deformable drop motion via buoyancy is examined and the time evolution of drop shape is obtained. This work is of interest in the field of coalescence. Understanding the interaction of a deformable drop with a planar wall is a first step toward understanding how two drops coalesce or how a drop interacts with an interface. In this regard, the experimentally observed phenomenon known as “dimpling” is crucial. A dimpled configuration is one in which the film trapped between the drop and the planar wall (or second drop, or fluid-fluid interface) is thinner near the rim than at the center. Details of the drainage of this “trapped” fluid are necessary to understanding coalescence. A multitude of researchers have developed analytic theories to model the dimpling and drainage phenomenon. These analytic theories are based upon the assumption that the trapped film is *sufficiently thin* to apply a lubrication type analysis; this assumption is examined in detail.

Thermocapillarity provides the mechanism for drop motion and deformation in chapter III. With recent advances in space technology, materials processing in space is rapidly becoming a reality. In the low-gravity environment of outer space, thermocapillary migration is a potential mechanism for separation techniques.

We employ a numerical method to examine wall interactions in chapters I-III. Specifically, we use a numerical technique based upon a boundary integral

reformulation of Stokes equation. In particular, the kernels in the integral reformulation derive from the Green's function corresponding to a no-slip planar boundary. By employing the wall Green's function we totally eliminate the need to numerically truncate and discretize the planar wall. This simplification has significant consequences in terms of numerical accuracy and speed.

Chapter IV is an independent digression from the theme of this thesis; here we examine a numerical technique developed by Ryskin and Leal for generating boundary-fitted orthogonal coordinate grids.

## Table of Contents

Aknowledgement .....	ii
Abstract .....	iii
Thesis Introduction .....	v
Chapter I: Low-Reynolds number hydrodynamic interaction of a solid parti- cle with a planar wall .....	1
Introduction .....	2
Formulation .....	4
(a) Theory .....	4
(b) Formulation for particle translation in an otherwise quiescent fluid .....	9
(c) Implementation .....	11
Numerical Results .....	13
(a) Sphere near a plane wall .....	13
(b) Ellipsoids near a plane wall .....	16
Conclusions .....	20
Appendix .....	21
(a) The Integrals $C_p^{nm}$ and $\hat{C}_p^{nm}$ .....	21
(b) Small $k$ expansions .....	22
(c) The Singular Contributions .....	23
References .....	24
Figure Captions .....	25
Table Captions .....	28

Figures .....	30
Tables .....	54
Chapter II: Buoyancy-driven motion of a deformable drop toward a planar wall at low Reynolds number .....	71
Introduction .....	72
Formulation .....	76
(a) Equations and boundary conditions .....	76
(b) Implementation .....	86
Numerical Results .....	89
(a) Preliminary testing .....	89
(b) Results .....	92
(c) Discussion .....	99
Appendix A .....	102
(a) The matrices $\mathbf{P}$ , $\mathbf{Q}$ and the vectors $\mathbf{S}$ and $\mathbf{W}$ .....	102
(b) The Integrals $C_p^{nm}$ and $\hat{C}_p^{nm}$ .....	104
(c) The Singular Contributions .....	107
Appendix B: The thin film trapped between a bubble and a planar wall .....	110
Introduction .....	111
Formulation .....	113
Discussion .....	122
References .....	125
Figure Captions .....	127
Appendix Figure Captions .....	131

Figures .....	132
Chapter III: Thermocapillary motion of a deformable drop toward a planar wall .....	173
Introduction .....	174
Formulation .....	176
(a) Equations and boundary conditions .....	176
(b) Implementation .....	184
Numerical Results .....	188
Conclusions .....	192
Appendix .....	193
(a) The integrands $P$ , $Q$ and $W$ .....	173
(b) Solution of equation (29) .....	195
References .....	197
Figure Captions .....	198
Figures .....	200
Chapter IV: A note on distortion functions for the strong constraint method of numerically generating orthogonal coordinate grids .....	213
Abstract .....	214
Introduction .....	215
Formulation .....	218
The Proof .....	220
Conclusions .....	224
Acknowledgements .....	225
References .....	226

Figure Captions .....	227
Figures .....	228
Thesis Conclusions .....	229

Chapter I

**Low-Reynolds number hydrodynamic interaction  
of a solid particle  
with a planar wall**

E.P. Ascoli, D.S. Dandy, and L.G. Leal

Dept. of Chemical Engineering

California Institute of Technology

Pasadena, California 91125

## Introduction

Knowledge of the hydrodynamic resistance of a solid body moving slowly through a viscous liquid is of importance in understanding a wide variety of low Reynolds number sedimentation phenomena. The majority of slow viscous flow resistance calculations have focused on situations where the fluid media extends to infinity in all directions. In all real situations, however, the fluid is externally bounded by rigid walls or free surfaces. When these external boundaries are located at finite distances from the particle, they can have significant effects on the particle motion. A variety of authors have theoretically considered the effects of walls on the creeping motion of small solid particles for specific cases where the particle and wall geometries are simple. In particular, Brenner (1961) used bipolar co-ordinates to obtain "exact" corrections to Stokes drag for a solid sphere moving perpendicular to a solid wall for the full range of wall to sphere distances. Wakiya (1957) considered slow viscous flow past ellipsoids between two parallel walls. For more general geometries, asymptotic theory has been developed using the method of reflections when the particle is, in some sense, far from the wall. For example, Brenner (1962, 1964) and Cox and Brenner (1967) have considered the problem of an arbitrary particle in the limiting case that the ratio of particle dimension to the distance from bounding walls is small. At the other extreme, when the particle-to-wall distance is small compared to the particle dimension, classical lubrication theory (Cox, 1974 and Reynolds, 1901) has been applied.

For more general cases, it is most convenient to adopt a numerical method. In particular, for low Reynolds number flows governed by the creeping motion equations, the most efficient approach is the boundary integral method pioneered by Youngren and Acrivos (1975) for uniform flow past a solid particle of *arbitrary* shape in an unbounded fluid medium. In their technique, the creeping flow problem was formulated as a system of linear integral equations of the first kind for the distribution of stokeslets over the particle surface. The unknown

densities of the stokeslets were exactly the desired particle surface stress forces. Subsequent numerical discretization of the integral system yielded an algebraic system which was easily solved for the particle surface stress forces.

The formulation of Youngren and Acrivos could also be applied to the case of a solid particle moving near a planar wall. Due to their choice of the stokeslet as the fundamental singular solution, however, surface stress forces would need to be determined at the planar wall as well as the particle surface. In general, this would necessitate truncation of the planar wall to a finite region, with subsequent distribution of elements on this finite region. The present work considers an alternative boundary integral formulation of the problem, with the fundamental singular solution, or more accurately the Green's function, selected to eliminate the need for determination of surface forces on the planar wall. The formulation will be sufficiently general to allow calculations for arbitrary particles in any base flow that satisfies Stokes equations and the no-slip condition on the planar wall. For simplicity, however, the method is *illustrated* for the specific case of axisymmetric ellipsoidal particles moving perpendicular to the planar wall in an otherwise quiescent fluid.

## Formulation

### (a) Theory

We consider the slow motion of a solid particle in the vicinity of an infinite, no-slip, planar boundary. The suspending fluid is assumed to be Newtonian with constant density. The problem is shown schematically in figure 1. The analysis presented here is based upon the creeping motion approximation in which the inertial terms in the equations of motion are neglected entirely. The governing equations, in dimensionless form, are thus:

$$0 = -\nabla p + \nabla^2 \mathbf{u} \quad (1)$$

$$0 = \nabla \cdot \mathbf{u} \quad (2)$$

The boundary conditions are

$$\mathbf{u} \longrightarrow 0 \quad \text{as } \|\mathbf{x}\| \longrightarrow \infty, \quad (3)$$

$$\mathbf{u} = 0 \quad \text{for } \mathbf{x} \in \mathbf{P} = \left\{ \mathbf{x} \in \mathbf{R}^3 : \mathbf{x} = (x, y, z) \text{ and } z = 0 \right\} \quad (4)$$

and on the surface of the particle

$$\mathbf{u} = \mathbf{u}_s(\mathbf{x}_s) \quad (\text{specified}) \quad (5)$$

For the case of a solid particle moving in an otherwise quiescent fluid,  $\mathbf{u}_s$  is constant on the surface. For the case of an imposed base flow at infinity,  $\mathbf{u}_b$ ,  $p_b$ , satisfying Stokes equation and the no-slip condition on the planar wall, the variables  $\mathbf{u}$  and  $p$  in equations (1-5) are to be interpreted as disturbance variables, i.e. the actual flow variables minus the base flow.

In the boundary integral method, equations (1) and (2) and the corresponding boundary conditions (3-5) are recast into an equivalent integral formulation. The current application of the technique differs from previous applications (general details of the boundary integral formulation may be found in Ladyzhenskaya, 1963) primarily in the choice of the so-called “fundamental solution” for

the system. The transformation of equations (1-5) into integral form is accomplished using the Greens formula for the Stokes system:

$$\int_{\Omega} ((\nabla^2 \mathbf{u} - \nabla p) \cdot \mathbf{w} - (\nabla^2 \mathbf{w} + \nabla q) \cdot \mathbf{u}) dV = \int_{\partial\Omega} (\mathbf{n} \cdot \mathbf{T} \cdot \mathbf{w} - \mathbf{n} \cdot \Sigma \cdot \mathbf{u}) dS \quad (6)$$

$\mathbf{x} \in \Omega$

where

$$\mathbf{T} = (\nabla \mathbf{u} + (\nabla \mathbf{u})^T) - p\mathbf{I} \quad (7)$$

$$\Sigma = (\nabla \mathbf{w} + (\nabla \mathbf{w})^T) + q\mathbf{I} \quad (8)$$

Equation (6) is valid for any sufficiently smooth fields  $\mathbf{u}$ ,  $p$  and  $\mathbf{w}$ ,  $q$  such that  $\mathbf{u}$  and  $\mathbf{w}$  are solenoidal. Here  $\Omega$  is a subset of  $\mathbf{R}^3$  and  $\partial\Omega$  is its boundary with outer normal  $\mathbf{n}$ . This formula, which relates the Stokes operator to its adjoint operator, is derived by direct application of the divergence theorem and algebraic manipulation. Solutions to appropriately selected adjoint operator systems may be superposed using equation (6).

Thus, in the "classical" boundary integral formulation, Youngren and Acrivos (1975, 1976), Lee and Leal (1982), Rallison and Acrivos (1978) all used the fundamental solution corresponding to a point force in an *unbounded* Newtonian fluid, i.e. the solution of

$$\begin{aligned} \delta(\mathbf{x} - \xi) \mathbf{e}_j &= \nabla_{\xi} \hat{\mathbf{q}}^j(\mathbf{x}, \xi) + \nabla_{\xi}^2 \hat{\mathbf{v}}^j(\mathbf{x}, \xi) \\ 0 &= \nabla_{\xi} \cdot \hat{\mathbf{v}}^j(\mathbf{x}, \xi) \end{aligned} \quad (9)$$

subject to the simple additional conditions

$$\hat{\mathbf{v}}^j(\mathbf{x}, \xi), \hat{\mathbf{q}}^j(\mathbf{x}, \xi) \longrightarrow 0 \quad \|\mathbf{x}\|, \|\xi\| \longrightarrow \infty \quad (10)$$

This "fundamental solution" is the so-called stokeslet solution

$$\begin{aligned} \hat{v}_i^j &= -\frac{1}{8\pi} \left\{ \frac{\delta_{ij}}{r} + \frac{r_i r_j}{r^3} \right\} \\ \hat{q}^j &= \frac{1}{4\pi} \left\{ \frac{r_j}{r^3} \right\} \\ \hat{\Sigma}_{kl}^j &= \frac{3}{4\pi} \left\{ \frac{r_k r_l r_j}{r^5} \right\} \end{aligned} \quad (11)$$

where  $\mathbf{r} = (\xi - \mathbf{x})$ . Physically,  $\hat{v}_i^j$  is the  $i^{\text{th}}$  component of the velocity at  $\xi$  due to a unit force, or stokeslet, applied at the point  $\mathbf{x}$  in the direction  $\mathbf{e}_j$ . The quantity  $-q^j$  is the corresponding pressure. Superposition is performed using equation (6) by identifying  $\mathbf{w}$  with  $\hat{\mathbf{v}}^j(\mathbf{x}, \xi)$ ,  $\Sigma$  with  $\hat{\Sigma}^j$  and  $q$  with  $\hat{q}^j$ . The result is the system of integral equations:

$$-(\mathbf{u}(\mathbf{x}))_j = \int_{\partial\Omega} \mathbf{n} \cdot \mathbf{T}(\xi) \cdot \hat{\mathbf{v}}^j(\xi, \mathbf{x}) dS_\xi - \int_{\partial\Omega} \mathbf{n} \cdot \hat{\Sigma}^j(\xi, \mathbf{x}) \cdot \mathbf{u}(\xi) dS_\xi$$

$\mathbf{x} \in \Omega \quad \text{for} \quad j = 1, 2, 3$

(12)

The first integral in equation (12) is termed the single layer potential and has density  $\mathbf{f} = \mathbf{n} \cdot \mathbf{T}$ . Similarly, the second integral is called the double layer potential with density  $\mathbf{u}$ . Equation (12) provides an integral representation for the solution of Stokes equation in terms of the values of the surface stress and velocity on  $\partial\Omega$ . However, equation (12) is, strictly speaking, only valid for  $\mathbf{x} \in \Omega$  but, in fact, the single layer potential is continuous at the boundary while, the double layer potential suffers a jump across the boundary given by

$$\lim_{\mathbf{x} \in \Omega \rightarrow \mathbf{x}_s} \left\{ \int_{\partial\Omega} \mathbf{n} \cdot \hat{\Sigma}^j(\xi, \mathbf{x}) \cdot \mathbf{u}(\xi) dS_\xi \right\}$$

$$= \frac{1}{2}(\mathbf{u}(\mathbf{x}_s))_j + \int_{\partial\Omega} \mathbf{n} \cdot \hat{\Sigma}^j(\xi, \mathbf{x}_s) \cdot \mathbf{u}(\xi) dS_\xi$$

$$\lim_{\mathbf{x} \in \Omega^c \rightarrow \mathbf{x}_s} \left\{ \int_{\partial\Omega} \mathbf{n} \cdot \hat{\Sigma}^j(\xi, \mathbf{x}) \cdot \mathbf{u}(\xi) dS_\xi \right\}$$

$$= -\frac{1}{2}(\mathbf{u}(\mathbf{x}_s))_j + \int_{\partial\Omega} \mathbf{n} \cdot \hat{\Sigma}^j(\xi, \mathbf{x}_s) \cdot \mathbf{u}(\xi) dS_\xi$$

where  $\mathbf{x}_s \in \partial\Omega$

(13)

Here  $\Omega^c = \mathbf{R}^3 / (\Omega \cup \partial\Omega)$  is the exterior to  $\Omega$  and its boundary  $\partial\Omega$ . Thus at the boundary, eqn(12) may be written as

$$-\frac{1}{2}(\mathbf{u}(\mathbf{x}_s))_j = \int_{\partial\Omega} \left( \mathbf{n} \cdot \mathbf{T}(\xi) \cdot \hat{\mathbf{v}}^j(\xi, \mathbf{x}_s) - \mathbf{n} \cdot \hat{\Sigma}^j(\xi, \mathbf{x}_s) \cdot \mathbf{u}(\xi) \right) dS_\xi$$

$\mathbf{x}_s \in \partial\Omega$

(14)

Note that the problem has not actually been solved but instead recast as a system of integral equations. The normal tractions,  $\mathbf{f}$ , are not known at the boundaries. The value of this boundary integral reformulation lies in the fact that knowledge of the boundary *velocity* (via boundary conditions) then allows direct calculation of the normal tractions via (14). The formulation (14) was used by Youngren and Acrivos (1975) to calculate the drag forces on solid particles in an unbounded domain. In that case,  $\Omega$  corresponds to the unbounded fluid and  $\partial\Omega$  to the surface of the particle.

However, when this “standard” formulation is applied to the current problem, depicted in figure 1, then necessarily  $\partial\Omega = S_P + \mathbf{P}$ . In this case, the normal tractions must be calculated both on the body surface and on the planar wall  $\mathbf{P}$ . Although the unknown normal tractions can be determined numerically, the planar wall must necessarily be truncated at a *finite* distance from the axis of symmetry, and the “remaining” portion of the wall discretized.

A more efficient path used in the following sections of this paper is to choose a fundamental solution, or more correctly a Greens function, that includes the no-slip boundary condition at the wall. Thus, instead of (11) we use the solution of the system

$$\begin{aligned} \delta(\mathbf{x} - \boldsymbol{\xi})\mathbf{e}_j &= \nabla_{\boldsymbol{\xi}}\mathbf{q}^j(\mathbf{x}, \boldsymbol{\xi}) + \nabla_{\boldsymbol{\xi}}^2\mathbf{v}^j(\mathbf{x}, \boldsymbol{\xi}) \\ 0 &= \nabla_{\boldsymbol{\xi}} \cdot \mathbf{v}^j(\mathbf{x}, \boldsymbol{\xi}) \end{aligned} \tag{15}$$

$$\mathbf{v}^j(\mathbf{x}, \boldsymbol{\xi}) = 0 \quad \boldsymbol{\xi} \in \mathbf{P} \quad \mathbf{x} \in \mathbf{R}^3 \tag{16}$$

as the fundamental solution or Green’s function to be superposed via (6). The solution to this system is discussed by Blake (1971) and stems from the work of

Oseen(1927). It is

$$\begin{aligned}
 v_i^j &= -\frac{1}{8\pi} \left\{ \frac{\delta_{ij}}{r} + \frac{r_i r_j}{r^3} - \frac{\delta_{ij}}{R} - \frac{R_i R_j}{R^3} \right. \\
 &\quad \left. + 2x_3 \Delta_j \frac{\partial}{\partial R_j} \left[ \frac{x_3 R_i}{R^3} - \frac{\delta_{i3}}{R} - \frac{R_i R_3}{R^3} \right] \right\} \\
 &= -\frac{1}{8\pi} \left\{ \frac{\delta_{ij}}{r} + \frac{r_i r_j}{r^3} - \frac{\delta_{ij}}{R} - \frac{R_i R_j}{R^3} \right. \\
 &\quad + 2x_3 \Delta_j \left[ x_3 \left( \frac{\delta_{ij}}{R^3} - \frac{3R_i R_j}{R^5} \right) + \frac{\delta_{i3}}{R^3} R_j \right. \\
 &\quad \left. \left. - \frac{1}{R^3} (\delta_{ij} R_3 + R_i \delta_{3j}) + \frac{3R_i R_j R_3}{R^5} \right] \right\} \tag{17}
 \end{aligned}$$

$$p^j = \frac{1}{4\pi} \left[ \frac{r_j}{r^3} - \frac{R_j}{R^3} - 2x_3 \Delta_j \left( \frac{\delta_{3j}}{R^3} - \frac{3R_j R_3}{R^5} \right) \right] \tag{18}$$

$$\begin{aligned}
 \Sigma_{ik}^j &= \frac{3}{4\pi} \left\{ \frac{r_i r_j r_k}{r^5} - \frac{R_i R_j R_k}{R^5} - 2x_3 \Delta_j \left[ -\frac{x_3}{R^5} \delta_{ik} R_j \right. \right. \\
 &\quad \left. \left. + \frac{\xi_3}{R^5} (R_i \delta_{jk} + \delta_{ij} R_k) + \frac{R_i \delta_{3j} R_k}{R^5} - \frac{5R_i R_j R_k \xi_3}{R^7} \right] \right\}. \tag{19}
 \end{aligned}$$

where  $\mathbf{r} = (\xi_1 - x_1, \xi_2 - x_2, \xi_3 - x_3)^T$ ,  $\mathbf{R} = (\xi_1 - x_1, \xi_2 - x_2, \xi_3 + x_3)^T$ ,  $r = [(\xi_1 - x_1)^2 + (\xi_2 - x_2)^2 + (\xi_3 - x_3)^2]^{1/2}$ ,  $R = [(\xi_1 - x_1)^2 + (\xi_2 - x_2)^2 + (\xi_3 + x_3)^2]^{1/2}$ , and  $R_3 = \xi_3 + x_3$ . The quantity  $\Delta_j$  has value +1 for  $j = 1, 2$  and -1 for  $j = 3$ . Note that the Greens function (17-19) consists of the fundamental solution (11) plus terms due to the presence of the wall. It corresponds to the velocity, pressure and stress fields for a point force in the fluid in the presence of a plane wall, upon which the no-slip condition has already been applied. Given the geometry of figure 1, the analog of equation (12) for this Greens function is

$$\begin{aligned}
 -(\mathbf{u}(\mathbf{x}))_j &= \int_{S_P} \left( \mathbf{n} \cdot \mathbf{T}(\xi) \cdot \mathbf{v}^j(\xi, \mathbf{x}) - \mathbf{n} \cdot \Sigma^j(\xi, \mathbf{x}) \cdot \mathbf{u}(\xi) \right) dS_\xi \\
 &\quad \mathbf{x} \in \mathbf{D} \quad \text{for } j = 1, 2, 3 \tag{20}
 \end{aligned}$$

In this expression,  $\mathbf{n}$  is the normal vector pointing inward to  $\mathbf{D}_c$ . Due to condition (16), the surface integration in (20) is over  $S_P$  and not  $S_P + \mathbf{P}$  as would be the case if the fundamental solution (11) were used. The additional wall terms are well behaved for  $\mathbf{x} \in S_P$ . As a result, each term above involving the kernel

$\mathbf{v}^j$  is continuous for  $\mathbf{x} \in S_P$ . The terms involving the kernel  $\Sigma^j$  suffer a jump across  $S_P$  but this discontinuity stems directly from the  $\mathbf{r}$  terms i.e. the terms present in the fundamental solution (11). Thus, the jump condition follows from eqn(13) and is

$$\begin{aligned}
 & \lim_{\mathbf{x} \in \mathbf{D} \rightarrow \mathbf{x}_s} \left\{ \int_{S_P} \mathbf{n} \cdot \Sigma^j(\xi, \mathbf{x}) \cdot \mathbf{u}(\xi) dS_\xi \right\} \\
 &= \frac{1}{2}(\mathbf{u}(\mathbf{x}_s))_j + \int_{S_P} \mathbf{n} \cdot \Sigma^j(\xi, \mathbf{x}_s) \cdot \mathbf{u}(\xi) dS_\xi \\
 & \lim_{\mathbf{x} \in \mathbf{D}_c \rightarrow \mathbf{x}_s} \left\{ \int_{S_P} \mathbf{n} \cdot \Sigma^j(\xi, \mathbf{x}) \cdot \mathbf{u}(\xi) dS_\xi \right\} \\
 &= -\frac{1}{2}(\mathbf{u}(\mathbf{x}_s))_j + \int_{S_P} \mathbf{n} \cdot \Sigma^j(\xi, \mathbf{x}_s) \cdot \mathbf{u}(\xi) dS_\xi \\
 & \qquad \qquad \qquad \mathbf{x}_s \in S_P \qquad \qquad \qquad (21)
 \end{aligned}$$

Thus, in terms of the Greens function (17-19) the system to be solved is:

$$\begin{aligned}
 -\frac{1}{2}(\mathbf{u}_s(\mathbf{x}_s))_j &= - \int_{S_P} \Sigma^j(\mathbf{x}_s, \xi) \cdot \mathbf{u}_s(\xi) \cdot \mathbf{n} dS_\xi + \int_{S_P} \mathbf{v}^j(\mathbf{x}_s, \xi) \cdot \mathbf{f}(\xi) dS_\xi \\
 \mathbf{x}_s &\in S_P \qquad \qquad \qquad (22)
 \end{aligned}$$

This is the primary result of this section. Equation (22) provides a relationship between the unknown tractions  $\mathbf{f}$  on the particle surface and the particle velocity for arbitrary particle-wall geometries and base flows.

**(b) Formulation for particle translation in an otherwise quiescent fluid**

For the case in which the particle translates in an otherwise quiescent fluid, the result (22) can be simplified further. In this case,  $\mathbf{u}(\mathbf{x}_s) = \mathbf{u}_s$  is a constant for  $\mathbf{x}_s \in S_P$ . Modifying the arguments of Ladyzhenskaya (1963) it can be shown that for a constant vector,  $\mathbf{C}$

$$\int_{S_P} \mathbf{n} \cdot \Sigma^j(\xi, \mathbf{x}) \cdot \mathbf{C} dS_\xi = \begin{cases} 0 & \mathbf{x} \in \mathbf{D} \\ -\frac{1}{2}\mathbf{C}_j & \mathbf{x} \in S_P \\ -\mathbf{C}_j & \mathbf{x} \in \mathbf{D}_c \end{cases}$$

Using this fact, we obtain a linear integral equation of the first kind for  $\mathbf{f}$

$$-(\mathbf{u}_s)_j = \int_{S_P} \mathbf{v}^j(\mathbf{x}_s, \xi) \cdot \mathbf{f}(\xi) dS_\xi \quad \mathbf{x}_s \in S_P \quad (23)$$

For the case of axisymmetric motion, i.e.,  $\mathbf{u}_s = -\mathbf{e}_z$  with the particle oriented such that it possesses axisymmetry about the  $z$  axis, these equations simplify further. Here, the particle is a body of revolution with the  $z$ -axis being the axis of revolution. For convenience, a cylindrical coordinate system is employed with  $\rho = \sqrt{x^2 + y^2}$ . There are several ways in which the particle surface may be represented. The simplest (used by Youngren and Acrivos, 1975) is to define the particle surface as  $(\rho(z), z)$  for  $\theta \in [0, 2\pi)$ , the functional dependence of  $\rho$  on  $z$  being given. This representation implicitly limits the types of surfaces which can be considered to those for which  $\rho$  is a single valued function of  $z$ . An equally simple, but more general representation, which avoids this potential problem, is to parametrically define the surface as  $(\rho(s), z(s))$  for  $\theta \in [0, 2\pi)$ , where  $s$  is a parametric independent variable. This was the approach taken here.

The dependence of the integrands on  $\theta$  in this system is known explicitly, and integration with respect to this variable may be performed. Although the resulting integration yields quite complex expressions, the net result is the reduction of the integration domain from two dimensions to one. The resulting equation for the unknown surface stress components,  $f_\rho$  and  $f_z$ , is

$$\begin{pmatrix} 0 \\ -1 \end{pmatrix} = - \int_{s_0}^{s_f} \mathbf{Q}(\mathbf{x}_s, \xi(s)) \cdot \begin{pmatrix} f_\rho \\ f_z \end{pmatrix} \rho(s) \left( \dot{\rho}^2(s) + \dot{z}^2(s) \right)^{1/2} ds$$

$\mathbf{x}_s \in S_P$   
(24)

where  $\dot{\rho}(s)$  and  $\dot{z}(s)$  are the derivatives of  $\rho$  and  $z$  with respect to  $s$  and

$$\begin{aligned} -8\pi Q_{11} &= C_1^{01} - \hat{C}_1^{01} + \rho\rho_0(C_3^{02} - \hat{C}_3^{02}) + (\rho^2 + \rho_0^2)(C_3^{01} - \hat{C}_3^{01}) \\ &\quad + \rho\rho_0(C_3^{00} - \hat{C}_3^{00}) - 2z_0z[\hat{C}_3^{01} \\ &\quad - 3\{(\rho^2 + \rho_0^2)\hat{C}_5^{01} + \rho\rho_0(\hat{C}_5^{02} + \hat{C}_5^{00})\}] \\ 8\pi Q_{12} &= \rho(r_3C_3^{01} - R_3\hat{C}_3^{01}) + \rho_0(r_3C_3^{00} - R_3\hat{C}_3^{00}) \\ &\quad + 2z_0[\rho\hat{C}_3^{01} + \rho_0\hat{C}_3^{00} + 3zR_3(\rho\hat{C}_5^{01} + \rho_0\hat{C}_5^{00})] \end{aligned}$$

$$\begin{aligned}
 8\pi Q_{21} &= \rho_o(r_3 C_3^{01} - R_3 \hat{C}_3^{01}) + \rho(r_3 C_3^{00} - R_3 \hat{C}_3^{00}) \\
 &\quad + 2z_o [\rho_o \hat{C}_3^{01} + \rho \hat{C}_3^{00} - 3z R_3 (\rho_o \hat{C}_5^{01} + \rho \hat{C}_5^{00})] \\
 -8\pi Q_{22} &= C_1^{00} - \hat{C}_1^{00} + r_3^2 C_3^{00} - R_3^2 \hat{C}_3^{00} \\
 &\quad + 2z_o z (\hat{C}_3^{00} - 3R_3^2 \hat{C}_5^{00}).
 \end{aligned}$$

Here the integration variable  $\xi$  has been written as  $(\rho, z)$  and  $(\rho_o, z_o)$  corresponds to  $\mathbf{x}$ , the fixed point in the integration. Also,  $r_3 = z - z_o$  and  $R_3 = z + z_o$ .

The expressions  $C_p^{nm}$  and  $\hat{C}_p^{nm}$  are defined as:

$$C_p^{nm} \equiv \frac{2}{\gamma^{p/2}} \int_0^\pi \frac{\sin^n 2x \cos^m 2x}{[1 - k^2 \sin^2 x]^{p/2}} dx \quad (25)$$

and

$$\hat{C}_p^{nm} \equiv \frac{2}{\gamma_R^{p/2}} \int_0^\pi \frac{\sin^n 2x \cos^m 2x}{[1 - k_R^2 \sin^2 x]^{p/2}} dx, \quad (26)$$

where

$$\begin{aligned}
 \gamma &= (\rho + \rho_o)^2 + r_3^2 \\
 k^2 &= \frac{4\rho\rho_o}{\gamma}
 \end{aligned}$$

and

$$\begin{aligned}
 \gamma_R &= (\rho + \rho_o)^2 + R_3^2 \\
 k_R^2 &= \frac{4\rho\rho_o}{\gamma_R}.
 \end{aligned}$$

Expressions (25-26) for  $C_p^{nm}$  and  $\hat{C}_p^{nm}$  have been analytically evaluated, and the results of the integrations are given in the appendix.

### (c) Implementation

System (24) may be discretized and numerically solved . The approach taken here is that used by Youngren and Acrivos(1975) , i.e., the method of Krylov-Bogoliubov (Kantorovich and Krylov, 1963 ). Specifically, the particle arc, which is given by  $(\rho(s), z(s))$ , for  $s \in [s_o, s_f]$ , is divided into N elements. This is accomplished by dividing the interval  $[s_o, s_f]$  into subintervals,  $\Delta s_j$ , with centers  $s_j$  ( $j = 1, \dots, N$ ). Each parametric value  $s_j$  corresponds to a point on

the arc  $\mathbf{x}_j = (\rho(s_j), z(s_j))$  and each  $\Delta s_j$  corresponds to a segment or element of the arc. The elements are assumed to be sufficiently small that the local normal tractions  $f_\rho$  and  $f_z$  may be assumed constant within each element. The resulting discretized system is:

$$\begin{pmatrix} 0 \\ -1 \end{pmatrix} \simeq - \sum_{j=1}^N \left\{ \left[ \int_{\Delta s_j} \mathbf{Q}(\mathbf{x}_i, \xi(s)) \rho(s) \left( \dot{\rho}^2(s) + \dot{z}^2(s) \right)^{1/2} ds \right] \cdot \begin{pmatrix} f_\rho(\mathbf{x}_j) \\ f_z(\mathbf{x}_j) \end{pmatrix} \right\} \quad (27)$$

$$1 \leq i \leq N$$

This is a linear system of  $2N$  equations in the  $2N$  unknowns  $f_\rho(\mathbf{x}_j), f_z(\mathbf{x}_j)$  where ( $1 \leq j \leq N$ ). Each coefficient

$$\left[ \int_{\Delta s_j} \mathbf{Q}(\mathbf{x}_i, \xi(s)) \rho(s) \left( \dot{\rho}^2(s) + \dot{z}^2(s) \right)^{1/2} ds \right] \quad (28)$$

for  $j \neq i$  was evaluated by gaussian quadrature. When  $j = i$ , and  $s = s_i$  then  $\xi(s) = \mathbf{x}_i$ , and the function  $\mathbf{Q}$  becomes unbounded. In this case, the region  $\Delta s_j$  is subdivided into three smaller regions, one of which is centered at the singular point  $s_j$  and is  $\Delta_j^{sing} = [s_j - \frac{\epsilon}{2}, s_j + \frac{\epsilon}{2}]$ . The constant  $\epsilon$  is assumed small enough that over  $\Delta_j^{sing}$  the arc may be accurately approximated by the tangent line through the point  $\mathbf{x}_j$ . Following Lee and Leal (1982), the singular contribution to equation (27) from over the interval  $\Delta_j^{sing}$  can be approximated analytically. The details of the singular contribution are given in the appendix. In the remaining two portions of the singular element,  $\Delta s_j$ , accurate Rhomberg integration was performed. The linear system was solved using a standard matrix inverter.

## Numerical Results

Axisymmetric flow calculations were performed on the class of ellipsoidal particles given by (figure 2a)

$$\rho^2/a^2 + z^2/b^2 = 1$$

or equivalently, written in parametric form

$$z = z_{gap} + b \left[ \sin \left( \pi s - \frac{\pi}{2} \right) + 1 \right]$$

$$\rho = a \cos \left( \pi s - \frac{\pi}{2} \right)$$

$$s \in [0, 1]$$

The parameters  $a$ ,  $b$  and  $z_{gap}$  have been made dimensionless with respect to the length,  $l$ , which is the radius of a sphere of equivalent volume. This nondimensionalization provides a relationship between  $a$  and  $b$ . In fact, if  $\alpha = b/a$  then  $b = \alpha^{2/3}$  and  $a = \alpha^{-1/3}$ . Thus  $\alpha$  and  $z_{gap}$ , the minimum particle to wall distance, are the only geometric variables in the system. The case of a sphere is recovered by setting  $\alpha = 1$ . The parametric variable  $s$  was chosen for simplicity, and in fact  $\pi s$  corresponds to the angle shown in figure 2b. A non-optimal strategy of constant element width,  $\Delta s$ , was employed. In all cases, the particle drag was normalized with respect to the theoretical values for an unbounded fluid (Lamb, 1945). The normalized drag force is denoted by  $\lambda$ .

### (a) Sphere near a plane wall

For the special case of a sphere, "exact" values of  $\lambda$  are given by (Brenner, 1961)

$$\lambda = \frac{4}{3} \sinh(\omega) \sum_{n=1}^{\infty} \frac{n(n+1)}{(2n-1)(2n+3)} \left\{ \frac{2 \sinh[(2n+1)\omega] + (2n+1) \sinh(2\omega)}{4 \sinh^2[(n+\frac{1}{2})\omega] - (2n+1)^2 \sinh^2(\omega)} - 1 \right\}$$

$$\text{where } \omega = \ln \left( z_{gap} + 1 + \sqrt{z_{gap}^2 + 2z_{gap}} \right)$$

(29)

Table 1 lists the results from expression (29) as well as numerical results obtained here with 10, 20, 30 and 40 elements on the surface of the sphere. Even for 10 elements, the numerical and theoretical results are in excellent agreement. For all values of  $z_{gap}$  in the range 100 to 0.25 the error is less than 0.5 percent for 10 elements, less than 0.09 percent for 20 elements, 0.05 percent for 30 elements and less than 0.03 percent for 40 elements. For smaller values of  $z_{gap}$  the accuracy deteriorates for all numbers of elements because the magnitude of the local stresses and stress gradients increase dramatically on the wall side of the sphere as  $z_{gap}$  decreases. Large stress gradients lead to a breakdown of the constant-within-each-element assumption and so degrade numerical accuracy.

The evolution of the local surface stresses as the sphere approaches the wall is plotted in figures 3a and 3b for the 40 element case. An increase in the number of elements in the small  $z_{gap}$  case improves the overall accuracy. This is demonstrated by the fact that with 40 elements and  $z_{gap} = 0.1$  the error in the normalized drag is 0.265%, as compared with 2.93 percent for 10 elements. In the closest case of  $z_{gap} = 0.05$  with 40 elements the error in drag is only 1.13 percent.

For the sake of comparison, sphere calculations were also performed using the classical boundary integral technique with the Stokeslet fundamental solution. This entailed integration over the planar wall. The planar wall was discretized by truncating at a radial distance denoted by  $\rho_t$  and placing  $N_{wall}$  elements in the interval from  $\rho = 0$  to  $\rho_t$ .  $N_{sphere}$  elements of constant  $\Delta s$  width were used on the sphere surface. On the wall, elements of constant as well as non-constant width,  $\Delta\rho$ , were employed. The non-constant width elements were selected so that the  $\Delta\rho$  was small near  $\rho = 0$  and increasing in size to  $\rho = \rho_t$ . \*

---

\* There are an infinite number of choices for such a non-constant distribution of elements. The current choice was made arbitrarily and for simplicity. If  $\hat{\rho}_j = \rho_t \left(\frac{j-\frac{1}{2}}{N_{wall}}\right)^2$  then the  $j^{th}$  element is the interval  $[(\hat{\rho}_{j-1} + \hat{\rho}_j)/2, (\hat{\rho}_{j+1} + \hat{\rho}_j)/2]$  for  $j = 2, 3, \dots, N_{wall} - 1$ . The first interval is  $[0, (\hat{\rho}_1 + \hat{\rho}_2)/2]$  and the last

The results are given in tables 2-5 where the numerical values for various combinations of  $N_{wall}$ ,  $N_{sphere}$  and  $\rho_t$  are compared to the exact solutions of Brenner. Although the accuracy obtained is quite good when the sphere is far from the wall for the majority of the cases considered, accuracy degrades rapidly as the sphere approaches the wall. As expected, when the sphere is near the wall the accuracy is best when the wall elements near  $\rho = 0$  are smallest since smaller elements are capable of resolving the large variation in wall surface traction. Thus for both constant and non-constant width elements the best accuracy near the wall for a given  $N_{wall}$  occurs when  $\rho_t$  is smallest.

The Stokeslet and Greens function methods are best compared on the basis of total number of elements,  $N_{total}$ , where  $N_{total} = N_{wall} + N_{sphere}$  for the Stokeslet case and  $N_{total}$  is taken to be the number of elements,  $N$ , on the particle surface for the Green's function method. Overall, for the same  $N_{total}$  the Greens function results are far superior in accuracy to the Stokeslet results. In particular, the Greens function results for  $N = N_{total} = 30$ , with few exceptions, are more accurate than any of the Stokeslet results for  $N_{total} = 60$  ( $N_{wall} = 30$ ,  $N_{sphere} = 30$ ). It is anticipated that the accuracy of the Stokeslet method may be improved by distributing more, smaller width elements near  $\rho = 0$  on the wall. Nevertheless, such redistributions are ad hoc and of unlimited variety. Further, such redistribution of points on the sphere surface for both the Greens function and Stokeslet methods could also undoubtedly lead to increased accuracy. Employing the Greens function entirely eliminates the need for ad hoc choices of *wall* element distributions and *wall* truncation distances. For the solid sphere problem Brenner's exact solution is known and the dependence of the accuracy of the Stokeslet method on the parameters  $N_{wall}$ ,  $\rho_t$  and the distribution of elements can be determined. In any realistic problem the choice

---

interval is  $[(\hat{\rho}_{N_{wall}-1} + \hat{\rho}_{N_{wall}-2})/2, \rho_t]$ .  $z_j=0$  for all intervals. This distribution corresponds approximately to a linear increase in the  $\Delta\rho$  width moving outward along the wall.

of these parameters may be difficult or unmotivated.

Figure 4 compares the computational time for the Greens function and the Stokeslet methods as a function of  $N_{total}$ . When  $N_{total}$  is small the Greens function method is approximately 1 1/2 times slower than the Stokeslet method. The longer computational time of the Greens function method for the same  $N_{total}$  is a direct consequence of the increased complexity of computing the Greens function kernels compared with the Stokeslet kernels. For larger  $N_{total}$ , the time required to invert either the Stokeslet or Greens function linear systems for the same  $N_{total}$  ( which is approximately the same since both systems are  $2N_{total} \times 2N_{total}$  in size) becomes more important and the *ratio* of computational times tends toward 1. Note, however, that for comparable accuracy the Greens function method requires less than 1/2 the total number of elements that the Stokeslet method requires. Thus, for a given level of accuracy the Green's function method is actually substantially faster than the Stokeslet method. All computations were performed on a Sun 3/160 workstation with a floating point accelerator. Absolute computational times were on the order of minutes (for instance, Stokeslet method calculations with  $N_{total} = 60$  took approximately 240 cpu seconds,  $N_{total}=40$  took 100 cpu seconds,  $N_{total}=20$  took 25 cpu seconds and  $N_{total}=12$  took 10 cpu seconds).

(b) **Ellipsoids near a plane wall**

Calculations were carried out for ellipsoids with axes ratios  $\alpha$  of 0.0625, 0.125, 0.25, 0.5, 2, 4, 8 and 16. The parameter  $z_{gap}$  ranged from 0.05 to 100. Computations were terminated for small  $z_{gap}$  when calculated local stresses grew large and differed significantly in neighboring elements (this generally occurred when the computed value of  $\lambda$  was of the order of several hundred).

Brenner (1962) developed an asymptotic theory for the case when an arbitrarily shaped particle is in motion far from the wall. More specifically, if  $R_{eq}$  is the equivalent radius of the particle (defined such that  $6\pi\mu UR_{eq}$  is the

force exerted on the particle when falling with velocity  $U$  in the absence of the wall) then Brenner's asymptotic theory is valid for  $z_c \stackrel{def}{=} z_{center}/R_{eq} \gg 1$  where  $z_{center}$  is the dimensional z-axis distance to the center of the particle. This asymptotic theory predicts an expression of the form

$$\lambda = \frac{1}{1 - \frac{9}{8z_c} + O(z_c^{-3})} \quad (30)$$

Note that  $z_c = (z_{gap} + \alpha^{2/3}) \frac{l}{R_{eq}}$  and for ellipsoidal particles  $R_{eq}$  is derived from the general expressions (Lamb, 1945):

$$\frac{R_{eq}}{l} = \frac{8}{3(\alpha^{4/3}\kappa_0 + \beta_0)}$$

and

$$\kappa_0 = \frac{\beta_0 \alpha^{2/3} - 2}{\alpha^2 - 1}$$

$$\beta_0 = \frac{\alpha^{1/3}}{\sqrt{\alpha^2 - 1}} \ln\left(\frac{\alpha + \sqrt{\alpha^2 - 1}}{\alpha - \sqrt{\alpha^2 - 1}}\right) \quad \text{for } \alpha^2 - 1 > 0$$

$$\beta_0 = \frac{2\alpha^{1/3}}{\sqrt{1 - \alpha^2}} \left(\frac{\pi}{2} - \arctan\left(\frac{\alpha}{\sqrt{1 - \alpha^2}}\right)\right) \quad \text{for } \alpha^2 - 1 < 0$$

Numerical results for the ellipsoid and sphere cases are compared with the large  $z_c$  theory in figures 5a-13a and in addition the ellipsoid numerics and large  $z_c$  theory are tabulated in tables 6-13. The most remarkable observation from these comparisons with the large  $z_c$  theory is that the numerical results agree quantitatively with the large  $z_c$  theory for values of  $z_c$  as small as 5., while *qualitative* agreement extends to even lower values of  $z_c$ , including the sharp upturn in  $\lambda$  for  $z_c = \frac{9}{8}$ . However, it is clear that the far-field results cannot literally capture the singularity in  $\lambda$  and other detailed behaviour for very small  $z_{gap}$  ( or  $z_c$ ). For this purpose, a more appropriate asymptotic analysis is via lubrication theory for flow in a thin film.

Using classical lubrication assumptions Cox (1974) developed an asymptotic theory which is valid for the case in which  $z_{lub} \stackrel{def}{=} bz_{gap}/a^2 = z_{gap}\alpha^{4/3} \ll 1$ . This theory predicts

$$\lambda = \frac{1}{\alpha^{4/3} \frac{R_{eq}}{l} z_{lub}} + O(\ln(z_{lub})) \quad (31)$$

Explicit in Cox’s lubrication theory is the assumption that as  $z_{lub} \rightarrow 0$  the approaching surfaces come together in *single point* contact. Thus, Cox’s theory is not valid for the case of a disk approaching a planar wall with the face of the disk parallel to the wall. In fact, the case of a disk of radius  $R$  approaching a planar wall in this manner was analyzed by Reynolds (1901) who predicted:

$$\lambda = \frac{R^4}{4R_{eq}\hat{z}_{gap}^3} \quad (32)$$

where  $\hat{z}_{gap}$  is the dimensional gap distance. Notice that as  $\hat{z}_{gap} \rightarrow 0$  equation (31) predicts  $\lambda$  increasing effectively as  $1/\hat{z}_{gap}$  while equation (32) predicts  $1/\hat{z}_{gap}^3$ . Necessarily, when single point contact will occur (as in all ellipsoid cases considered in this paper) then equation (31) predicts the correct limiting behavior for sufficiently small  $\hat{z}_{gap}$ . Nevertheless, ellipsoids with sufficiently small values of  $\alpha$  resemble disks with radii  $R = bl$ , and we may thus expect Reynolds result, equation (32), to provide a reasonable approximation for some *intermediate*  $\hat{z}_{gap}$  distances, and sufficiently small values of  $\alpha$ . For these ellipsoid cases, equation (32) may be written as

$$\lambda = \frac{\alpha^{8/3}}{4\left(\frac{R_{eq}}{l}\right)z_{lub}^3} \quad (33)$$

Numerical results for small  $z_{lub}$  values are plotted in figures 5b-13b together with the asymptotic formula (31) and, where relevant, (33). For the case  $\alpha = 1$ , we also show Brenner’s analytic theory for a sphere (equation 29).

The results for  $\alpha = 1, 2$  and  $4$  clearly approach the lubrication asymptote. On the other hand, for  $\alpha = 8$  and  $16$ , we were not able to capture the approach to asymptotic behaviour because computations were terminated for  $z_{gap} = 0.05$  and in these cases this corresponds to  $z_{lub}$  values well outside the range of validity of Cox’s lubrication theory.

The numerical results for  $\alpha < 1$  demonstrate the transition between Reynolds’ result for the disk (33) and the lubrication theory (31) at “intermediate” values of  $z_{lub}$  for small  $\alpha$ . In particular, as  $\alpha$  decreases from  $0.5$  to  $0.0625$ , we see that

the numerical results agree closely with (33) over a significant range of  $z_{lub}$  before (presumably) reverting to the lubrication asymptote for even smaller values of  $z_{lub}$ .

It should be noted, in all of the comparisons between our results and Cox's lubrication theory, that the latter is based on the implicit assumption that there exist extremely localized regions of high stresses and stress gradients near the point of smallest gap. Due to resolution difficulties, the current numerics break down when localized high stresses and stress gradients occur. Despite this fact, the numerics is able to provide information indicating trends, asymptotes and approximate regions of validity of Cox's lubrication theory. In particular, the numerics clearly indicate that Reynolds lubrication theory is a better approximation than Cox's theory for small  $\alpha$  cases (0.125 and 0.0625 in particular) and intermediate  $z_{lub}$  values.

## Conclusions

The wall Greens function formulation of the boundary integral method for low Reynolds number flow was carefully tested against the analytic results of Brenner for the translation of a solid sphere toward a plane wall, and was found to yield highly accurate results up to dimensionless gaps of 0.05. When compared to the boundary integral formulation using the Stokeslet fundamental solution, the Greens function formulation was found to be more accurate for the same total number of elements. In fact, the Greens function method required approximately half the number of elements that the Stokeslet method required to maintain the same level of accuracy. Although, the Greens function formulation was slower computationally for the same  $N_{total}$  the requirement of less elements to maintain the same level of accuracy easily compensates timewise for this disadvantage. The solid ellipsoid results compared extremely well with the far-field asymptotic results of Brenner for distances as small as  $z_c = 5$ . The current numerics as well as Brenner's analytic theory for a sphere (equation 29), indicate an upper bound of  $z_{lub} = 0.05$  for the range of predictive validity of Cox's lubrication theory for the particle geometries considered here. Although as  $z_{lub} \rightarrow 0$  Cox's lubrication theory necessarily predicts the correct limiting behavior of  $\lambda$ , for the near disk-like ellipsoids having  $\alpha$  values of 0.25, 0.125 and 0.0625, the numerics indicate that Reynolds lubrication theory for a disk is a more accurate approximation for intermediate  $z_{lub}$ , values in the range of  $0.05 < z_{lub} < 0.1$ .

## Appendix

(a) The integrals  $C_p^{nm}$  and  $\hat{C}_p^{nm}$

Using standard integral tables, the integrals denoted by  $C_p^{nm}$  and  $\hat{C}_p^{nm}$  can be reduced to expressions involving the complete elliptic integrals of the first and second kind given by:

$$K(k) = 2 \int_0^\pi \frac{dx}{[1 - k^2 \sin^2 x]^{1/2}} \quad (A1)$$

$$E(k) = 2 \int_0^\pi \frac{dx}{[1 - k^2 \sin^2 x]^{3/2}} \quad (A2)$$

The final expressions for  $C_p^{nm}$  are:

$$C_1^{00} = \frac{4}{\gamma^{1/2}} K \quad (A3)$$

$$C_1^{01} = C_1^{00} - \frac{8}{k^2 \gamma^{1/2}} (K - E) \quad (A4)$$

$$C_3^{00} = \frac{4}{\hat{k}^2 \gamma^{3/2}} E \quad (A5)$$

$$C_3^{01} = \frac{4}{k^2 \gamma^{3/2}} \left[ 2K - \frac{1 + \hat{k}^2}{\hat{k}^2} E \right] \quad (A6)$$

$$C_3^{20} = \frac{16}{k^4 \gamma^{3/2}} [(1 + \hat{k}^2)K - 2E] \quad (A7)$$

$$C_3^{03} = C_3^{01} - C_3^{20} + \frac{32}{3k^6 \gamma^{3/2}} [(k^2 - 8)E + (8 - 5k^2)K] \quad (A8)$$

$$C_5^{00} = \frac{4}{3\hat{k}^2 \gamma^{5/2}} \left[ \frac{2(1 + \hat{k}^2)}{\hat{k}^2} E - K \right] \quad (A9)$$

$$C_5^{01} = \frac{4}{3k^2 \hat{k}^2 \gamma^{5/2}} \left[ (1 + \hat{k}^2)K - \frac{2}{\hat{k}^2} (\hat{k}^2 + k^4)E \right] \quad (A10)$$

$$C_5^{20} = \frac{16}{3k^4 \gamma^{5/2}} \left[ \frac{1 + \hat{k}^2}{\hat{k}^2} E - 2K \right] \quad (A11)$$

$$C_p^{02} = C_p^{00} - C_p^{20} \quad (A12)$$

where

$$\hat{k}^2 = 1 - k^2$$

The corresponding expressions for  $\hat{C}_p^{nm}$  are obtained from the above by replacing  $\gamma$  with  $\gamma_R$  and  $k$  with  $k_R$ .

(b) Small  $k$  Expansions

When  $k$  and/or  $k_R \rightarrow 0$ , numerical inaccuracy necessitates the use of asymptotic expansions for the expressions  $C_p^{nm}$  and  $\hat{C}_p^{nm}$ . These asymptotic expansions are obtained by performing a generalized binomial expansion in  $k^2$  on the integrands given in Eqs. (25) and (26). The results, accurate to  $O(k^4)$  as  $k \rightarrow 0$  are:

$$C_1^{00} = \frac{2\pi}{\gamma^{1/2}} \left(1 + \frac{1}{8}k^2\right) \quad (A13)$$

$$C_1^{01} = -\frac{\pi k^2}{4\gamma^{1/2}} \quad (A14)$$

$$C_3^{00} = \frac{2\pi}{\gamma^{3/2}} \left(1 + \frac{3}{8}k^2\right) \quad (A15)$$

$$C_3^{01} = -\frac{3\pi k^2}{4\gamma^{3/2}} \quad (A16)$$

$$C_3^{20} = \frac{\pi}{\gamma^{3/2}} \left(1 + \frac{3}{8}k^2\right) \quad (A17)$$

$$C_3^{03} = -\frac{9\pi k^2}{16\gamma^{3/2}} \quad (A18)$$

$$C_5^{00} = \frac{2\pi}{\gamma^{5/2}} \left(1 + \frac{5}{8}k^2\right) \quad (A19)$$

$$C_5^{01} = -\frac{5\pi k^2}{4\gamma^{5/2}} \quad (A20)$$

$$C_5^{20} = \frac{\pi}{\gamma^{5/2}} \left(1 + \frac{5}{8}k^2\right) \quad (A21)$$

Again, the corresponding expressions for  $\hat{C}_p^{nm}$  are obtained from the above by replacing  $\gamma$  with  $\gamma_R$  and  $k$  with  $k_R$ .

(c) The Singular Contributions

The numerical integration breaks down as  $\xi \rightarrow \mathbf{x}$  since the kernel becomes unbounded in this case. To include this integrable singular contribution it is necessary to approximate the integral analytically. This is accomplished by Taylor series expanding the singular terms about the point  $(\rho_o, z_o)$  in (26). The details involved in carrying out these expansions are analogous to those used by Lee and Leal (1982), the differences being only in the choice of parametrization of the surface. It is important to note, however, that only those terms in the kernel  $\mathbf{Q}$  stemming from the fundamental solution (11) must be considered, since  $R \neq 0$  for  $z > 0$ . Hence we consider the integral

$$\begin{aligned}
 \mathbf{a} &= \int_{s_i - \epsilon/2}^{s_i + \epsilon/2} \int_0^{2\pi} \rho [\dot{\rho}^2 + \dot{z}^2]^{1/2} \left\{ \frac{\mathbf{f}}{r} + \frac{\mathbf{f} \cdot \mathbf{r}}{r^3} \mathbf{r} \right\} d\theta ds \\
 &= \int_{s_i - \epsilon/2}^{s_i + \epsilon/2} \rho [\dot{\rho}^2 + \dot{z}^2]^{1/2} ds \left\{ \mathbf{i} \left[ f_\rho C_1^{01} + (\rho^2 + \rho_o^2) f_\rho C_3^{01} \right. \right. \\
 &\quad \left. \left. + \rho \rho_o f_\rho (C_3^{00} + C_3^{02}) + f_z r_3 (\rho C_3^{01} + \rho_o C_3^{00}) \right] \right. \\
 &\quad \left. + \mathbf{k} \left[ f_z C_1^{00} + f_\rho r_3 (\rho C_3^{00} + \rho_o C_3^{01}) + f_z r_3^2 C_3^{00} \right] \right\}, \tag{A21}
 \end{aligned}$$

where  $s_i$  is the value of the arclength parameter of the  $i$ th node, and  $\mathbf{i}$  and  $\mathbf{k}$  are the cartesian base vectors. After carrying out the expansions, the  $\mathbf{i}$  component of the integral is

$$\begin{aligned}
 a_i &\simeq 2\epsilon \left\{ f_{z_o} \frac{\dot{\rho}_o \dot{z}_o}{[\dot{\rho}_o^2 + \dot{z}_o^2]^{1/2}} + f_{\rho_o} \left[ \frac{\dot{\rho}_o^2 + 2\dot{z}_o^2}{[\dot{\rho}_o^2 + \dot{z}_o^2]^{1/2}} \right. \right. \\
 &\quad \left. \left. - [\dot{\rho}_o^2 + \dot{z}_o^2]^{1/2} \ln \left( \frac{\epsilon}{16\rho_o} [\dot{\rho}_o^2 + \dot{z}_o^2]^{1/2} \right) \right] \right\}, \tag{A22}
 \end{aligned}$$

and the  $\mathbf{k}$  component is

$$\begin{aligned}
 a_k &\simeq 2\epsilon \left\{ f_{\rho_o} \frac{\dot{\rho}_o \dot{z}_o}{[\dot{\rho}_o^2 + \dot{z}_o^2]^{1/2}} + f_{z_o} \left[ \frac{\dot{z}_o^2}{[\dot{\rho}_o^2 + \dot{z}_o^2]^{1/2}} \right. \right. \\
 &\quad \left. \left. + [\dot{\rho}_o^2 + \dot{z}_o^2]^{1/2} \left( 1 - \ln \frac{\epsilon}{16\rho_o} [\dot{\rho}_o^2 + \dot{z}_o^2]^{1/2} \right) \right] \right\}, \tag{A23}
 \end{aligned}$$

where the subscript  $\circ$  denotes evaluation at the singular point.

## References

- Blake, J.R. 1971 *Proc. Camb. Phil. Soc.* **70**, 303.
- Brenner, H. 1961 *Chem. Eng. Sci.* **16**, 242.
- Brenner, H. 1962 *J. Fluid Mech.* **12**, 35.
- Brenner, H. 1964 *J. Fluid Mech.* **18**, 144.
- Cox, R.G. 1974 *Int. J. Multiphase Flow* **1**, 343.
- Cox, R.G. & Brenner, H. 1967 *J. Fluid Mech.* **28**, 391.
- Kantorovich, L.V. & Krylov, V.I. 1963 *Approximate Methods of Higher Analysis*, Interscience.
- Ladyzhenskaya, O.A. 1963 *The Mathematical Theory of Viscous Incompressible Flow*, Gordon and Breach, New York.
- Lamb, H. 1945 *Hydrodynamics*, Dover, New York.
- Lee, S.H. & Leal, L.G. 1982 *J. Colloid Interface Sci.* **87**, 81.
- Odqvist, F.K.G. 1930 *Math. Z.* **32**, 329.
- Oseen, C.W. 1927 *Hydrodynamik*, Akademische Verlagsgesellschaft.
- Rallison, J.M. & Acrivos, A. 1978 *J. Fluid Mech.* **89**, 91.
- Reynolds, O. 1901 *Papers on Mechanical and Physical Subjects*, vol. II , pp. 228-310, Cambridge University Press.
- Wakiya, S. 1957 *J. Phys. Soc. Japan* **12**, 1130.
- Youngren, G.K. & Acrivos, A. 1975 *J. Fluid Mech.* **69** , 377.
- Youngren, G.K. & Acrivos, A. 1976 *J. Fluid Mech.* **76** , 433.

## Figure captions

Figure 1: Schematic of the general problem.

Figure 2: (a) Ellipsoid geometrical parameters. (b) The parametrization variable  $s$ .

Figure 3: (a) Evolution of the  $z$  component of the local surface tractions as  $z_{gap}$  decreases; ———  $z_{gap} = 100$ ; .....  $z_{gap} = 10$ ; - - - -  $z_{gap} = 1$ ; - - -  $z_{gap} = 0.05$ . (b) Evolution of the  $\rho$  component of the local surface tractions as  $z_{gap}$  decreases; ———  $z_{gap} = 100$ ; .....  $z_{gap} = 10$ ; - - - -  $z_{gap} = 1$ ; - - -  $z_{gap} = 0.05$ . Note that in figure (b) the  $z_{gap} = 100$  curve and the  $z_{gap} = 10$  curve are visually indistinguishable. In both figures (a) and (b) the arbitrary constant due to pressure has been chosen so that  $f_\rho = 0$  at  $s = 0.5$ .

Figure 4: Comparison of computational time between the wall Greens function technique and the Stokeslet fundamental solution technique.  $T_{rat}$  representing the ratio of computational times, (Greens method)/(Stokeslet method), is plotted against  $N_{total}$ .

Figure 5: (a) Large  $z_c$  results:  $\square$  numerical results for  $\alpha = 16$  and 40 elements ; solid line represents the asymptotic predictions as given by eqn(30). (b) Small  $z_{lub}$  results:  $\square$  numerical results for  $\alpha = 16$  and 40 elements ; solid line represents Cox’s lubrication theory as given by eqn(31).

Figure 6: (a) Large  $z_c$  results:  $\square$  numerical results for  $\alpha = 8$  and 40 elements ; solid line represents the asymptotic predictions as given by eqn(30). (b) Small  $z_{lub}$  results:  $\square$  numerical results for  $\alpha = 8$  and 40 elements ; solid line represents Cox’s lubrication theory as given by eqn(31).

Figure 7: (a) Large  $z_c$  results:  $\square$  numerical results for  $\alpha = 4$  and 40 elements ; solid line represents the asymptotic predictions as given by eqn(30). (b) Small  $z_{lub}$  results:  $\square$  numerical results for  $\alpha = 4$  and 40 elements ; solid line represents Cox’s lubrication theory as given by eqn(31).

Figure 8: (a) Large  $z_c$  results:  $\square$  numerical results for  $\alpha = 2$  and 40 elements ; solid line represents the asymptotic predictions as given by eqn(30). (b) Small  $z_{lub}$  results:  $\square$  numerical results for  $\alpha = 2$  and 40 elements ; solid line represents Cox's lubrication theory as given by eqn(31).

Figure 9: (a)  $\square$  numerical results for the sphere case ( $\alpha = 1$ ) with 40 elements; solid line represents the theoretical predictions of Brenner (1961) as given by eqn(29); dashed line represents Cox's lubrication theory as given by eqn(31). (b)  $\square$  numerical results for the sphere case with 40 elements; solid line represents the theoretical predictions of Brenner (1961) as given by eqn(29); dashed line represents the far-field asymptotic predictions as given by eqn(30).

Figure 10: (a) Large  $z_c$  results:  $\square$  numerical results for  $\alpha = 0.5$  and 40 elements ; solid line represents the asymptotic predictions as given by eqn(30). (b) Small  $z_{lub}$  results:  $\square$  numerical results for  $\alpha = 0.5$  and 40 elements ; solid line represents Cox's lubrication theory as given by eqn(31).

Figure 11: (a) Large  $z_c$  results:  $\square$  numerical results for  $\alpha = 0.25$  and 40 elements ; solid line represents the asymptotic predictions as given by eqn(30). (b) Small  $z_{lub}$  results:  $\square$  numerical results for  $\alpha = 0.25$  and 40 elements ; solid line represents Cox's lubrication theory as given by eqn(31); dashed line represents Reynolds lubrication theory given by eqn(33).

Figure 12: (a) Large  $z_c$  results:  $\square$  numerical results for  $\alpha = .125$  and 40 elements ; solid line represents the asymptotic predictions as given by eqn(30). (b) Small  $z_{lub}$  results:  $\square$  numerical results for  $\alpha = 0.125$  and 40 elements ; solid line represents Cox's lubrication theory as given by eqn(31); dashed line represents Reynolds lubrication theory given by eqn(33).

Figure 13: (a) Large  $z_c$  results:  $\square$  numerical results for  $\alpha = 0.0625$  and 40 elements ; solid line represents the asymptotic predictions as given by

eqn(30). (b) Small  $z_{lub}$  results:  $\square$  numerical results for  $\alpha = 0.0625$  and 40 elements ; solid line represents Cox's lubrication theory as given by eqn(31); dashed line represents Reynolds lubrication theory as given by eqn(33).

## Table captions

Table 1: A comparison of numerical results using the wall Greens function with the theoretical results of Brenner (eqn(29)) for the case of a sphere. Results for number of elements,  $N$ , equal to 10, 20, 30 and 40 are shown.

Table 2: A comparison of numerical results generated using the Stokeslet fundamental solution and  $N_{sphere} = 6$ ,  $N_{wall} = 6$  with the theoretical results of Brenner (eqn(29)) for the case of a sphere. (a) constant width wall elements, (b) non-constant width wall elements

Table 3: A comparison of numerical results generated using the Stokeslet fundamental solution and  $N_{sphere} = 10$ ,  $N_{wall} = 10$  with the theoretical results of Brenner (eqn(29)) for the case of a sphere. (a) constant width wall elements, (b) non-constant width wall elements

Table 4: A comparison of numerical results generated using the Stokeslet fundamental solution and  $N_{sphere} = 20$ ,  $N_{wall} = 20$  with the theoretical results of Brenner (eqn(29)) for the case of a sphere. (a) constant width wall elements, (b) non-constant width wall elements

Table 5: A comparison of numerical results generated using the Stokeslet fundamental solution and  $N_{sphere} = 30$ ,  $N_{wall} = 30$  with the theoretical results of Brenner (eqn(29)) for the case of a sphere. (a) constant width wall elements, (b) non-constant width wall elements

Table 6: A comparison of numerical results with the asymptotic theory of Brenner (eqn(30)) for  $N=40$  and  $\alpha = 16$ .

Table 7: A comparison of numerical results with the asymptotic theory of Brenner (eqn(30)) for  $N=40$  and  $\alpha = 8$ .

Table 8: A comparison of numerical results with the asymptotic theory of Brenner (eqn(30)) for  $N=40$  and  $\alpha = 4$ .

Table 9: A comparison of numerical results with the asymptotic theory of Brenner (eqn(30)) for  $N=40$  and  $\alpha = 2$ .

Table 10: A comparison of numerical results with the asymptotic theory of Brenner (eqn(30)) for  $N=40$  and  $\alpha = .5$ .

Table 11: A comparison of numerical results with the asymptotic theory of Brenner (eqn(30)) for  $N=40$  and  $\alpha = .25$ .

Table 12: A comparison of numerical results with the asymptotic theory of Brenner (eqn(30)) for  $N=40$  and  $\alpha = .125$ .

Table 13: A comparison of numerical results with the asymptotic theory of Brenner (eqn(30)) for  $N=40$  and  $\alpha = .0625$ .

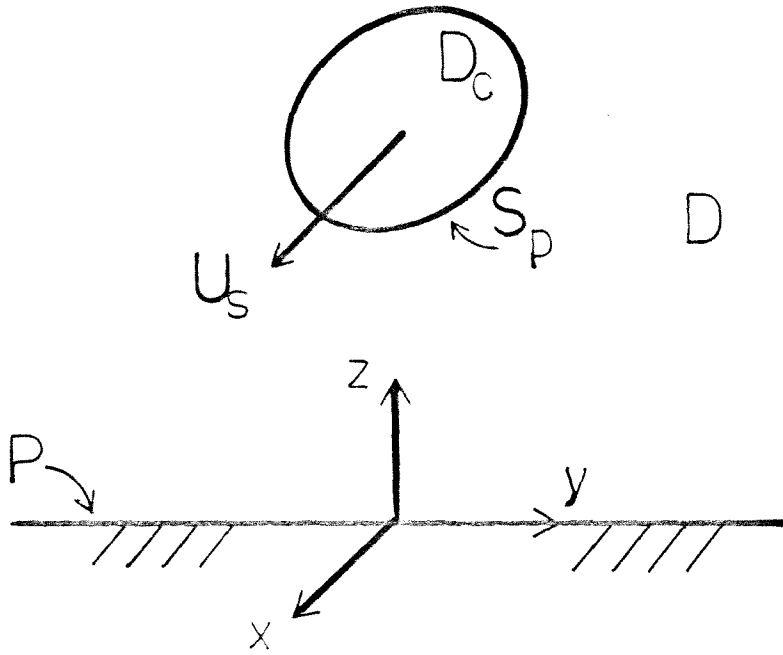


Figure 1

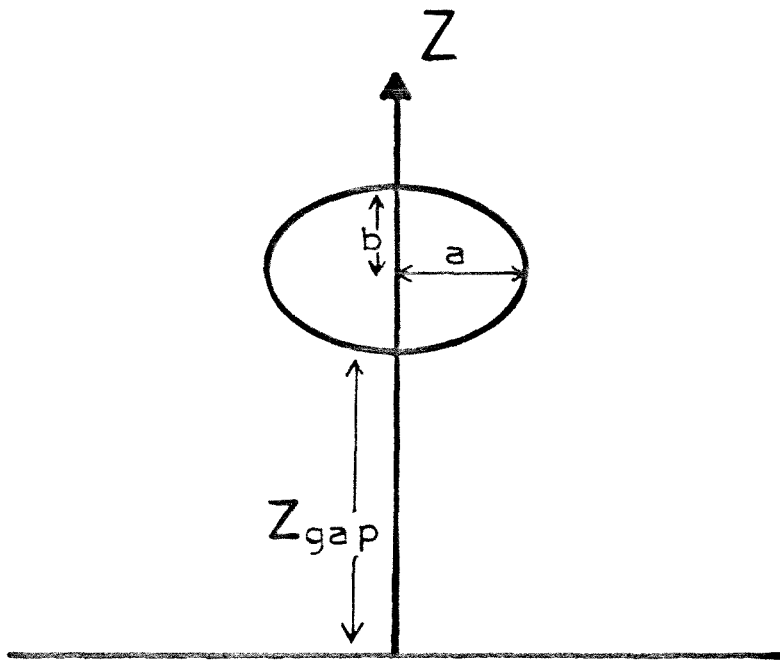


Figure 2(a)

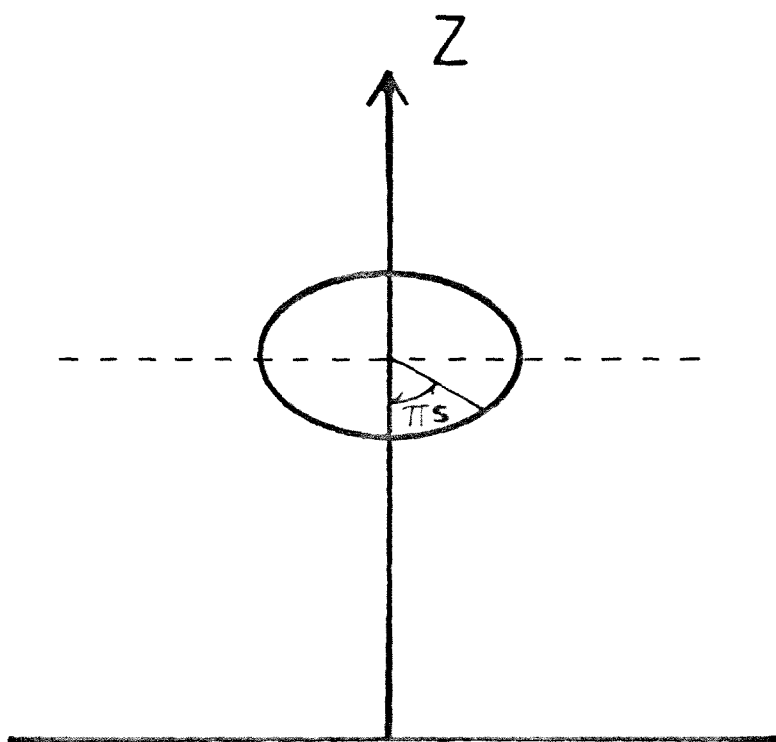


Figure 2(b)

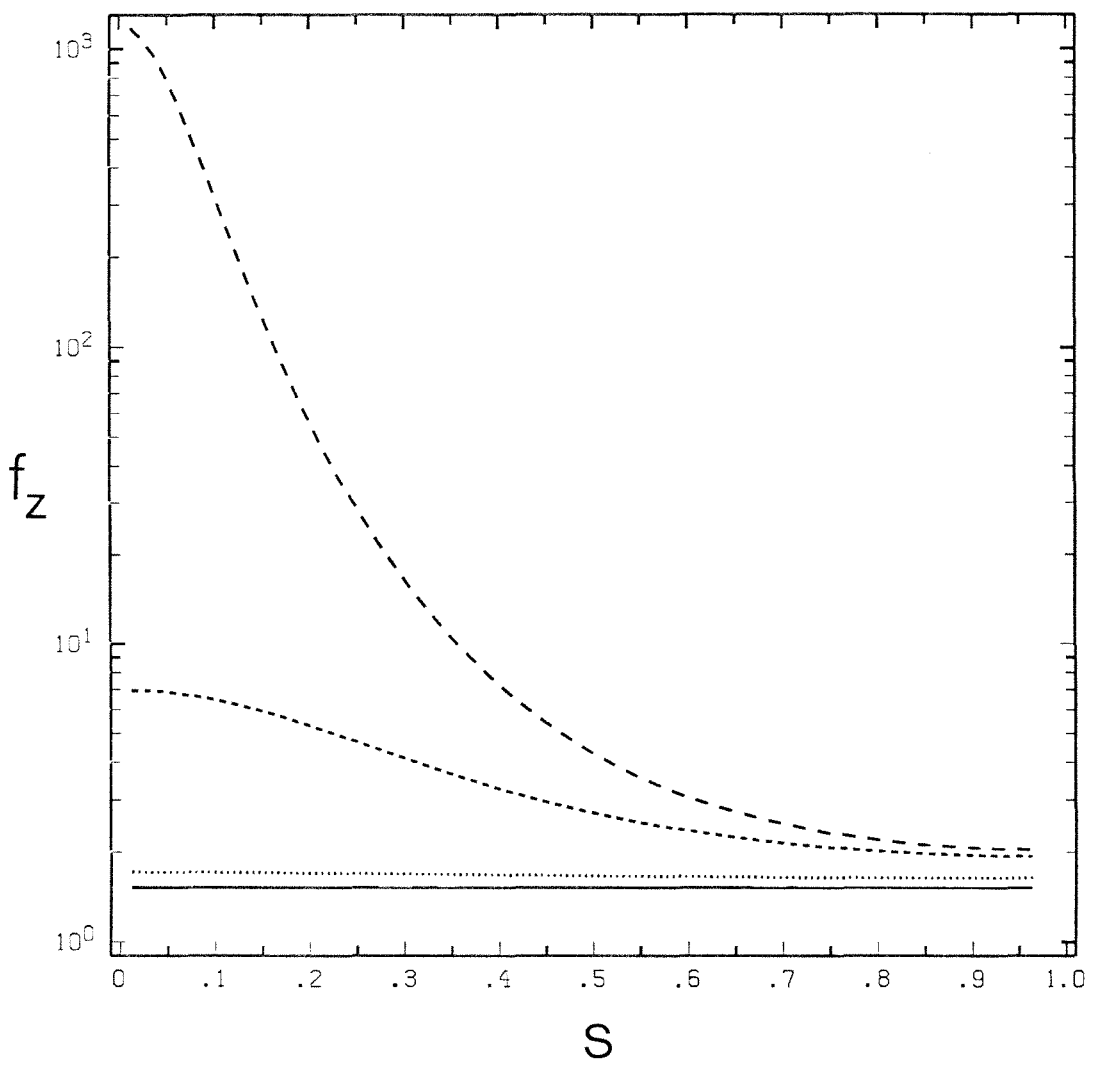


Figure 3(a)

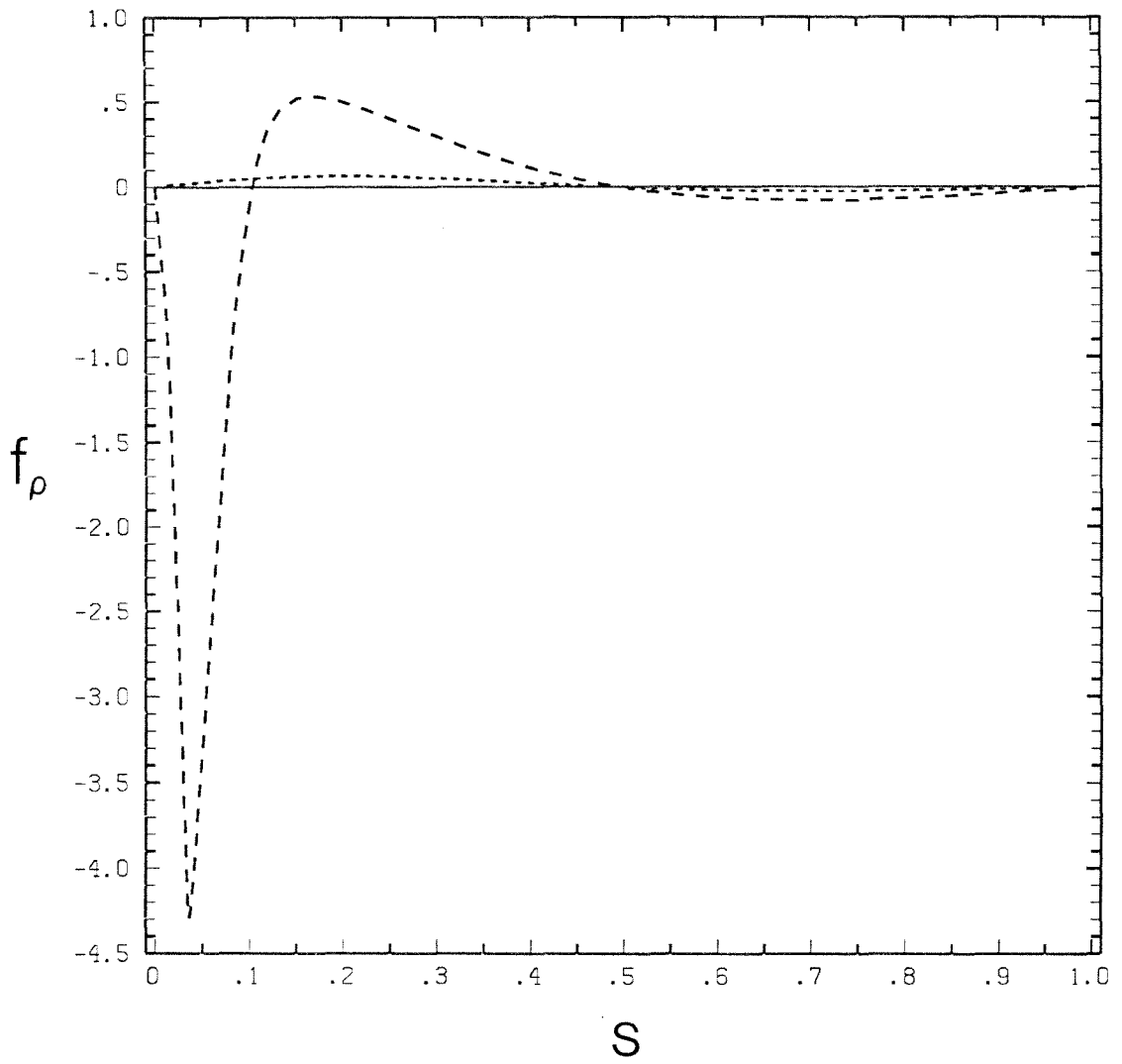


Figure 3(b)

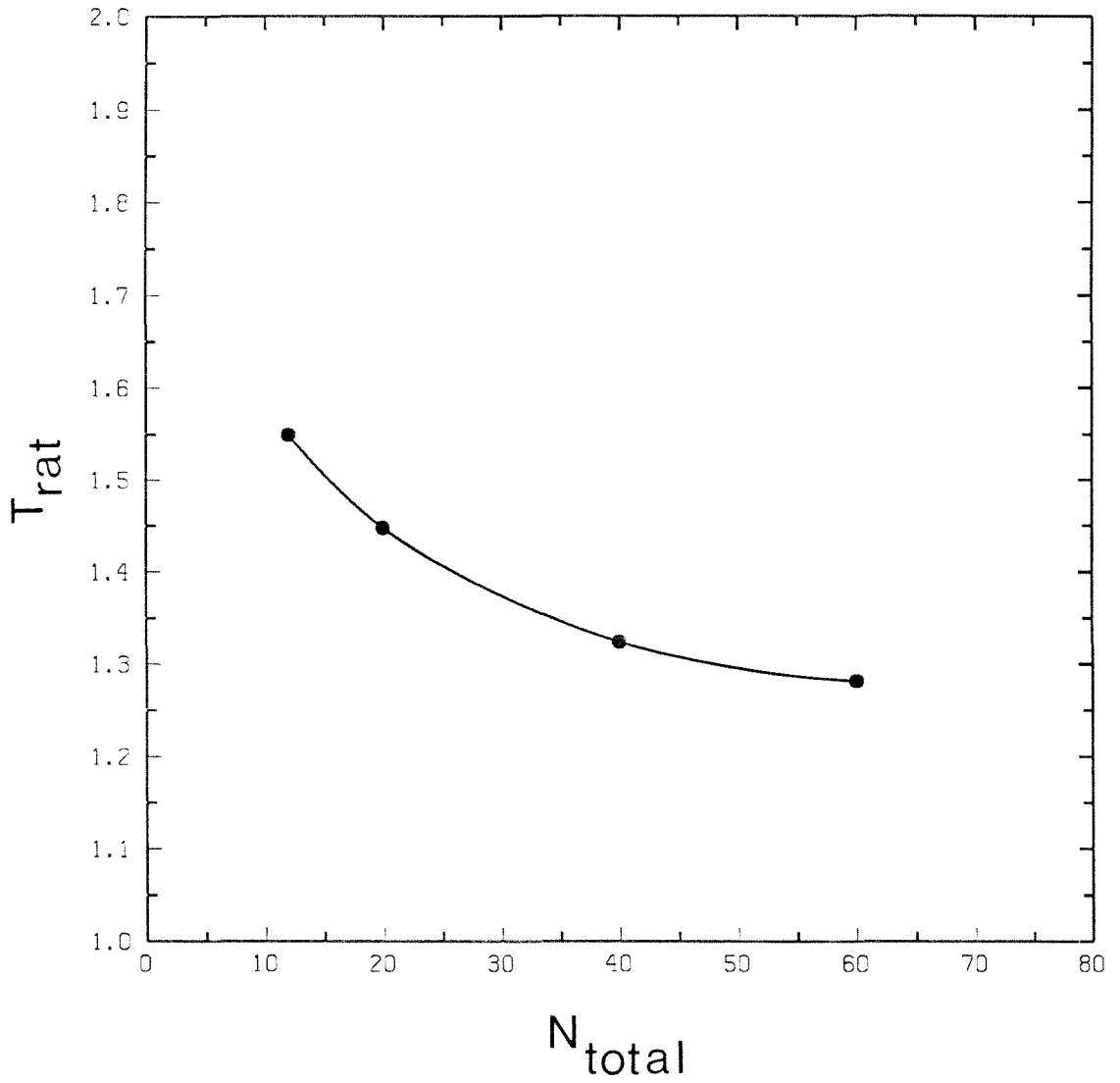


Figure 4

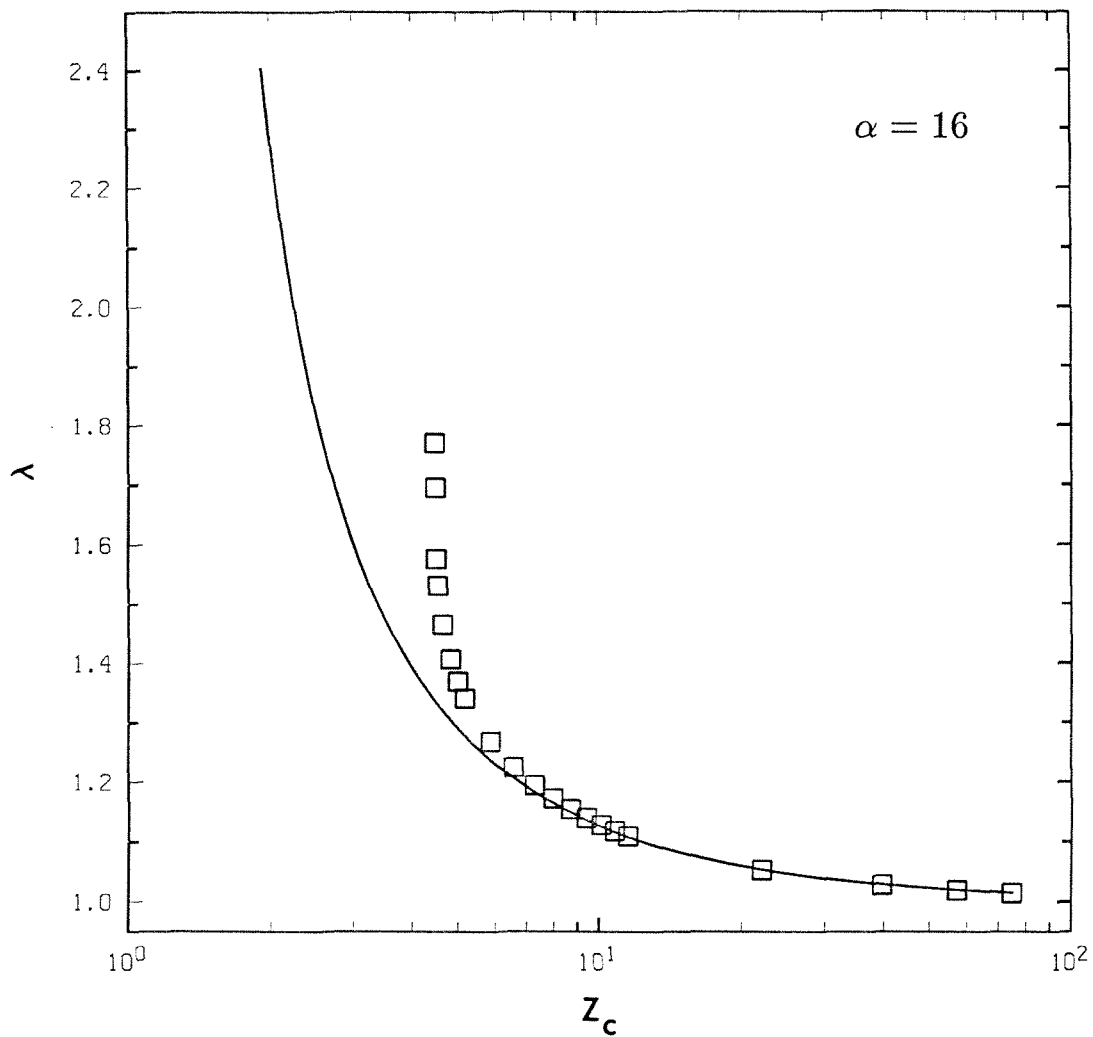


Figure 5(a)

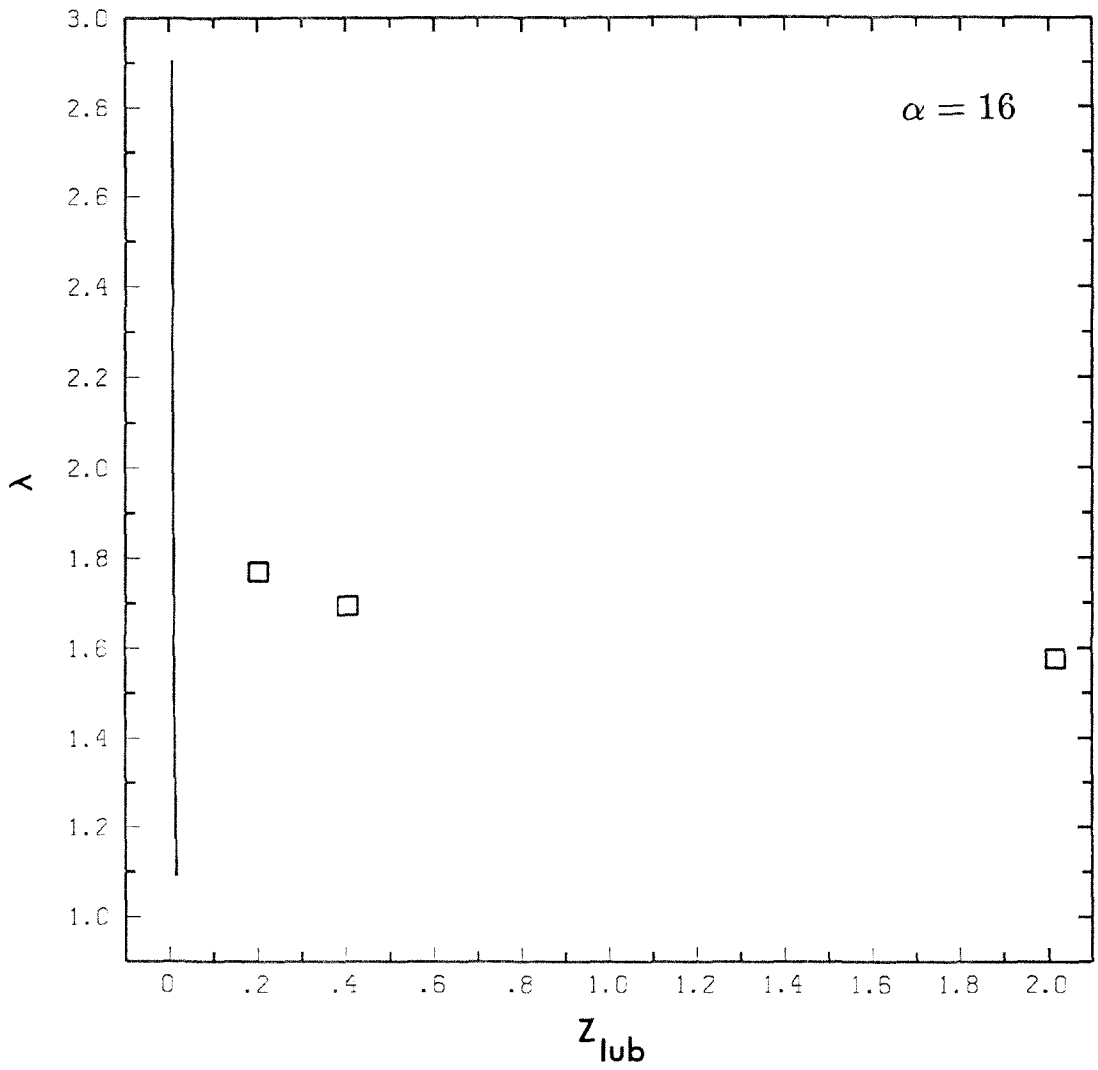


Figure 5(b)

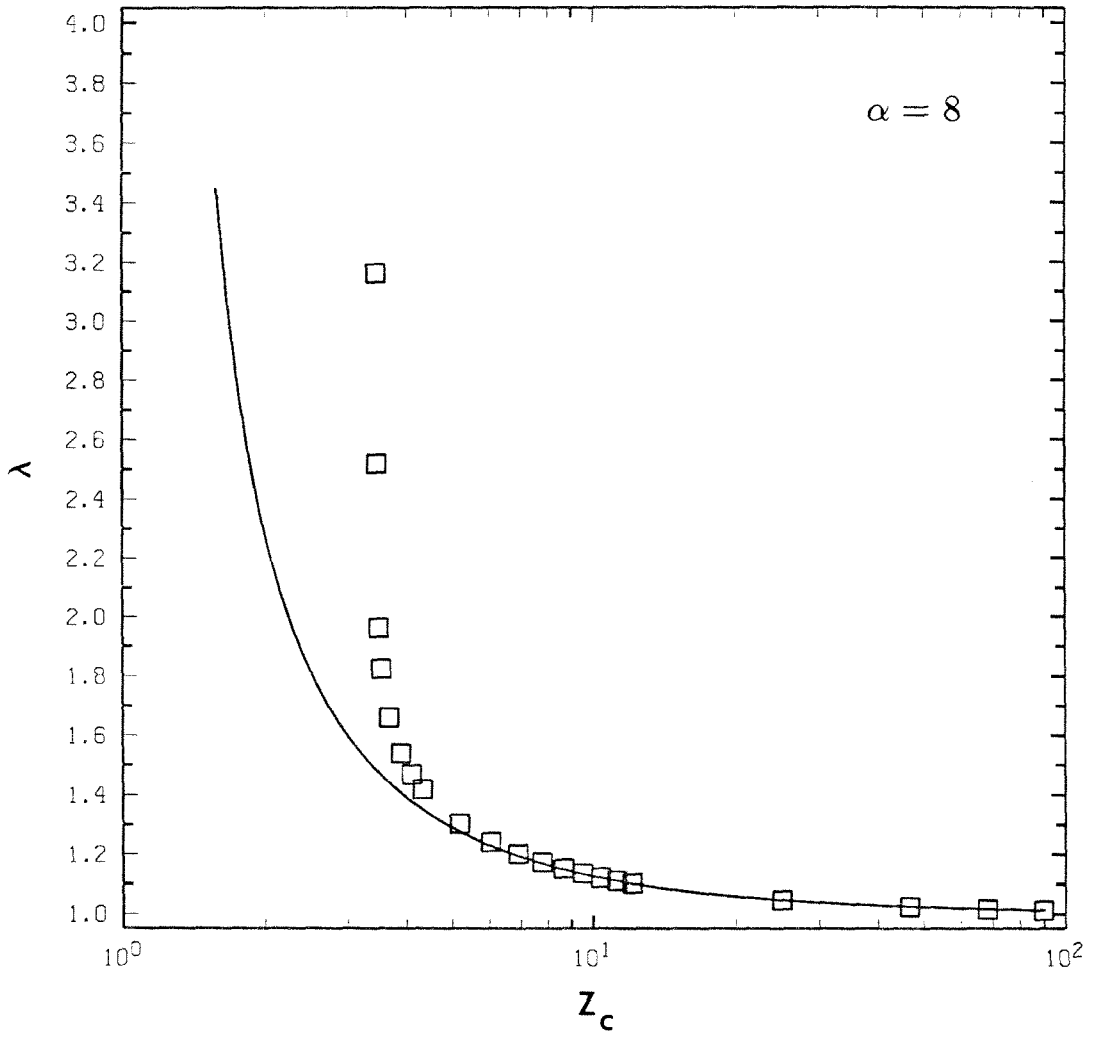


Figure 6(a)

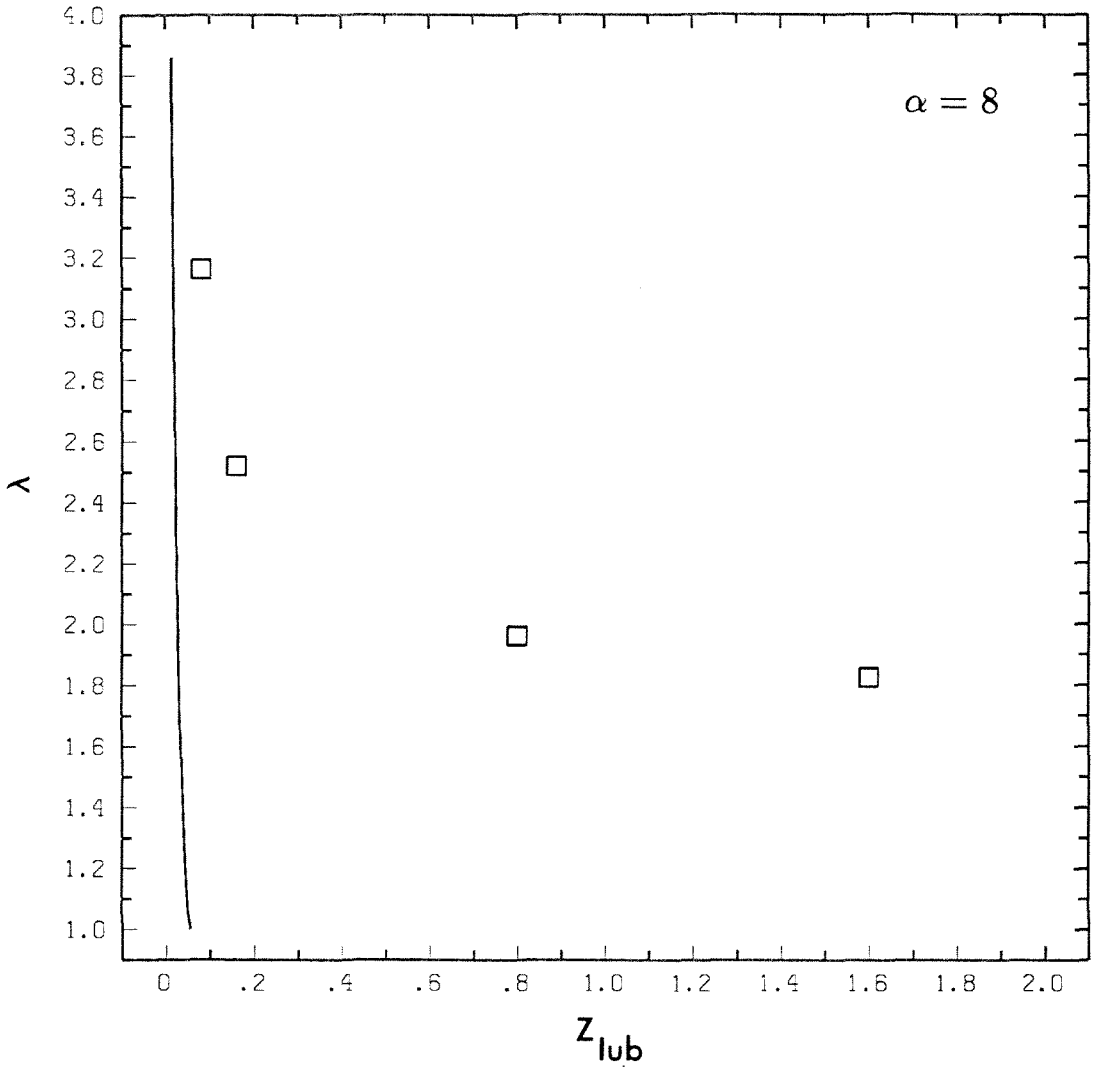


Figure 6(b)

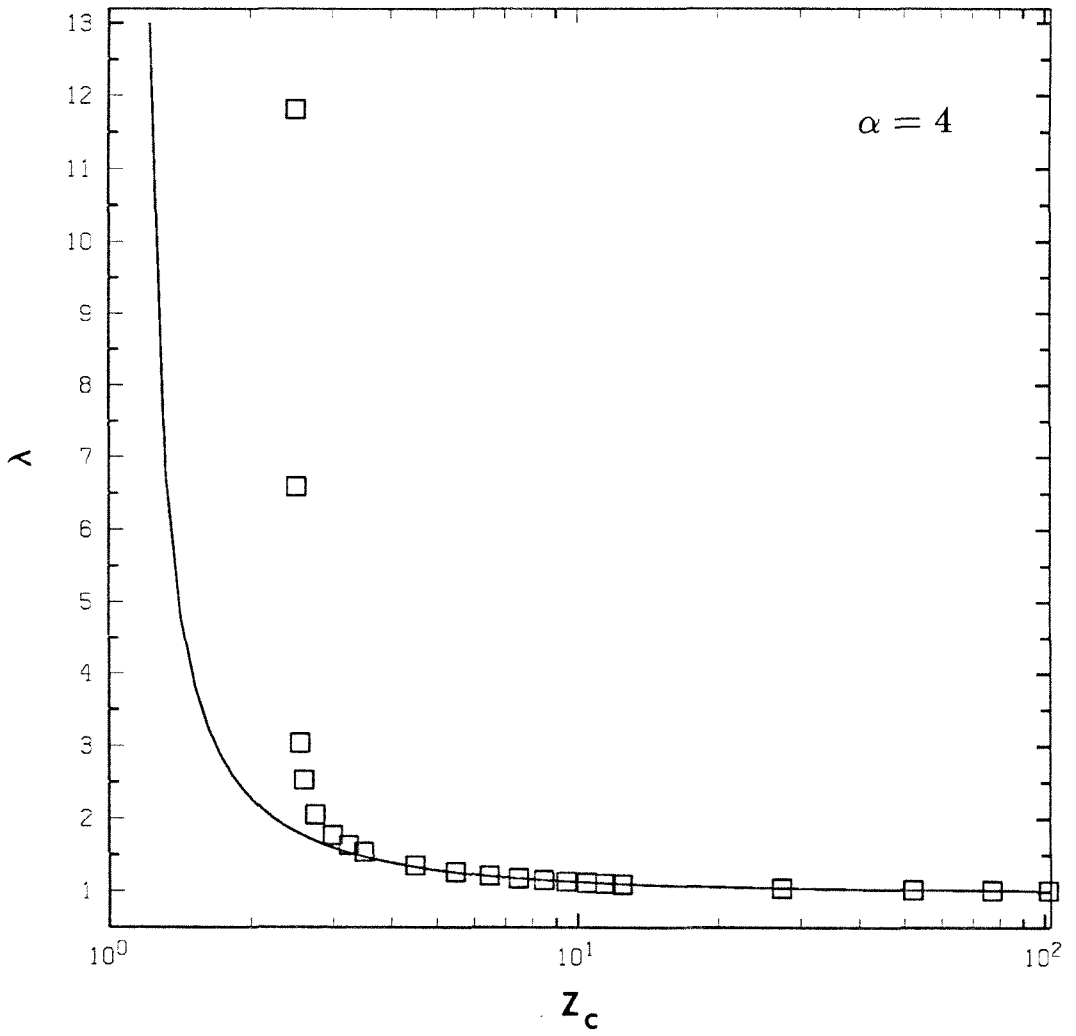


Figure 7(a)

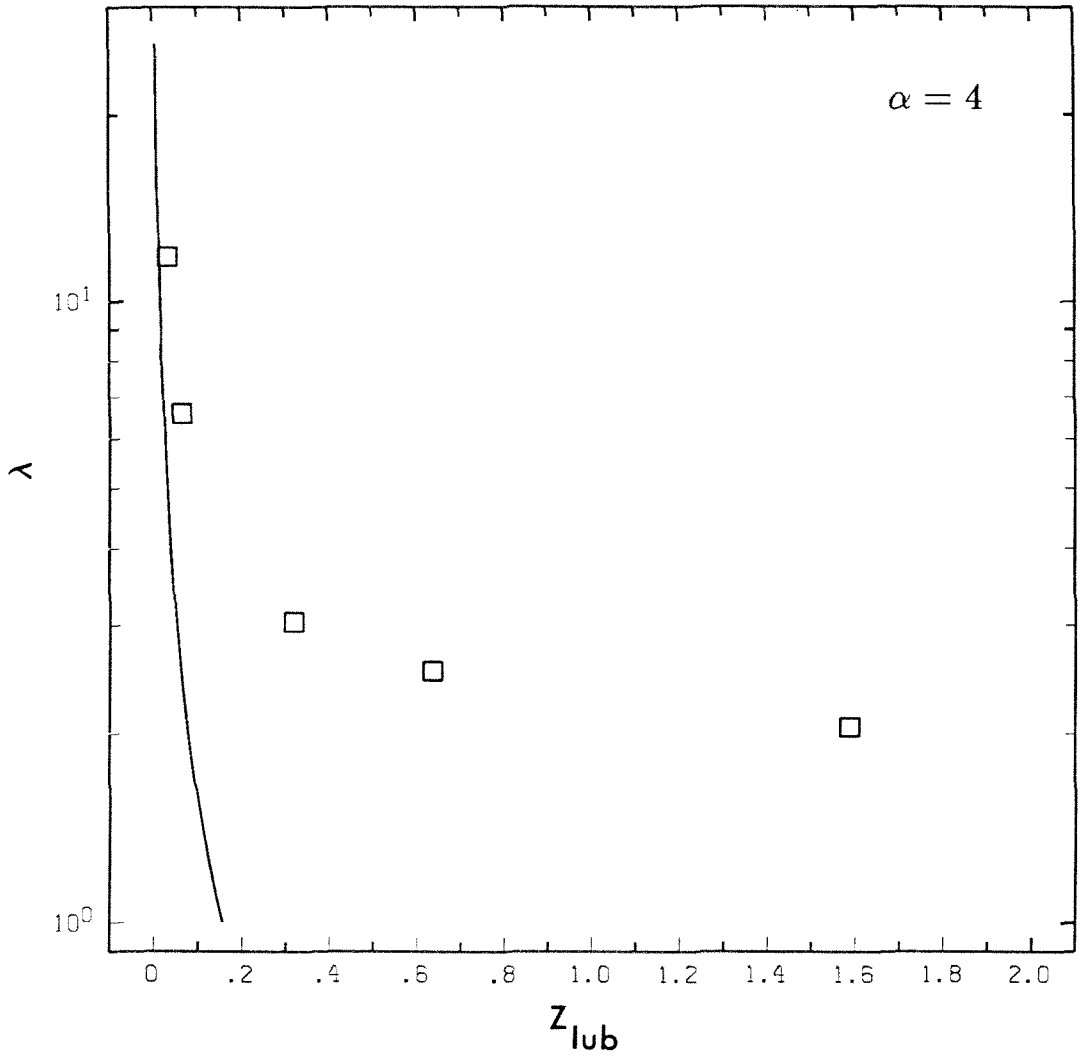


Figure 7(b)

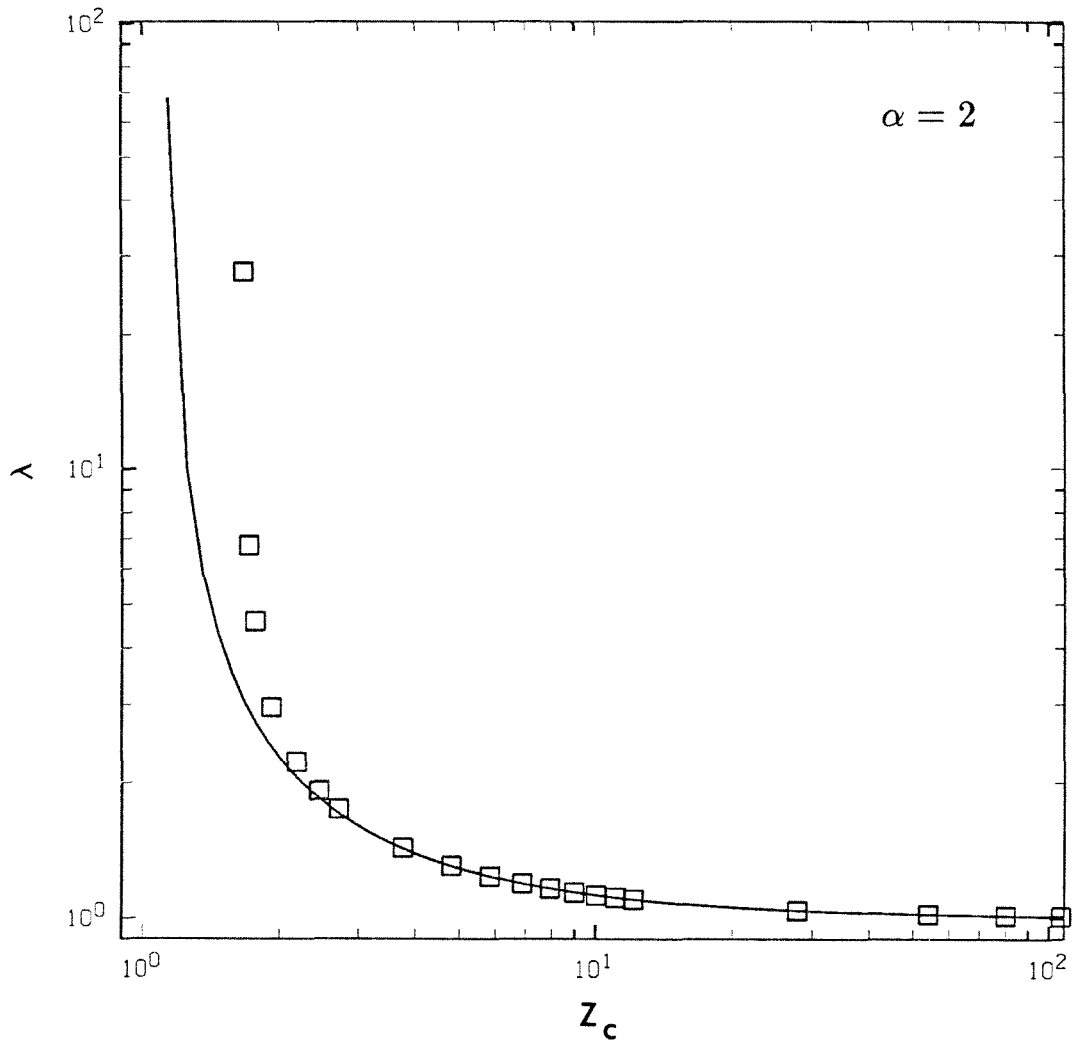


Figure 8(a)

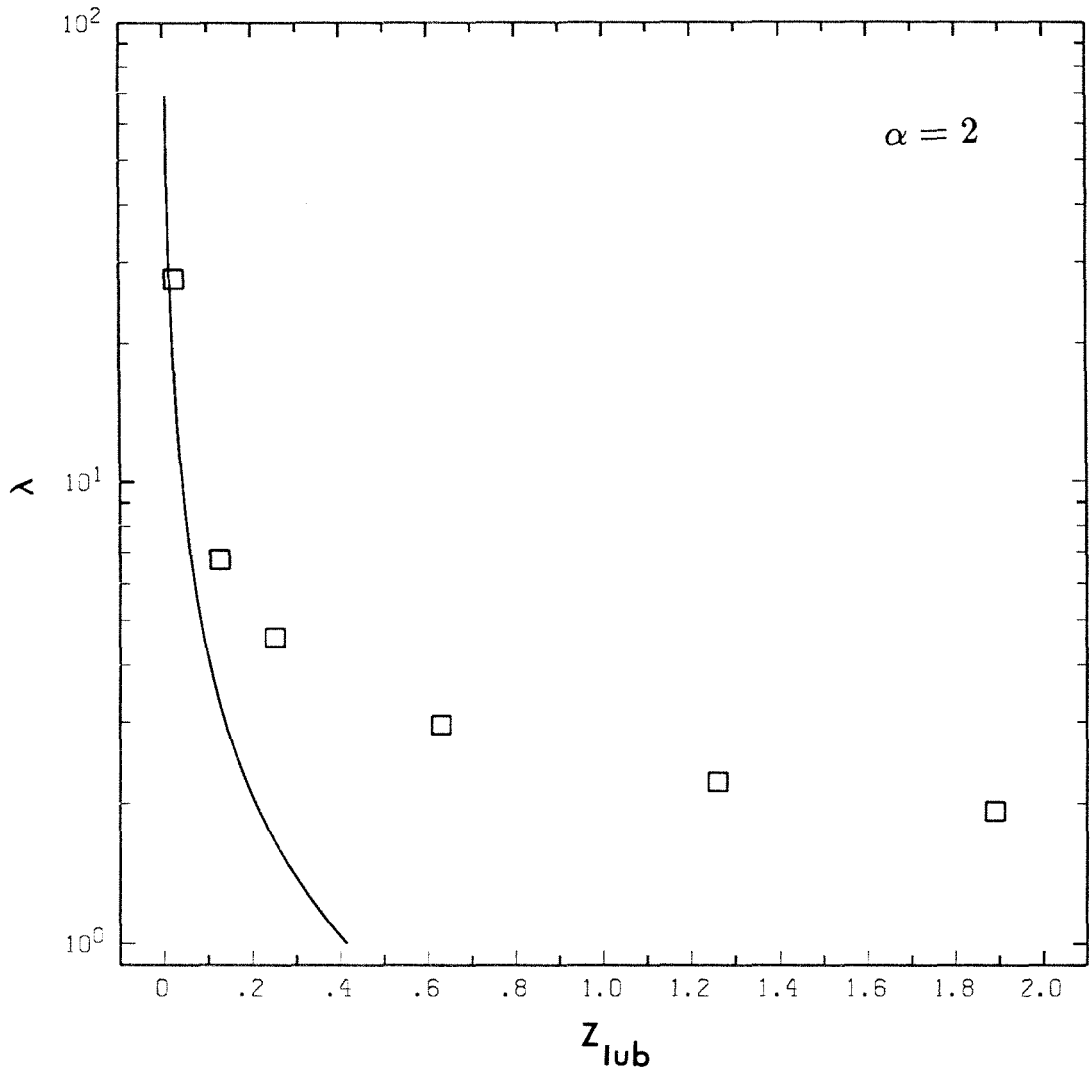


Figure 8(b)

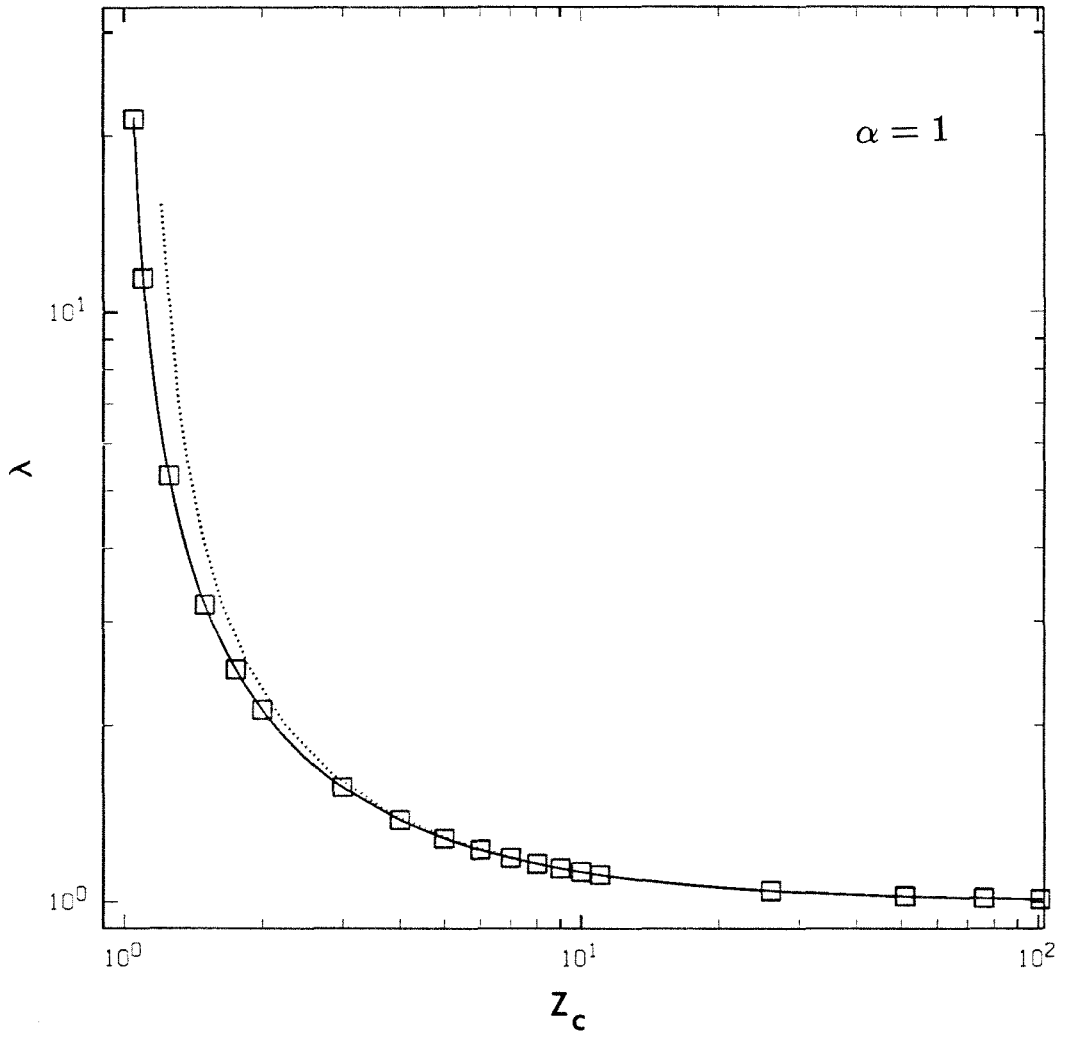


Figure 9(a)

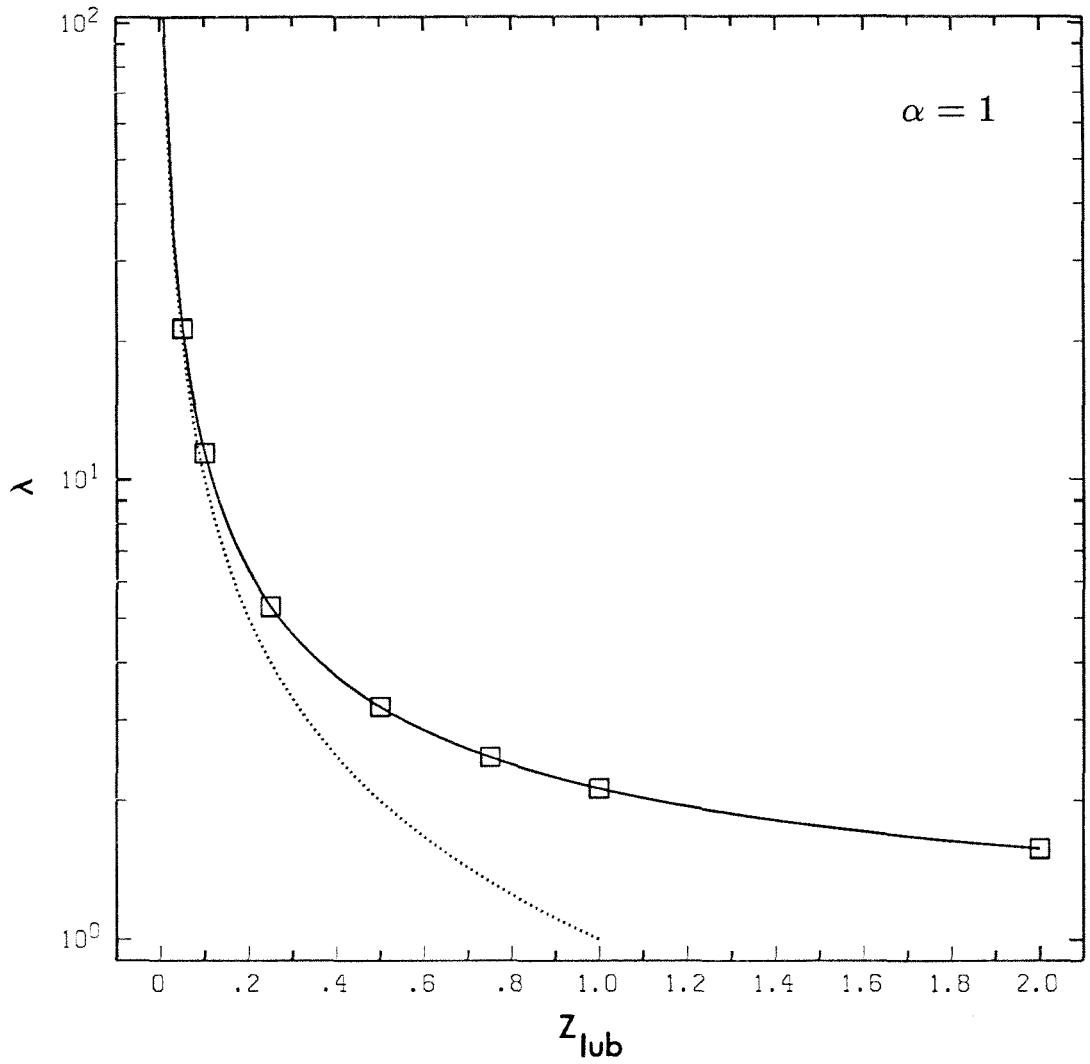


Figure 9(b)

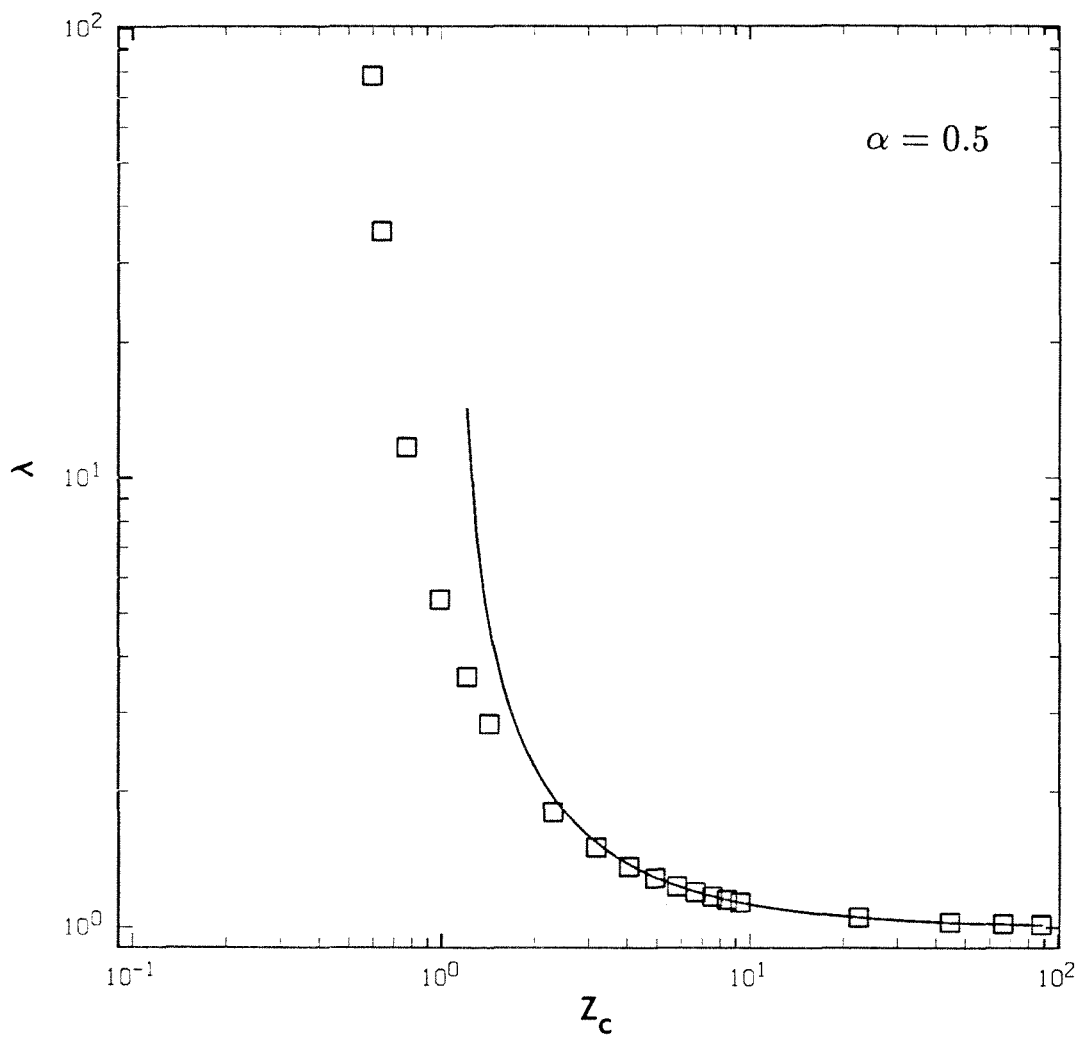


Figure 10(a)

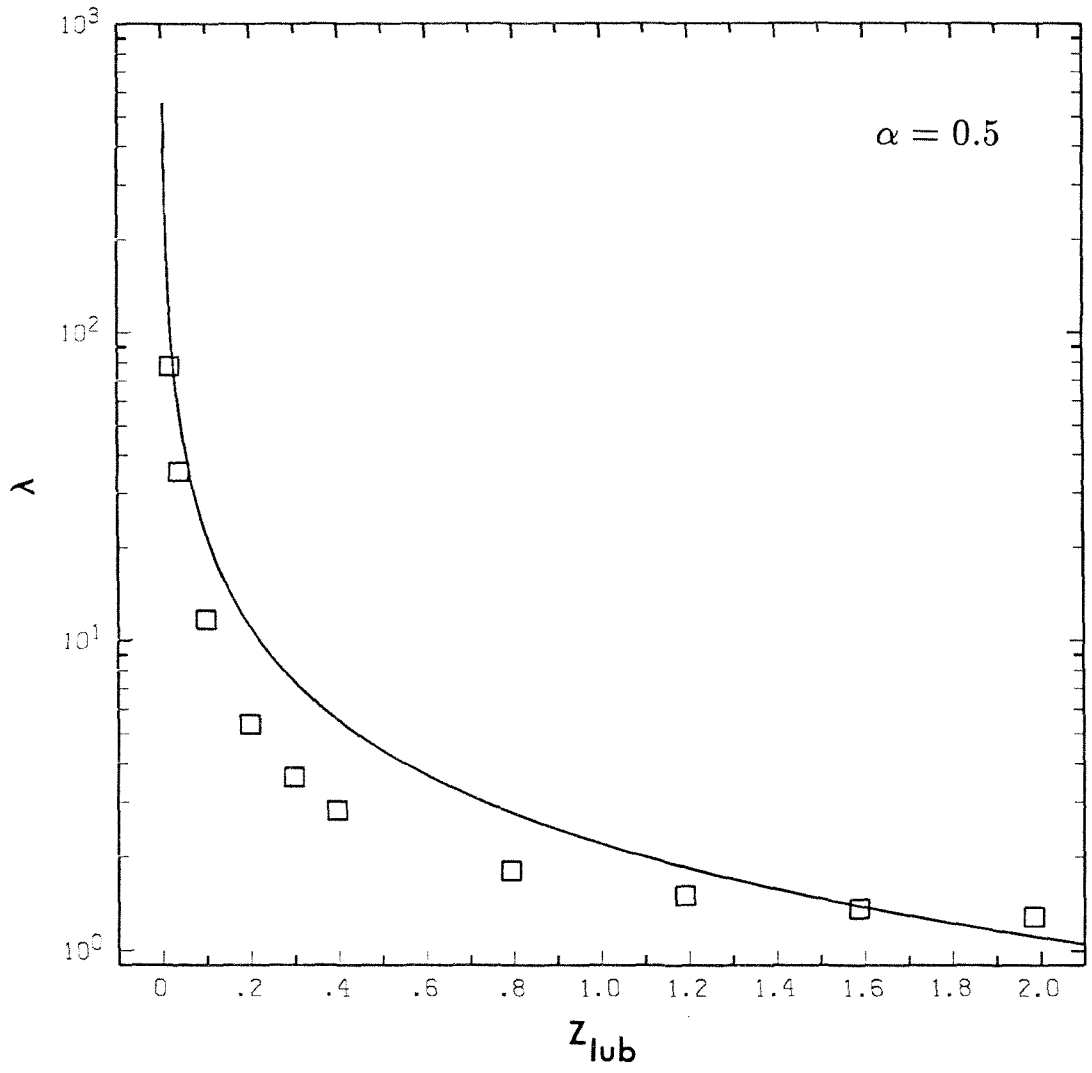


Figure 10(b)

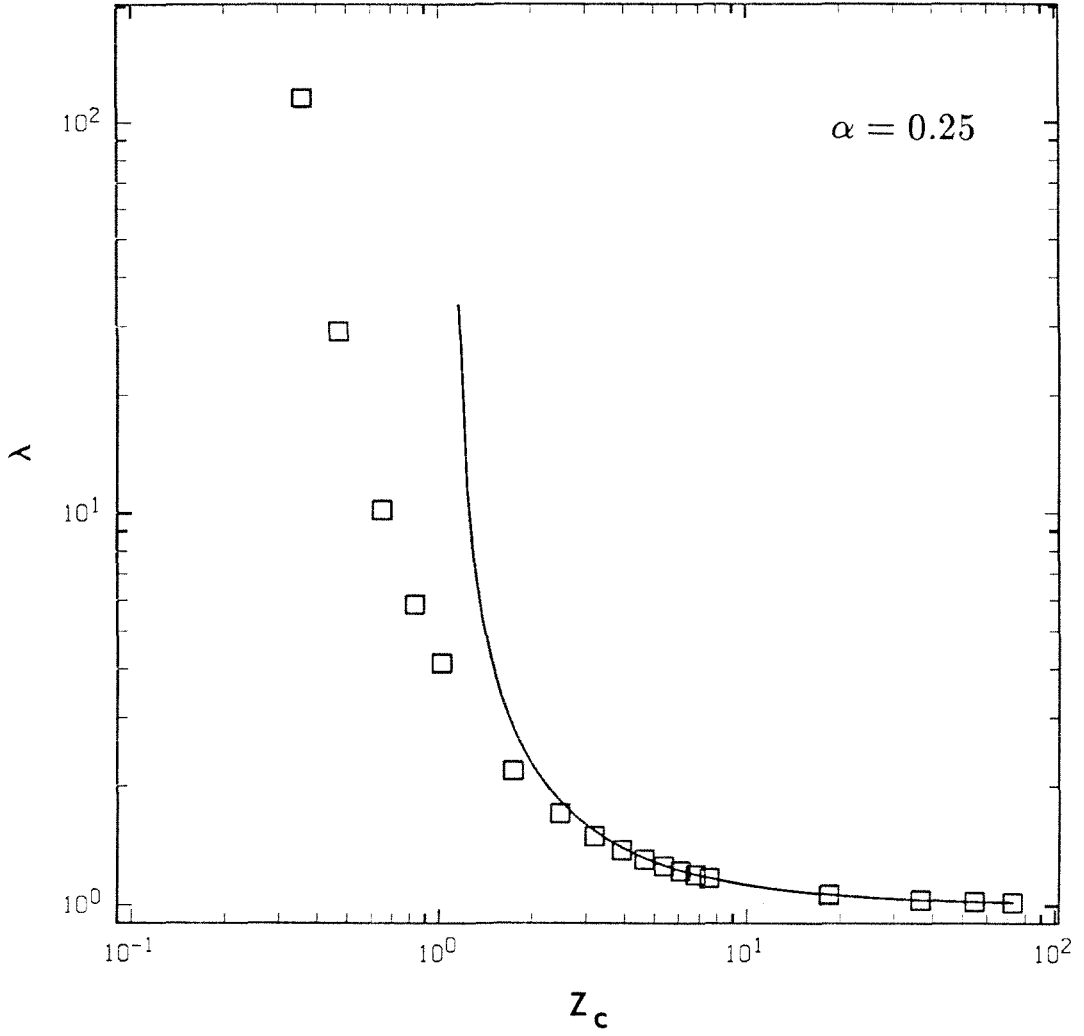


Figure 11(a)

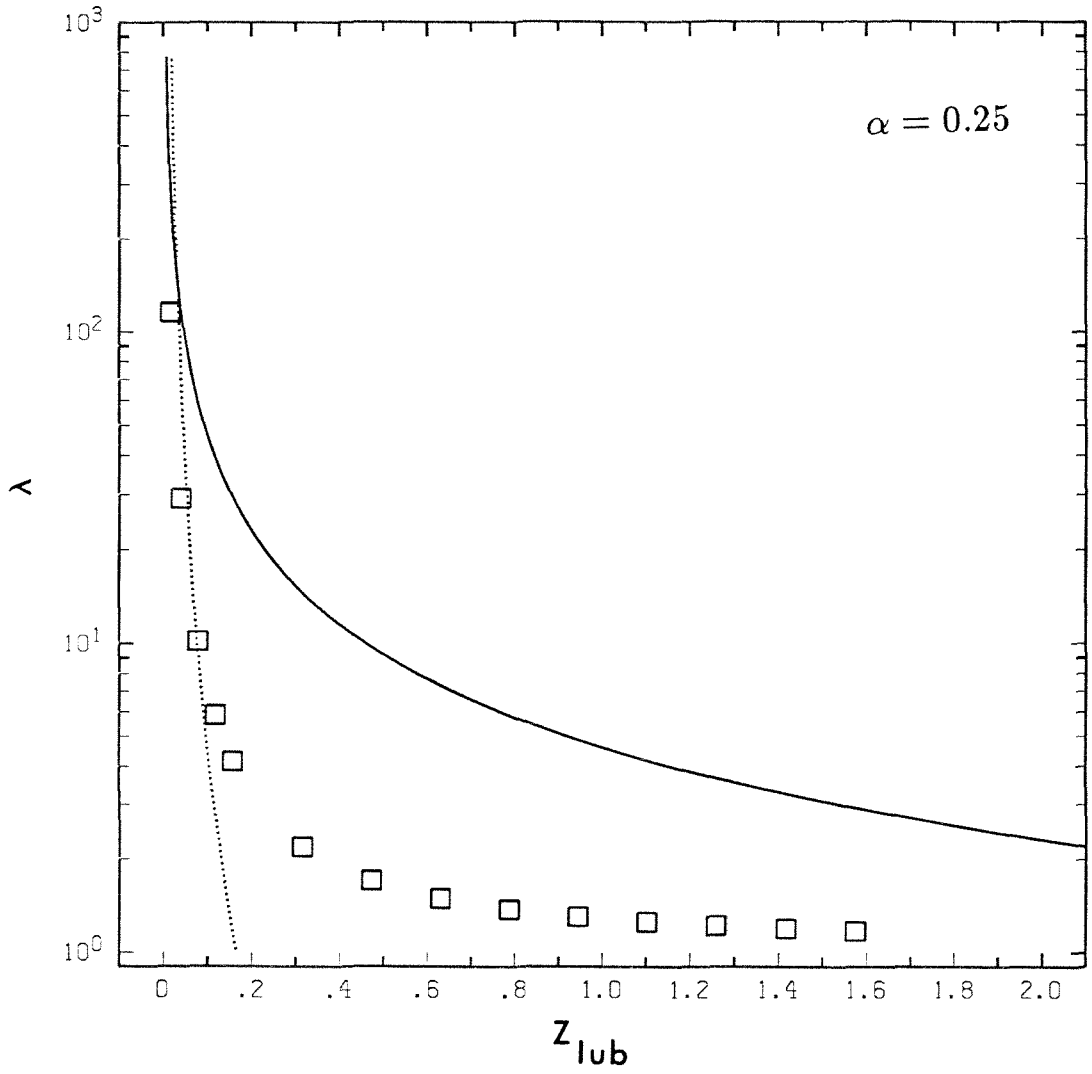


Figure 11(b)

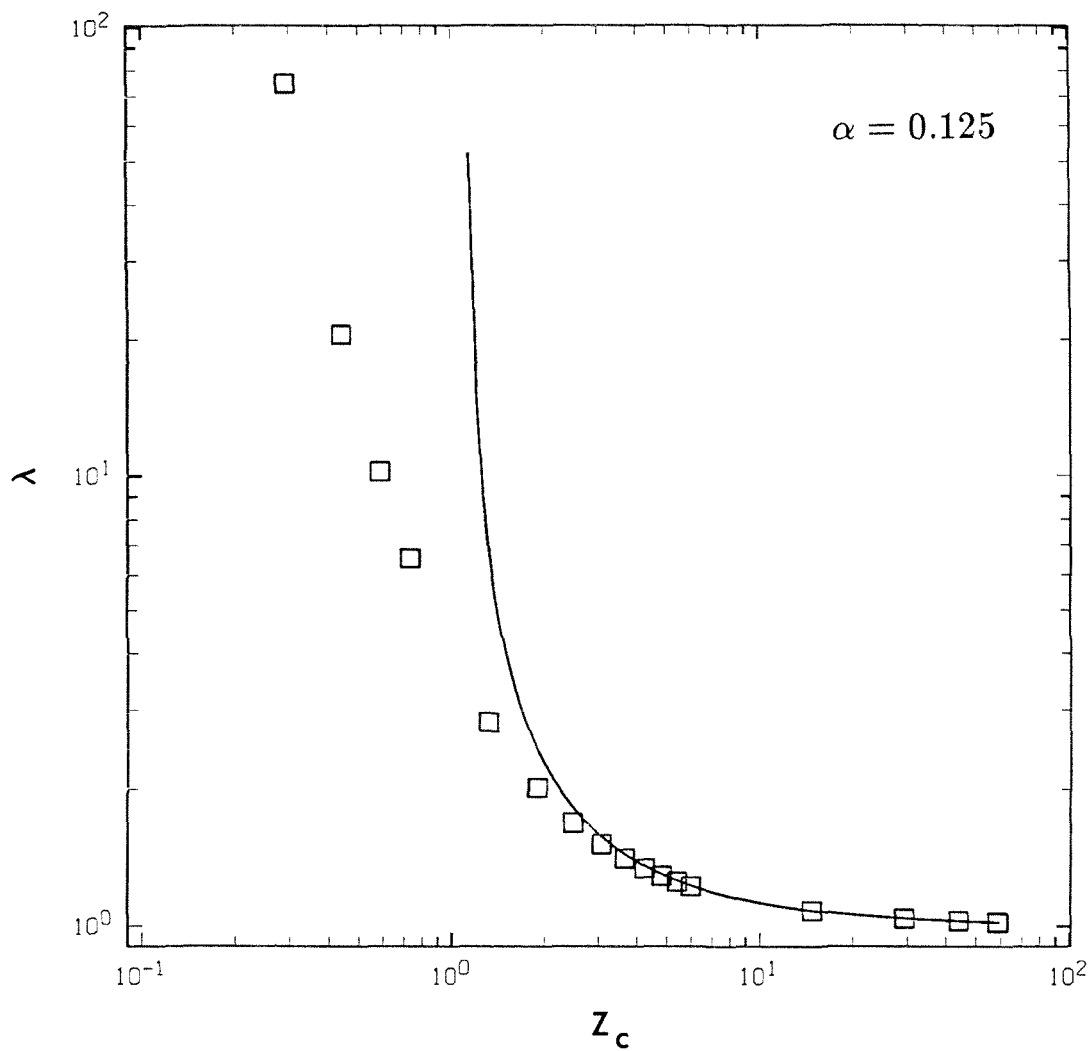


Figure 12(a)

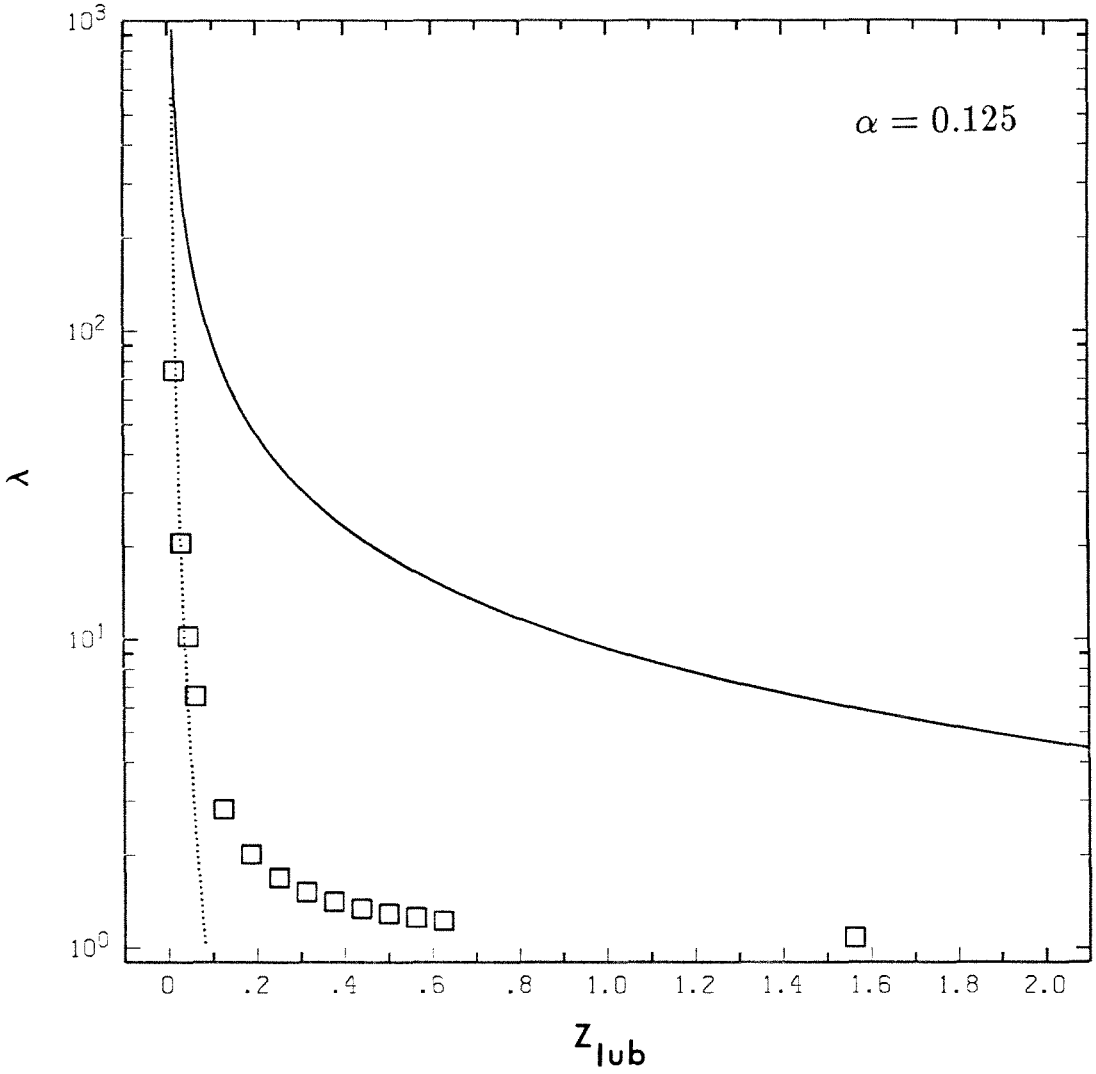


Figure 12(b)

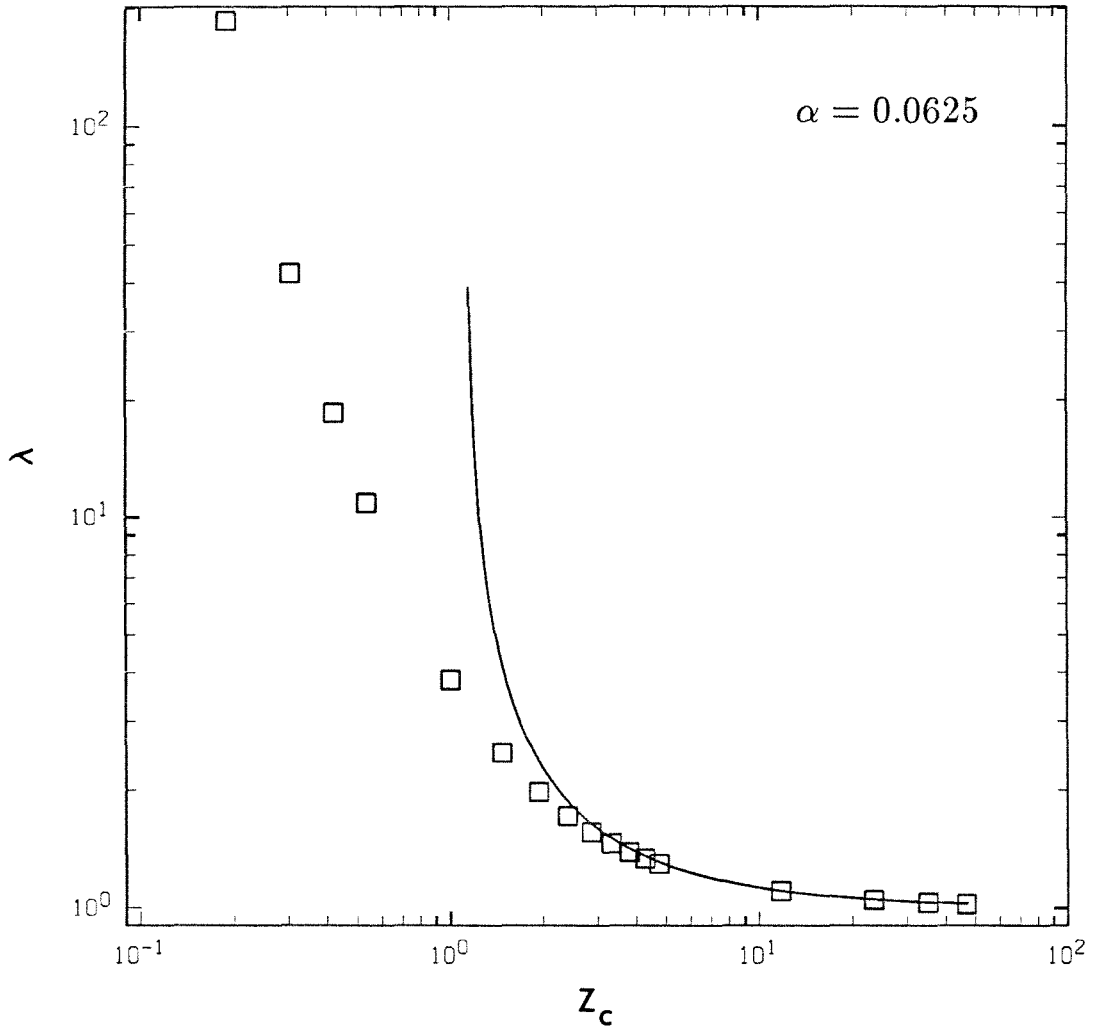


Figure 13(a)

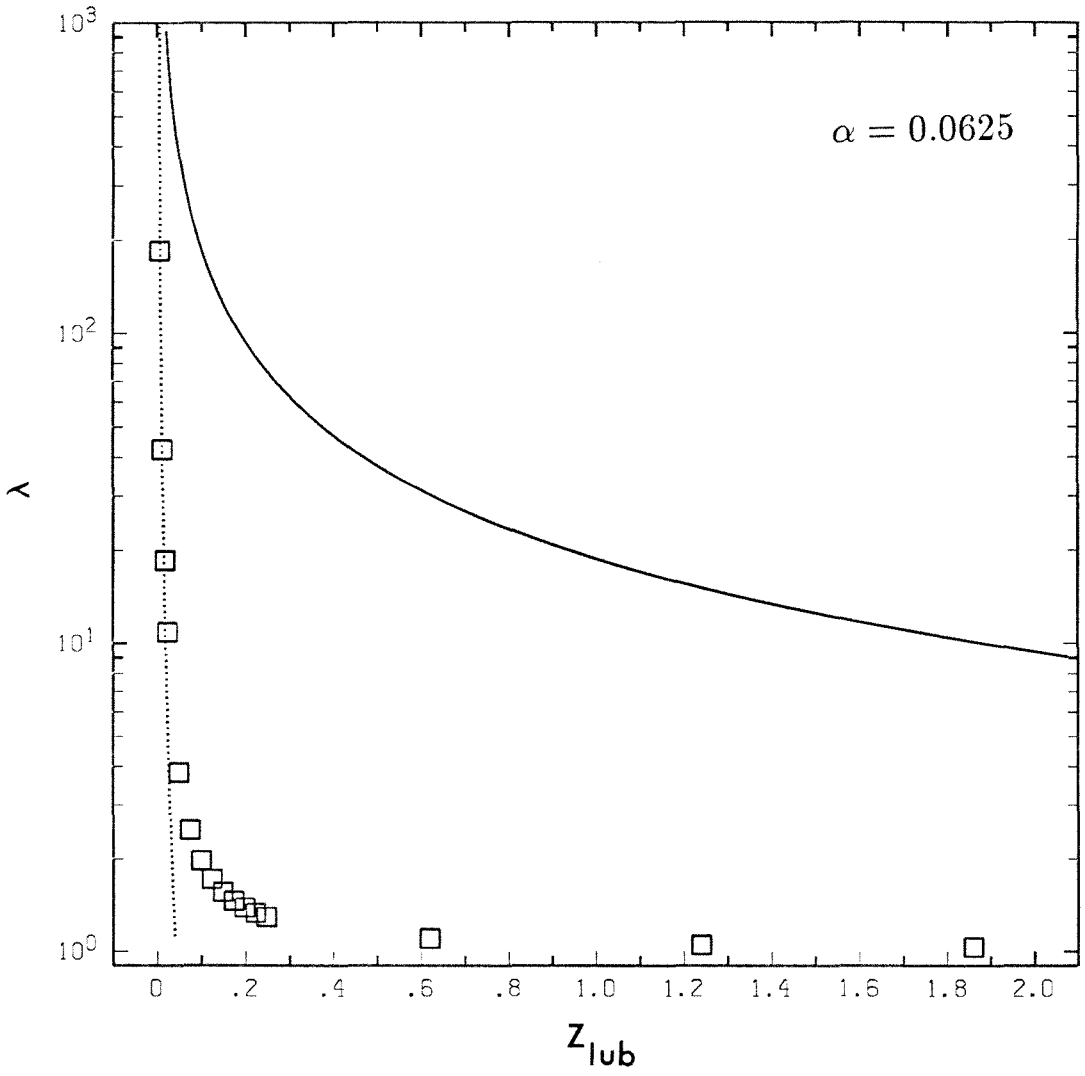


Figure 13(b)

$z_{g-up}$	N = 10		N = 20		N = 30		N = 40		
	$\lambda$ (theoretical)	$\lambda$ (numerical)	Error*	$\lambda$ (numerical)	Error	$\lambda$ (numerical)	Error	$\lambda$ (numerical)	Error
100.	1.011263	1.01532	.401	1.01222	.095	1.01167	.040	1.01148	.021
75.	1.015024	1.01910	.402	1.01598	.094	1.01543	.040	1.01524	.021
50.	1.022553	1.02665	.401	1.02352	.095	1.02296	.040	1.02277	.021
25.	1.045196	1.04937	.399	1.04617	.093	1.04560	.039	1.0454	.020
10.	1.113503	1.11768	.375	1.11428	.067	1.11367	.015	1.11347	-.003
9.	1.126194	1.13032	.366	1.12688	.061	1.12627	.007	1.12606	-.012
8.	1.142068	1.14632	.372	1.14283	.067	1.14222	.013	1.14201	-.005
7.	1.162491	1.16688	.378	1.16334	.073	1.16271	.019	1.16249	-.0001
6.	1.189737	1.19428	.382	1.19065	.077	1.19001	.023	1.18980	.005
5.	1.227889	1.23264	.387	1.22889	.082	1.22823	.028	1.22800	.009
4.	1.285087	1.29008	.389	1.28618	.085	1.28548	.031	1.28525	.013
3.	1.380204	1.38558	.389	1.38140	.087	1.38066	.033	1.38041	.015
2.	1.569205	1.57532	.390	1.57057	.087	1.56974	.034	1.56946	.016
1.	2.125536	2.13369	.384	2.12730	.083	2.12620	.031	2.12584	.014
0.75	2.489273	2.49864	.376	2.49123	.079	2.48998	.028	2.48957	.012
0.5	3.205390	3.21674	.354	3.20751	.066	3.20603	.020	3.20558	.006
0.25	5.305324	5.31976	.272	5.30508	-.005	5.30405	-.024	5.30393	-.026
0.10	11.459157	11.79521	2.93	11.40327	-.488	11.41799	-.359	11.42883	-.265
0.05	21.585818	26.60858	23.3	21.56331	-.104	21.29163	-1.36	21.34026	-1.14

Table 1.

\*Error is defined as

$$100 \times \frac{\lambda(\text{numerical}) - \lambda(\text{theoretical})}{\lambda(\text{theoretical})}$$

$N_{sphere} = 6 \quad N_{wall} = 6$					
$z_{gap}$	$\lambda$ (analytic)	$\lambda$ $x_{truncat} = 25.$	Error	$\lambda$ $x_{truncat} = 50.$	Error
100.	1.011263	1.015590	0.428	1.018810	0.746
75.	1.015024	1.018660	0.358	1.023150	0.801
50.	1.022553	1.026260	0.363	1.032010	0.925
25.	1.045196	1.052580	0.706	1.056430	1.07
10.	1.113503	1.125140	1.05	1.125940	1.12
9.	1.126194	1.138050	1.05	1.138890	1.13
8.	1.142068	1.154130	1.06	1.154960	1.13
7.	1.162491	1.174800	1.06	1.175150	1.09
6.	1.189737	1.202420	1.07	1.200600	0.913
5.	1.227889	1.241260	1.09	1.232290	0.358
4.	1.285087	1.299680	1.14	1.269840	-1.19
3.	1.380204	1.394650	1.05	1.308740	-5.18
2.	1.569205	1.556630	-0.801	1.336160	-14.9
1.	2.125536	1.790740	-15.8	1.331850	-37.3
0.75	2.489273	1.841520	-26.0	1.324160	-46.8
0.5	3.205390	1.875680	-41.5	1.314010	-59.0
0.25	5.305324	1.885720	-64.5	1.301850	-75.5
0.1	11.45916	1.878580	-83.6	1.294010	-88.7
0.05	21.58582	1.874220	-91.3	1.291440	-94.0

Table 2(a).

$N_{sphere} = 6 \quad N_{wall} = 6$					
$z_{gap}$	$\lambda$ (analytic)	$\lambda$ $x_{truncate} = 25.$	Error	$\lambda$ $x_{truncate} = 50.$	Error
100.	1.011263	1.015480	0.417	1.018690	0.734
75.	1.015024	1.018490	0.341	1.023010	0.787
50.	1.022553	1.026000	0.337	1.031910	0.915
25.	1.045196	1.052360	0.685	1.056490	1.08
10.	1.113503	1.125430	1.071	1.126320	1.15
9.	1.126194	1.138440	1.087	1.139300	1.16
8.	1.142068	1.154660	1.103	1.155600	1.18
7.	1.162491	1.175500	1.119	1.176710	1.22
6.	1.189737	1.203290	1.139	1.205120	1.29
5.	1.227889	1.242210	1.166	1.245240	1.41
4.	1.285087	1.300720	1.216	1.305390	1.58
3.	1.380204	1.399000	1.362	1.403730	1.70
2.	1.569205	1.598540	1.869	1.596800	1.76
1.	2.125536	2.185370	2.82	2.292810	7.87
0.75	2.489273	2.566520	3.10	2.937180	18.0
0.5	3.205390	3.403570	6.18	4.742860	48.0
0.25	5.305324	7.652900	44.2	13.30720	151.
0.1	11.45916	30.20205	164.	115.2971	906.
0.05	21.5858	35.74634	61.0	-	-

Table 2(b).

$N_{sphere} = 10 \quad N_{wall} = 10$					
$z_{gap}$	$\lambda$ (analytic)	$\lambda$ $x_{truncate} = 25.$	Error	$\lambda$ $x_{truncate} = 50.$	Error
100.	1.011263	1.008330	-0.290	1.011540	0.027
75.	1.015024	1.011400	-0.357	1.015860	0.082
50.	1.022553	1.018990	-0.348	1.024650	0.205
25.	1.045196	1.045130	-0.006	1.048880	0.352
10.	1.113503	1.117210	0.333	1.117560	0.364
9.	1.126194	1.130050	0.342	1.130260	0.361
8.	1.142068	1.146030	0.347	1.146180	0.360
7.	1.162491	1.166540	0.348	1.166740	0.366
6.	1.189737	1.193830	0.344	1.194300	0.386
5.	1.227889	1.231980	0.333	1.233000	0.416
4.	1.285087	1.289180	0.319	1.290090	0.389
3.	1.380204	1.384720	0.327	1.377360	-0.206
2.	1.569205	1.576370	0.457	1.505340	-4.07
1.	2.125536	2.083520	-1.98	1.637900	-22.9
0.75	2.489273	2.320980	-6.76	1.654970	-33.5
0.5	3.205390	2.612240	-18.5	1.658980	-48.2
0.25	5.305324	2.937680	-44.6	1.647910	-68.9
0.1	11.45916	3.139810	-72.6	1.634120	-85.7
0.05	21.58582	3.208300	-85.1	1.628570	-92.5

Table 3(a).

$N_{sphere} = 10 \quad N_{wall} = 10$					
$z_{gap}$	$\lambda$ (analytic)	$\lambda$ $x_{truncate} = 25.$	Error	$\lambda$ $x_{truncate} = 50.$	Error
100.	1.011263	1.008260	-0.297	1.011460	0.019
75.	1.015024	1.011300	-0.367	1.015770	0.073
50.	1.022553	1.018820	-0.365	1.024570	0.197
25.	1.045196	1.044970	-0.022	1.048880	0.352
10.	1.113503	1.117260	0.337	1.117840	0.389
9.	1.126194	1.130130	0.350	1.130600	0.391
8.	1.142068	1.146180	0.360	1.146570	0.394
7.	1.162491	1.166760	0.367	1.167120	0.398
6.	1.189737	1.194180	0.373	1.194560	0.405
5.	1.227889	1.232540	0.379	1.233040	0.420
4.	1.285087	1.290050	0.386	1.290850	0.448
3.	1.380204	1.385750	0.402	1.387280	0.513
2.	1.569205	1.576420	0.460	1.580980	0.750
1.	2.125536	2.142720	0.808	2.172760	2.22
0.75	2.489273	2.520320	1.25	2.563390	2.98
0.5	3.205390	3.294110	2.77	3.327460	3.81
0.25	5.305324	5.750570	8.39	6.182470	16.5
0.1	11.45916	13.27579	15.9	25.47089	122.
0.05	21.58582	21.02722	-2.59	27.62877	28.0

Table 3(b).

$N_{sphere} = 20 \quad N_{wall} = 20$							
$z_{gap}$	$\lambda$ (analytic)	$\lambda$ $x_{truncate} = 25.$	Error	$\lambda$ $x_{truncate} = 50.$	Error	$\lambda$ $x_{truncate} = 100.$	Error
100.	1.011263	1.005340	-0.586	1.008550	-0.268	1.011310	0.005
75.	1.015024	1.008420	-0.651	1.012870	-0.212	1.015470	0.044
50.	1.022553	1.016020	-0.639	1.021630	-0.090	1.023340	0.077
25.	1.045196	1.042100	-0.296	1.045780	0.056	1.046120	0.088
10.	1.113503	1.113980	0.043	1.114390	0.080	1.114270	0.069
9.	1.126194	1.126790	0.053	1.127060	0.077	1.126930	0.065
8.	1.142068	1.142760	0.061	1.142900	0.073	1.142810	0.065
7.	1.162491	1.163260	0.066	1.163270	0.067	1.163320	0.071
6.	1.189737	1.190540	0.067	1.190430	0.058	1.190820	0.091
5.	1.227889	1.228680	0.064	1.228440	0.045	1.229440	0.126
4.	1.285087	1.285790	0.055	1.285470	0.030	1.286430	0.105
3.	1.380204	1.380630	0.031	1.380790	0.042	1.373560	-0.481
2.	1.569205	1.568760	-0.028	1.572100	0.184	1.501380	-4.32
1.	2.125536	2.126090	0.026	2.078760	-2.20	1.633810	-23.1
0.75	2.489273	2.496450	0.288	2.316190	-6.95	1.650860	-33.7
0.5	3.205390	3.212790	0.231	2.607630	-18.6	1.654870	-48.4
0.25	5.305324	4.881460	-7.99	2.933810	-44.7	1.643760	-69.0
0.1	11.45916	7.284840	-36.4	3.136340	-72.6	1.629750	-85.8
0.05	21.58582	8.783280	-59.3	3.204850	-85.2	1.623890	-92.5

Table 4(a).

$N_{\text{sphere}} = 20 \quad N_{\text{wall}} = 20$							
$z_{\text{gap}}$	$\lambda$ (analytic)	$\lambda$ $x_{\text{truncate}} = 25.$	Error	$\lambda$ $x_{\text{truncate}} = 50.$	Error	$\lambda$ $x_{\text{truncate}} = 100.$	Error
100.	1.011263	1.005310	-0.589	1.008510	-0.272	1.011290	0.026
75.	1.015024	1.008370	-0.656	1.012820	-0.217	1.015460	0.043
50.	1.022553	1.015940	-0.647	1.021590	-0.094	1.023330	0.076
25.	1.045196	1.042010	-0.305	1.045780	0.056	1.046140	0.090
10.	1.113503	1.113970	0.042	1.114490	0.089	1.114490	0.089
9.	1.126194	1.126800	0.054	1.127190	0.088	1.127190	0.088
8.	1.142068	1.142780	0.062	1.143080	0.089	1.143080	0.089
7.	1.162491	1.163300	0.070	1.163520	0.089	1.163530	0.089
6.	1.189737	1.190620	0.074	1.190790	0.089	1.190810	0.090
5.	1.227889	1.228820	0.076	1.228980	0.089	1.229030	0.093
4.	1.285087	1.286060	0.076	1.286240	0.090	1.286370	0.100
3.	1.380204	1.381200	0.072	1.381500	0.094	1.381850	0.119
2.	1.569205	1.570230	0.065	1.570960	0.112	1.572140	0.187
1.	2.125536	2.126880	0.063	2.130670	0.242	2.137710	0.573
0.75	2.489273	2.491240	0.079	2.498970	0.390	2.515210	1.04
0.5	3.205390	3.210330	0.154	3.231620	0.818	3.290070	2.64
0.25	5.305324	5.344480	0.738	5.463540	2.98	5.757460	8.52
0.1	11.45916	12.07906	5.41	13.84710	20.8	15.27464	33.3
0.05	21.58582	24.72773	14.6	30.57144	41.6	36.88208	70.9

Table 4(b).

$N_{sphere} = 30 \quad N_{wall} = 30$							
$z_{gap}$	$\lambda$ (analytic)	$\lambda$ $x_{truncat} = 25.$	Error	$\lambda$ $x_{truncat} = 50.$	Error	$\lambda$ $x_{truncat} = 100.$	Error
100.	1.011263	1.004810	-0.638	1.008020	-0.321	1.010770	-0.049
75.	1.015024	1.007900	-0.702	1.012330	-0.265	1.014930	-0.009
50.	1.022553	1.015500	-0.690	1.021090	-0.143	1.022790	0.023
25.	1.045196	1.041570	-0.347	1.045230	0.003	1.045570	0.036
10.	1.113503	1.113410	-0.008	1.113840	0.030	1.113760	0.023
9.	1.126194	1.126220	0.002	1.126520	0.029	1.126410	0.019
8.	1.142068	1.142190	0.011	1.142380	0.027	1.142230	0.014
7.	1.162491	1.162690	0.017	1.162770	0.024	1.162580	0.008
6.	1.189737	1.189970	0.020	1.189960	0.019	1.189740	0.0003
5.	1.227889	1.228130	0.020	1.228010	0.010	1.227860	-0.002
4.	1.285087	1.285290	0.016	1.285000	-0.007	1.285370	0.022
3.	1.380204	1.380240	0.003	1.379710	-0.036	1.381670	0.106
2.	1.569205	1.568640	-0.036	1.568270	-0.060	1.566050	-0.201
1.	2.125536	2.121690	-0.181	2.131500	0.281	1.935660	-8.93
0.75	2.489273	2.483940	-0.214	2.487960	-0.053	2.054850	-17.5
0.5	3.205390	3.207130	0.054	3.089850	-3.60	2.166220	-32.4
0.25	5.305324	5.347030	0.786	4.141040	-21.9	2.250720	-57.6
0.1	11.45916	10.288800	-10.2	5.206130	-54.6	2.280410	-80.1
0.05	21.58582	14.86634	-31.1	5.719160	-73.5	2.285870	-89.4

Table 5(a).

$N_{sphere} = 30 \quad N_{wall} = 30$							
$z_{gap}$	$\lambda$ (analytic)	$\lambda$ $x_{truncate} = 25.$	Error	$\lambda$ $x_{truncate} = 50.$	Error	$\lambda$ $x_{truncate} = 100.$	Error
100.	1.011263	1.004790	-0.640	1.007990	-0.324	1.010750	-0.051
75.	1.015024	1.007860	-0.706	1.012300	-0.268	1.014920	-0.010
50.	1.022553	1.015440	-0.696	1.021060	-0.146	1.022780	0.022
25.	1.045196	1.041510	-0.353	1.045220	0.002	1.045580	0.037
10.	1.113503	1.113400	-0.009	1.113880	0.034	1.113890	0.035
9.	1.126194	1.126220	0.002	1.126570	0.033	1.126580	0.034
8.	1.142068	1.142200	0.012	1.142450	0.033	1.142460	0.034
7.	1.162491	1.162700	0.018	1.162870	0.033	1.162880	0.033
6.	1.189737	1.190010	0.023	1.190110	0.031	1.190120	0.032
5.	1.227889	1.228200	0.025	1.228260	0.030	1.228270	0.031
4.	1.285087	1.285420	0.026	1.285440	0.027	1.285480	0.031
3.	1.380204	1.380520	0.023	1.380540	0.024	1.380640	0.032
2.	1.569205	1.569440	0.015	1.569500	0.019	1.569850	0.041
1.	2.125536	2.125380	-0.007	2.125960	0.020	2.128290	0.130
0.75	2.489273	2.488790	-0.019	2.490180	0.036	2.495210	0.238
0.5	3.205390	3.204310	-0.034	3.208820	0.107	3.223820	0.575
0.25	5.305324	5.305440	0.002	5.339160	0.638	5.437470	2.49
0.1	11.45916	11.56424	0.917	12.03615	5.04	13.49018	17.7
0.05	21.58582	22.63316	4.85	25.79175	19.5	32.16383	49.0

Table 5(b).

$\alpha = 16.$			
$z_{gap}$	$\lambda$ (numerical)	$z_c$	$\lambda$ (asymptotic)
100.	1.01435	74.777	1.01527
75.	1.01914	57.199	1.02006
50.	1.02832	39.621	1.02922
25.	1.05308	22.043	1.05378
10.	1.10978	11.496	1.10848
9.	1.11824	10.793	1.11637
8.	1.12814	10.090	1.12549
7.	1.13991	9.386	1.13617
6.	1.15417	8.683	1.14884
5.	1.17184	7.980	1.16411
4.	1.19446	7.277	1.18286
3.	1.22476	6.574	1.20646
2.	1.26837	5.871	1.23705
1.	1.34110	5.168	1.27828
.75	1.36965	4.992	1.29093
.5	1.40751	4.816	1.30478
.25	1.46549	4.640	1.32002
.1	1.53117	4.535	1.32992
.05	1.57603	4.500	1.33336

Table 6.

$\alpha = 8.$			
$z_{gap}$	$\lambda$ (numerical)	$z_c$	$\lambda$ (asymptotic)
100.	1.01207	89.886	1.01267
75.	1.01615	68.278	1.01675
50.	1.02410	46.671	1.02470
25.	1.04646	25.064	1.04699
10.	1.10290	12.100	1.10251
9.	1.11197	11.236	1.11127
8.	1.12280	10.371	1.12167
7.	1.13598	9.507	1.13421
6.	1.15240	8.643	1.14964
5.	1.17346	7.779	1.16908
4.	1.20156	6.914	1.19432
3.	1.24125	6.050	1.22843
2.	1.30296	5.186	1.27705
1.	1.41896	4.321	1.35196
.75	1.46892	4.105	1.37747
.5	1.53981	3.889	1.40698
.25	1.66105	3.673	1.44149
.1	1.82506	3.544	1.46515
.05	1.96295	3.500	1.47361

Table 7.

$\alpha = 4.$			
$z_{gap}$	$\lambda$ (numerical)	$z_c$	$\lambda$ (asymptotic)
100.	1.01071	101.844	1.01117
75.	1.01436	77.008	1.01483
50.	1.02157	52.173	1.02204
25.	1.04246	27.338	1.04292
10.	1.09928	12.437	1.09945
9.	1.10896	11.444	1.10902
8.	1.12074	10.450	1.12064
7.	1.13538	9.457	1.13502
6.	1.15408	8.464	1.15330
5.	1.17884	7.470	1.17730
4.	1.21337	6.477	1.21021
3.	1.26542	5.483	1.25812
2.	1.35293	4.490	1.33432
1.	1.54041	3.497	1.47436
.75	1.63163	3.248	1.52984
.5	1.77322	3.000	1.60003
.25	2.05364	2.752	1.69164
.1	2.53087	2.603	1.76139
.05	3.04164	2.553	1.78788

Table 8.

$\alpha = 2.$			
$z_{gap}$	$\lambda$ (numerical)	$z_c$	$\lambda$ (asymptotic)
100.	1.01075	106.311	1.01070
75.	1.01429	80.149	1.01424
50.	1.02134	53.986	1.02128
25.	1.04218	27.823	1.04214
10.	1.10217	12.126	1.10266
9.	1.11287	11.080	1.11301
8.	1.12609	10.033	1.12629
7.	1.14280	8.987	1.14301
6.	1.16477	7.940	1.16507
5.	1.19490	6.894	1.19502
4.	1.23849	5.847	1.23824
3.	1.30731	4.801	1.30606
2.	1.43323	3.754	1.42789
1.	1.74818	2.708	1.71081
.75	1.92492	2.446	1.85157
.5	2.23158	2.184	2.06186
.25	2.96188	1.923	2.41007
.1	4.58656	1.766	2.75545
.05	6.77456	1.714	2.91152

Table 9.

$\alpha = .5$			
$z_{gap}$	$\lambda$ (numerical)	$z_c$	$\lambda$ (asymptotic)
100.	1.01336	88.224	1.01292
75.	1.01771	66.306	1.01726
50.	1.02644	44.388	1.02600
25.	1.05306	22.470	1.05270
10.	1.13646	9.320	1.13729
9.	1.15254	8.443	1.15373
8.	1.17288	7.566	1.17466
7.	1.19939	6.689	1.20218
6.	1.23535	5.813	1.38341
5.	1.28687	4.936	1.29520
4.	1.36657	4.059	1.38341
3.	1.50544	3.182	1.54679
2.	1.80346	2.306	1.95279
1.	2.83343	1.429	4.70040
.75	3.61590	1.210	14.2601
.5	5.36885	0.991	-
.25	11.70260	0.771	-
.1	35.25879	0.640	-
.05	78.14056	0.596	-

Table 10.

$\alpha = .25$			
$z_{gap}$	$\lambda$ (numerical)	$z_c$	$\lambda$ (asymptotic)
100.	1.01566	72.919	1.01567
75.	1.02096	54.761	1.02097
50.	1.03168	36.604	1.03171
25.	1.06473	18.446	1.06495
10.	1.17243	7.551	1.17506
9.	1.19379	6.825	1.19737
8.	1.22107	6.099	1.22619
7.	1.25710	5.372	1.26487
6.	1.30680	4.646	1.31950
5.	1.37954	3.920	1.40254
4.	1.49545	3.193	1.54388
3.	1.70634	2.467	1.83820
2.	2.19247	1.741	2.82674
1.	4.14864	1.015	-
.75	5.85589	0.833	-
.5	10.17695	0.651	-
.25	29.15676	0.467	-
.1	115.89697	0.361	-

Table 11.

$\alpha = .125$			
$z_{gap}$	$\hat{\lambda}$ (numerical)	$z_c$	$\hat{\lambda}$ (asymptotic)
100.	1.01880	58.675	1.01955
75.	1.02545	44.043	1.02621
50.	1.03896	29.410	1.03977
25.	1.10271	14.778	1.08240
10.	1.22426	5.999	1.23081
9.	1.25345	5.414	1.26231
8.	1.29113	4.829	1.30376
7.	1.34151	4.243	1.36077
6.	1.41211	3.658	1.44413
5.	1.51755	3.073	1.57759
4.	1.69024	2.487	1.82572
3.	2.01721	1.902	2.44756
2.	2.82202	1.317	6.86285
1.	6.55029	0.731	-
.75	10.22585	0.585	-
.5	20.58526	0.439	-
.25	74.75567	0.292	-

Table 12.

$\alpha = .0625$			
$z_{gap}$	$\lambda$ (numerical)	$z_c$	$\lambda$ (asymptotic)
100.	1.02249	46.744	1.02466
75.	1.03093	35.076	1.03314
50.	1.04817	23.409	1.05049
25.	1.10271	11.741	1.10597
10.	1.29578	4.741	1.31116
9.	1.33633	4.274	1.35727
8.	1.38921	3.807	1.41944
7.	1.46081	3.340	1.50780
6.	1.56266	2.874	1.64332
5.	1.71775	2.407	1.87752
4.	1.97840	1.940	2.37983
3.	2.49057	1.474	4.22706
2.	3.83087	1.007	-
1.	10.88625	0.540	-
.75	18.58634	0.424	-
.5	42.29466	0.307	-
.25	185.11381	0.190	-

Table 13.

Chapter II

Buoyancy-driven motion of a deformable drop  
toward a planar wall  
at low Reynolds number

E.P. Ascoli, D.S. Dandy, and L.G. Leal

Dept. of Chemical Engineering

California Institute of Technology

Pasadena, California 91125

## Introduction

The slow viscous motions of deformable drops are of interest in processes such as coalescence, emulsion formation, mixing and separation. Further, in “real” systems bounding surfaces are obviously present and little is known about the effects of such bounding surfaces on *deformable* drops. Haberman and Sayre (1958) obtained approximate solutions for a spherical drop traveling in steady motion along the axis of a tube. Bart (1968) solved the problem of the slow unsteady settling of a fluid sphere toward a flat fluid interface. However, in each of these analyses, the assumption of spherical (or near-spherical) shape is a fundamental limitation.

A multitude of investigators have theoretically considered the effects of a planar wall on drops and bubbles when the separation distance between the wall and the drop or bubble is very small. In these investigations, the focus has been on the dynamics of the thin film between the bounding wall and the drop or bubble, without attempting to resolve the dynamics that lead to the thin-film configuration. Experimentally, (Hartland (1967, 1969), Platinakov (1964)) “dimpled” configurations (i.e. shapes in which the film between the drop or bubble and the wall is thinner near the rim than at the center) have been observed for a wide range of parameters. Theoretically, the analyses have been based upon the lubrication approximation in an attempt to model the dynamics of film-drainage. Unfortunately, many of the simplifying assumption made have been ad hoc, and largely unmotivated. Several of the most important assumptions are listed below.

- (I) The film has been assumed sufficiently thin that the lubrication approximation is valid (Frankel and Mysels (1962), Hartland (1969), Dimitrov and Ivanov (1978), Lin and Slattery (1982)). Specifically, if  $h$  is a measure of the film thickness and  $R$  is a measure of the radial extent of the film then  $h/R \ll 1$ . This is the key assumption underlying film-drainage theory. In particular, it has been implicitly assumed that the lubrication approx-

imation has not neglected the necessary physics to predict the onset and evolution of dimpling.

- (II) Viscous effects in the drop have generally been neglected. In particular, focus has been placed on the two limiting cases of “fully mobile” ( zero tangential stress) and “fully immobile” interfaces (no-slip applied at the fluid-fluid interface). (Frankel and Mysels (1962), Hartland (1969), Dimitrov and Ivanov (1978), Lin and Slattery (1982)).
- (III) Gravitational effects in the film have frequently been neglected ( Hartland (1969), Dimitrov and Ivanov (1978), Lin and Slattery (1982)).
- (IV) In addition to assumption (I), a wide variety of geometrical assumptions have been made:
  - (a) The film has been assumed to be nearly a plane parallel to the wall. (Dimitrov and Ivanov (1978))
  - (b) “Dimpled” configurations have been assumed as initial film shapes. For instance, the dimple has been assumed to consist of two parabolas with the radius of curvature at the apex varying with time in the central parabola and constant in the peripheral parabola (Hartland and Robinson (1977)).
  - (c) The drop has been assumed nearly spherical outside of the film region (Lin and Slattery (1982), Dimitrov and Ivanov (1978)).
  - (d) At the edge of the film, geometrical details of drop shape have been assumed nearly invariant with time (Dimitrov and Ivanov (1978) Lin and Slattery (1982)).

The list of thin film investigations referenced above is by no means complete but it is exemplary.

In this paper we present an efficient numerical scheme for determining the buoyancy driven motion of a deformable viscous drop normal to a planar no-slip surface. The complete time evolution of drop shape from spherical far from the wall to highly deformed near the wall is studied. No limitation on “film” thickness is made. Viscous effects in the drop phase are not neglected. Gravity

is not neglected. The only geometrical assumptions are that the motions are axisymmetric and the drop is initially spherical *far* from the wall.

Being numerical in nature, the current scheme is subject to numerical errors as well as time limitations. For this reason, the results obtained pertain strictly to the initial stages of thin film formation. Nevertheless the dynamics of dimple formation are captured. The goal of the study is to explore the listed film-drainage assumptions using a complete numerical scheme. In addition, this study is intended to provide information and insight into the details and mechanism behind dimple formation. Drop shapes obtained with the current numerical scheme may potentially be used as starting configurations for thin film analytic theories.

The technique that we use is based on the well known boundary integral method which has already been used successfully in a variety of applications. Youngren and Acrivos applied the method to calculate the slow viscous flow past a single solid particle (1975). Later, Youngren and Acrivos (1976) applied the technique to calculate the steady-state deformation of an inviscid drop in an extensional flow, and Rallison and Acrivos (1978) considered viscous drops in an extensional flow. Lee and Leal (1982) and later Geller, Lee and Leal (1986) used the boundary integral method to calculate the motion of a solid sphere normal to a deformable interface. Recently, Chi (1986) considered the motion of a deformable drop normal to a deformable fluid-fluid interface, also using the boundary integral method. The current application of the method differs from these previous studies in the choice of the so called fundamental solution of the Stokes' system. Previous work implemented a fundamental solution originating with Odqvist (1930) and discussed by Ladyzhenskaya (1963). Here, a fundamental solution (or more appropriately a Green's Function) presented by Blake (1971) will be employed. This Green's function is appropriate for systems involving an infinite, planar, wall and was successfully used by Ascoli, Dandy and Leal (1988) to determine the hydrodynamic resistance on a solid particle

in creeping flow moving in the presence of a planar wall. Its use in the present application represents a significant simplification and numerical timesaving over the previous boundary integral formulations.

## Formulation

### (a) Equations and boundary conditions

We consider the slow motion of a deformable drop normal to a no-slip, infinite, planar surface (figure 1a). Fluid 1, which composes the drop, and fluid 2, in which the drop is suspended are both assumed to be Newtonian with constant density. In addition, the fluids are assumed to be immiscible with an interface characterized by a constant surface tension. All motions and deformations are assumed axisymmetric about the  $z$ -axis, which passes through the drop center and is normal to the planar wall. Gravity is assumed to act along the  $z$ -axis, toward the wall if fluid 1 is more dense than fluid 2, or away from the wall if fluid 1 is less dense than fluid 2. The analysis presented is based upon the creeping motion approximation in which the inertial terms in the equations of motion are neglected entirely. The corresponding small Reynolds numbers ( $Re_1, Re_2$ ) of the system are

$$Re_1 = \frac{U a}{\nu_1} \ll 1.$$

$$Re_2 = \frac{U a}{\nu_2} \ll 1.$$

The characteristic length,  $a$ , is the radius of a sphere of equal volume and  $\nu_1, \nu_2$  are the respective kinematic viscosities of fluid 1 and fluid 2. The characteristic velocity,  $U$ , is the terminal velocity of an equal volume spherical drop in the absence of a wall and is given by the Hadamard (1911) and Rybczynski (1911) result

$$U = \frac{1}{3} \frac{a^2 g}{\nu_2} \left| \frac{\rho_1}{\rho_2} - 1 \right| \left( \frac{1 + \lambda}{1 + \frac{3}{2}\lambda} \right)$$

where  $\lambda = \mu_1/\mu_2$  is the ratio of dynamic viscosities while  $\rho_1$  and  $\rho_2$  are the respective fluid densities. The governing Stokes equations are then:

$$\begin{aligned} 0 &= -\nabla p_1 + \nabla^2 \mathbf{u}_1 \\ 0 &= \nabla \cdot \mathbf{u}_1 \end{aligned} \tag{1}$$

for the drop, and similarly

$$\begin{aligned} 0 &= -\nabla p_2 + \nabla^2 \mathbf{u}_2 \\ 0 &= \nabla \cdot \mathbf{u}_2. \end{aligned} \quad (2)$$

for the surrounding fluid. Here, velocities are made dimensionless with  $U$  and lengths with  $a$ . Fluid 1 and Fluid 2 pressures and stresses are made dimensionless with  $\mu_1 U/a$  and  $\mu_2 U/a$  respectively. The boundary conditions are

$$\mathbf{u}_2 \longrightarrow 0 \quad \text{as } \|\mathbf{x}\| \longrightarrow \infty, \quad (3)$$

with the no-slip condition at the wall,

$$\mathbf{u}_2 = 0 \quad \text{for } \mathbf{x} \in \mathbf{P} = \left\{ \mathbf{x} \in \mathbf{R}^3 : \mathbf{x} = (x, y, z) \text{ and } z = 0 \right\} \quad (4)$$

and continuity of velocity and stress at the drop interface  $\mathbf{x} \in S_I$ :

$$\mathbf{u}_1 = \mathbf{u}_2 \stackrel{def}{=} \mathbf{u}^I \quad (5)$$

$$(\lambda \mathbf{n} \cdot \mathbf{T}^{(1)} - \mathbf{n} \cdot \mathbf{T}^{(2)}) = -\frac{\mathbf{n}}{Ca} \nabla \cdot \mathbf{n} - \mathbf{n}z \left\{ 3 \frac{(1 + \frac{3}{2}\lambda)}{(1 + \lambda)} \right\} \stackrel{def}{=} \mathcal{F} \quad (6)$$

The vector  $\mathbf{n}$  is the outer normal to the drop surface. The pressures  $p_1$  and  $p_2$  are modified pressures \* which represent the pressure contribution in the fluid due solely to motion. Gravity thus enters the problem through equation (6). The term in curly braces in (6) gives the contribution due to gravity.  $Ca = \mu_2 U/\gamma$  is the capillary number.

Given a drop configuration at dimensionless time  $t$ , (time made dimensionless with respect to  $a/U$ ) equations (1-6) determine the instantaneous velocity field. The drop surface,  $S_I$ , is assumed to deform in accordance with the instantaneous interface velocity field, thus, determining a new drop configuration.

---

\* If  $P$  represents absolute pressure in a fluid of density  $\rho$  then modified pressure,  $p$ , is defined as  $p = P - \rho g w$  where  $w$  measures distance in the direction opposite to gravity. Here,  $w$  corresponds to  $\pm z$ , the sign is determined by the direction in which gravity acts.

In this manner, the time evolution of the drop is determined. The kinematic condition used to deform the drop surface is

$$\frac{d\mathbf{x}_s}{dt} = \mathbf{n}(\mathbf{x}_s) \left( \mathbf{n}(\mathbf{x}_s) \cdot \mathbf{u}^I(\mathbf{x}_s) \right) \quad (7)$$

In other words, the drop surface is deformed pointwise along the normal with the normal projection of the surface velocity.

Equations (1) and (2) and the corresponding boundary conditions will be recast into a boundary integral formulation. Ascoli, Dandy and Leal (1988) presented the boundary integral formulation appropriate for the case where an infinite, no-slip, planar wall is present. There, the formulation was applied to determine the hydrodynamic resistances on solid particles in creeping flow near a no-slip planar wall. Here, the formulation is extended to the two fluid problem.

Briefly, the reformulation begins with the Green's formula for the Stokes system:

$$\int_{\Omega} ((\nabla^2 \mathbf{u} - \nabla p) \cdot \mathbf{w} - (\nabla^2 \mathbf{w} + \nabla q) \cdot \mathbf{u}) dV = \int_{\partial\Omega} (\mathbf{n} \cdot \mathbf{T} \cdot \mathbf{w} - \mathbf{n} \cdot \Sigma \cdot \mathbf{u}) dS \quad (8)$$

where

$$\mathbf{T} = (\nabla \mathbf{u} + (\nabla \mathbf{u})^T) - p\mathbf{I} \quad (9)$$

$$\Sigma = (\nabla \mathbf{w} + (\nabla \mathbf{w})^T) + q\mathbf{I} \quad (10)$$

Equation (8) is valid for any sufficiently smooth fields  $\mathbf{u}$ ,  $p$  and  $\mathbf{w}$ ,  $q$  such that  $\mathbf{u}$  and  $\mathbf{w}$  are solenoidal. Here  $\Omega$  is a subset of  $\mathbf{R}^3$  and  $\partial\Omega$  is its boundary with outward normal  $\mathbf{n}$ . This formula relates the Stokes operator to its adjoint. When appropriate adjoint operator problems are solved, their solutions may be superposed via equation (8) to yield the desired integral formulation. In particular, consider the following adjoint operator problem:

$$\begin{aligned} \delta(\mathbf{x} - \xi)\mathbf{e}_j &= \nabla_{\xi} \mathbf{q}^j(\mathbf{x}, \xi) + \nabla_{\xi}^2 \mathbf{v}^j(\mathbf{x}, \xi) \\ 0 &= \nabla_{\xi} \cdot \mathbf{v}^j(\mathbf{x}, \xi) \end{aligned} \quad (11)$$

$$\mathbf{v}^j(\mathbf{x}, \xi) = 0 \quad \xi \in \mathbf{P} \quad \mathbf{x} \in \mathbf{R}^3 \quad (12)$$

The solution to this system is discussed by Blake (1971) and stems from the work of Oseen (1930). It is

$$\begin{aligned} v_i^j &= \hat{v}_i^j + \hat{\hat{v}}_i^j \\ q^j &= \hat{q}^j + \hat{\hat{q}}^j \\ \Sigma_{ik}^j &= \hat{\Sigma}_{ik}^j + \hat{\hat{\Sigma}}_{ik}^j \end{aligned} \quad (13)$$

where

$$\begin{aligned} \hat{v}_i^j &= -\frac{1}{8\pi} \left\{ \frac{\delta_{ij}}{r} + \frac{r_i r_j}{r^3} \right\} \\ \hat{q}^j &= \frac{1}{4\pi} \left\{ \frac{r_j}{r^3} \right\} \\ \hat{\Sigma}_{ik}^j &= \frac{3}{4\pi} \left\{ \frac{r_k r_i r_j}{r^5} \right\} \end{aligned}$$

and

$$\begin{aligned} \hat{\hat{v}}_i^j &= -\frac{1}{8\pi} \left\{ -\frac{\delta_{ij}}{R} - \frac{R_i R_j}{R^3} \right. \\ &\quad \left. + 2x_3 \Delta_j \frac{\partial}{\partial R_j} \left[ \frac{x_3 R_i}{R^3} - \frac{\delta_{i3}}{R} - \frac{R_i R_3}{R^3} \right] \right\} \\ &= -\frac{1}{8\pi} \left\{ -\frac{\delta_{ij}}{R} - \frac{R_i R_j}{R^3} \right. \\ &\quad \left. + 2x_3 \Delta_j \left[ x_3 \left( \frac{\delta_{ij}}{R^3} - \frac{3R_i R_j}{R^5} \right) + \frac{\delta_{i3}}{R^3} R_j \right. \right. \\ &\quad \left. \left. - \frac{1}{R^3} (\delta_{ij} R_3 + R_i \delta_{3j}) + \frac{3R_i R_j R_3}{R^5} \right] \right\} \\ \hat{\hat{q}}^j &= \frac{1}{4\pi} \left[ -\frac{R_j}{R^3} - 2x_3 \Delta_j \left( \frac{\delta_{3j}}{R^3} - \frac{3R_j R_3}{R^5} \right) \right] \\ \hat{\hat{\Sigma}}_{ik}^j &= \frac{3}{4\pi} \left\{ -\frac{R_i R_j R_k}{R^5} - 2x_3 \Delta_j \left[ -\frac{x_3}{R^5} \delta_{ik} R_j \right. \right. \\ &\quad \left. \left. + \frac{\xi_3}{R^5} (R_i \delta_{jk} + \delta_{ij} R_k) + \frac{R_i \delta_{3j} R_k}{R^5} - \frac{5R_i R_j R_k \xi_3}{R^7} \right] \right\}. \end{aligned}$$

where  $\mathbf{r} = (\xi_1 - x_1, \xi_2 - x_2, \xi_3 - x_3)^T$ ,  $\mathbf{R} = (\xi_1 - x_1, \xi_2 - x_2, \xi_3 + x_3)^T$ ,  $r = [(\xi_1 - x_1)^2 + (\xi_2 - x_2)^2 + (\xi_3 - x_3)^2]^{1/2}$ ,  $R = [(\xi_1 - x_1)^2 + (\xi_2 - x_2)^2 + (\xi_3 + x_3)^2]^{1/2}$ .

$x_3)^2]^{1/2}$ , and  $R_3 = \xi_3 + x_3$ . The quantity  $\Delta_j$  has value +1 for  $j = 1, 2$  and  $-1$  for  $j = 3$ . Here  $\hat{v}_i^j$ ,  $\hat{q}^j$  and  $\hat{\Sigma}_{ik}^j$  is the classical “fundamental solution” to Stokes system employed by previous researchers . This fundamental solution satisfies the system

$$\begin{aligned} \delta(\mathbf{x} - \xi)\mathbf{e}_j &= \nabla_\xi \hat{\mathbf{q}}^j(\mathbf{x}, \xi) + \nabla_\xi^2 \hat{\mathbf{v}}^j(\mathbf{x}, \xi) \\ 0 &= \nabla_\xi \cdot \hat{\mathbf{v}}^j(\mathbf{x}, \xi) \\ \hat{\mathbf{v}}^j(\mathbf{x}, \xi), \hat{q}^j(\mathbf{x}, \xi) &\longrightarrow 0 \quad \|\mathbf{x}\|, \|\xi\| \longrightarrow \infty \end{aligned} \quad (14)$$

Physically,  $\hat{v}_i^j$  is the  $i^{th}$  component of the velocity at  $\xi$  due to a unit force, or Stokeslet, applied at the point  $\mathbf{x}$  in the direction  $\mathbf{e}_j$ . The quantity  $-\hat{q}^j$  is the corresponding pressure.

The Green’s function (13) can be viewed as the fundamental solution to Stokes equations plus additional terms to account for the presence of the planar wall. Solution (13) is superposed via equation (8) by identifying  $\mathbf{w}$  with  $\mathbf{v}^j(\mathbf{x}, \xi)$ ,  $\Sigma$  with  $\Sigma^j$  and  $q$  with  $\hat{q}^j(\mathbf{x}, \xi)$  yielding the integral equation:

$$\begin{aligned} -(\mathbf{u}(\mathbf{x}))_j &= \int_{\partial\Omega} \left( \mathbf{n} \cdot \mathbf{T}(\xi) \cdot \mathbf{v}^j(\mathbf{x}, \xi) - \mathbf{n} \cdot \Sigma^j(\mathbf{x}, \xi) \cdot \mathbf{u}(\xi) \right) dS_\xi \\ \mathbf{x} \in \Omega \quad \text{for} \quad j &= 1, 2, 3 \end{aligned} \quad (15)$$

For the geometry of figure 1a, equation (15) may be written for each fluid giving

$$\begin{aligned} -\lambda(\mathbf{u}_1(\mathbf{x}))_j &= \lambda \int_{S_I} \left( \mathbf{n} \cdot \mathbf{T}^{(1)}(\xi) \cdot \mathbf{v}^j(\mathbf{x}, \xi) - \mathbf{n} \cdot \Sigma^j(\mathbf{x}, \xi) \cdot \mathbf{u}^I(\xi) \right) dS_\xi \\ \mathbf{x} \in \Omega_1 \\ (\mathbf{u}_2(\mathbf{x}))_j &= \int_{S_I + \mathbf{P}} \left( \mathbf{n} \cdot \mathbf{T}^{(2)}(\xi) \cdot \mathbf{v}^j(\mathbf{x}, \xi) - \mathbf{n} \cdot \Sigma^j(\mathbf{x}, \xi) \cdot \mathbf{u}^I(\xi) \right) dS_\xi \\ \mathbf{x} \in \Omega_2 \end{aligned} \quad (16)$$

Here  $S_I$  and  $S_I + \mathbf{P}$  are the boundaries of fluid 1 and fluid 2. Due to conditions (4) and (12) the contribution from the planar wall  $\mathbf{P}$  in equation (16) is zero and thus

$$-\lambda(\mathbf{u}_1(\mathbf{x}))_j = \lambda \int_{S_I} \left( \mathbf{n} \cdot \mathbf{T}^{(1)}(\xi) \cdot \mathbf{v}^j(\mathbf{x}, \xi) - \mathbf{n} \cdot \Sigma^j(\mathbf{x}, \xi) \cdot \mathbf{u}^I(\xi) \right) dS_\xi$$

$$\mathbf{x} \in \Omega_1$$

$$(\mathbf{u}_2(\mathbf{x}))_j = \int_{S_I} \left( \mathbf{n} \cdot \mathbf{T}^{(2)}(\xi) \cdot \mathbf{v}^j(\mathbf{x}, \xi) - \mathbf{n} \cdot \Sigma^j(\mathbf{x}, \xi) \cdot \mathbf{u}^I(\xi) \right) dS_\xi$$

$$\mathbf{x} \in \Omega_2 \quad (17)$$

If the fundamental solution set  $\hat{\mathbf{v}}^j, \hat{q}^j, \hat{\Sigma}^j$  had been used in the formulation instead of the Green's function (13) then a term of the form

$$\int_{\mathbf{P}} \mathbf{n} \cdot \mathbf{T}^{(2)}(\xi) \cdot \hat{\mathbf{v}}^j(\mathbf{x}, \xi) dS_\xi$$

would be present.

The pressures in the inner and outer fluid domains may be obtained by first applying  $\Delta_{\mathbf{x}}^2$  to each of the equations in (17). Using the governing equations (1) and (2) this allows the gradients of the pressures to be written in terms of surface integrals. Integrating yields the pressures to within constants. The results are:

$$p_1(\mathbf{x}) - \bar{p}_1 = - \int_{S_I} \left( \mathbf{n} \cdot \mathbf{T}^{(1)}(\xi) \cdot \Psi(\mathbf{x}, \xi) - \mathbf{n} \cdot \Phi(\mathbf{x}, \xi) \cdot \mathbf{u}^I(\xi) \right) dS_\xi$$

$$\mathbf{x} \in \Omega_1 \quad (18)$$

$$p_2(\mathbf{x}) - p_2^\infty = \int_{S_I} \left( \mathbf{n} \cdot \mathbf{T}^{(2)}(\xi) \cdot \Psi(\mathbf{x}, \xi) - \mathbf{n} \cdot \Phi(\mathbf{x}, \xi) \cdot \mathbf{u}^I(\xi) \right) dS_\xi$$

$$\mathbf{x} \in \Omega_2 \quad (19)$$

The terms  $\bar{p}_1$  and  $p_2^\infty$  are the constants of integration. In particular,  $p_2^\infty$  corresponds to the pressure in the outer fluid as  $z \rightarrow \infty$ . The kernels  $\Psi$  and  $\Phi$  are given by

$$\Psi_k(\mathbf{x}, \xi) = \frac{1}{4\pi} \left[ \frac{r_k}{r^3} - \frac{R_k}{R^3} + \frac{2x_3 \delta_{k3}}{R^3} + \frac{6\xi_3 R_k R_3}{R^5} \right] \quad (20)$$

$$\begin{aligned} \Phi_{ik}(\mathbf{x}, \xi) = \frac{1}{2\pi} \left[ \frac{\delta_{ik}}{r^3} - \frac{3r_i r_k}{r^5} + \frac{\delta_{ik}}{R^3} + \frac{3R_i R_k}{R^5} - \frac{6x_3 R_3 \delta_{ik}}{R^5} \right. \\ \left. + \frac{6\xi_3 (\delta_{i3} R_k + \delta_{k3} R_i)}{R^5} - \frac{30\xi_3 R_3 R_i R_k}{R^7} \right] \quad (21) \end{aligned}$$

The next step in the formulation is to write equations (17) for points  $\mathbf{x} = \mathbf{x}_s \in S_I$ . The limit  $\mathbf{x} \rightarrow \mathbf{x}_s \in S_I$  is a singular limit in the sense that the portions of the kernels  $\mathbf{v}^j(\xi, \mathbf{x})$  and  $\Sigma^j(\xi, \mathbf{x})$  corresponding to the fundamental singular solutions  $\hat{\mathbf{v}}^j, \hat{\Sigma}^j$  become unbounded. The remaining portions of the kernels,  $\hat{\mathbf{v}}^j(\xi, \mathbf{x})$  and  $\hat{\Sigma}^j(\xi, \mathbf{x})$  corresponding to the wall corrections are well behaved for  $\mathbf{x} \in S_I$ . It is well known (Ladyzhenskaya (1963)) that

$$\int_{S_I} \mathbf{n} \cdot \mathbf{T}^{(2)}(\xi) \cdot \hat{\mathbf{v}}^j(\mathbf{x}, \xi) dS_\xi$$

is continuous as a function of  $\mathbf{x}$  across  $S_I$  while

$$\begin{aligned} & \lim_{\mathbf{x} \in \Omega_1 \rightarrow \mathbf{x}_s} \left\{ \int_{S_I} \mathbf{n} \cdot \hat{\Sigma}^j(\mathbf{x}, \xi) \cdot \mathbf{u}(\xi) dS_\xi \right\} \\ &= \frac{1}{2}(\mathbf{u}(\mathbf{x}_s))_j + \int_{S_I} \mathbf{n} \cdot \hat{\Sigma}^j(\mathbf{x}_s, \xi) \cdot \mathbf{u}(\xi) dS_\xi \\ & \lim_{\mathbf{x} \in \Omega_2 \rightarrow \mathbf{x}_s} \left\{ \int_{S_I} \mathbf{n} \cdot \hat{\Sigma}^j(\mathbf{x}, \xi) \cdot \mathbf{u}(\xi) dS_\xi \right\} \\ &= -\frac{1}{2}(\mathbf{u}(\mathbf{x}_s))_j + \int_{S_I} \mathbf{n} \cdot \hat{\Sigma}^j(\mathbf{x}_s, \xi) \cdot \mathbf{u}(\xi) dS_\xi \\ & \mathbf{x}_s \in S_I \end{aligned} \tag{22}$$

These facts imply that

$$\int_{S_I} \mathbf{n} \cdot \mathbf{T}^{(2)}(\xi) \cdot \mathbf{v}^j(\mathbf{x}, \xi) dS_\xi$$

is continuous across  $S_I$  while

$$\begin{aligned} & \lim_{\mathbf{x} \in \Omega_1 \rightarrow \mathbf{x}_s} \left\{ \int_{S_I} \mathbf{n} \cdot \Sigma^j(\mathbf{x}, \xi) \cdot \mathbf{u}(\xi) dS_\xi \right\} \\ &= \frac{1}{2}(\mathbf{u}(\mathbf{x}_s))_j + \int_{S_I} \mathbf{n} \cdot \Sigma^j(\mathbf{x}_s, \xi) \cdot \mathbf{u}(\xi) dS_\xi \\ & \lim_{\mathbf{x} \in \Omega_2 \rightarrow \mathbf{x}_s} \left\{ \int_{S_I} \mathbf{n} \cdot \Sigma^j(\mathbf{x}, \xi) \cdot \mathbf{u}(\xi) dS_\xi \right\} \\ &= -\frac{1}{2}(\mathbf{u}(\mathbf{x}_s))_j + \int_{S_I} \mathbf{n} \cdot \Sigma^j(\mathbf{x}_s, \xi) \cdot \mathbf{u}(\xi) dS_\xi \end{aligned}$$

$$\mathbf{x}_s \in S_I \quad (23)$$

In view of jump conditions (23), equations (17) may be re-written for  $\mathbf{x}_s \in S_I$  as

$$-\frac{1}{2}\lambda(\mathbf{u}^I(\mathbf{x}_s))_j = \lambda \int_{S_I} \left( \mathbf{n} \cdot \mathbf{T}^{(1)}(\xi) \cdot \mathbf{v}^j(\mathbf{x}_s, \xi) - \mathbf{n} \cdot \Sigma^j(\mathbf{x}_s, \xi) \cdot \mathbf{u}^I(\xi) \right) dS_\xi \quad (24)$$

$$\frac{1}{2}(\mathbf{u}^I(\mathbf{x}_s))_j = \int_{S_I} \left( \mathbf{n} \cdot \mathbf{T}^{(2)}(\xi) \cdot \mathbf{v}^j(\mathbf{x}_s, \xi) - \mathbf{n} \cdot \Sigma^j(\mathbf{x}_s, \xi) \cdot \mathbf{u}^I(\xi) \right) dS_\xi \quad (25)$$

Subtracting equation (25) from equation (24) and using condition (6) gives

$$\frac{1}{2}(\mathbf{u}^I(\mathbf{x}_s))_j = + \int_{S_I} \Sigma^j(\mathbf{x}_s, \xi) \cdot \mathbf{u}^I(\xi) \cdot \mathbf{n} dS_\xi - \int_{S_I} \mathbf{v}^j(\mathbf{x}_s, \xi) \cdot \mathbf{f}^{(1)}(\xi) dS_\xi \quad (26)$$

and

$$-\frac{1}{2}(\mathbf{u}^I(\mathbf{x}_s))_j = -\frac{\lambda-1}{\lambda+1} \int_{S_I} \Sigma^j(\mathbf{x}_s, \xi) \cdot \mathbf{u}^I(\xi) \cdot \mathbf{n} dS_\xi + \frac{1}{(\lambda+1)} \int_{S_I} \mathbf{v}^j(\mathbf{x}, \xi) \cdot \mathcal{F} dS_\xi \quad (27)$$

$$\mathbf{x}_s \in S_I,$$

where  $\mathbf{f}^{(i)} \stackrel{def}{=} \mathbf{n} \cdot \mathbf{T}^{(i)}$  for  $i = 1, 2$ . Due to condition (12), all integrations are over  $S_I$  alone. From a numerical point of view this is a major simplification. There is no need to solve for unknown normal tractions on the plane wall.

There are several ways in which the drop surface may be represented. One possibility is to define the surface as  $(\rho(z), z)$  for  $\theta \in [0, 2\pi)$ , where  $\rho = \sqrt{x^2 + y^2}$  and  $\theta$  are cylindrical coordinates. However, this representation implicitly limits the types of surfaces which can be considered to those for which  $\rho$  is a single valued function of  $z$ . Alternately, a spherical coordinate system could be employed, with  $\rho_{sphere} = \sqrt{x^2 + y^2 + z^2}$  and polar angle  $\phi$  measured from the  $z$ -axis, to give a representation  $(\rho_{sphere}(\phi), \phi)$  for  $\theta \in [0, 2\pi)$  and  $\phi \in [0, \pi)$ . Again this representation is limited to those surfaces which yield single valued functions  $\rho_{sphere}(\phi)$ . An equally simple, but more general representation

which avoids this potential problem is to parametrically define the surface as  $(\rho(s), z(s))$  for  $\theta \in [0, 2\pi)$ , where  $s$  is a parametric independent variable lying in the interval  $[s_o, s_f]$ . This is the approach taken here. In particular  $s$  is chosen to be normalized arclength.

In terms of the functions  $\rho(s)$  and  $z(s)$  which define the surface, the components of the unit normal to the surface are

$$\begin{aligned} n_\rho &= \frac{\dot{z}}{(\dot{\rho}^2 + \dot{z}^2)^{1/2}} \\ n_z &= -\frac{\dot{\rho}}{(\dot{\rho}^2 + \dot{z}^2)^{1/2}}, \end{aligned} \tag{28}$$

and the curvature is

$$\nabla \cdot \mathbf{n} = \frac{\dot{z}}{\rho(\dot{\rho}^2 + \dot{z}^2)^{1/2}} + \frac{\dot{\rho}\ddot{z} - \ddot{\rho}z}{(\dot{\rho}^2 + \dot{z}^2)^{3/2}}. \tag{29}$$

where dots indicate differentiation with respect to the variable  $s$ .

Due to axisymmetry, the integral representation of the problem, equation (27), can be further simplified. The dependence of the integrands on  $\theta$  is known and integration with respect to  $\theta$  can be performed. Although the resulting integration yields quite complex expressions, the net result is a reduction of the integration domain from two dimensions to one. The results are

$$\begin{aligned} \frac{1}{2} \begin{pmatrix} u_\rho^I(\mathbf{x}) \\ u_z^I(\mathbf{x}) \end{pmatrix} &= + \int_{s_o}^{s_f} \mathbf{P}(\mathbf{x}, \xi) \cdot \begin{pmatrix} u_\rho^I(\xi) \\ u_z^I(\xi) \end{pmatrix} d\hat{s} \\ &\quad - \int_{s_o}^{s_f} \mathbf{Q}(\mathbf{x}, \xi) \cdot \begin{pmatrix} f_\rho^{(1)}(\xi) \\ f_z^{(1)}(\xi) \end{pmatrix} d\hat{s} \quad \mathbf{x} \in S_I, \end{aligned} \tag{30}$$

and

$$\begin{aligned} \frac{1}{2} \begin{pmatrix} u_\rho^I(\mathbf{x}) \\ u_z^I(\mathbf{x}) \end{pmatrix} &= \frac{\lambda - 1}{\lambda + 1} \int_{s_o}^{s_f} \mathbf{P}(\mathbf{x}, \xi) \cdot \begin{pmatrix} u_\rho^I(\xi) \\ u_z^I(\xi) \end{pmatrix} d\hat{s} \\ &\quad - \frac{1}{(\lambda + 1)} \int_{s_o}^{s_f} \mathbf{Q}(\mathbf{x}, \xi) \cdot \begin{pmatrix} \mathcal{F}_\rho(\xi) \\ \mathcal{F}_z(\xi) \end{pmatrix} d\hat{s} \end{aligned} \tag{31}$$

$\mathbf{x} \in S_I$

where

$$d\hat{s} = ds \rho \left( \dot{\rho}^2 + \dot{z}^2 \right)^{1/2}.$$

The components of the matrices  $\mathbf{P}$  and  $\mathbf{Q}$  are listed in the appendix.

This system provides a relationship between the velocity of the fluid 1/fluid 2 interface, the interfacial stress and the interfacial curvature. Given the set of surface variables  $\rho$ ,  $z$ ,  $\dot{\rho}$ ,  $\dot{z}$ ,  $\bar{\rho}$ , and  $\bar{z}$  at time  $t$ , this system allows calculation of the instantaneous interfacial velocity and stress. Once the interfacial velocity is determined, the interface is deformed in accordance with the kinematic condition (7).

At any instant, once the interfacial velocities and stresses are known, velocities and pressures in the interior of the fluid domain may be calculated from the  $\theta$ -integrated forms of equations (17) and (18):

$$\begin{aligned} \mathbf{u}_1(\mathbf{x}_1) = & + \int_{s_o}^{s_f} \mathbf{P}(\mathbf{x}_1, \xi) \cdot \begin{pmatrix} u_\rho^I(\xi) \\ u_z^I(\xi) \end{pmatrix} d\hat{s} \\ & - \int_{s_o}^{s_f} \mathbf{Q}(\mathbf{x}_1, \xi) \cdot \begin{pmatrix} f_\rho^{(1)}(\xi) \\ f_z^{(1)}(\xi) \end{pmatrix} d\hat{s} \end{aligned} \quad \mathbf{x}_1 \in \Omega_1, \quad (32)$$

$$\begin{aligned} \mathbf{u}_2(\mathbf{x}_2) = & - \int_{s_o}^{s_f} \mathbf{P}(\mathbf{x}_2, \xi) \cdot \begin{pmatrix} u_\rho^I(\xi) \\ u_z^I(\xi) \end{pmatrix} d\hat{s} \\ & + \int_{s_o}^{s_f} \mathbf{Q}(\mathbf{x}_2, \xi) \cdot \begin{pmatrix} f_\rho^{(2)}(\xi) \\ f_z^{(2)}(\xi) \end{pmatrix} d\hat{s} \end{aligned} \quad \mathbf{x}_2 \in \Omega_2, \quad (33)$$

$$\begin{aligned} p_1(\mathbf{x}_1) - \bar{p}_1 = & + \int_{s_o}^{s_f} \mathbf{W}(\mathbf{x}_1, \xi) \cdot \begin{pmatrix} u_\rho^I(\xi) \\ u_z^I(\xi) \end{pmatrix} d\hat{s} \\ & - \int_{s_o}^{s_f} \mathbf{S}(\mathbf{x}_1, \xi) \cdot \begin{pmatrix} f_\rho^{(1)}(\xi) \\ f_z^{(1)}(\xi) \end{pmatrix} d\hat{s} \end{aligned} \quad \mathbf{x}_1 \in \Omega_1, \quad (34)$$

$$\begin{aligned} p_2(\mathbf{x}_2) - p_2^\infty = & - \int_{s_o}^{s_f} \mathbf{W}(\mathbf{x}_2, \xi) \cdot \begin{pmatrix} u_\rho^I(\xi) \\ u_z^I(\xi) \end{pmatrix} d\hat{s} \\ & + \int_{s_o}^{s_f} \mathbf{S}(\mathbf{x}_2, \xi) \cdot \begin{pmatrix} f_\rho^{(2)}(\xi) \\ f_z^{(2)}(\xi) \end{pmatrix} d\hat{s} \end{aligned} \quad \mathbf{x}_2 \in \Omega_2, \quad (35)$$

The components of the vectors  $\mathbf{W}$  and  $\mathbf{S}$  are given in the appendix.

(b) Implementation

System (30, 31) may be discretized and numerically solved . The approach taken here employs the method of Krylov-Bogoliubov (Kantorovich and Krylov, 1963 ). Specifically, the particle arc  $(\rho(s), z(s))$ ,  $s \in [s_o, s_f]$  is divided into  $N$  elements. This is accomplished by dividing the interval  $[s_o, s_f]$  into subintervals,  $\Delta s_j$ , with centers  $s_j$  ( $j = 1, \dots, N$ ). Each parametric value,  $s_j$ , corresponds to a point on the arc  $\mathbf{x}_j = (\rho(s_j), z(s_j))$  and each  $\Delta s_j$  corresponds to a segment or element of the arc. The elements are assumed to be sufficiently small so that the local normal tractions  $f_\rho^{(1)}$ ,  $f_z^{(1)}$  and velocities  $u_\rho^I$ ,  $u_z^I$  may be assumed constant within each element. The resulting discretized system is:

$$\frac{1}{2} \begin{pmatrix} u_\rho^I(\mathbf{x}_i) \\ u_z^I(\mathbf{x}_i) \end{pmatrix} \simeq + \sum_{j=1}^N \left\{ \left[ \int_{\Delta s_j} \mathbf{P}(\mathbf{x}_i, \xi) d\hat{s} \right] \cdot \begin{pmatrix} u_\rho^I(\mathbf{x}_j) \\ u_z^I(\mathbf{x}_j) \end{pmatrix} \right\} - \sum_{j=1}^N \left\{ \left[ \int_{\Delta s_j} \mathbf{Q}(\mathbf{x}_i, \xi) d\hat{s} \right] \cdot \begin{pmatrix} f_\rho^{(1)}(\mathbf{x}_j) \\ f_z^{(1)}(\mathbf{x}_j) \end{pmatrix} \right\} \quad (36)$$

$$\frac{1}{2} \begin{pmatrix} u_\rho^I(\mathbf{x}_i) \\ u_z^I(\mathbf{x}_i) \end{pmatrix} \simeq \frac{\lambda - 1}{\lambda + 1} \sum_{j=1}^N \left\{ \left[ \int_{\Delta s_j} \mathbf{P}(\mathbf{x}_i, \xi) d\hat{s} \right] \cdot \begin{pmatrix} u_\rho^I(\mathbf{x}_j) \\ u_z^I(\mathbf{x}_j) \end{pmatrix} \right\} - \frac{1}{\lambda + 1} \sum_{j=1}^N \left\{ \left[ \int_{\Delta s_j} \mathbf{Q}(\mathbf{x}_i, \xi) \cdot \begin{pmatrix} \mathcal{F}_\rho(\mathbf{x}_j) \\ \mathcal{F}_z(\mathbf{x}_j) \end{pmatrix} d\hat{s} \right] \right\} \quad (37)$$

$1 \leq i \leq N$

Each coefficient

$$\mathbf{A}_i^j \stackrel{def}{=} \left[ \int_{\Delta s_j} \mathbf{P}(\mathbf{x}_i, \xi) d\hat{s} \right] \quad (38)$$

$$\mathbf{B}_i^j \stackrel{def}{=} \left[ \int_{\Delta s_j} \mathbf{Q}(\mathbf{x}_i, \xi) d\hat{s} \right] \quad (39)$$

and inhomogeneous term

$$\left[ \int_{\Delta s_j} \mathbf{Q}(\mathbf{x}_i, \xi) \cdot \begin{pmatrix} \mathcal{F}_\rho(\mathbf{x}_j) \\ \mathcal{F}_z(\mathbf{x}_j) \end{pmatrix} d\hat{s} \right] \quad (40)$$

for  $j \neq i$  can be easily evaluated by standard numerical integration schemes. Here Gaussian quadrature was used. For  $j = i$  and  $s = s_i$  then  $\xi(s) = \mathbf{x}_i$ ,

and the functions  $\mathbf{P}$  and  $\mathbf{Q}$  become unbounded. In this case, the region  $\Delta s_j$  is subdivided into three smaller regions, one of which is centered at the singular point  $s_j$  and is  $\Delta_j^{sing} = [s_j - \frac{\epsilon}{2}, s_j + \frac{\epsilon}{2}]$ . The constant,  $\epsilon$  is assumed small enough that over  $\Delta_j^{sing}$  the arc may be accurately approximated by the tangent line through the point  $\mathbf{x}_j$ . Following Lee and Leal (1982), the singular contributions to (38-40) from over the interval  $\Delta_j^{sing}$  can be approximated analytically. The details of the singular contribution are given in the appendix. In the remaining two portions of the singular element  $\Delta s_j$  accurate Rhomberg integration was performed.

Equations (36) and (37) are linear systems in stress and velocity. The structure of these systems is best shown as follows. Denoting

$$\begin{pmatrix} b_\rho(\mathbf{x}_i) \\ b_z(\mathbf{x}_i) \end{pmatrix} \stackrel{def}{=} \sum_{j=1}^N \left[ \int_{\Delta s_j} \mathbf{Q}(\mathbf{x}_i, \xi) \cdot \begin{pmatrix} \mathcal{F}_\rho(\mathbf{x}_j) \\ \mathcal{F}_z(\mathbf{x}_j) \end{pmatrix} d\hat{s} \right] \quad (41)$$

$$\hat{\mathbf{A}} \stackrel{def}{=} \begin{pmatrix} \mathbf{A}_1^1 & \mathbf{A}_1^2 & \dots & \mathbf{A}_1^N \\ \mathbf{A}_2^1 & \mathbf{A}_2^2 & \dots & \mathbf{A}_2^N \\ \vdots & \vdots & \ddots & \vdots \\ \mathbf{A}_N^1 & \mathbf{A}_N^2 & \dots & \mathbf{A}_N^N \end{pmatrix} \quad (42)$$

and

$$\mathbf{u} \stackrel{def}{=} \begin{pmatrix} u_\rho^I(\mathbf{x}_1) \\ u_z^I(\mathbf{x}_1) \\ u_\rho^I(\mathbf{x}_2) \\ u_z^I(\mathbf{x}_2) \\ \vdots \\ u_\rho^I(\mathbf{x}_N) \\ u_z^I(\mathbf{x}_N) \end{pmatrix}, \quad \mathbf{b} \stackrel{def}{=} \begin{pmatrix} b_\rho(\mathbf{x}_1) \\ b_z(\mathbf{x}_1) \\ b_\rho(\mathbf{x}_2) \\ b_z(\mathbf{x}_2) \\ \vdots \\ b_\rho(\mathbf{x}_N) \\ b_z(\mathbf{x}_N) \end{pmatrix}, \quad (43)$$

leads to the linear system

$$\frac{1}{2}\mathbf{u} = \frac{\lambda - 1}{\lambda + 1}\hat{\mathbf{A}} \cdot \mathbf{u} - \frac{1}{\lambda + 1}\mathbf{b}. \quad (44)$$

Rearranging, the desired result may be obtained:

$$\mathcal{U} = \frac{1}{\lambda + 1} \left( \frac{1}{2} \frac{\lambda - 1}{\lambda + 1} \hat{\mathbf{A}} - \mathbf{I} \right)^{-1} \mathbf{b} \quad (45)$$

In a manner analogous to Equations (42) and (43) we can construct a matrix  $\hat{\mathbf{B}}$  (with components  $B_i^j$ ) and column vector  $f$ . Then using the matrix  $\hat{\mathbf{A}}$  and vector  $\mathcal{U}$  from above, Eq. (36) can be written for the system of equations as

$$\mathcal{U} = -2\hat{\mathbf{B}} \cdot f + 2\hat{\mathbf{A}} \cdot \mathcal{U}. \quad (46)$$

Rearranging Eq. (46), the stress can be found by solving the system

$$f = \hat{\mathbf{B}}^{-1} \left[ \left( \hat{\mathbf{A}} - \frac{1}{2} \mathbf{I} \right) \cdot \mathcal{U} \right]. \quad (47)$$

Given the details of the initial shape and curvature, then matrices  $\hat{\mathbf{A}}$  and  $\hat{\mathbf{B}}$  can be evaluated along with the vector  $\mathbf{b}$  and equation (45) yields the surface velocity. If desired, the resulting velocities may be used in equation (47) to determine the unknown stresses. This procedure amounts to solving two linear systems both of size  $2N$  by  $2N$ . Note that this is more efficient than solving the single  $4N$  by  $4N$  system. Once a shape and velocity distribution at time  $t$  is known, equation (7) is used to determine a new shape and subsequent velocity distribution. Equation (7) is discretized as follows:

$$\begin{aligned} \rho(s, t + \Delta t) &= \rho(s, t) + n_\rho(s, t) \left[ u_\rho^I(s, t) n_\rho(s, t) \right. \\ &\quad \left. + u_z^I(s, t) n_z(s, t) \right] \Delta t \\ z(s, t + \Delta t) &= z(s, t) + n_z(s, t) \left[ u_\rho^I(s, t) n_\rho(s, t) \right. \\ &\quad \left. + u_z^I(s, t) n_z(s, t) \right] \Delta t \end{aligned} \quad (48)$$

Equation (48) determines a new set of surface locations  $(\rho(s_j), z(s_j))$  for  $j = 1, \dots, N$  at time  $t + \Delta t$ . Cubic splines are used to determine  $\rho(s), \dot{\rho}(s), \ddot{\rho}(s), z(s), \dot{z}(s), \ddot{z}(s)$  for  $s \in [s_o, s_f]$ . The  $t + \Delta t$  velocities are then calculated using these shape details and the process is repeated, marching forward in time.

## Numerical Results

### (a) Preliminary Testing

As an initial test of the use of the wall Green's function, drag calculations were performed on solid ellipsoids moving axisymmetrically toward the wall. Agreement with existing theory was excellent. For further details the reader is referred to Ascoli, Dandy and Leal (1988).

Hadamard (1911) and Rybczynski (1911) theoretically determined velocity and stress fields for the case of uniform flow past a spherical drop. The current case of a drop approaching a planar wall degenerates to the Hadamard-Rybczynski case when the drop is sufficiently far from the wall. Figure (2) shows a typical comparison between the theoretical predictions of Hadamard-Rybczynski and numerically generated results for a spherical drop with center located 1000 radii away from the wall. For the numerical results 31 elements were used. Surface velocities and local surface stress forces for  $\lambda = 3$  are plotted against  $\phi/\pi$  where  $\phi$  is the angle made with the horizontal through the sphere center. Agreement is excellent.

In the present problem, the drop moves under the influence of a constant buoyancy force and thus the drag on the drop should remain constant with the velocity of the drop changing as the wall is approached. Surface integration of equation (6) (and application of the divergence and surface divergence theorem) indicates that the *exact* solution of equation (31) does indeed incorporate a constant buoyancy force. Here equation (31) is solved numerically and surface tractions are obtained via equation (30) from the velocities obtained from (31). The constraint of constant buoyancy force is not applied explicitly or directly in equation (30). Thus, the constancy of this computed value may be used as a check of the accuracy of the technique for all ranges of drop to wall distance. The numerically computed drag is normalized by the theoretical drag on an equal volume spherical drop in the absence of a wall (the Hadamard-Rybczynski result). Ideally, then, the numerically computed normalized drag should equal

1.0 throughout the range of computations.

Thirty-two surface elements were used in the calculations reported below. This number was chosen based on preliminary testing with 12, 22, 32, 42, and 48 elements. Testing indicated that 12 elements were inadequate to resolve highly deformed shapes. With 12 elements, jagged corners in the spline fit of the surface were noticeable near the planar wall where high deformations occurred. Clearly, these jagged corners were not physical but were instead artifacts of insufficient numerical resolution of the surface. The poor spline fit was accompanied by inaccurate values of drag. Twenty-two elements were found to be adequate for all but the most deformed drop configurations, where calculated drag values differed by up to 10% from the theoretical normalized value of 1.0. Forty-two, forty-eight and thirty-two elements produced smooth drop shapes that were visually indistinguishable. A slight improvement in accuracy of the drag values (of the order of 0.1% and 0.3% respectively) was noted for 42 and 48 points when the drop shape was highly deformed. However, this gain in accuracy was significantly outweighed by the increase in computation time required for the larger number of points.

In the course of computations, errors in drop volume, though extremely small at each given time/shape calculation, were found to accumulate. Typically a calculation using 32 elements beginning with a spherical drop shape 15 radii away and terminating with a highly deformed drop within one undeformed radius of the wall was found to have a total accumulated error in volume of the order of 5%. With a timestep of 0.005 and a run time of approximately 20 dimensionless time units this corresponds to roughly 0.00125% error in volume per iteration. The accumulated errors were found to be largest for drops with the highest deformation. The amount of accumulated error varied with the number of elements, being least with the largest number of elements. Again, although slightly improved accuracy in volume was obtained by using 40 and 48 elements, the additional computational time did not warrant the use of more than 32 el-

ements. Instead, for all the results presented below, a periodic renormalization of the length scaling was performed during the computations to maintain a constant drop volume.

Preliminary testing was performed to determine the distance from the wall at which the assumption of a spherical starting shape is reasonable. For this purpose, spherical drop shapes were assumed starting with the center of mass,  $Z_{center} = 25$ , and run until  $Z_{center}$  reached 15 undeformed radii. During these tests, the center of mass velocity,  $V_{center}$ , differed from the normalized value of one by as much as 6.4 % for  $Ca = 3$ ,  $\lambda = 0.3$ . However, the maximum deviation in radial distance from a spherical shape

$$\max \sqrt{[(z_i - Z_{center})^2 + \rho_i^2] - 1}$$

for this case was less than 2%. For  $Ca = 1$  and  $Ca = .3$ , the maximum deviation from a spherical constant radius was less than 0.85% and 0.25% respectively for the  $\lambda$  values considered. These results indicate that a starting position of  $Z_{center}=15$  with a spherical initial shape is an excellent assumption for the  $Ca=0.3$  and 1 cases and a reasonable assumption for  $Ca=3$ .

Hartland (1969) performed a series of experiments involving drops of golden syrup containing potassium iodide falling under the influence of gravity through sextol phthalate towards a planar wall. Although the intent of his experiments was to study the later stages of dimple formation when the golden syrup drops are extremely close to the wall, his photographic results for the early stages of dimple formation provide experimental details of the gross shape of the entire drop to which the current numerics may be compared. Hartland's physical parameters for the high viscosity golden syrup drop ( $\rho_1 = 1.580$  gm /cc,  $\rho_2 = 1.069$  g/cc,  $\mu_1 = 175$  poise,  $\mu_2 = 137$  poise,  $\gamma = 23.6$  dyne/cm, with drop volume of .25cc ) give  $U = 0.234$  cm/s,  $Ca = 1.358$ ,  $\lambda = 1.478$ , and  $Re_1 = 8.25 \times 10^{-4}$ ,  $Re_2 = 7.13 \times 10^{-4}$ . Numerical results are shown in Figure (3) for the case of  $Ca = 1$ ,  $\lambda = 1$  with  $Z_{axis} = 0.155$ . This is the smallest value of  $Z_{axis}$  obtained numerically for these parameters. Hartland's photograph corresponds to  $Z_{axis}$

between 0.153 and 0.128. The agreement in gross shape detail is exceptional.

(b) Results

Thirty-two elements with a time step of 0.005 were employed in the calculations presented. Each run was terminated when the calculated value of the normalized drag differed from 1 by more than 2%. Results are reported here for  $\lambda$  of 3, 1 and 0.3, with  $Ca$  equal to 3, 1 and 0.3 for each  $\lambda$ . For all calculations the initial shape was taken to be spherical, with the sphere center at 15 radii from the wall as indicated above.

The calculated drop shapes are shown in figures (4-12) for all nine combinations of  $\lambda$  and  $Ca$ . The elapsed time between each shape shown is 1 dimensionless time unit (i.e. the time increment required for the undeformed drop in an unbounded fluid to translate a distance equal to its own radius).

Dimpling was observed for *all* values of  $Ca$  and  $\lambda$  considered. Shape evolution naturally divides into two regimes: evolution prior to the point of dimpling and evolution after a dimple has formed. The transition configurations, i.e. the numerically determined film configurations at the timestep immediately prior to the formation of a dimple, are shown in figure (13). These transition configurations all display a small, approximately flat region at the wall side of the drop near  $\rho = 0$ . In each case, the dimple first forms in this flat region, at a relatively *small* radial distance from the  $z$ -axis. The apex of the dimple then moves radially outward.

The pertinent questions at this point are 1) what role do  $Ca$  and  $\lambda$  play in determining the configurations shown in (13), 2) why does a dimple form once configurations (13) are established and 3) what effect do  $Ca$  and  $\lambda$  have once a dimple has formed.

Increasing  $Ca$  results in an overall increase in deformability of the drop throughout its *entire* range of motion. This is obvious from figures (4-12). In addition, increasing capillary number results in "onset" of dimpling farther from the wall. This statement may be made more precise by defining  $Z_{center}$ ,

the  $z$ -axis location of the drop center of mass and  $Z_{axis}$ , the distance along the  $z$ -axis from the plane to the nearest axis point of the drop (figure 1b). At the instant when dimpling is first numerically observed,  $Z_{axis}$  and  $Z_{center}$  are largest for  $Ca = 3$ . The  $Z_{center}$  and  $Z_{axis}$  values when dimpling is first observed both decrease with decreasing  $Ca$ . This is easily seen in figures (13) for the configuration immediately prior to dimpling.

The depth of the dimpled region, and the location of the “center” of the dimple are best discussed in terms of  $Z_{min}$  and  $\rho_{min}$  (figure 1b).  $Z_{min}$  denotes the minimum distance along the  $z$ -direction between the drop and the plane wall, while  $\rho_{min}$  denotes the radial distance in cylindrical coordinates to the position on the drop at which  $Z_{min}$  occurs. Once a dimpled configuration has formed, for a given  $Z_{axis}$ , the depth of the dimple  $Z_{axis} - Z_{min}$  increases with increasing  $Ca$ . In particular, for  $Ca = 0.3$  dimpling is barely noticeable at the point where the calculation was terminated. However, at a given  $Z_{axis}$  location, as  $Ca$  increased to 1 and 3, the depth of the dimple region increased dramatically. This effect is illustrated in figures 14 and 15 for the case  $\lambda = 1$ .

Increasing  $Ca$  also produces an increase in the deviation from sphericity at the side of the drop farthest from the wall. In fact, for  $Ca = 3.0$ , flattening and eventual indentation of the side of the drop farthest from the wall was observed.

The effect of  $Ca$  on the normalized center of mass velocity is much less than what might be anticipated from the large effect that  $Ca$  has on the drop shape.  $V_{center}$  plotted versus  $Z_{center}$  is shown in figure 16 for the case  $\lambda = 1$ . Deviation from the non-deforming spherical results (solid line) is small. Far from the wall, these deviations are due to blunting of the wall side of the drop (and subsequent shift of the drop center of mass away from the wall). Near the wall, deformation allows a mechanism of motion which the spherical drop is not allowed.

Conversely, fixing  $Ca$ , what is the effect of  $\lambda$  variation? Calculated shape details are remarkably insensitive to  $\lambda$ . For  $Ca$  fixed at 0.3 and  $\lambda$  varying, figures (4), (7) and (10) are nearly indistinguishable as are the corresponding configu-

rations shown in figure (13). For  $Ca$  fixed at 3 and 1, very slight configurational differences are observed. In particular, figure (13) demonstrates that increasing  $\lambda$  corresponds to slightly larger values of  $Z_{axis}$  and  $Z_{center}$  immediately prior to dimpling. Even after dimpling has occurred, the effect of varying  $\lambda$  in the  $Ca = 1$  and 3 cases is relatively small. The general trends in the dimpled configuration are shown in figures (17) and (18). The  $\rho_{min}$  value where the dimple is first formed is insensitive to  $\lambda$  ( figure 18, where the dark circle denotes this value). The shapes of the curves in figures 17 and 18 are remarkably similar for different  $\lambda$ . In short, the “dynamics” is roughly the same for each  $\lambda$ . Once again, the value of  $\lambda$  determines the starting ( $Z_{axis}$  values where the curves begin).

Variation in  $\lambda$  does have a significant effect on the normalized center of mass velocity. This is demonstrated in figure (19). At a given  $Z_{center}$  location, drops with higher viscosity relative to the suspending fluid show a larger wall interaction (corresponding to lower  $V_{center}$ ). This effect diminishes significantly in the latest stages of deformation when the drop is closest to the wall. Thus, the major effect of  $\lambda$  is to set the relative *rate* at which the drop evolves, up to the point of dimpling.

Thus far, the gross geometrical details of deformation and the relative rate at which this deformation takes place have been correlated with  $Ca$  and  $\lambda$ . A careful examination of the velocity and modified pressure fields provides additional insight into the dynamics of dimple formation.

Equations (32-35) allow computation of velocity and pressure fields in the two fluid domains. Figure 20a shows the velocity field obtained for  $Ca = 1$ ,  $\lambda = 1$  in a dimpled configuration. Here the velocity is calculated relative to a fixed wall. Figure 20b shows the analogous velocity field, with velocity measured relative to the center of mass of the drop. Figures 21 and 22a,b show the velocity fields for the dimpled configurations with parameters  $Ca = 0.3$ ,  $\lambda = 1$  and  $Ca = 3$ ,  $\lambda = 1$  respectively. These figures indicate that, once a dimple is formed, the largest relative motion occurs in the immediate vicinity of the dimple. The downward

motion of the film at  $\rho = 0$  is small in comparison to the downward motion of the dimpled region. In short, the dimples increase in depth ( $Z_{axis} - Z_{min}$ ) with time.

It is instructive to focus on the velocity fields in the film region immediately prior to the dimple formation. Figures 23 and 24 show the radial and  $z$ -components of the velocity in the film for  $Ca = 1$  and  $\lambda = 1$ . At the next numerical timestep a dimple has formed at the radial position marked by the vertical line at the wall. From these plots it is easily seen how a dimple will form in terms of velocity field variation. Near  $\rho = 0$  the face of the drop nearest the wall is approximately flat. The downward component of velocity increases as one moves radially outward. Although this increase in downward velocity is *small*, near  $\rho = 0$  the surface is nearly flat and thus only a slight increase in downward velocity is required to form the dimple.

Stokes equations are physically a balance between the forces due to modified pressure and the forces due to flux of momentum. Momentum fluxes correspond to velocity variation. We have examined the velocity fields. The next step is to consider the modified pressure fields.

Film drainage theory employing the lubrication approximation stresses the importance of variation in pressure with radial distance. Variation of pressure with  $z$  is neglected. The velocities calculated at the surface of the film are directly related to the assumed variation in pressure. As a consequence, the evolution of the film shape is critically dependent on the assumed variation in pressure. What do the numerically calculated pressure fields look like after a dimple has formed? Figures 25-27 show calculated modified pressure fields corresponding to the configurations of figures 20-22. The most obvious variation in pressure occurs at the outer edge of the film region. Here  $p_2$  rapidly decreases radially outward. Equivalently,  $\frac{\partial p_2}{\partial \rho}$  is negative and *large* in absolute magnitude. In each case,  $p_2$  in the film region decreases with  $z$  at a fixed  $\rho$  location. In other words,  $\frac{\partial p_2}{\partial z}$  is negative in the film region. For the significantly dimpled case of

$Ca = 3$ ,  $\frac{\partial p_2}{\partial \rho}$  is positive from  $\rho = 0$  outward to the dimple and negative radially beyond the dimple. For the  $Ca = 1$  and  $Ca = 3$  cases, where the dimple is in its infancy compared to the  $Ca = 3$  case,  $\frac{\partial p_2}{\partial \rho}$  is negative throughout the film region. For  $Ca = 3$ ,  $\frac{\partial p_2}{\partial \rho}$  and  $\frac{\partial p_2}{\partial z}$  are extremely small in the nearly stagnant central flow region. For the other cases  $\frac{\partial p_2}{\partial \rho}$  and  $\frac{\partial p_2}{\partial z}$  are roughly of the same order of magnitude near  $\rho = 0$ .  $\frac{\partial p_2}{\partial \rho}$  grows rapidly more negative near the edge of the film region, while here  $\frac{\partial p_2}{\partial z}$  is small in magnitude in comparison.

What do the pressure fields look like, immediately prior to dimple formation? Figure 28 shows the modified pressure for the  $Ca = 1$ ,  $\lambda = 1$  case immediately prior to dimple formation. The largest pressure variation is at the edge of the drop, where pressure rapidly decreases radially outward. In contrast, for this configuration, the dimple first forms at  $\rho = 0.125$  where radial pressure variation is *small* relative to pressure variation with  $z$ . This is flagrantly at odds with thin film lubrication analysis.

How does the pressure field vary as the drop approaches the wall? In particular, how does  $\frac{\partial p_2}{\partial z}$  vary near the center of the drop, as the drop approaches the wall? The evolution of pressure fields as the  $Ca = 1$ ,  $\lambda = 1$  drop approaches the wall is shown in figures 29-31. For each plot, a radial distance is fixed and pressure is calculated for  $z$ -values beginning at the wall and up to the drop surface. Each curve in the figures then corresponds to a different  $Z_{center}$  location. These figures illustrate the fact that for small  $\rho$  and large  $Z_{center}$   $\frac{\partial p_2}{\partial z}$  is positive near the drop surface. As  $Z_{center}$  decreases (i.e. the drop moves toward the wall)  $\frac{\partial p_2}{\partial z}$  becomes negative over the entire film height. As the drop moves closer to the wall  $\frac{\partial p_2}{\partial z}$  eventually decreases in magnitude.

Summarizing, pressure variation with  $z$  may be negligible in the latest stages of dimple formation. In contrast, when the dimple first forms, pressure variation with  $z$  is not small relative to pressure variation with  $\rho$ .

The significance of a negative  $\frac{\partial p_2}{\partial z}$  when the drop is in the configuration depicted in figures 23 and 24 may be seen from an elementary analysis of Stokes

equation in fluid 2.

Writing system (2) in radial coordinates yields (velocities and pressures refer to fluid 2):

$$\begin{aligned}\frac{\partial p}{\partial \rho} &= \frac{\partial}{\partial \rho} \left( \frac{1}{\rho} \frac{\partial \rho v_\rho}{\partial \rho} \right) + \frac{\partial^2 v_\rho}{\partial z^2} \\ \frac{\partial p}{\partial z} &= \frac{1}{\rho} \frac{\partial}{\partial \rho} \left( \rho \frac{\partial v_z}{\partial \rho} \right) + \frac{\partial^2 v_z}{\partial z^2} \\ \frac{1}{\rho} \frac{\partial \rho v_\rho}{\partial \rho} + \frac{\partial v_z}{\partial z} &= 0\end{aligned}$$

The continuity equation may be used to rewrite each of the momentum equations as:

$$\begin{aligned}\frac{\partial p}{\partial \rho} &= \frac{\partial}{\partial z} \left[ -\frac{\partial v_z}{\partial \rho} + \frac{\partial v_\rho}{\partial z} \right] \\ \frac{\partial p}{\partial z} &= \frac{1}{\rho} \frac{\partial}{\partial \rho} \left( \rho \left[ \frac{\partial v_z}{\partial \rho} - \frac{\partial v_\rho}{\partial z} \right] \right)\end{aligned}$$

Integrating these equations from 0 to  $\rho$  and from  $z_0$  to  $z$  gives

$$-\frac{\partial v_z}{\partial \rho} + \frac{\partial v_\rho}{\partial z} = \int_{z_0}^z \frac{\partial p}{\partial \rho} dz + F(\rho) \quad (49)$$

$$-\frac{\partial v_z}{\partial \rho} + \frac{\partial v_\rho}{\partial z} = -\frac{1}{\rho} \int_0^\rho \rho \frac{\partial p}{\partial z} d\rho + \frac{G(z)}{\rho} \quad (50)$$

Finiteness at  $\rho = 0$  implies  $G = 0$ . Further, pressure is harmonic (apply the divergence operator to the Stokes equation and use continuity to confirm this result). Thus

$$0 = \frac{1}{\rho} \frac{\partial}{\partial \rho} \left( \rho \frac{\partial p}{\partial \rho} \right) + \frac{\partial^2 p}{\partial z^2}$$

Differentiating equation (50) with respect to  $z$  and applying  $\frac{1}{\rho} \frac{\partial}{\partial \rho} \rho()$  to equation (49) then using the harmonicity of pressure leads to the two results that

$$\frac{\partial p}{\partial \rho} \Big|_{\rho=0} = 0$$

$$\frac{1}{\rho} \frac{\partial}{\partial \rho} \left( \rho F(\rho) \right) = \frac{\partial p}{\partial z} \Big|_{z=z_0}$$

The first result is an obvious consequence of axisymmetry. Solving (once again assuming finiteness at  $\rho = 0$ ) gives

$$\begin{aligned} -\frac{\partial v_z}{\partial \rho} + \frac{\partial v_\rho}{\partial z} &= -\frac{1}{\rho} \int_0^\rho \rho \frac{\partial p}{\partial z} d\rho \\ &= \int_{z_0}^z \frac{\partial p}{\partial \rho} dz - \frac{1}{\rho} \int_0^\rho \rho \frac{\partial p}{\partial z} \Big|_{z=z_0} d\rho \end{aligned}$$

This equation applies in any rectangle  $[0, \rho] \times [z_0, z]$  contained in the fluid 2 domain. In particular, applying this equation on the line  $z = z_0$ ,  $\rho \in [0, \rho_f]$  where  $z_0$  is a small distance below the film depicted in figures 23 and 24 and  $\rho_f$  is the radial location where dimpling first occurs results in:

$$\frac{\partial(-v_z)}{\partial \rho} \Big|_{z=z_0, \rho=\rho_f} = -\frac{\partial v_\rho}{\partial z} \Big|_{z=z_0, \rho=\rho_f} - \frac{1}{\rho_f} \int_0^{\rho_f} \rho \frac{\partial p}{\partial z} \Big|_{z=z_0} d\rho \quad (51)$$

Physically, this equation represents a force balance. It may be re-written as

$$\int_0^{2\pi} \int_0^{\rho_f} \rho \Delta z \frac{\partial p}{\partial z} \Big|_{z=z_0} d\rho = 2\pi \Delta z \rho \left( \frac{\partial v_z}{\partial \rho} - \frac{\partial v_\rho}{\partial z} \right) \Big|_{z=z_0, \rho=\rho_f}$$

The left side is the  $z$  component of the force due to pressure exerted on the faces of an infinitesimal cylinder of radius  $\rho$  and height  $\Delta z$ . The right side corresponds to the momentum flux forces across the infinitesimal perimeter.

Figure 23 indicates that  $\frac{\partial v_\rho}{\partial z} \Big|_{z=z_0, \rho=\rho_f}$  will be nearly zero or small and positive. Dimpling at  $\rho_f$  can only occur in this configuration if  $\frac{\partial(-v_z)}{\partial \rho} \Big|_{z=z_0, \rho=\rho_f}$  is positive. Assuming that  $z_0$  is sufficiently close to the film surface that continuity of velocity will ensure what happens at  $(\rho_f, z_0)$  is representative of what happens at the film surface,  $(\rho_f, z_{film})$ , then it is absolutely necessary that  $\frac{\partial p}{\partial z} \Big|_{z=z_0}$  be negative in a region near the drop surface.

This analysis indicates that  $z$  pressure variation is a key ingredient to the *initial* formation of a dimple. This has direct impact on the range of validity

of the lubrication assumption. In particular, lubrication theory where  $z$  pressure variation is neglected is inadequate to resolve the initial stages of dimple formation. In the later stages of deformation, *after* a dimple has formed (and  $z$  pressure variation has diminished) lubrication theory may provide a valid representation of the dynamics of the problem.

(c) Discussion

The current numerics compares well with the Hadamard-Rybczynski (1911) results when the drop is far from the wall. For a highly deformed configuration near the wall, the numerics compares well in gross detail with the experimental results of Hartland. Numerical accuracy degrades rapidly when the drop is extremely close to the wall. For this reason, numerical results were not obtained in the latest stages of dimple formation and film drainage. Nevertheless, the initial stages of dimple formation are captured.

The assumptions relevant to film drainage theory listed in the introduction may now be assessed.

- (I) Films have been assumed thin in the sense that  $\epsilon \stackrel{def}{=} h/R \ll 1$ . This assumption has been used to neglect various terms in the equations of motion in the context of “lubrication” or boundary layer approximations. It is anticipated that the simplifying approximations made in these theories are increasingly accurate as  $\epsilon \rightarrow 0$ . Taking  $h$  to be  $Z_{axis}$  at the instant the dimple forms and  $R$  to be the undeformed radius of the drop (for the numerical cases shown, this choice of  $R$  provides a reasonable measure of the radial extent of the film region), at the onset of dimpling, the current numerics predicts  $\epsilon$  in the range 0.1 to 0.3. These values of  $\epsilon$  are by no means vanishingly small. In particular, based on the assumption of vanishingly small  $\epsilon$ , lubrication theory neglects  $z$  pressure variation in the film region. This assumption is incorrect at the initial stages of dimple formation. In fact, a decrease in pressure with  $z$  in the film region has been shown to be crucial to the formation of a dimple. For the range of  $Ca$  and  $\lambda$  values considered here

$\epsilon$  is not sufficiently small at the *onset* of dimpling for lubrication theory to be accurate. In the later stages of dimple evolution, as  $\epsilon$  decreases in magnitude, lubrication theory may provide a valid approximation.

- (II) Jones and Wilson (1978) applied thin film arguments to the related problem of a drop approaching a deformable interface. They considered the film as composed of a dimple region and a central film region. Tangential stress in the central film is of the order of  $\mu_2 \hat{u}_t / h$  while the stress in the drop is of the order  $\mu_1 \hat{u}_t / R$ . Viscosity ratio,  $\lambda$ , is assumed to be  $O(1)$  while  $\epsilon = h/R$  is assumed small. Continuity of velocities indicates  $\hat{u}_t$  in the central film and in the drop are of the same order. The conclusion Jones and Wilson reach is that the tangential stresses cannot match to leading order and thus  $\frac{\partial v_t}{\partial n} = 0$ . The drop viscous contribution to the tangential stress does not come into play. In the dimple region this analysis breaks down. Here the appropriate length scaling in the drop is  $h$  (the order of size of the dimple) and the drop tangential stress is of the same order as the film tangential stress. Thus Jones and Wilson conclude that viscous effects in the drop must be considered in the dimple region. Immediately prior to dimple formation, their argument indicates  $\frac{\partial v_\rho}{\partial z} = 0$  throughout the film region. Figure 23 indicates that  $\frac{\partial v_\rho}{\partial z}$  is *small* at the interface in the central region of the film. This may be deceptive since in the initial stages of dimple formation equation (51) indicates that an accurate estimate for  $\frac{\partial v_\rho}{\partial z}$  at the interface may be crucial. Thus, it is difficult to clearly assess the error of this approximation.

- (III) The dimensional equivalent of equation (6), when rescaled, provides the necessary information to determine when gravity effects may be neglected relative to surface tension effects. Scaling  $\rho$  with  $R$  and  $z$  with  $h$ , leads to the parameter

$$M = 3\left(\frac{R}{a}\right)^2 \left(\frac{1 + \frac{3}{2}\lambda}{1 + \lambda}\right) Ca$$

Roughly speaking,  $M$  is the ratio of gravitational effects to surface tension

effects.  $M \ll 1$  indicates gravity is negligible relative to surface tension. Only in the limit  $Ca \ll 1$  will  $M$  be small. None of the numerical cases considered here approach this limit.

- (IV) Drop deformation increases with increasing  $Ca$ . Thus the assumption of spherical drop shape outside the film region is limited to  $Ca \ll 1$ . Similarly, outside of the dimpled region invariance of drop shape is limited to the small  $Ca$  regime.

Dimple evolution is observed to occur in several stages. Initially a configuration is established in which the drop is nearly flat at the central region of the film, then gradually sloping upward at the edge of the film. In this configuration,  $\frac{\partial p_2}{\partial z}$  is observed to be negative near  $\rho = 0$ . A negative value of  $\frac{\partial p_2}{\partial z}$  has been shown to be crucial to the observed increase in downward velocity as one moves radially outward. It is this increase in downward velocity that forms the initial dimple. Lubrication theory neglects the observed variation of pressure with  $z$ . As a consequence, lubrication theory will not be valid in the initial stages of dimple formation.

In the later stages of dimple growth (here observed for  $Ca = 3$ ), velocity at the central region of the film is dramatically smaller than near the dimple. Here fluid is “trapped” by the dimple and corresponding pressure fields indicate that pressure increases moving radially outward to the dimple, then decrease radially beyond the dimple to the stagnant fluid value. The quantity,  $\frac{\partial p_2}{\partial z}$ , is seen to decrease in magnitude in the later stages of dimple evolution. It is for this latest stage of dimple evolution that the lubrication assumption of negligible pressure variation with  $z$  may be valid.

### Appendix A

(a) The matrices  $\mathbf{P}$ ,  $\mathbf{Q}$  and the vectors  $\mathbf{S}$  and  $\mathbf{W}$

In section 2 it was shown that after integrating analytically in the axial direction, the integrands reduce to the form

$$\begin{pmatrix} P_{11} & P_{12} \\ P_{21} & P_{22} \end{pmatrix} \begin{pmatrix} u_{\rho}^I \\ u_z^I \end{pmatrix} \quad (A1)$$

and

$$\begin{pmatrix} Q_{11} & Q_{12} \\ Q_{21} & Q_{22} \end{pmatrix} \begin{pmatrix} f_{\rho}^{(i)} \\ f_z^{(i)} \end{pmatrix}, \quad (A2)$$

$$\begin{pmatrix} W_1 \\ W_2 \end{pmatrix} \begin{pmatrix} u_{\rho}^I \\ u_z^I \end{pmatrix}$$

$$\begin{pmatrix} S_1 \\ S_2 \end{pmatrix} \begin{pmatrix} f_{\rho}^{(i)} \\ f_z^{(i)} \end{pmatrix}$$

The elements of the matrices  $\mathbf{P}$  and  $\mathbf{Q}$  along with the vectors  $\mathbf{S}$  and  $\mathbf{W}$  are:

$$\begin{aligned} \frac{4\pi}{3} P_{11} = & \rho\rho_o^2 n_{\rho} (C_5^{03} - \hat{C}_5^{03}) + \rho_o [\rho n_z (r_3 C_5^{02} - R_3 \hat{C}_5^{02}) \\ & + n_{\rho} (2\rho^2 + \rho_o^2) (C_5^{02} - \hat{C}_5^{02})] + \rho n_{\rho} (2\rho_o^2 + \rho^2) (C_5^{01} - \hat{C}_5^{01}) \\ & + n_z (\rho^2 + \rho_o^2) (r_3 C_5^{01} - R_3 \hat{C}_5^{01}) + \rho\rho_o [\rho n_{\rho} (C_5^{00} - \hat{C}_5^{00}) \\ & + n_z (r_3 C_5^{00} - R_3 \hat{C}_5^{00})] - 2x_3 \{-x_3 n_{\rho} (\rho \hat{C}_5^{01} + \rho_o \hat{C}_5^{00} \\ & + z \{2\rho_o n_{\rho} \hat{C}_5^{02} + (2\rho n_{\rho} + n_z R_3) \hat{C}_5^{01}\}) + 10x_3 z [\rho\rho_o^2 n_{\rho} \hat{C}_7^{03} \\ & + \rho_o \{\rho n_z R_3 + n_{\rho} (2\rho^2 + \rho_o^2)\} \hat{C}_7^{02} + \{\rho n_{\rho} (2\rho_o^2 + \rho^2) \\ & + n_z R_3 (\rho^2 + \rho_o^2)\} \hat{C}_7^{01} + \rho\rho_o (\rho n_{\rho} + n_z R_3) \hat{C}_7^{00}] \end{aligned} \quad (A3)$$

$$\begin{aligned} -\frac{4\pi}{3} P_{12} = & \rho\rho_o n_{\rho} (r_3 C_5^{02} - R_3 \hat{C}_5^{02}) + \rho n_z (r_3^2 C_5^{01} - R_3^2 \hat{C}_5^{01}) \\ & + n_{\rho} (\rho^2 + \rho_o^2) (r_3 C_5^{01} - R_3 \hat{C}_5^{01}) + \rho_o \{\rho n_{\rho} (r_3 C_5^{00} - R_3 \hat{C}_5^{00}) \\ & + n_z (r_3^2 C_5^{00} - R_3^2 \hat{C}_5^{00})\} - 2x_3 [-x_3 n_z (\rho \hat{C}_5^{01} + \rho_o \hat{C}_5^{00}) \\ & + z n_{\rho} R_3 \hat{C}_5^{01}] + 10x_3 z R_3 [\rho\rho_o n_{\rho} \hat{C}_7^{02} \\ & + \{\rho n_z R_3 + (\rho^2 + \rho_o^2) n_{\rho}\} \hat{C}_7^{01} + \rho_o (\rho n_{\rho} + n_z R_3) \hat{C}_7^{00}] \end{aligned} \quad (A4)$$

$$\begin{aligned}
 -\frac{4\pi}{3}P_{21} = & \rho_o^2 n_\rho (r_3 C_5^{02} - R_3 \hat{C}_5^{02}) + 2\rho\rho_o n_\rho (r_3 C_5^{01} - R_3 \hat{C}_5^{01}) \\
 & + \rho_o n_z (r_3^2 C_5^{01} - R_3^2 \hat{C}_5^{01}) + \rho^2 n_\rho (r_3 C_5^{00} - R_3 \hat{C}_5^{00}) \\
 & + \rho n_z (r_3^2 C_5^{00} - R_3^2 \hat{C}_5^{00}) + 2x_3 [-x_3 n_\rho R_3 \hat{C}_5^{00} \\
 & + zn_z (\rho_o \hat{C}_5^{01} + \rho \hat{C}_5^{00}) + \rho_o^2 n_\rho \hat{C}_5^{02} \\
 & + \rho_o (2\rho n_\rho + n_z R_3) \hat{C}_5^{01} \rho (\rho n_\rho + n_z R_3) \hat{C}_5^{00}] \\
 & - 10x_3 z R_3 [\rho_o^2 n_\rho \hat{C}_7^{02} + \rho_o (2\rho n_\rho + n_z R_3) \hat{C}_7^{01} \\
 & + \rho (\rho n_\rho + n_z R_3) \hat{C}_7^{00}]
 \end{aligned} \tag{A5}$$

$$\begin{aligned}
 \frac{4\pi}{3}P_{22} = & \rho_o n_\rho (r_3^2 C_5^{01} - R_3^2 \hat{C}_5^{01}) + \rho n_\rho (r_3^2 C_5^{00} - R_3^2 \hat{C}_5^{00}) \\
 & + n_z (r_3^3 C_5^{00} - R_3^3 \hat{C}_5^{00} + 2x_3 [-x_3 R_3 n_z \hat{C}_5^{00} \\
 & + z \{ \rho_o n_\rho \hat{C}_5^{01} + (\rho n_\rho + 2n_z R_3) \hat{C}_5^{00} \}] \\
 & + 2x_3 R_3 [\rho_o n_\rho \hat{C}_5^{01} + (\rho n_\rho + n_z R_3) \hat{C}_5^{00}] \\
 & - 10x_3 z R_3^2 [\rho_o n_\rho \hat{C}_7^{01} + (\rho n_\rho + n_z R_3) \hat{C}_7^{00}]
 \end{aligned} \tag{A6}$$

$$\begin{aligned}
 -8\pi Q_{11} = & C_1^{01} - \hat{C}_1^{01} + \rho\rho_o (C_3^{02} - \hat{C}_3^{02}) + (\rho^2 + \rho_o^2)(C_3^{01} - \hat{C}_3^{01}) \\
 & + \rho\rho_o (C_3^{00} - \hat{C}_3^{00}) - 2x_3 z [\hat{C}_3^{01} \\
 & - 3\{(\rho^2 + \rho_o^2)\hat{C}_5^{01} + \rho\rho_o(\hat{C}_5^{02} + \hat{C}_5^{00})\}]
 \end{aligned} \tag{A7}$$

$$\begin{aligned}
 8\pi Q_{12} = & \rho(r_3 C_3^{01} - R_3 \hat{C}_3^{01}) + \rho_o(r_3 C_3^{00} - R_3 \hat{C}_3^{00}) \\
 & + 2x_3 [\rho \hat{C}_3^{01} + \rho_o \hat{C}_3^{00} + 3z R_3 (\rho \hat{C}_5^{01} + \rho_o \hat{C}_5^{00})]
 \end{aligned} \tag{A8}$$

$$\begin{aligned}
 8\pi Q_{21} = & \rho_o(r_3 C_3^{01} - R_3 \hat{C}_3^{01}) + \rho(r_3 C_3^{00} - R_3 \hat{C}_3^{00}) \\
 & + 2x_3 [\rho_o \hat{C}_3^{01} + \rho \hat{C}_3^{00} - 3z R_3 (\rho_o \hat{C}_5^{01} + \rho \hat{C}_5^{00})]
 \end{aligned} \tag{A9}$$

$$\begin{aligned}
 -8\pi Q_{22} = & C_1^{00} - \hat{C}_1^{00} + r_3^2 C_3^{00} - R_3^2 \hat{C}_3^{00} \\
 & + 2x_3 z (\hat{C}_3^{00} - 3R_3^2 \hat{C}_5^{00}).
 \end{aligned} \tag{A10}$$

$$S_1 = -\frac{1}{4\pi} \left[ \rho (C_3^{00} - \hat{C}_3^{00}) + \rho_o (C_3^{01} - \hat{C}_3^{01}) + 6\rho\xi_3 R_3 \hat{C}_5^{00} + 6\rho_o \xi_3 R_3 \hat{C}_5^{01} \right] \tag{A11}$$

$$S_2 = \frac{1}{4\pi} \left[ r_3 C_3^{00} - R_3 \hat{C}_3^{00} + 2x_3 \hat{C}_3^{00} + 6\xi_3 R_3^2 \hat{C}_5^{00} \right] \tag{A12}$$

$$\begin{aligned}
 W_1 = & -\frac{1}{\pi} \left[ n_\rho \left( \frac{1}{2} C_3^{00} + \frac{1}{2} \hat{C}_3^{00} - 3x_3 R_3 \hat{C}_5^{00} \right) + \rho^2 n_\rho \left( \frac{-3}{2} C_5^{00} + \frac{3}{2} \hat{C}_5^{00} - 15\xi_3 R_3 \hat{C}_7^{00} \right) \right. \\
 & + \rho n_z \left( \frac{-3}{2} r_3 C_5^{00} + \frac{3}{2} R_3 \hat{C}_5^{00} - 15\xi_3 R_3^2 \hat{C}_7^{00} \right) \\
 & + 2\rho\rho_0 n_\rho \left( \frac{-3}{2} C_5^{01} + \frac{3}{2} \hat{C}_5^{01} - 15\xi_3 R_3 \hat{C}_7^{01} \right) \\
 & + \rho_0 n_z \left( \frac{-3}{2} r_3 C_5^{01} + \frac{3}{2} R_3 \hat{C}_5^{01} - 15\xi_3 R_3^2 \hat{C}_7^{01} \right) + \\
 & \left. + \rho_0^2 n_\rho \left( \frac{-3}{2} C_5^{02} + \frac{3}{2} \hat{C}_5^{02} - 15\xi_3 R_3 \hat{C}_7^{02} \right) + 3\rho_0 n_z \xi_3 \hat{C}_5^{01} + 3\rho n_z \xi_3 \hat{C}_5^{00} \right] \quad (A13)
 \end{aligned}$$

$$\begin{aligned}
 W_2 = & \frac{1}{\pi} \left[ n_z \left( \frac{1}{2} C_3^{00} + \frac{1}{2} \hat{C}_3^{00} - 3x_3 R_3 \hat{C}_5^{00} \right) + \rho n_\rho \left( \frac{-3}{2} r_3 C_5^{00} + \frac{3}{2} R_3 \hat{C}_5^{00} - 15\xi_3 R_3^2 \hat{C}_7^{00} \right) \right. \\
 & + n_z \left( \frac{-3}{2} r_3^2 C_5^{00} + \frac{3}{2} R_3^2 \hat{C}_5^{00} - 15\xi_3 R_3^3 \hat{C}_7^{00} \right) \\
 & + \rho_0 n_\rho \left( \frac{-3}{2} r_3 C_5^{01} + \frac{3}{2} R_3 \hat{C}_5^{01} - 15\xi_3 R_3^2 \hat{C}_7^{01} \right) \\
 & \left. + 3\rho_0 n_\rho \xi_3 \hat{C}_5^{01} + 3(\rho n_\rho + 2R_3 n_z) \xi_3 \hat{C}_5^{00} \right] \quad (A14)
 \end{aligned}$$

The symbols  $C_p^{nm}$  and  $\hat{C}_p^{nm}$  represent various elliptic integral functions, and these will be listed in the next section. The point  $(\rho, z)$  corresponds to the location of integration, and  $(\rho_0, x_3)$  is the singular point. Also,  $r_3 = z - x_3$  and  $R_3 = z + x_3$ .

(b) The Integrals  $C_p^{nm}$  and  $\hat{C}_p^{nm}$

The elliptic integral arise from analytic integration of the trigonometric functions appearing in the surface integrals. All of the elliptic integrals shown in the previous section are of the form

$$C_p^{nm} \equiv \frac{2}{\gamma^{p/2}} \int_0^\pi \frac{\sin^n 2x \cos^m 2x}{[1 - k^2 \sin^2 x]^{p/2}} dx \quad (A15)$$

and

$$\hat{C}_p^{nm} \equiv \frac{2}{\gamma_R^{p/2}} \int_0^\pi \frac{\sin^n 2x \cos^m 2x}{[1 - k_R^2 \sin^2 x]^{p/2}} dx, \quad (A16)$$

where

$$\begin{aligned}\gamma &= (\rho + \rho_0)^2 + r_3^2 \\ k^2 &= \frac{4\rho\rho_0}{\gamma}\end{aligned}$$

and

$$\begin{aligned}\gamma_R &= (\rho + \rho_0)^2 + R_3^2 \\ k_R^2 &= \frac{4\rho\rho_0}{\gamma_R}.\end{aligned}$$

Using standard integral tables, all integrals of the form shown in Eq. (A15) or (A16) can be reduced to the two functions

$$\begin{aligned}K(k) &= 2 \int_0^\pi \frac{dx}{[1 - k^2 \sin^2 x]^{1/2}} \\ E(k) &= 2 \int_0^\pi \frac{dx}{[1 - k^2 \sin^2 x]^{3/2}}.\end{aligned}$$

The elliptic integrals appearing in Eqs. (A3)-(A14) are listed below:

$$C_1^{00} = \frac{4}{\gamma^{1/2}} K \quad (\text{A17})$$

$$C_1^{01} = C_1^{00} - \frac{8}{k^2 \gamma^{1/2}} (K - E) \quad (\text{A18})$$

$$C_3^{00} = \frac{4}{\hat{k}^2 \gamma^{3/2}} E \quad (\text{A19})$$

$$C_3^{01} = \frac{4}{k^2 \gamma^{3/2}} \left[ 2K - \frac{1 + \hat{k}^2}{\hat{k}^2} E \right] \quad (\text{A20})$$

$$C_3^{20} = \frac{16}{k^4 \gamma^{3/2}} [(1 + \hat{k}^2)K - 2E] \quad (\text{A21})$$

$$C_3^{03} = C_3^{01} - C_3^{20} + \frac{32}{3k^6 \gamma^{3/2}} [(k^2 - 8)E + (8 - 5k^2)K] \quad (\text{A22})$$

$$C_5^{00} = \frac{4}{3\hat{k}^2 \gamma^{5/2}} \left[ \frac{2(1 + \hat{k}^2)}{\hat{k}^2} E - K \right] \quad (\text{A23})$$

$$C_5^{01} = \frac{4}{3k^2 \hat{k}^2 \gamma^{5/2}} \left[ (1 + \hat{k}^2)K - \frac{2}{\hat{k}^2} (\hat{k}^2 + k^4)E \right] \quad (\text{A24})$$

$$C_5^{20} = \frac{16}{3k^4 \gamma^{5/2}} \left[ \frac{1 + \hat{k}^2}{\hat{k}^2} E - 2K \right] \quad (\text{A25})$$

$$C_5^{03} = C_5^{01} - C_5^{20} + \frac{32}{3k^6\gamma^{5/2}} \left[ \frac{1+7\hat{k}^2}{\hat{k}^2} E - (8-3k^2)K \right] \quad (A26)$$

$$C_7^{00} = \frac{4}{15\hat{k}^4\gamma^{7/2}} \left[ \frac{1}{\hat{k}^2} (23\hat{k}^2 + 8k^4) E - 4(1 + \hat{k}^2)K \right] \quad (A27)$$

$$C_7^{01} = \frac{4}{15k^2\hat{k}^4\gamma^{7/2}} \left[ \frac{1}{\hat{k}^2} (-6 + 9k^2 - 19k^4 + 8k^6) E + 2(3\hat{k}^2 + 2k^4)K \right] \quad (A28)$$

$$C_7^{20} = \frac{16}{15\hat{k}^2k^4\gamma^{7/2}} \left[ \frac{2}{\hat{k}^2} (\hat{k}^2 + k^4) E - (1 + \hat{k}^2)K \right] \quad (A29)$$

$$C_7^{03} = C_7^{01} - C_7^{20} + \frac{32}{15\hat{k}^2k^6\gamma^{7/2}} \left[ -\frac{1}{\hat{k}^2} (8 - 13k^2 + 3k^4) E + (8 - 9k^2)K \right] \quad (A30)$$

$$C_p^{02} = C_p^{00} - C_p^{20} \quad (A31)$$

where

$$\hat{k}^2 = 1 - k^2$$

— small  $k$  expansions —

A numerical difficulty arises when  $\rho$  and/or  $\rho_o \rightarrow 0$ , because even in double precision arithmetic, terms in numerators do not cancel as fast as denominators go to zero. In reality, all of the elliptic integrals listed above approach constant values as  $k \rightarrow 0$ , and to reflect this fact, it is necessary to do a generalized binomial expansion in  $k^2$  on the integrand in Eq. (11). The result of the expansion in an infinite series in powers of  $k^2$ ; we have truncated the series at the  $O(k^4)$  term, under the assumption that the remainder is vanishingly small. Thus in the limit as  $k \rightarrow 0$ , the integrals in Eqs. (A17)-(A31) reduce to the following:

$$C_1^{00} = \frac{2\pi}{\gamma^{1/2}} \left( 1 + \frac{1}{8}k^2 \right) \quad (A32)$$

$$C_1^{01} = -\frac{\pi k^2}{4\gamma^{1/2}} \quad (A33)$$

$$C_3^{00} = \frac{2\pi}{\gamma^{3/2}} \left( 1 + \frac{3}{8}k^2 \right) \quad (A34)$$

$$C_3^{01} = -\frac{3\pi k^2}{4\gamma^{3/2}} \quad (\text{A35})$$

$$C_3^{20} = \frac{\pi}{\gamma^{3/2}} \left(1 + \frac{3}{8}k^2\right) \quad (\text{A36})$$

$$C_3^{03} = -\frac{9\pi k^2}{16\gamma^{3/2}} \quad (\text{A37})$$

$$C_5^{00} = \frac{2\pi}{\gamma^{5/2}} \left(1 + \frac{5}{8}k^2\right) \quad (\text{A38})$$

$$C_5^{01} = -\frac{5\pi k^2}{4\gamma^{5/2}} \quad (\text{A39})$$

$$C_5^{20} = \frac{\pi}{\gamma^{5/2}} \left(1 + \frac{5}{8}k^2\right) \quad (\text{A40})$$

$$C_5^{03} = -\frac{15\pi k^2}{16\gamma^{5/2}} \quad (\text{A41})$$

$$C_7^{00} = \frac{2\pi}{\gamma^{7/2}} \left(1 + \frac{7}{8}k^2\right) \quad (\text{A42})$$

$$C_7^{01} = -\frac{7\pi k^2}{4\gamma^{7/2}} \quad (\text{A43})$$

$$C_7^{20} = \frac{\pi}{\gamma^{7/2}} \left(1 + \frac{7}{8}k^2\right) \quad (\text{A44})$$

$$C_7^{03} = -\frac{21\pi k^2}{16\gamma^{7/2}} \quad (\text{A45})$$

(c) The singular contributions

As mentioned in §2, the numerical integration breaks down when  $\xi \rightarrow \mathbf{x}$  since the kernel becomes unbounded in this case. To include this integrable singular contribution it is necessary to approximate the integral analytically. This is accomplished by Taylor series expanding the singular terms about the point  $(\rho_o, z_o)$  in Eqs(A3-A10). The details involved in carrying out these expansions are analogous to those used by Lee and Leal(1982), the differences being only in the choice of parametrization of the surface. It is important to note, however,

that only those terms in the kernels  $\mathbf{Q}$  and  $\mathbf{P}$  stemming from the fundamental solution to Stokes system must be considered, since  $R \neq 0$  for  $z > 0$ .

— the single layer —

Here we consider the integral

$$\begin{aligned}
 \mathbf{a} &= \int_{s_i - \epsilon/2}^{s_i + \epsilon/2} \int_0^{2\pi} \rho [\dot{\rho}^2 + \dot{z}^2]^{1/2} \left\{ \frac{\mathbf{f}}{r} + \frac{\mathbf{f} \cdot \mathbf{r}}{r^3} \mathbf{r} \right\} d\theta ds \\
 &= \int_{s_i - \epsilon/2}^{s_i + \epsilon/2} \rho [\dot{\rho}^2 + \dot{z}^2]^{1/2} ds \left\{ \mathbf{i} \left[ f_\rho C_1^{01} + (\rho^2 + \rho_o^2) f_\rho C_3^{01} \right. \right. \\
 &\quad \left. \left. + \rho \rho_o f_\rho (C_3^{00} + C_3^{02}) + f_z r_3 (\rho C_3^{01} + \rho_o C_3^{00}) \right] \right. \\
 &\quad \left. + \mathbf{k} \left[ f_z C_1^{00} + f_\rho r_3 (\rho C_3^{00} + \rho_o C_3^{01}) + f_z r_3^2 C_3^{00} \right] \right\}, \tag{A46}
 \end{aligned}$$

where  $s_i$  is the value of the arclength parameter of the  $i$ th node, and  $\mathbf{i}$  and  $\mathbf{k}$  are the cartesian base vectors. After carrying out the expansions, the  $\mathbf{i}$  component of the integral is

$$\begin{aligned}
 a_i &\simeq 2\epsilon \left\{ f_{z_o} \frac{\dot{\rho}_o \dot{z}_o}{[\dot{\rho}_o^2 + \dot{z}_o^2]^{1/2}} + f_{\rho_o} \left[ \frac{\dot{\rho}_o^2 + 2\dot{z}_o^2}{[\dot{\rho}_o^2 + \dot{z}_o^2]^{1/2}} \right. \right. \\
 &\quad \left. \left. - [\dot{\rho}_o^2 + \dot{z}_o^2]^{1/2} \ln \left( \frac{\epsilon}{16\rho_o} [\dot{\rho}_o^2 + \dot{z}_o^2]^{1/2} \right) \right] \right\}, \tag{A47}
 \end{aligned}$$

and the  $\mathbf{k}$  component is

$$\begin{aligned}
 a_k &\simeq 2\epsilon \left\{ f_{\rho_o} \frac{\dot{\rho}_o \dot{z}_o}{[\dot{\rho}_o^2 + \dot{z}_o^2]^{1/2}} + f_{z_o} \left[ \frac{\dot{z}_o^2}{[\dot{\rho}_o^2 + \dot{z}_o^2]^{1/2}} \right. \right. \\
 &\quad \left. \left. + [\dot{\rho}_o^2 + \dot{z}_o^2]^{1/2} \left( 1 - \ln \frac{\epsilon}{16\rho_o} [\dot{\rho}_o^2 + \dot{z}_o^2]^{1/2} \right) \right] \right\}, \tag{A48}
 \end{aligned}$$

where the subscript  $o$  denotes evaluation at the singular point.

— the double layer —

The singular contribution to the double layer takes the form

$$\mathbf{b} = \int_{s_i - \epsilon/2}^{s_i + \epsilon/2} \int_0^{2\pi} \rho [\dot{\rho}^2 + \dot{z}^2]^{1/2} \left\{ \frac{(\mathbf{n} \cdot \mathbf{r}) \mathbf{r} (\mathbf{r} \cdot \mathbf{u})}{r^5} \right\} d\theta ds \tag{A49}$$

After carrying out the expansions, the **i** component of the integral is

$$\begin{aligned}
 b_i \simeq \epsilon u_\rho \left\{ \frac{559\dot{z}_o}{384\rho_o} + \frac{1}{3(\dot{\rho}_o^2 + \dot{z}_o^2)^2} \left[ \frac{\dot{\rho}_o^2}{\rho_o} (6\dot{\rho}_o^2\dot{z}_o + 6\dot{\rho}_o\dot{z}_o^2 - \dot{\rho}_o^2 - \dot{z}_o^2) \right. \right. \\
 \left. \left. - 2\dot{\rho}_o^2\ddot{z}_o(2\dot{\rho}_o + 3\dot{z}_o) - 2\dot{\rho}_o\dot{z}_o\ddot{\rho}_o(3\dot{\rho}_o + 2\dot{z}_o) \right] \right\} \\
 + \frac{\epsilon u_z}{3(\dot{\rho}_o^2 + \dot{z}_o^2)^2} \left[ 2\dot{\rho}_o(\dot{z}_o\ddot{\rho}_o - \dot{\rho}_o\ddot{z}_o) - \frac{\dot{\rho}_o\dot{z}_o}{\rho_o}(\dot{\rho}_o^2 - \dot{z}_o^2) \right],
 \end{aligned} \tag{A50}$$

and the **k** component is

$$\begin{aligned}
 b_k \simeq \frac{\epsilon u_{\rho_o}}{\dot{\rho}_o^2 + z dsq} \left\{ \frac{\dot{\rho}_o\dot{z}_o}{3\rho_o} + \frac{\dot{\rho}_o\dot{z}_o^2}{3} \frac{2\ddot{\rho}_o + \dot{z}_o\ddot{\rho}_o + \dot{\rho}_o\ddot{z}_o}{\dot{\rho}_o^2 + z dsq} \right. \\
 \left. + \frac{4\dot{\rho}_o\dot{z}_o}{3(\dot{\rho}_o^2 + \dot{z}_o^2)^2} \left[ \dot{\rho}_o^2(\dot{\rho}_o\ddot{z}_o - \ddot{\rho}_o\dot{z}_o) + \dot{z}_o^2(\dot{\rho}_o^2\dot{z}_o - \dot{\rho}_o\dot{z}_o^2) \right] \right\} \\
 + \frac{\epsilon u_{z_o}}{3(\dot{\rho}_o^2 + z dsq)} \left\{ \frac{\dot{z}_o^2}{\rho_o} + \frac{2\dot{z}_o^2(\ddot{\rho}_o\dot{z}_o - \dot{\rho}_o\ddot{z}_o)}{\dot{\rho}_o^2 + \dot{z}_o^2} \right. \\
 \left. + \frac{4\dot{z}_o^2}{(\dot{\rho}_o^2 + \dot{z}_o^2)^2} (\dot{\rho}_o^2 - \dot{z}_o^2)(\dot{\rho}_o\ddot{z}_o - \ddot{\rho}_o\dot{z}_o) \right\}.
 \end{aligned} \tag{A51}$$

Appendix B

The thin film trapped between a bubble and a planar wall

E.P. Ascoli and L.G. Leal

Dept. of Chemical Engineering

California Institute of Technology

Pasadena, California 91125

## Introduction

In chapter II we numerically examined the buoyancy driven axisymmetric motion of a deformable drop toward a planar wall. Focus was placed on the phenomenon known as dimpling. In particular, immediately prior to dimpling, the drops were found to be nearly flat at the central region of the interface nearest the wall. A dimple developed, within this flat region, at a small radial distance from the axis of symmetry (taken to be the  $z$ -axis). In these initial stages of dimpling, each instantaneous configuration was accompanied by a decrease in modified pressure with  $z$  near the dimple region. This decrease in modified pressure with  $z$  was shown to be crucial in establishing the momentum fluxes which inevitably lead to dimple formation. In the later stages of dimple evolution, modified pressure variation with  $z$  in the dimple region decreased in magnitude relative to radial pressure variation.

A multitude of "film drainage" theories have been developed to describe the shape evolution of the film trapped between the drop and the planar wall (consult Chapter II for further details). These theories have one key geometrical assumption in common. The height of the film is assumed to be vanishingly small relative to its radial extent. This assumption has been invoked to justify the lubrication approximation. In turn, the lubrication approximation neglects variation of modified pressure with  $z$ . The results of Chapter II indicate that the necessary physics for predicting initial dimple formation for intermediate ranges of physical parameters is lost when modified pressure variation in  $z$  is neglected. The authors suggest that initial dimple formation takes place for geometrical configurations where the film is not sufficiently thin to warrant neglect of variation in pressure with  $z$ . In the later stages of dimple evolution, where variation in modified pressure diminishes, the lubrication assumption will be valid.

Lubrication theory is an asymptotic theory, where the small parameter is the ratio of film height to radial extent. As applied in existing film drainage theory, only the leading order result is sought. In principle, higher order corrections

in the small parameter may be obtained. Presumably, higher order corrections extend the domain of validity of the approximate solutions to larger values of the small parameter. The obvious question is: Can higher order corrections predict the details of *initial* dimple formation? Unfortunately, careful scaling and non-dimensionalization of the governing equations has not been done. In addition, film drainage theory has been complicated by peripheral assumptions (i.e. neglect of gravity in the film and ad hoc geometrical closure conditions at the outermost edge of the film).

In this study, we will focus on the film trapped between a bubble and a planar wall. Bubbles form dimples (Platikinov (1964), Derjaguin and Kussakov (1939)) , and the overall geometrical features are roughly the same as for drops. The bubble assumption allows neglect of the complications due to circulation in the enclosed phase. We will develop a coherent asymptotic thin film theory in the small parameter,  $\epsilon$ , the ratio of film height to film radial extent. We assume that in initial film shape (for which  $\epsilon$  is “small” ) is provided as an initial configuration. The analysis will include the effects of gravity in the film. Higher order corrections in  $\epsilon$  will be obtained and the question of initial dimple formation examined in this context.

## Formulation

We consider the slow viscous motion of a deformable bubble normal to a planar wall (figure B1). Gravity will be assumed to act upward along the  $z$ -axis. The motion is assumed axisymmetric. Stokes equations govern the motion in the outer fluid. In dimensional form, the Stokes equations are (bar denotes dimensional variables):

$$\begin{aligned}\frac{\partial \bar{p}_h}{\partial \bar{r}} &= \mu \left[ \frac{\partial}{\partial \bar{r}} \left( \frac{1}{\bar{r}} \frac{\partial \bar{r} \bar{v}_r}{\partial \bar{r}} \right) + \frac{\partial^2 \bar{v}_r}{\partial \bar{z}^2} \right] \\ \frac{\partial \bar{p}_h}{\partial \bar{z}} &= \mu \left[ \frac{1}{\bar{r}} \frac{\partial}{\partial \bar{r}} \left( \bar{r} \frac{\partial \bar{v}_z}{\partial \bar{r}} \right) + \frac{\partial^2 \bar{v}_z}{\partial \bar{z}^2} \right] + \rho g_r \\ \frac{1}{\bar{r}} \frac{\partial \bar{r} \bar{v}_r}{\partial \bar{r}} + \frac{\partial \bar{v}_z}{\partial \bar{z}} &= 0\end{aligned}$$

For convenience we will work with modified pressure,  $\bar{p}$  less the constant bubble pressure  $\bar{p}_b$ . Thus, define

$$\bar{p} = \bar{p}_h - \bar{p}_b - \rho g_r \bar{z}$$

Then the Stokes equations become

$$\begin{aligned}\frac{\partial \bar{p}}{\partial \bar{r}} &= \mu \left[ \frac{\partial}{\partial \bar{r}} \left( \frac{1}{\bar{r}} \frac{\partial \bar{r} \bar{v}_r}{\partial \bar{r}} \right) + \frac{\partial^2 \bar{v}_r}{\partial \bar{z}^2} \right] \\ \frac{\partial \bar{p}}{\partial \bar{z}} &= \mu \left[ \frac{1}{\bar{r}} \frac{\partial}{\partial \bar{r}} \left( \bar{r} \frac{\partial \bar{v}_z}{\partial \bar{r}} \right) + \frac{\partial^2 \bar{v}_z}{\partial \bar{z}^2} \right]\end{aligned}$$

Let  $G$  denote a measure of the height of the film and  $R$  denote a measure of its radial extent. In addition, let  $U$  denote a measure of the magnitude of the  $z$  component of velocity. We rescale  $z$  with  $G$ ,  $\rho$  with  $R$  and  $\bar{v}_z$  with  $U$ . The continuity equation implies that

$$O(\bar{v}_r) = RU/G$$

Rescaling  $\bar{v}_r$  with  $RU/G$  and defining the small parameter  $\epsilon = G/R$  yields

$$\frac{G\epsilon^2}{\mu U} \frac{\partial \bar{p}}{\partial r} = \epsilon^2 \frac{\partial}{\partial r} \left( \frac{1}{r} \frac{\partial r v_r}{\partial r} \right) + \frac{\partial^2 v_r}{\partial z^2} \quad (B1a)$$

$$\frac{G\epsilon^2}{\mu U} \frac{\partial \bar{p}}{\partial z} = \frac{\epsilon^4}{r} \frac{\partial}{\partial r} \left( r \frac{\partial v_z}{\partial r} \right) + \epsilon^2 \frac{\partial^2 v_z}{\partial z^2} \quad (B1b)$$

$$\frac{1}{r} \frac{\partial r v_r}{\partial r} + \frac{\partial v_z}{\partial z} = 0 \quad (B1c)$$

The corresponding boundary conditions are no-slip at the planar wall and force equilibrium at the interface. Thus, at the planar wall

$$v_r = v_z = 0$$

For a bubble, a force balance at the interface becomes

$$\mathbf{n} \cdot \mathbf{T} = \frac{\gamma\epsilon}{\mu U} \mathbf{n} \nabla_s \cdot \mathbf{n} + \frac{g_r G^2 \rho}{\mu U} g \mathbf{n} \quad (B2)$$

Here, the dimensional stress is defined as

$$\bar{\mathbf{T}} = \mu \left( \bar{\nabla} \bar{\mathbf{u}} + (\bar{\nabla} \bar{\mathbf{u}})^T \right) - \mathbf{I} \bar{p} = \bar{\mathbf{\Gamma}} - \mathbf{I} \bar{p}$$

The corresponding dimensionless stress is

$$\mathbf{T} = \frac{\bar{\mathbf{T}}}{\mu U / G} = \mathbf{\Gamma} - \frac{G\epsilon^2}{\mu U} \mathbf{I} \bar{p}$$

The function,  $g = g(r)$ , is the interface height and is made dimensionless with respect to  $G$ . The vector,  $\mathbf{n}$ , is the outward normal to the bubble and is given by

$$n_r = \frac{\epsilon \dot{g}}{(1 + \epsilon^2 \dot{g}^2)^{\frac{1}{2}}}$$

$$n_z = \frac{-1}{(1 + \epsilon^2 \dot{g}^2)^{\frac{1}{2}}}$$

The term  $\nabla_s \cdot \mathbf{n}$  is the dimensionless surface gradient operating on the normal to the interface:

$$\nabla_s \cdot \mathbf{n} = \epsilon \left[ \frac{\dot{g}}{r(1 + \epsilon^2 \dot{g}^2)^{\frac{1}{2}}} + \frac{\ddot{g}}{(1 + \epsilon^2 \dot{g}^2)^{\frac{3}{2}}} \right]$$

The force balance (B2) at the interface has a tangential and normal component. Dotting the tangent vector,  $\mathbf{t}$ , into equation (B2) shows:

$$\mathbf{n} \cdot \mathbf{T} \cdot \mathbf{t} = 0$$

The tangent vector,  $\mathbf{t}$ , can be expressed in terms of the normal vector as  $t_r = -n_z$  and  $t_z = n_r$ . Expanding the tangential component of the interfacial force balance gives

$$0 = \frac{\epsilon^2 \dot{g}^2 - 1}{1 + \epsilon^2 \dot{g}^2} \left( \epsilon \frac{\partial v_z}{\partial r} + \frac{1}{\epsilon} \frac{\partial v_r}{\partial z} \right) + 2 \frac{\epsilon \dot{g}}{1 + \epsilon^2 \dot{g}^2} \left( \frac{\partial v_r}{\partial r} - \frac{\partial v_z}{\partial z} \right) \quad (B3)$$

At the interface, the normal component of the force balance is

$$\mathbf{n} \cdot \mathbf{T} \cdot \mathbf{n} = \frac{\gamma \epsilon}{\mu U} \nabla_s \cdot \mathbf{n} + \frac{g_r G^2 \rho}{\mu U} g$$

and this expression may be expanded:

$$\begin{aligned} & \frac{\epsilon^2 \dot{g}^2}{1 + \epsilon^2 \dot{g}^2} \left( 2 \frac{\partial v_r}{\partial r} - \frac{G}{\mu U} \bar{p} \right) - \frac{1}{1 + \epsilon^2 \dot{g}^2} \left( 2 \frac{\partial v_z}{\partial z} - \frac{G}{\mu U} \bar{p} \right) - 2 \frac{\epsilon \dot{g}}{1 + \epsilon^2 \dot{g}^2} \left( \epsilon \frac{\partial v_z}{\partial r} + \frac{1}{\epsilon} \frac{\partial v_r}{\partial z} \right) \\ &= \frac{\gamma \epsilon^2}{\mu U} \left[ \frac{\dot{g}}{r(1 + \epsilon^2 \dot{g}^2)^{\frac{1}{2}}} + \frac{\ddot{g}}{(1 + \epsilon^2 \dot{g}^2)^{\frac{3}{2}}} \right] + \frac{g_r G^2 \rho}{\mu U} g \end{aligned} \quad (B4)$$

A scaling for pressure has yet to be determined. The characteristic pressure scale,  $p_c$ , will take the form  $p_c = \frac{\mu U}{G \epsilon^q}$ . The exponent  $q$  must be determined from the governing equations.

We will assume the following regular asymptotic expansions

$$v_r = \sum_{j=0}^{\infty} \epsilon^j v_r^{(j)} \quad (B5a)$$

$$v_z = \sum_{j=0}^{\infty} \epsilon^j v_z^{(j)} \quad (B5b)$$

$$p = \frac{\bar{p}}{p_c} = \sum_{j=0}^{\infty} \epsilon^j p^{(j)} \quad (B5c)$$

No-slip at the planar wall gives

$$v_r^{(j)} = v_z^{(j)} = 0 \quad \text{at} \quad z = 0, \quad j \geq 0 \quad (B6)$$

Equation (B3) immediately gives the result that

$$\frac{\partial v_r^{(0)}}{\partial z} = 0 \quad (B7)$$

We now determine  $q$ . In particular, we may assume  $q \leq 2$ , otherwise equations (B1a,b) give  $p^{(0)} = \text{constant}$ . Pressure is indeterminate to within a constant, and so this is a trivial leading order result. The only choice for  $q$  which gives nontrivial zero order solutions satisfying equations (B1a, b, c), (B6) and (B7) is  $q = 2$ . Thus  $p_c = \frac{\mu U}{G\epsilon^2}$ .

With this pressure scaling, equations (B1a, b) become

$$\frac{\partial \bar{p}}{\partial r} = \epsilon^2 \frac{\partial}{\partial r} \left( \frac{1}{r} \frac{\partial r v_r}{\partial r} \right) + \frac{\partial^2 v_r}{\partial z^2} \quad (\text{B8a})$$

$$\frac{\partial \bar{p}}{\partial z} = \frac{\epsilon^4}{r} \frac{\partial}{\partial r} \left( r \frac{\partial v_z}{\partial r} \right) + \epsilon^2 \frac{\partial^2 v_z}{\partial z^2} \quad (\text{B8b})$$

Using the assumed expansions for pressure and velocity (B5a, b, c) in equation (B8a) leads to

$$\begin{aligned} \frac{\partial p^{(0)}}{\partial r} &= \frac{\partial^2 v_r^{(0)}}{\partial z^2} \\ \frac{\partial p^{(1)}}{\partial r} &= \frac{\partial^2 v_r^{(1)}}{\partial z^2} \end{aligned}$$

and for  $j \geq 2$

$$\frac{\partial p^{(j)}}{\partial r} = \frac{\partial}{\partial r} \left( \frac{1}{r} \frac{\partial r v_r^{(j-2)}}{\partial r} \right) + \frac{\partial^2 v_r^{(j)}}{\partial z^2}$$

Similarly for the  $z$ -momentum equations (B8b):

$$\begin{aligned} \frac{\partial p^{(0)}}{\partial z} &= \frac{\partial p^{(1)}}{\partial z} = 0 \\ \frac{\partial p^{(2)}}{\partial z} &= \frac{\partial^2 v_z^{(0)}}{\partial z^2} \\ \frac{\partial p^{(3)}}{\partial z} &= \frac{\partial^2 v_z^{(1)}}{\partial z^2} \end{aligned}$$

and for  $j \geq 4$ :

$$\frac{\partial p^{(j)}}{\partial z} = \frac{1}{r} \frac{\partial}{\partial r} \left( r \frac{\partial v_z^{(j-4)}}{\partial r} \right) + \frac{\partial^2 v_z^{(j-2)}}{\partial z^2}$$

Continuity gives for  $j \geq 0$

$$0 = \frac{1}{r} \frac{\partial r v_r^{(j)}}{\partial r} + \frac{\partial v_z^{(j)}}{\partial z}$$

Expanding equation (B3) for small  $\epsilon$  gives:

$$0 = \left[ -\epsilon + 2 \sum_{j=0}^{\infty} (-1)^j \epsilon^{2j+3} \dot{g}^{2j+2} \right] \left( \sum_{k=0}^{\infty} \epsilon^k \left\{ \frac{\partial v_z^{(k)}}{\partial r} + \frac{\partial v_r^{(k+2)}}{\partial z} \right\} + \frac{1}{\epsilon^2} \frac{\partial v_r^{(0)}}{\partial z} + \frac{1}{\epsilon} \frac{\partial v_r^{(1)}}{\partial z} \right) \\ + 2 \sum_{j=0}^{\infty} \left( (-1)^j \epsilon^{2j+1} \dot{g}^{2j+1} \right) \sum_{k=0}^{\infty} \epsilon^k \left( \frac{\partial v_r^{(k)}}{\partial r} - \frac{\partial v_z^{(k)}}{\partial z} \right)$$

This equation gives the following results to  $O(1)$ ,  $O(\epsilon)$ ,  $O(\epsilon^2)$  and to  $O(\epsilon^3)$  respectively

$$\frac{\partial v_r^{(1)}}{\partial z} = 0 \\ -\frac{\partial v_z^{(0)}}{\partial r} - \frac{\partial v_r^{(2)}}{\partial z} + 2\dot{g} \frac{\partial v_r^{(0)}}{\partial r} - 2\dot{g} \frac{\partial v_z^{(0)}}{\partial z} = 0 \\ -\left( \frac{\partial v_z^{(1)}}{\partial r} + \frac{\partial v_r^{(3)}}{\partial z} \right) + 2\dot{g} \left( \frac{\partial v_r^{(1)}}{\partial r} - \frac{\partial v_z^{(1)}}{\partial z} \right) = 0 \\ -\frac{\partial v_r^{(4)}}{\partial z} - \frac{\partial v_z^{(2)}}{\partial r} + 2\dot{g}^2 \left( \frac{\partial v_z^{(0)}}{\partial r} + \frac{\partial v_r^{(2)}}{\partial z} \right) + 2\dot{g} \left( \frac{\partial v_r^{(2)}}{\partial r} - \frac{\partial v_z^{(2)}}{\partial z} \right) \\ -2\dot{g}^3 \left( \frac{\partial v_r^{(0)}}{\partial r} - \frac{\partial v_z^{(0)}}{\partial z} \right) = 0$$

One additional scale is yet to be determined. We have assumed  $\bar{v}_z$  is scaled with  $U$ , but have left  $U$  unspecified. We did not use boundary condition (4) to determine the scaling for pressure. This boundary condition provides the necessary information to determine  $U$ . Examining this boundary condition indicates that for  $p^{(0)}$  to be non-trivial (non-constant) necessarily one or both of the terms  $\alpha_1 = \frac{\gamma \epsilon^2}{\mu U}$  and  $\beta_1 = \frac{G^2 g_r \rho}{\mu U} = 3\epsilon^2 \frac{R^2}{a^2} \frac{U_\infty}{U}$  must be of order  $\frac{1}{\epsilon^2}$  ( $U_\infty = \frac{1}{3} \frac{g_r \rho a^2}{\mu}$  is the steady velocity of a spherical bubble of equivalent volume radius  $a$  moving in the absence of a wall due to gravity). Three cases arise. Defining  $M = \frac{\beta_1}{\alpha_1} = 3 \frac{R^2}{a^2} C a_\infty$  where  $C a_\infty = \frac{\mu U_\infty}{\gamma}$  then

**Case 1**  $M \ll 1$

This balance indicates that gravity is negligible compare to surface tension. In particular,  $\alpha_1 = O(\frac{1}{\epsilon^2})$  and this determines  $U = \frac{\gamma \epsilon^4}{\mu}$ .

**Case 2**  $M \gg 1$

Surface tension effects are negligible compared to gravity effects. Thus,  $\beta_1 = O(\frac{1}{\epsilon^2})$  and this determines  $U = 3\epsilon^4 \frac{R^2}{a^2} U_\infty$ .

**Case 3**  $M = O(1)$

The effects due to gravity are of the same order as the effects due to surface tension. For convenience, we set  $U = \frac{\gamma\epsilon^4}{\mu}$

All three cases may be conveniently considered at once in the following analysis. First, we define  $\beta = \epsilon^2\beta_1$  and  $\alpha = \epsilon^2\alpha_1$ . Then case 1 corresponds to  $\beta = 0, \alpha = 1$ . Case 2 corresponds to  $\beta = 1, \alpha = 0$ . While, case 3 is obtained by setting  $\beta = M, \alpha = 1$ .

The normal stress balance at the interface becomes:

$$\begin{aligned} & \sum_{j=0}^{\infty} (-1)^j \epsilon^{2j+2} \dot{g}^{2j+2} \left( 2 \sum_{k=0}^{\infty} \epsilon^k \frac{\partial v_r^{(k)}}{\partial r} - \frac{1}{\epsilon^2} \sum_{k=0}^{\infty} \epsilon^k p^{(j)} \right) \\ & + \sum_{j=0}^{\infty} (-1)^j \epsilon^{2j} \dot{g}^{2j} \left( 2 \sum_{k=0}^{\infty} \epsilon^k \frac{\partial v_z^{(k)}}{\partial z} - \frac{1}{\epsilon^2} \sum_{k=0}^{\infty} \epsilon^k p^{(k)} \right) \\ & - 2 \sum_{j=0}^{\infty} (-1)^j \epsilon^{2j+2} \dot{g}^{2j+1} \sum_{k=0}^{\infty} \epsilon^k \left( \frac{\partial v_z^{(k)}}{\partial r} + \frac{\partial v_r^{(k+2)}}{\partial z} \right) \\ & = \frac{1}{\epsilon^2} \left( -\beta g + \alpha \left( \frac{\dot{g}}{r} + \ddot{g} \right) \right) + \\ & \quad \alpha \left( -\frac{1}{2} \frac{\dot{g}^3}{r} - \frac{3}{2} \dot{g}^2 \ddot{g} \right) \\ & \quad + \epsilon^2 \alpha \left( \frac{3}{4} \frac{\dot{g}^5}{r} + \frac{15}{4} \dot{g}^4 \ddot{g} \right) \\ & \quad + \epsilon^4 \alpha \left( -\frac{15}{8} \frac{\dot{g}^7}{r} - \frac{105}{8} \dot{g}^6 \ddot{g} \right) + O(\epsilon^6) \end{aligned}$$

Balancing terms to orders  $O(\epsilon^{-2}), O(\epsilon^{-1}), O(1), O(\epsilon)$  and  $O(\epsilon^2)$  respectively, we find

$$\begin{aligned} p^{(0)}(r) &= -\alpha \left( \frac{\dot{g}}{r} + \ddot{g} \right) - \beta g \\ p^{(1)} &= 0 \end{aligned}$$

$$p^{(2)} - 2\frac{\partial v_z^{(0)}}{\partial z} = \alpha\left(\frac{1}{2}\frac{\dot{g}^3}{r} + \frac{3}{2}\dot{g}^2\ddot{g}\right)$$

$$p^{(3)} = 2\frac{\partial v_z^{(1)}}{\partial z} + 2\dot{g}^2 p^{(1)}$$

$$p^{(4)} = -2\dot{g}\left(\frac{\partial v_z^{(0)}}{\partial r} + \frac{\partial v_r^{(2)}}{\partial z}\right) + 2\frac{\partial v_z^{(2)}}{\partial z} + 2\dot{g}^2\left(\frac{\partial v_r^{(0)}}{\partial r} - \frac{\partial v_z^{(0)}}{\partial z}\right)$$

All of the necessary relations are now determined. We may easily solve the resulting systems to first order.

$$v_z^{(0)} = -\frac{z^3}{6}\frac{1}{r}\frac{d}{dr}\left(r\frac{dp^{(0)}}{dr}\right) + \frac{z^2}{2}\frac{1}{r}\frac{d}{dr}\left(rg\frac{dp^{(0)}}{dr}\right)$$

$$v_r^{(0)} = \frac{z^2}{2}\frac{dp^{(0)}}{dr} - zg\frac{dp^{(0)}}{dr}$$

$$p^{(0)}(r) = -\alpha\left(\frac{\dot{g}}{r} + \ddot{g}\right) - \beta g$$

For the case  $M = O(1)$ , higher order terms are easily calculated:

$$v_r^{(1)} = v_z^{(1)} = p^{(1)} = 0$$

$$v_r^{(2)} = -\frac{z^4}{12}\frac{d}{dr}\left(\frac{1}{r}\frac{d}{dr}\left(r\frac{dp^{(0)}}{dr}\right)\right) + \frac{z^3}{3}\frac{d}{dr}\left(\frac{1}{r}\frac{d}{dr}\left(rg\frac{dp^{(0)}}{dr}\right)\right) + \frac{z^2}{2}\frac{dH(r)}{dr} + zK(r)$$

$$v_z^{(2)} = \frac{z^5}{60}\frac{1}{r}\frac{d}{dr}\left(r\frac{d}{dr}\left(\frac{1}{r}\frac{d}{dr}\left(r\frac{dp^{(0)}}{dr}\right)\right)\right) - \frac{z^4}{12}\frac{1}{r}\frac{d}{dr}\left(r\frac{d}{dr}\left(\frac{1}{r}\frac{d}{dr}\left(rg\frac{dp^{(0)}}{dr}\right)\right)\right) \\ - \frac{z^3}{6}\frac{1}{r}\frac{d}{dr}\left(r\frac{dH}{dr}\right) - \frac{z^2}{2}\frac{1}{r}\frac{d}{dr}\left(r\frac{dK}{dr}\right)$$

$$p^{(2)} = \frac{-1}{2}(z^2 + g^2)\frac{1}{r}\frac{d}{dr}\left(r\frac{dp^{(0)}}{dr}\right) + (z + g)\frac{1}{r}\frac{d}{dr}\left(rg\frac{dp^{(0)}}{dr}\right) + \alpha\left(\frac{1}{2}\frac{\dot{g}^3}{r} + \frac{3}{2}\dot{g}^2\ddot{g}\right)$$

$$H(r) = \frac{-1}{2}\frac{g^2}{r}\frac{d}{dr}\left(r\frac{dp^{(0)}}{dr}\right) + \frac{g}{r}\frac{d}{dr}\left(rg\frac{dp^{(0)}}{dr}\right) \\ + \alpha\left(\frac{1}{2}\frac{\dot{g}^3}{r} + \frac{3}{2}\dot{g}^2\ddot{g}\right)$$

$$K(r) = -3\frac{\partial v_z^{(0)}(r, g)}{\partial r} + 2\dot{g}\left(\frac{\partial v_r^{(0)}(r, g)}{\partial r} - \frac{\partial v_z^{(0)}(r, g)}{\partial z}\right) - g\frac{dH}{dr}$$

$$\begin{aligned}
 K(r) &= -\frac{3}{2}g^3 \left( \frac{d}{dr} \left( \frac{1}{r} \frac{d}{dr} \left( r \frac{dp^{(0)}}{dr} \right) \right) \right) \\
 &\quad - 7g^2 \dot{g} \frac{d^2 p^{(0)}}{dr^2} - \left( \frac{7}{2} \frac{g^2 \dot{g}}{r} + 5g\dot{g}^2 \right) \frac{dp^{(0)}}{dr} \\
 &\quad - \alpha \left( \frac{3}{2} \frac{g\dot{g}^2 \ddot{g}}{r} - \frac{1}{2} \frac{g\dot{g}^3}{r^2} + \frac{3}{2} g\dot{g}^2 (\ddot{g}) + 3g\dot{g}\ddot{g}^2 \right) \\
 p^{(3)} &= v_r^{(3)} = v_z^{(3)} = 0
 \end{aligned}$$

And for ( $j \geq 4$ ):

$$\begin{aligned}
 p^{(j)} &= \frac{\partial v_z^{(j-2)}}{\partial z} + \int_0^z \frac{1}{r} \frac{\partial}{\partial r} \left( r \frac{\partial v_z^{(j-4)}}{\partial r} \right) dz + \Pi_j(r) \\
 v_r^{(j)} &= zV_j(r) + \frac{z^2}{2} \dot{\Pi}_j(r) + \int_0^z \frac{\partial v_z^{(j-2)}}{\partial r} dz \\
 &\quad + \int_0^z \int_0^\phi \int_0^\psi \frac{\partial}{\partial r} \left( \frac{1}{r} \frac{\partial}{\partial r} \left( r \frac{\partial v_z^{(j-4)}}{\partial r} (r, \xi) \right) \right) d\xi d\psi d\phi \\
 v_z^{(j)} &= - \int_0^z \frac{1}{r} \frac{\partial}{\partial r} \left( r v_r^{(j)} \right) dz
 \end{aligned}$$

The functions  $\Pi_j(r)$  and  $V_j(r)$  are determined by the conditions at the interface. In particular to  $O(\epsilon^{j-2})$  in the normal stress balance the term  $p^{(j)}$  occurs and all other  $O(\epsilon^{j-2})$  terms have indices less than  $j$ . Thus  $\Pi_j$ , and consequently  $p^{(j)}$  are determined by this equation and the solutions at previous orders. Note that

$$\frac{\partial v_r^{(j)}}{\partial z} = V_j(r) + \frac{\partial v_z^{(j-2)}}{\partial r} + \int_0^z \frac{\partial p^{(j)}}{\partial r} dz$$

The tangential stress balance to  $O(\epsilon^{j-1})$  contains the term  $\frac{\partial v_r^{(j)}}{\partial z}$  and all other terms have indices less than  $j$ . Thus, this equation determines  $V_j$  in terms of previous order solutions. It is easily seen that  $j^{th}$  order pressures and velocities for  $j$  odd are zero in this expansion.

For the extreme cases of  $M \ll 1$  and  $M \gg 1$  some knowledge of the size of  $M$  relative to  $\epsilon$  is required. For  $M \ll 1$ ,  $U = \frac{\gamma\epsilon^4}{\mu}$

$$p^{(0)}(r) = -\left(\frac{\dot{g}}{r} + \bar{g}\right)$$

and if  $M = O(\epsilon^\psi)$  then for  $\psi > k \geq 0$  the above expansion will be valid for  $j = 0, 1, \dots, k$ .

Similarly, for  $M \gg 1$ ,  $U = 3\epsilon^4 \frac{R^2}{a^2} U_\infty$

$$p^{(0)}(r) = -g$$

and if  $\frac{1}{M} = O(\epsilon^\psi)$  then for  $\psi > k \geq 0$  the above expansion will be valid for  $j = 0, 1, \dots, k$ .

In the context of the quasi-steady assumption, these velocities and pressures are assumed to apply instantaneously and may be used to deform the film region of the interface. The film region of the interface is given by the locus of points  $\bar{g}(r) - \bar{z} = 0$ . Necessarily the convected derivative of the function  $\bar{g}(r) - \bar{z} = 0$  must be zero, thus

$$0 = \frac{\partial \bar{g}}{\partial t} + \bar{v}_r \frac{\partial \bar{g}}{\partial \bar{r}} - \bar{v}_z$$

Defining the characteristic time  $t_c = \frac{G}{U}$  gives

$$0 = \frac{\partial g}{\partial t} + v_r \dot{g} - v_z$$

Employing the zero order solution:

$$\begin{aligned} -\frac{\partial g}{\partial t} &= -\beta g^2 \left( \dot{g}^2 + \frac{g\dot{g}}{3r} + \frac{1}{3}g\ddot{g} \right) + \alpha g^2 \dot{g} \left( (\ddot{g}) + \frac{\ddot{g}}{r} - \frac{\dot{g}}{r^2} \right) \\ &+ \frac{\alpha g^3}{3} \left( (\ddot{g}) + \frac{2(\ddot{g})}{r} - \frac{\ddot{g}}{r^2} + \frac{\dot{g}}{r^3} \right) + O(\epsilon^2) \end{aligned} \quad (B9)$$

Higher order corrections to this equation are readily obtained from higher order velocity results.

## Discussion

For the case  $M \ll 1$  (i.e.  $\beta = 0$  and  $\alpha = 1$ ), equation (B9) exactly matches the results of Hartland (1969). Unfortunately, Hartland used this equation to study *drops* for which the parameter  $M$  was  $O(1)$ . Similarly, Lin and Slattery (1982) employed Hartland's ( $M \ll 1$ ) result to study bubbles (or "fully mobile" drops). They employed the results of Derjaguin and Kussakov (1939) which implicitly assume  $M = O(1)$ . Specifically, Derjaguin and Kussakov (1939) studied the approach of small air bubbles in water toward a glass plate and showed that a dimple is formed in the base of the bubble with a barrier ring at a radius

$$R = \left(\frac{3\bar{V}_b}{4\pi}\right)^{\frac{2}{3}} \left(\frac{2\rho g r}{3\gamma}\right)^{\frac{1}{2}}$$

Where  $\bar{V}_b$  is the bubble volume. Using this expression to determine  $M$  yields  $M = \frac{3}{2}$ . This indicates that both gravity and surface tension effects are equally important for the cases considered. Lin and Slattery (1982) used the results of Derjaguin and Kussakov to determine fundamental geometrical parameters in their analysis.

The present results, with gravitational effects included, are new. In addition, the higher order corrections are new. The scaling arguments leading to these results are concise and straightforward in contrast to the scaling arguments that have appeared in the literature (i.e. Lin and Slattery (1982) who use a small Reynolds number argument to neglect various terms in Stokes equation).

There are several deceptive aspects to the solution obtained. First, the thin-film solution contains *no* constants or free parameters, *to any order* in  $\epsilon$ . This *suggests* that the thin film solution is *entirely* determined and details at the edge of the film region are inconsequential. This is *not* the case. Equation (B9) requires derivatives of  $g(r)$  to at least the fourth order at the edge of the film. Although an initial film configuration will allow determination of these derivatives at the initial instant, subsequent shape evolution will critically depend on how these derivatives change in time.

Where is the edge of the film? The preceding analysis has assumed that  $g(r)$  is expandable in a Taylor series in small  $\epsilon$ . This expansion will decay rapidly in convergence when curvature of the interface becomes  $O(1)$ . In particular, the edge of the film region is typified by  $O(1)$  curvature and *rapid* increase in  $g(r)$  with  $r$ . Chapter II has demonstrated that drops with  $O(1)$  capillary number show significant variation in geometrical detail at the edge of the dimple region. The same effect is expected for bubbles. A detailed examination of the edge of the dimpled region is indicated. The authors are currently attempting a detailed theoretical analysis of the edge of the dimpled region.

What do these results indicate about the details of the interior region of the film? We have taken the approach that an initial film configuration will be provided and its evolution in time may then be analyzed via equation (B9). What does equation (B9) predict for simple starting configurations? Suppose, as an initial configuration, that the entire film region is flat (i.e.  $g(r) = 1$ ) In this case, *to all orders* in  $\epsilon$ , the pressures will be constant. Derivatives of the leading order pressure solution drive the velocities to all orders. As a consequence, *no motion* will occur in the film region. Similarly, in the interior of any region where the interface is locally flat, no motion will be predicted. It is possible that equation (B9) will predict  $O(1)$  velocity fields (we have scaled velocity in anticipation of  $O(1)$  velocity variation) when only minute deviations from a flat interface occur. This possibility is not only unappealing but seems unlikely as well.

Zero velocity for a nearly flat interface does not agree with the observations or predictions of Chapter II concerning the *initial formation* of a dimple for the drop case. Further, variation of pressure with  $z$  enters the inner solution to order  $\epsilon^2$ . Like velocity variation, the order  $\epsilon^2$  pressure variation in  $z$  will be non-zero only if the film is not flat. Further, this pressure correction is  $O(\epsilon^2)$  and is therefore small compared to the leading order pressure term (which contains no  $z$  pressure dependence). Once again, the obvious suggestion is that the ordering

of terms which arises by necessity in a lubrication based analysis is inappropriate in the earliest stages of dimple formation.

## References

- Ascoli, E.P., Dandy, D.S. & Leal, L.G. *Low-Reynolds number hydrodynamic interaction of a solid particle with a planar wall* submitted to *Int. J. Numer. Methods Fluids*.
- Bart, E. 1968 *Chem. Eng. Sci.* **23**,193.
- Blake, J.R. 1971 *Proc. Phil. Soc.* **70**, 303.
- Brenner, H. 1961 *Chem. Eng. Sci.* **16**, 242.
- Brenner, H. 1962 *J. Fluid Mech.* **12**, 35.
- Brenner, H. 1964 *J. Fluid Mech.* **18**, 144.
- Chi, B.K. 1986 PhD Thesis, California Institute of Technology, May 19.
- Cox, R.G. 1974 *Int. J. Multiphase Flow* **1**, 343.
- Cox, R.G. & Brenner, H. 1967 *J. Fluid Mech.* **28**, 391.
- Derjaguin B., and M. Kussakov, 1939 *Acta Physicochim.* **10**, 25.
- Dimitrov, D.S. & Ivanov, I.B. 1978 *J. Colloid Interface Sci.* **64**,97.
- Frankel, S.P. & Mysels, K.J. 1962 *J. Phys. Chem.* **66**,190.
- Geller, A.S., Lee, S.H. & Leal, L.G. 1986 *J. Fluid Mech.* **168**,27.
- Haberman, W. L. & Sayer, R. M. 1958 David Taylor Model Basin Report No. 1143, Washington, D. C.
- Hadamard, J. S. 1911 *C. R. Acad. Sci. (Paris)* **152**,1735.
- Hartland, S. 1967 *Chem. Eng. Sci.*, **22**,1675.
- Hartland, S. 1969 *Chem. Eng. Prog. Symp. Ser.*, No. 91 **65**,82.
- Hartland, S. & Robinson, J.D. 1977 *J. Colloid Interface Sci.* **60**,72.
- Jones, A.F. & Wilson, S.D.R. 1978 *J. Fluid Mech.* **87**,263.
- Kantorovich, L.V. & Krylov, V.I. 1963 *Approximate Methods of Higher Analysis*, Interscience.

- Ladyzhenskaya, O.A. 1963 *The Mathematical Theory of Viscous Incompressible Flow*, Gordon and Breach, New York.
- Lee, S.H. & Leal, L.G. 1982 *J. Colloid Interface Sci.* **87**, 81.
- Lin, C.Y. & Slattery, J.C. 1982 *AIChE Journal* **28**, 147.
- Odqvist, F.K.G. 1930 *Math. Z.* **32**, 329.
- Oseen, C.W. 1927 *Hydrodynamik*, Akademische Verlagsgesellschaft.
- Platikanov, D. 1964 *J. Phys. Chem.* **68**, 3619.
- Rallison, J.M. & Acrivos, A. 1978 *J. Fluid Mech.* **89**, 91.
- Rybczynski, W. 1911 *Bull. Acad. Sci. Cracovie (Ser. A)* **40**
- Wakiya, S. 1957 *J. Phys. Soc. Japan* **12**, 1130.
- Youngren, G.K. & Acrivos, A. 1975 *J. Fluid Mech.* **69**, 377.
- Youngren, G.K. & Acrivos, A. 1976 *J. Fluid Mech.* **76**, 433.

## Figure Captions

Figure 1: (a) Schematic of the problem. (b) An illustration of the quantities  $Z_{center}$ ,  $Z_{axis}$ ,  $Z_{min}$ , and  $\rho_{min}$ .

Figure 2: a)  $\square$  : numerical  $u_\rho$  calculations for a spherical shape with  $\lambda = 3$ ; Solid line is Hadamard-Rybczynski analytic results; b)  $\square$  : numerical  $u_z$  calculations for a spherical shape with  $\lambda = 3$ ; Solid line is Hadamard-Rybczynski analytic results; c)  $\square$  : numerical  $f_\rho$  calculations for a spherical shape with  $\lambda = 3$ ; Solid line is Hadamard-Rybczynski analytic results; d)  $\square$  : numerical  $f_z$  calculations for a spherical shape with  $\lambda = 3$ ; Solid line is Hadamard-Rybczynski analytic results.

Figure 3: Comparison with the experimental results of Hartland (1969) The left half of the figure corresponds to the numerical results for  $Ca = 1$ ,  $\lambda = 1$ , and  $Z_{axis} = 0.155$ . The right half of the figure is an experimental photograph for  $Ca = 1.358$ ,  $\lambda = 1.478$  and a  $Z_{axis}$  value between 0.153 and 0.128.

Figure 4: Evolution of drop shape for  $Ca = 0.3$  and  $\lambda = 0.3$ . The dimensionless time between shape curves is 1.

Figure 5: Evolution of drop shape for  $Ca = 1$  and  $\lambda = 0.3$ . The dimensionless time between shape curves is 1.

Figure 6: Evolution of drop shape for  $Ca = 3$  and  $\lambda = 0.3$ . The dimensionless time between shape curves is 1.

Figure 7: Evolution of drop shape for  $Ca = 0.3$  and  $\lambda = 1$ . The dimensionless time between shape curves is 1.

Figure 8: Evolution of drop shape for  $Ca = 1$  and  $\lambda = 1$ . The dimensionless time between shape curves is 1.

Figure 9: Evolution of drop shape for  $Ca = 3$  and  $\lambda = 1$ . The dimensionless time between shape curves is 1.

Figure 10: Evolution of drop shape for  $Ca = 0.3$  and  $\lambda = 3$ . The dimensionless time between shape curves is 1.

Figure 11: Evolution of drop shape for  $Ca = 1$  and  $\lambda = 3$ . The dimensionless time between shape curves is 1.

Figure 12: Evolution of drop shape for  $Ca = 3$  and  $\lambda = 3$ . The dimensionless time between shape curves is 1.

Figure 13: Drop configurations at the timestep immediately prior to dimpling.

Figure 14:  $Z_{min}$  vs.  $Z_{axis}$  for  $\lambda$  fixed at 1 and  $Ca$  varying. Solid line corresponds to  $Z_{min} = Z_{axis}$  (i.e. no dimpling). .....  $Ca = 0.3$ ; - - - -  $Ca = 1$ ; - - -  $Ca = 3$ .

Figure 15:  $\rho_{min}$  vs.  $Z_{axis}$  for  $\lambda$  fixed at 1 and  $Ca$  varying. Solid line corresponds to  $\rho_{min} = 0$  (i.e. no dimpling). .....  $Ca = 0.3$ ; - - - -  $Ca = 1$ ; - - -  $Ca = 3$ .

Figure 16:  $V_{center}$  vs.  $Z_{center}$  for  $\lambda$  fixed at 1 and  $Ca$  varying. .....  $Ca = 0.3$ ; - - - -  $Ca = 1$ ; - - -  $Ca = 3$ . Solid line corresponds to the results of Bart (1968) for a spherical drop ( $Ca = \infty$  limit).

Figure 17:  $Z_{min}$  vs.  $Z_{axis}$  for  $Ca$  fixed at 3 and  $\lambda$  varying. Solid line corresponds to  $Z_{min} = Z_{axis}$  (i.e. no dimpling). .....  $\lambda = 0.3$ ; - - - -  $\lambda = 1$ ; - - -  $\lambda = 3$ .

Figure 18:  $\rho_{min}$  vs.  $Z_{axis}$  for  $Ca$  fixed at 3 and  $\lambda$  varying. Solid line corresponds to  $\rho_{min} = 0$  (i.e. no dimpling). .....  $\lambda = 0.3$ ; - - - -  $\lambda = 1$ ; - - -  $\lambda = 3$ .

Figure 19:  $V_{center}$  vs.  $Z_{center}$  for  $Ca$  fixed at 1 and  $\lambda$  varying. .....  $\lambda = 0.3$ ; - - - -  $\lambda = 1$ ; - - -  $\lambda = 3$ . Solid line corresponds to the results of Brenner (1961) for a solid sphere ( $\lambda = \infty$  limit).

Figure 20: a) Velocity field for  $Ca = 1$ ,  $\lambda = 1$ ,  $Z_{center} = 0.615$ . The horizontal arrow below the wall corresponds in length to  $\frac{1}{10}U$  and thus indicates scale. Velocities are measured relative to an origin fixed on the wall.

b) As above, except velocities are measured relative to an origin fixed at the center of mass of the drop.

Figure 21: Velocity field for  $Ca = 0.3$ ,  $\lambda = 1$ ,  $Z_{center} = 0.787$ . The horizontal arrow below the wall corresponds in length to  $\frac{1}{10}U$  and thus indicates scale.

Figure 22: Velocity field for  $Ca = 3$ ,  $\lambda = 1$ ,  $Z_{center} = 0.477$ . a) The entire film. The horizontal arrow below the wall corresponds in length to  $\frac{1}{10}U$  and thus indicates scale. b) The central region of the film. The horizontal arrow below the wall corresponds in length to  $\frac{1}{100}U$  and thus indicates scale.

Figure 23: The  $\rho$ -component of velocity for  $Ca = 1$ ,  $\lambda = 1$ ,  $Z_{center} = 0.757$ . The next numerical timestep corresponds to the first formation of a dimple. The vertical line below the wall corresponds to the radial location at which the dimple initially forms. The horizontal arrow below the wall corresponds in length to  $\frac{1}{10}U$  and thus indicates scale.

Figure 24: The  $z$ -component of velocity for  $Ca = 1$ ,  $\lambda = 1$ ,  $Z_{center} = 0.757$ . The next numerical timestep corresponds to the first formation of a dimple. The vertical line below the wall corresponds to the radial location at which the dimple initially forms. The horizontal arrow below the wall corresponds in length to  $\frac{1}{10}U$  and thus indicates scale.

Figure 25: a) Pressure for  $Ca = 1$ ,  $\lambda = 1$ , and  $Z_{center} = 0.615$  plotted against radial distance. ....  $z = 0.01$ ; - - -  $z = 0.06$ ; - - -  $z = 0.12$ .  
b) The shape and  $z$ -values corresponding to a).

Figure 26: a) Pressure for  $Ca = 0.3$ ,  $\lambda = 1$ , and  $Z_{center} = 0.787$  plotted against radial distance. ....  $z = 0.01$ ; - - -  $z = 0.05$ ; - - -  $z = 0.087$ .  
b) The shape and  $z$ -values corresponding to a).

Figure 27: a) Pressure for  $Ca = 3$ ,  $\lambda = 1$ , and  $Z_{center} = 0.477$  plotted against radial distance. ....  $z = 0.01$ ; - - -  $z = 0.065$ ; - - -  $z = 0.11$ .  
b) The shape and  $z$ -values corresponding to a).

Figure 28: a) Pressure for  $Ca = 1$ ,  $\lambda = 1$ , and  $Z_{center} = 0.757$  plotted against radial distance. The next numerical timestep corresponds to the first formation of a dimple at  $\rho = 0.125$ . .....  $z = 0.01$ ; - - - -  $z = 0.1$ ; - - -  $z = 0.17$ . b) The shape and  $z$ -values corresponding to a).

Figure 29: Pressure for  $Ca = 1$ ,  $\lambda = 1$ , and  $\rho = 0.01$  plotted against vertical distance. Each curve corresponds to a different  $Z_{center}$  location. ....  $Z_{center} = 0.615$  ( $Z_{axis} = 0.1549$ ); - - - -  $Z_{center} = 0.6918$  ( $Z_{axis} = 0.1756$ ); - - -  $Z_{center} = 0.757$  ( $Z_{axis} = 0.1970$ ); .....  $Z_{center} = 1.320$  ( $Z_{axis} = 0.5221$ ); .....  $Z_{center} = 1.192$  ( $Z_{axis} = 1.028$ ).

Figure 30: Pressure for  $Ca = 1$ ,  $\lambda = 1$ , and  $\rho = 0.26$  plotted against vertical distance. Each curve corresponds to a different  $Z_{center}$  location. ....  $Z_{center} = 0.615$  ( $Z_{axis} = 0.1549$ ); - - - -  $Z_{center} = 0.6918$  ( $Z_{axis} = 0.1756$ ); - - -  $Z_{center} = 0.757$  ( $Z_{axis} = 0.1970$ ); .....  $Z_{center} = 1.320$  ( $Z_{axis} = 0.5221$ ); .....  $Z_{center} = 1.192$  ( $Z_{axis} = 1.028$ ).

Figure 31: Pressure for  $Ca = 1$ ,  $\lambda = 1$ , and  $\rho = 0.5$  plotted against vertical distance. Each curve corresponds to a different  $Z_{center}$  location. ....  $Z_{center} = 0.615$  ( $Z_{axis} = 0.1549$ ); - - - -  $Z_{center} = 0.6918$  ( $Z_{axis} = 0.1756$ ); - - -  $Z_{center} = 0.757$  ( $Z_{axis} = 0.1970$ ); .....  $Z_{center} = 1.320$  ( $Z_{axis} = 0.5221$ ); .....  $Z_{center} = 1.192$  ( $Z_{axis} = 1.028$ ).

## Appendix Figure Captions

Figure B 1: Schematic of the problem.

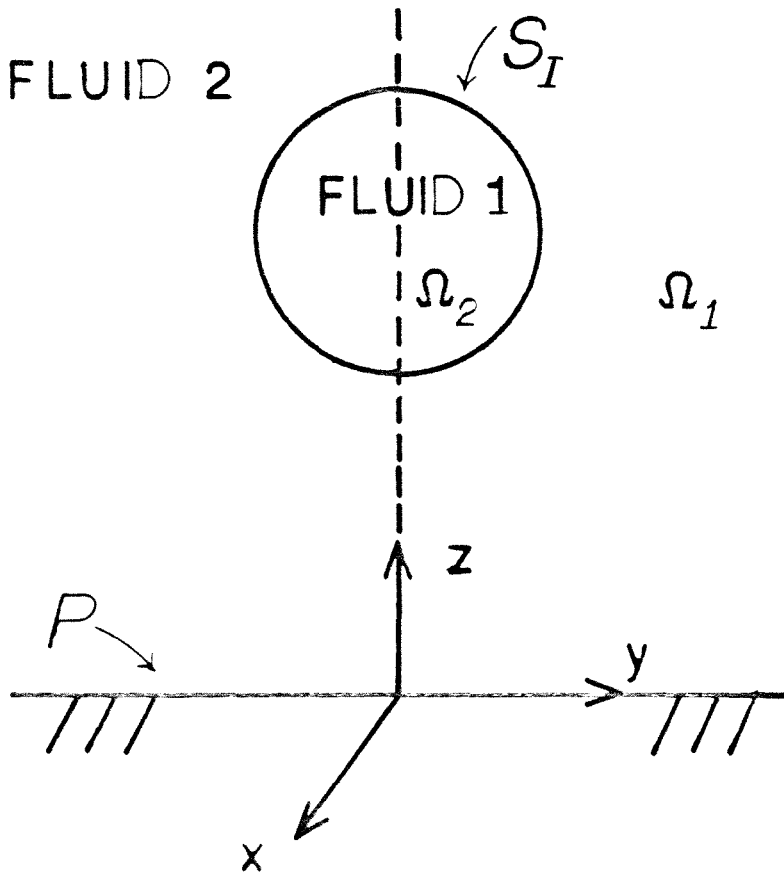


Figure 1(a)

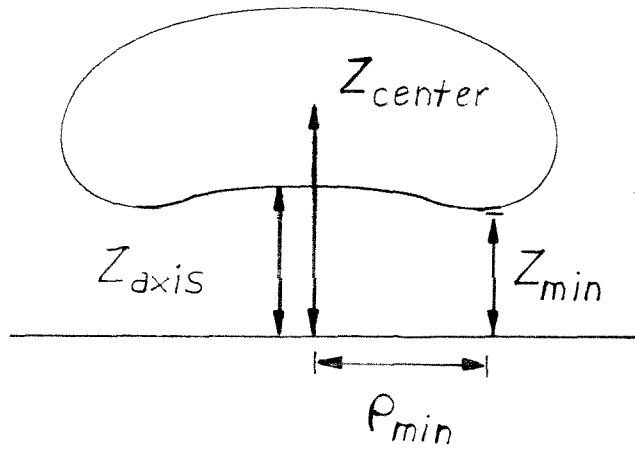


Figure 1(b)

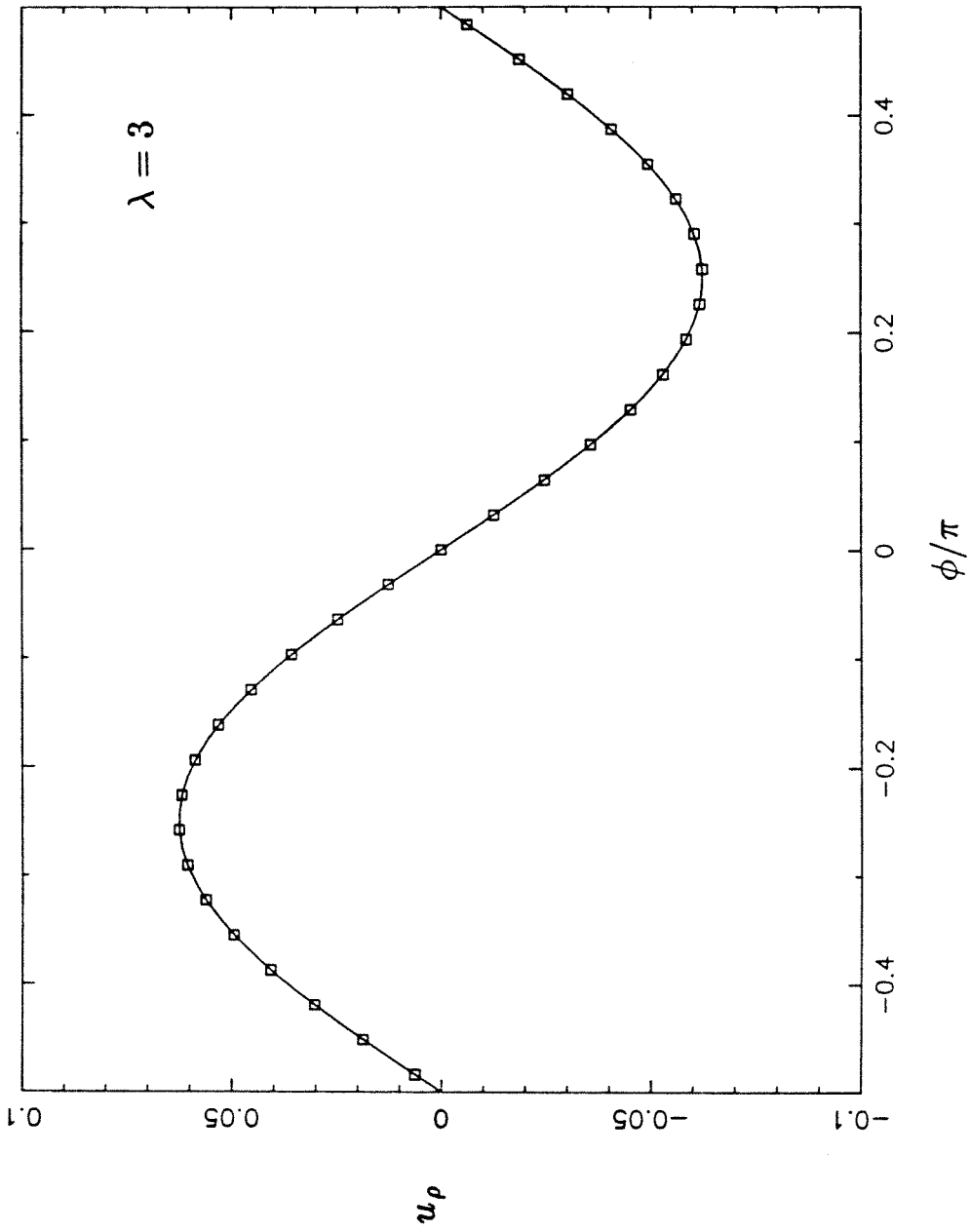


Figure 2 (a)

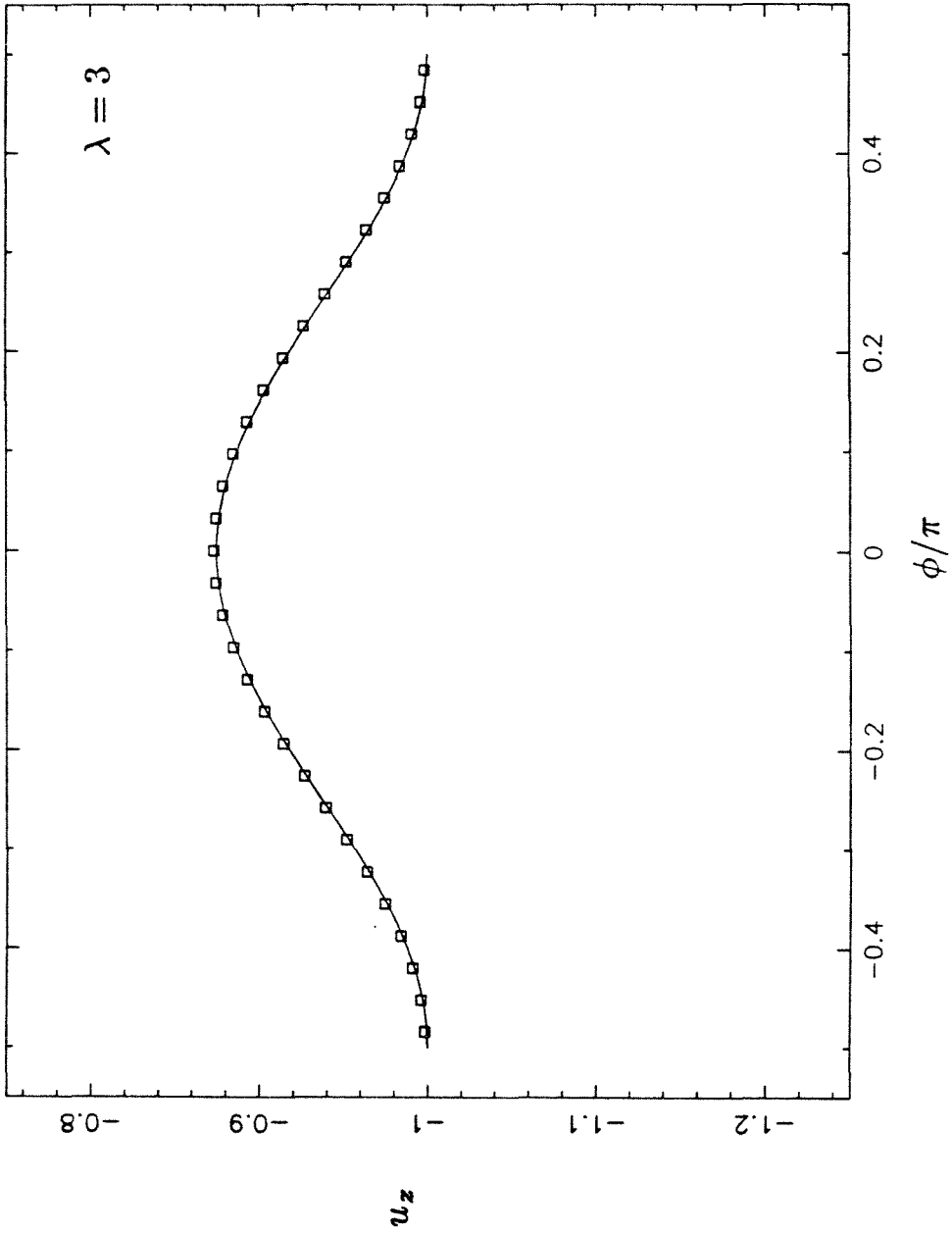


Figure 2 (b)

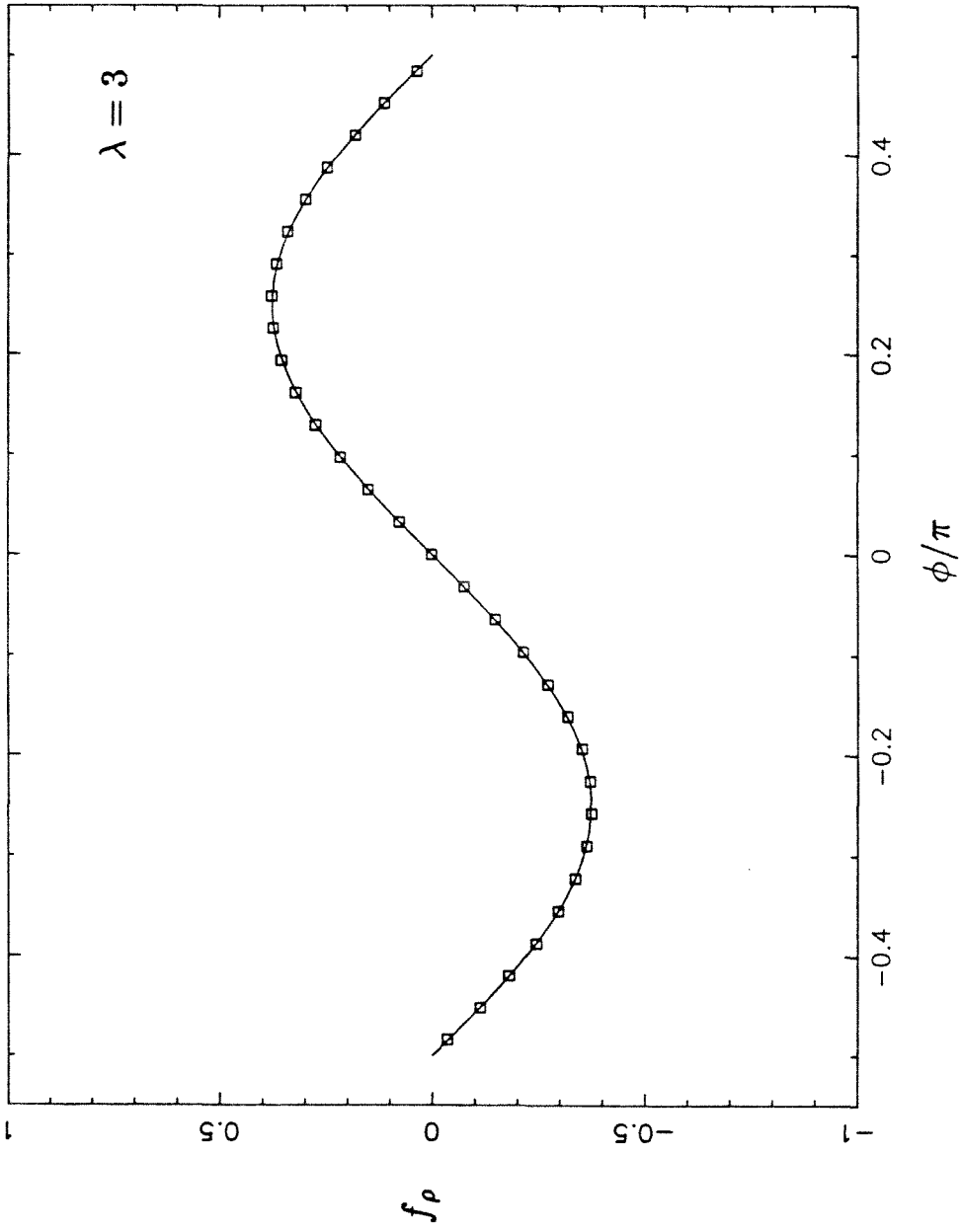


Figure 2(c)

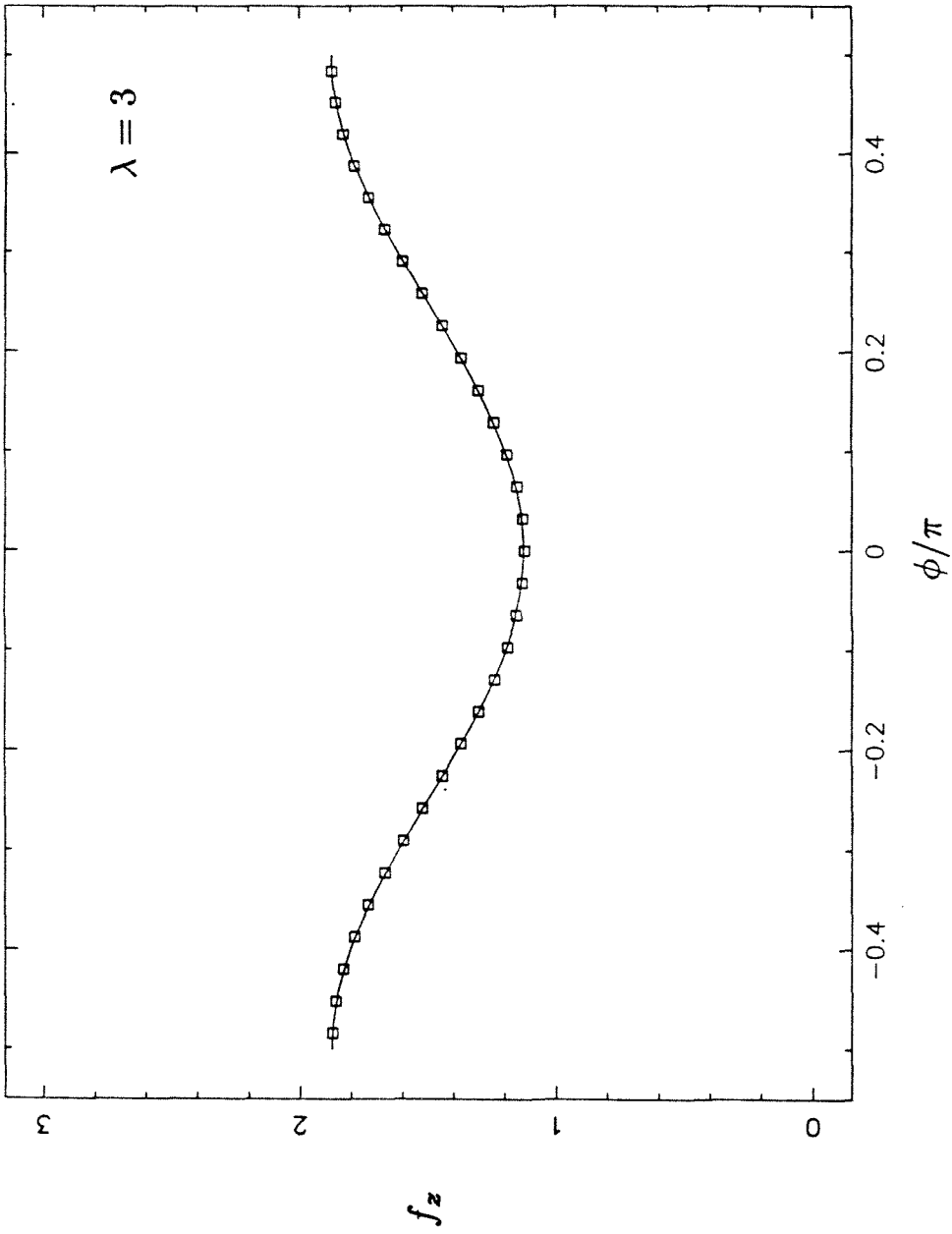


Figure 2(d)

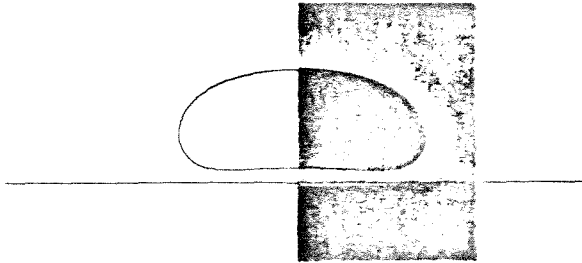


Figure 3

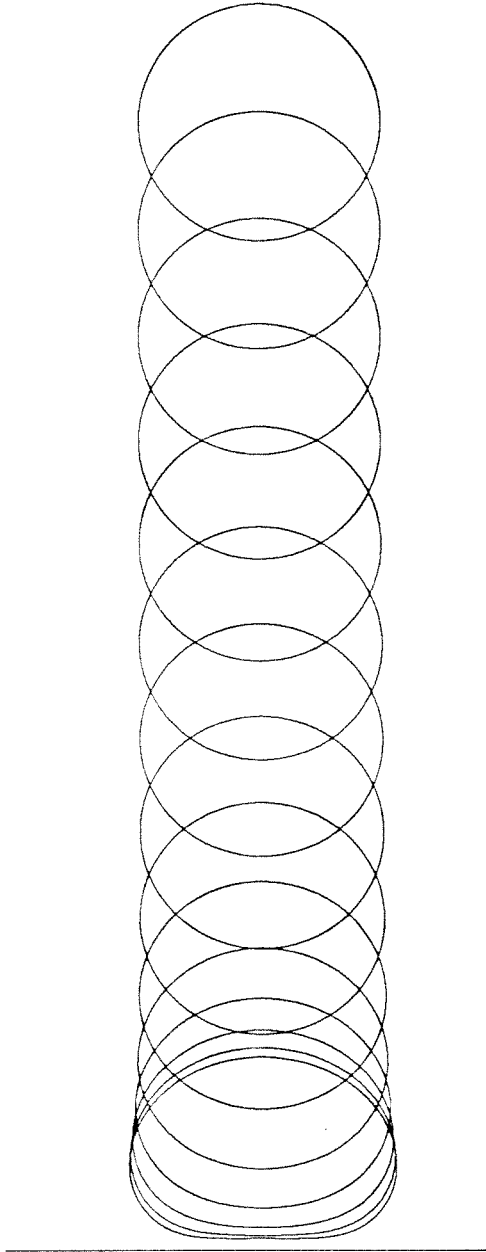


Figure 4

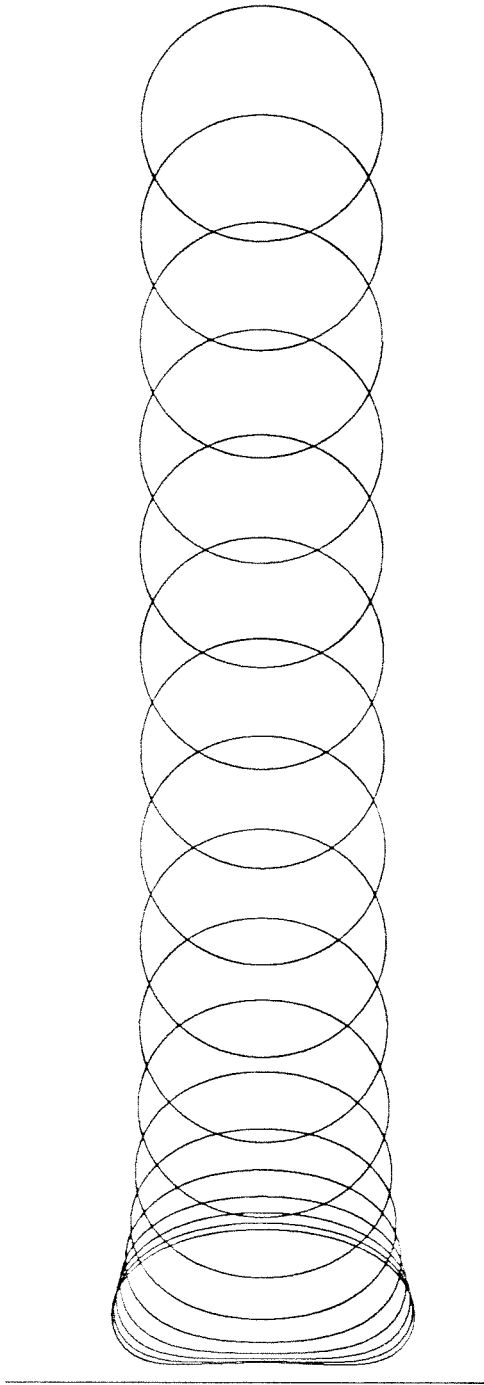


Figure 5

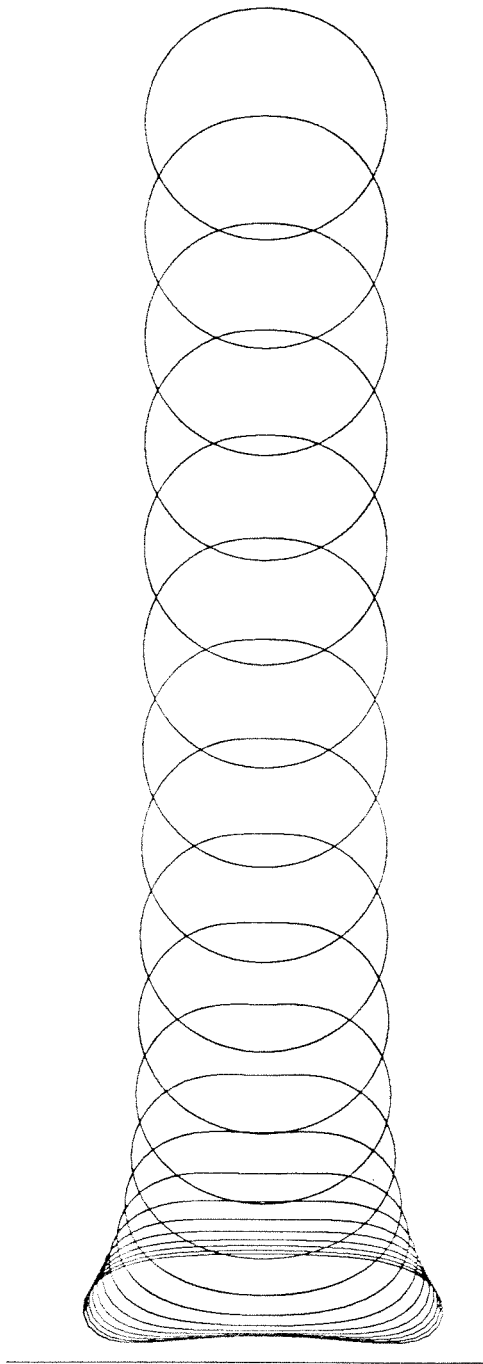


Figure 6

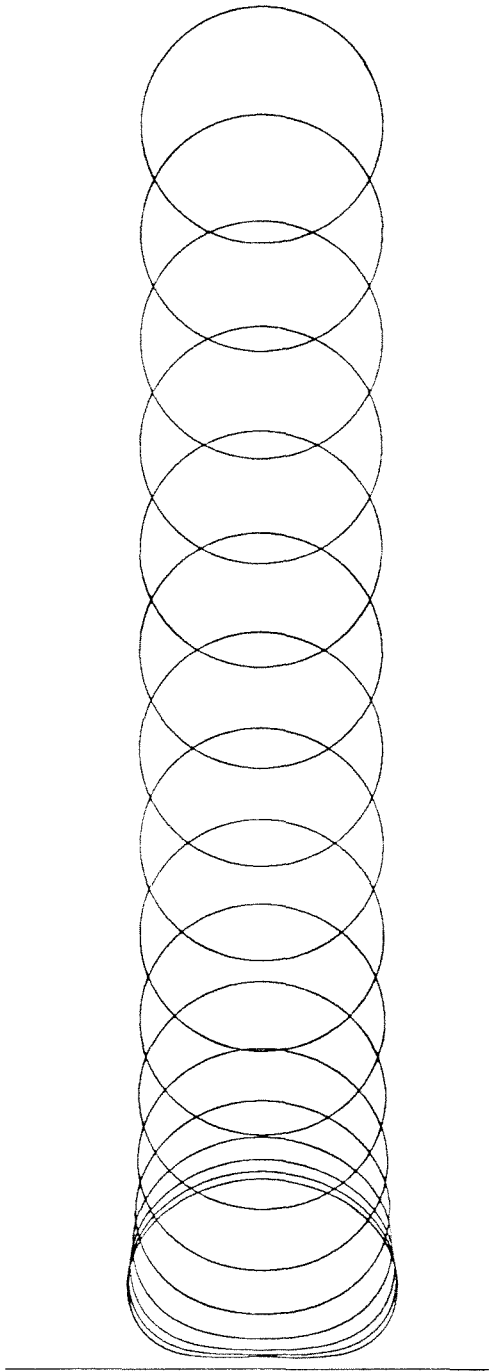


Figure 7

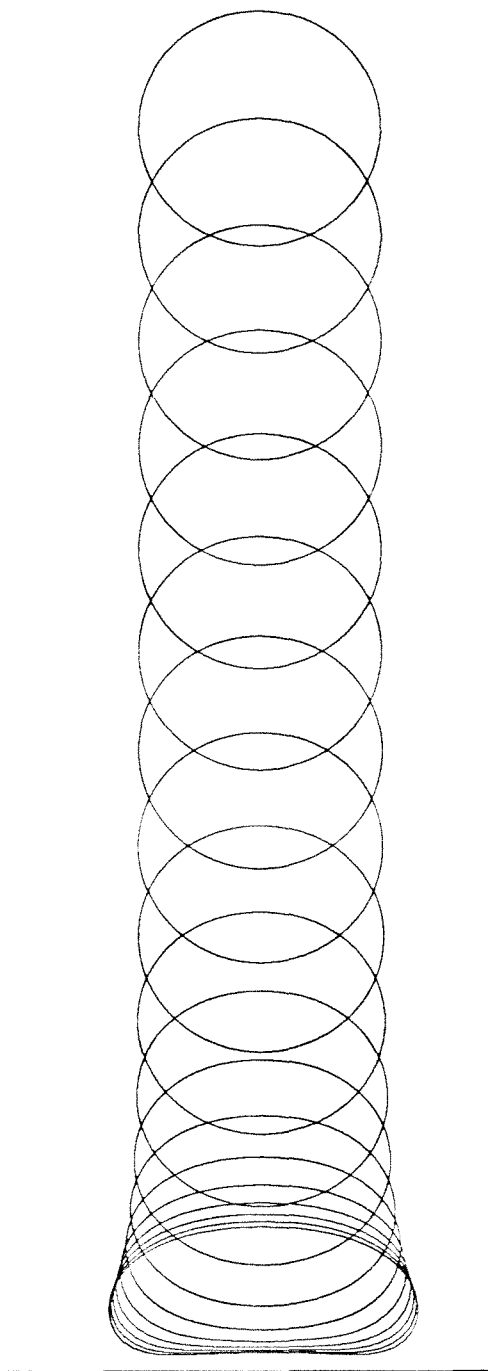


Figure 8

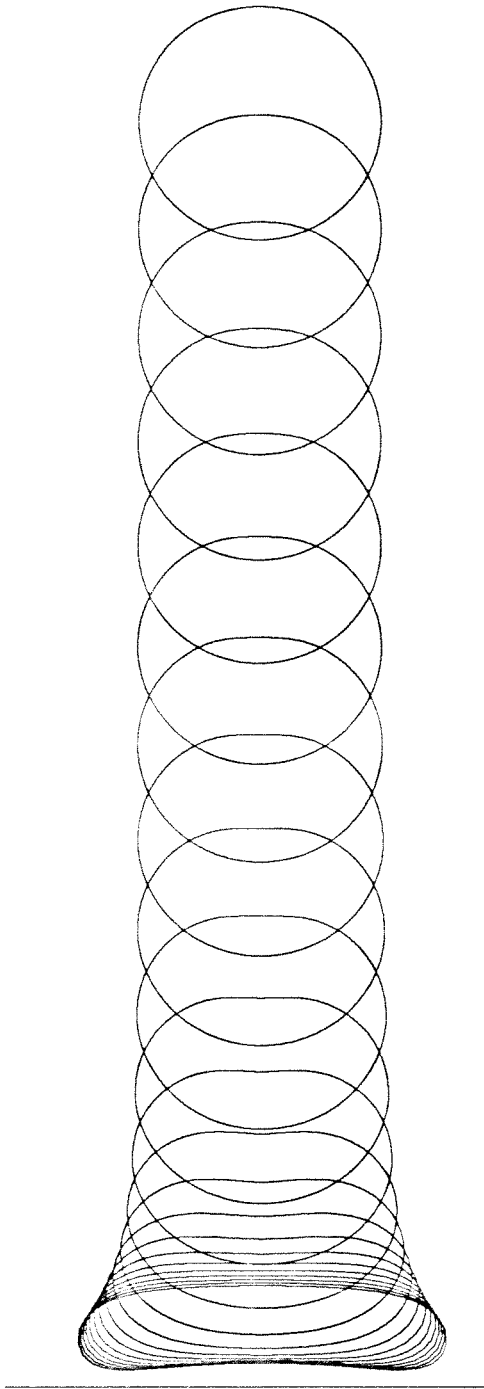


Figure 9

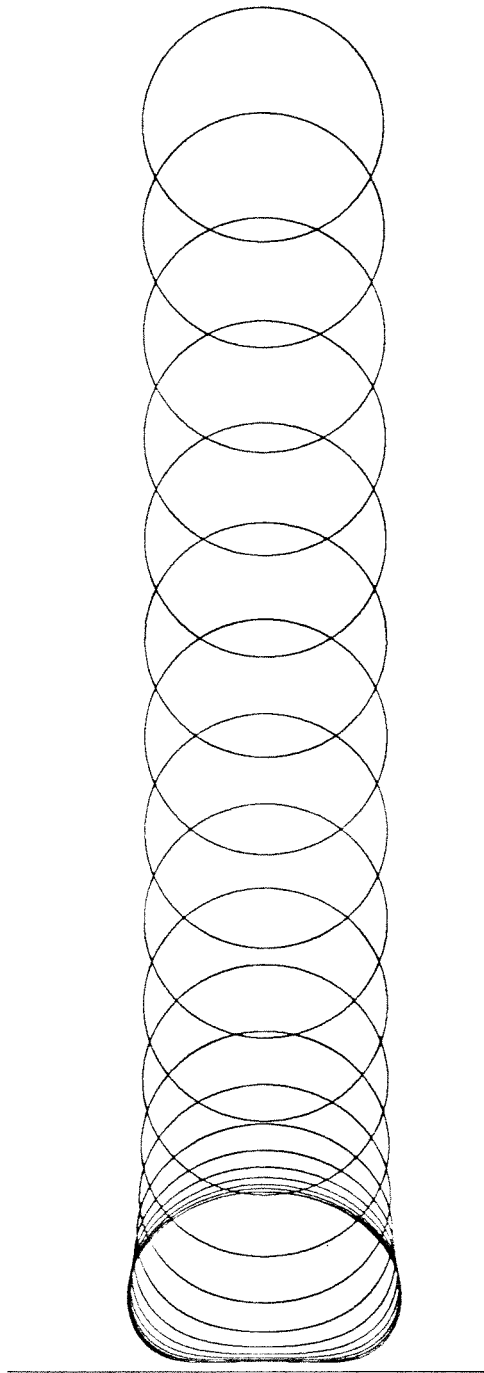
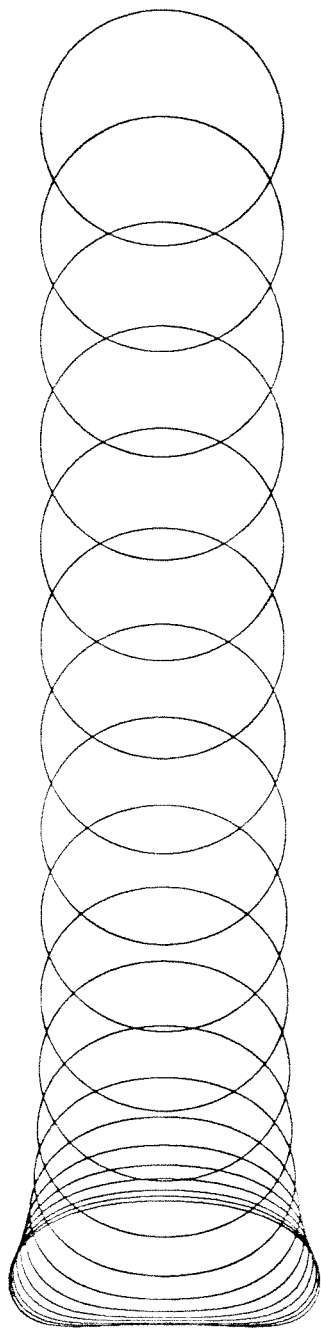


Figure 10



---

Figure 11

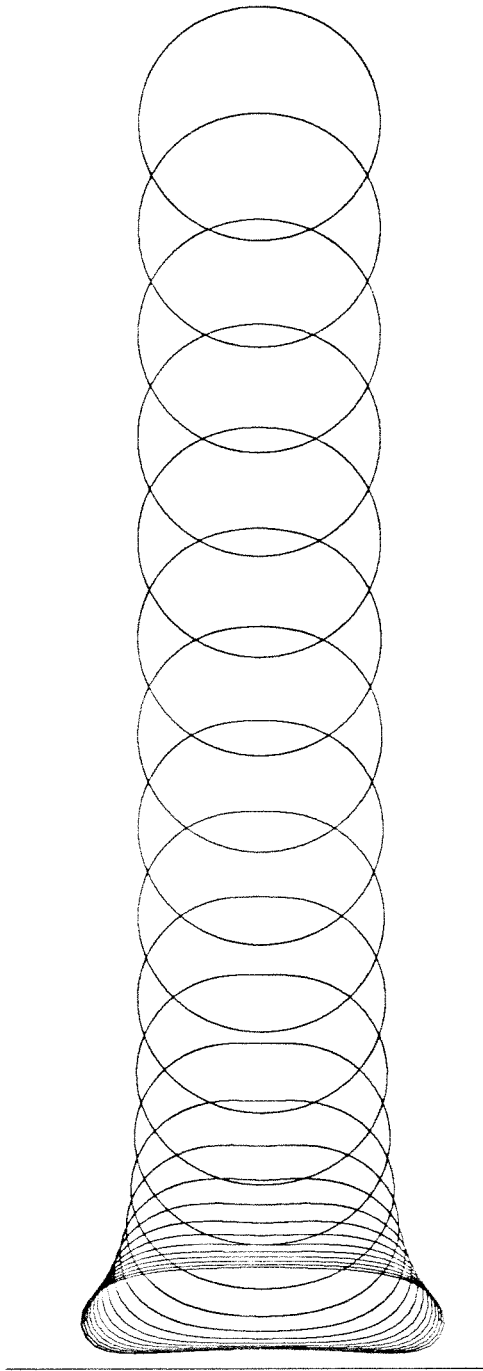
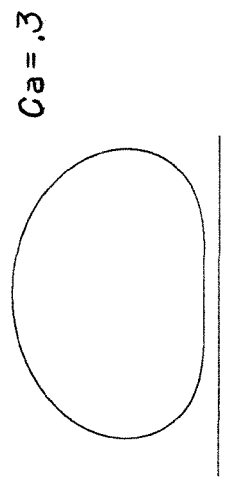
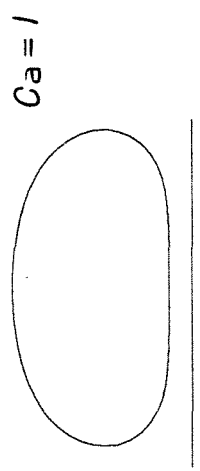
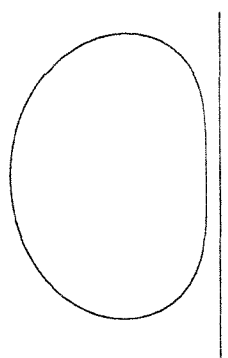
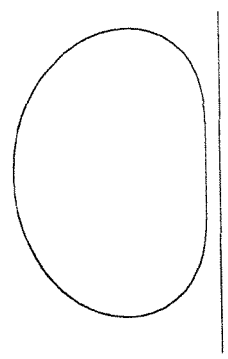


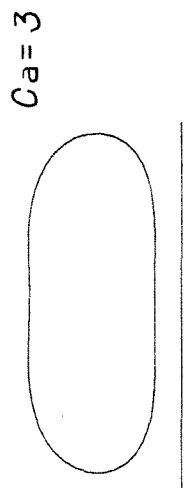
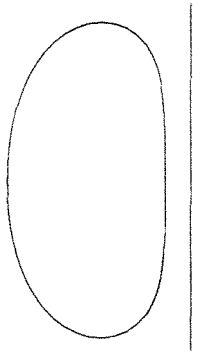
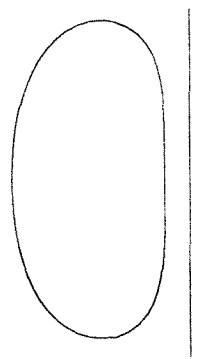
Figure 12



$\lambda = 3$



$\lambda = 3$



$\lambda = 3$

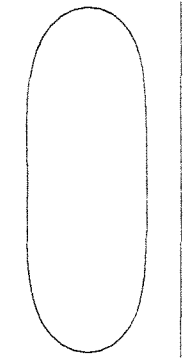
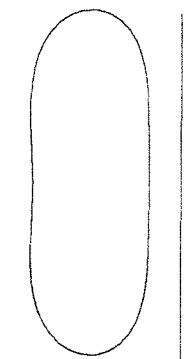


Figure 13

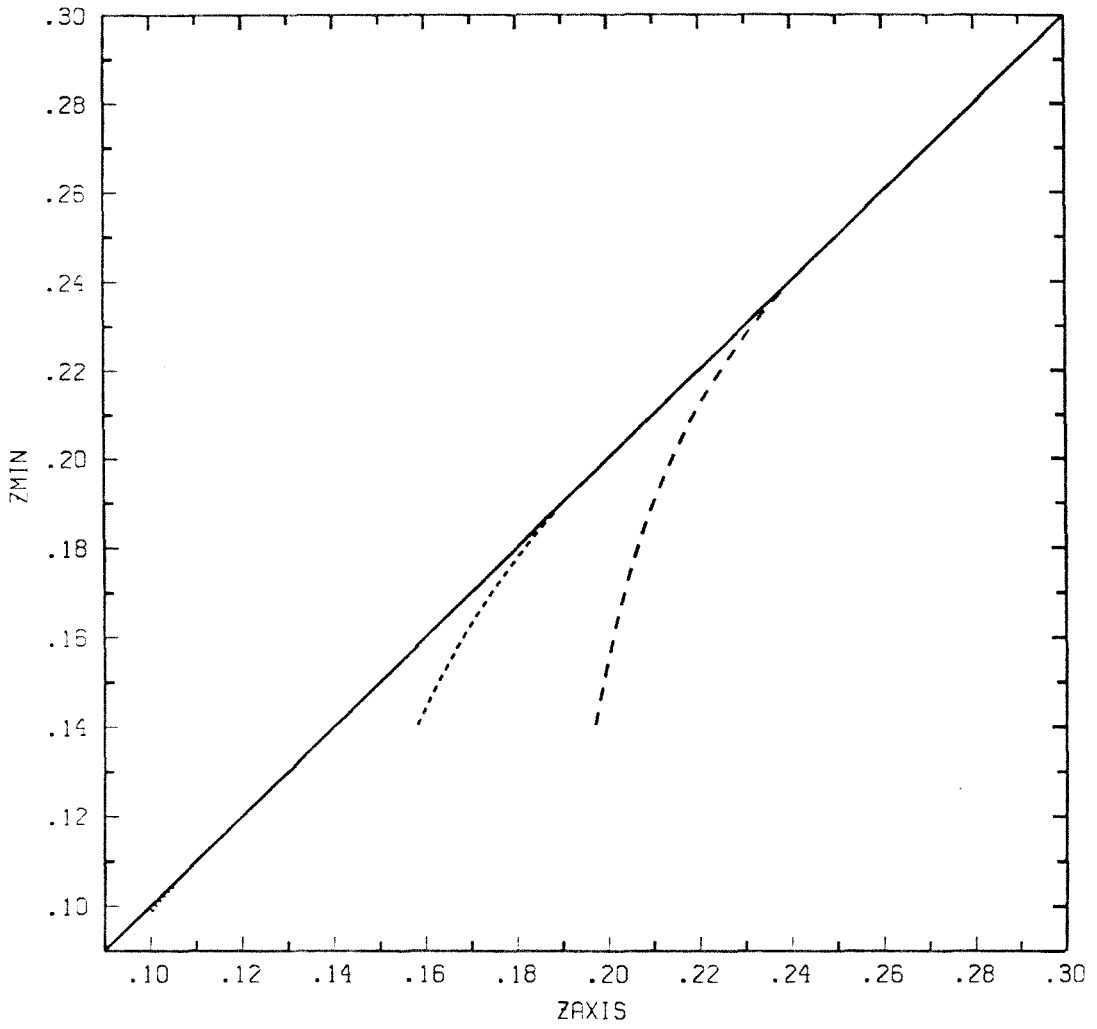


Figure 14

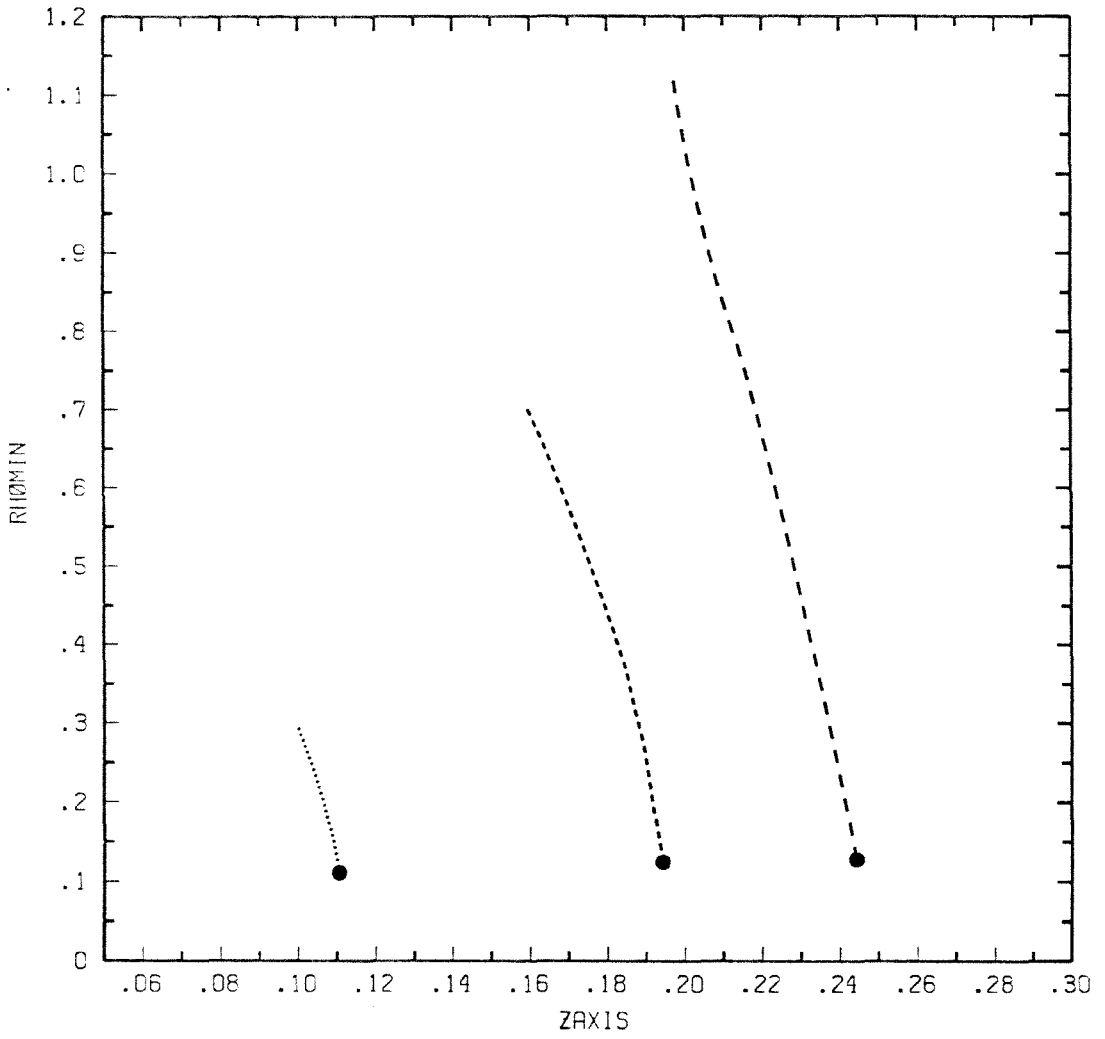


Figure 15

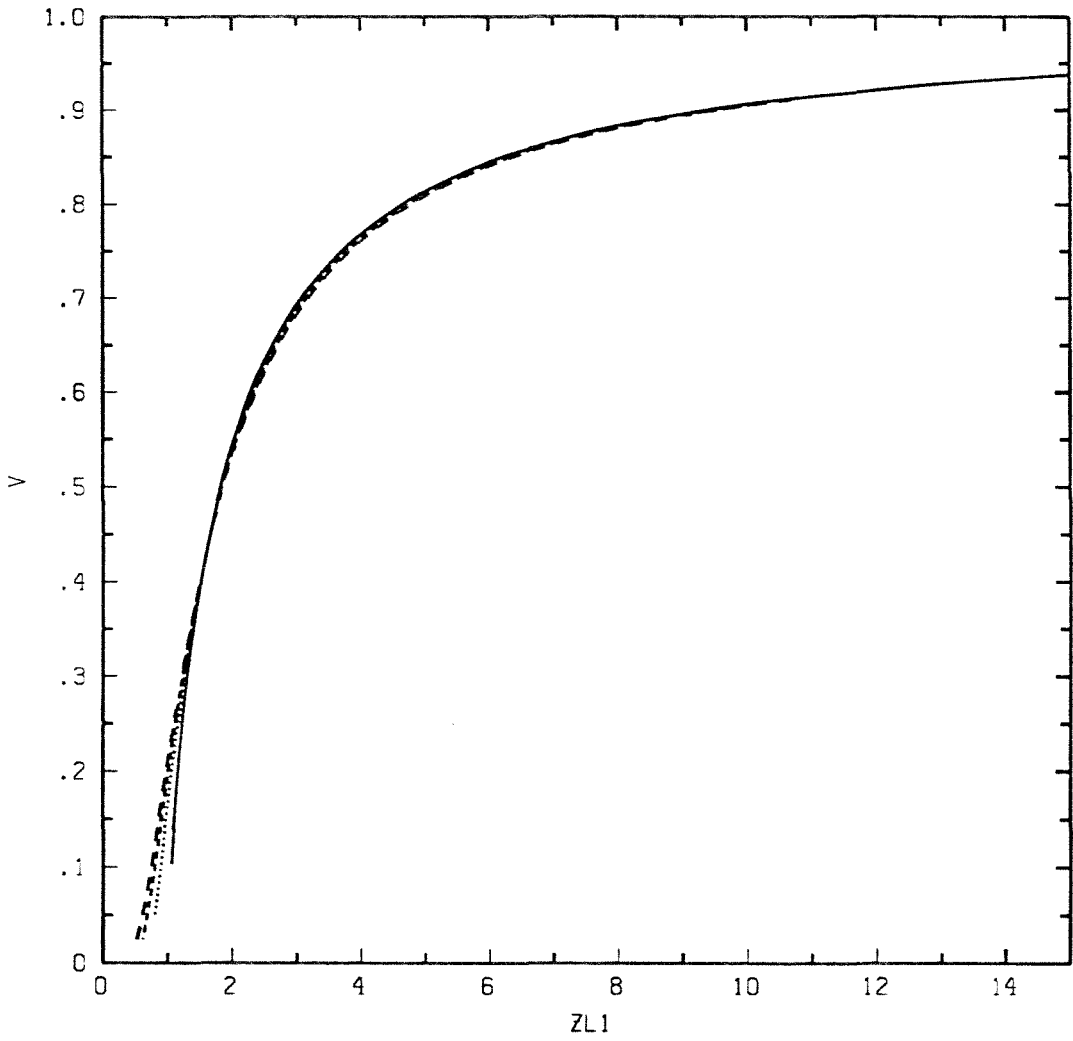


Figure 16

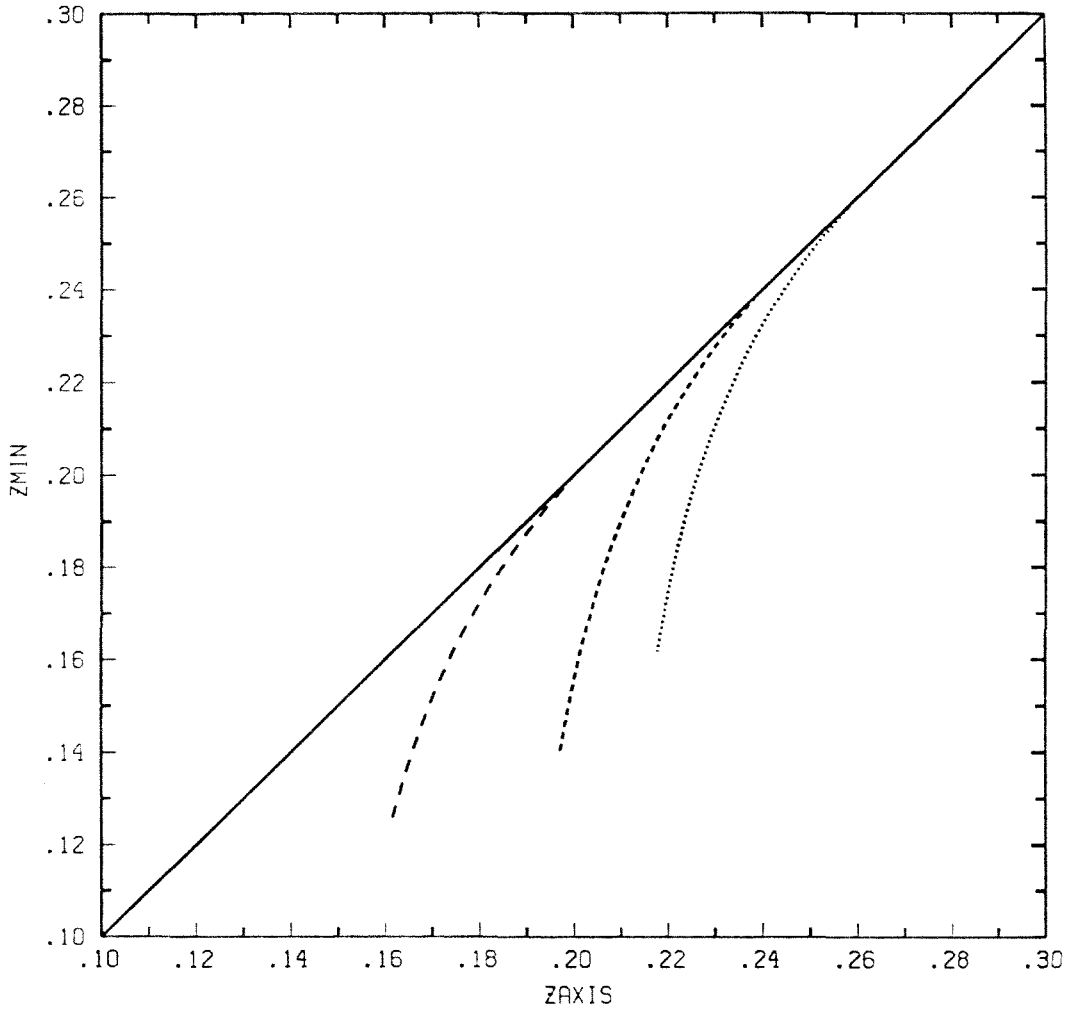


Figure 17

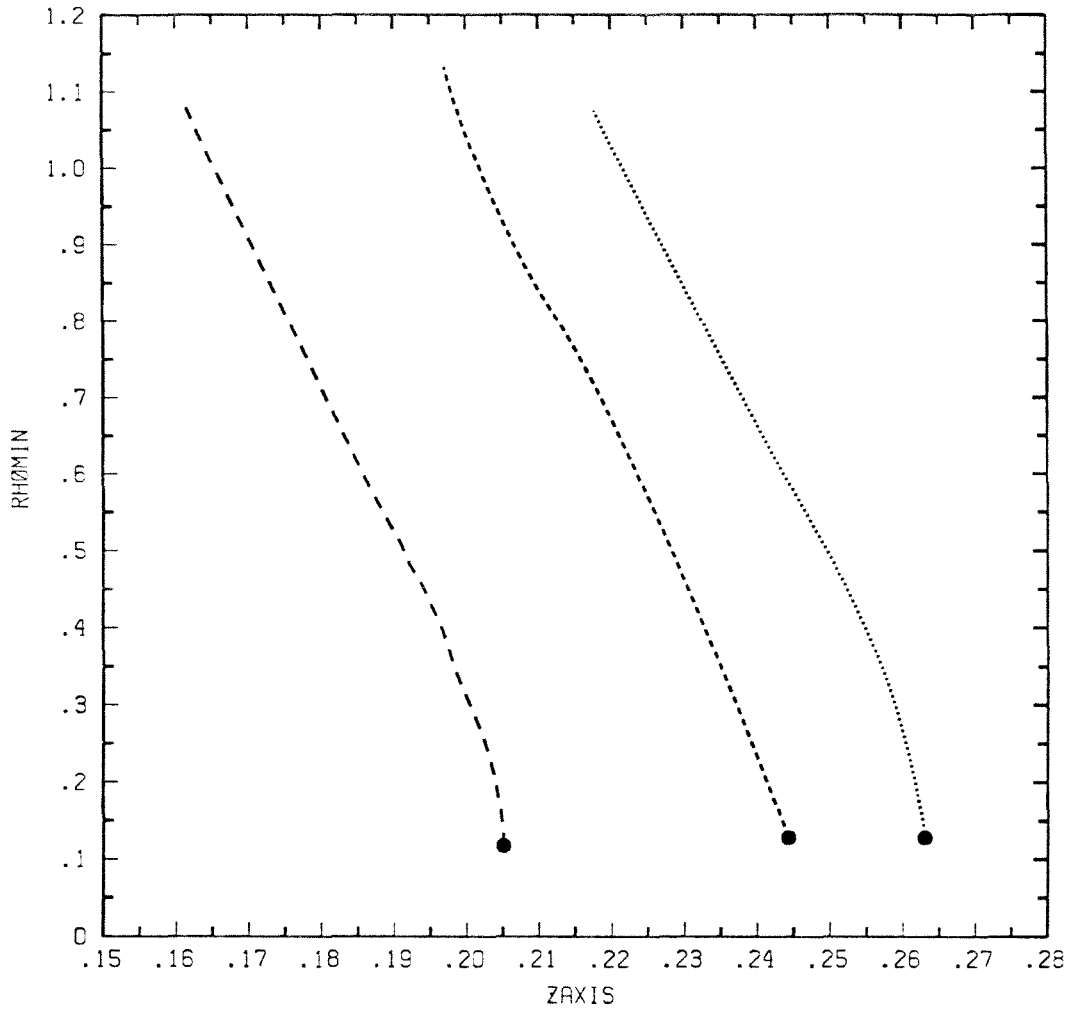


Figure 18

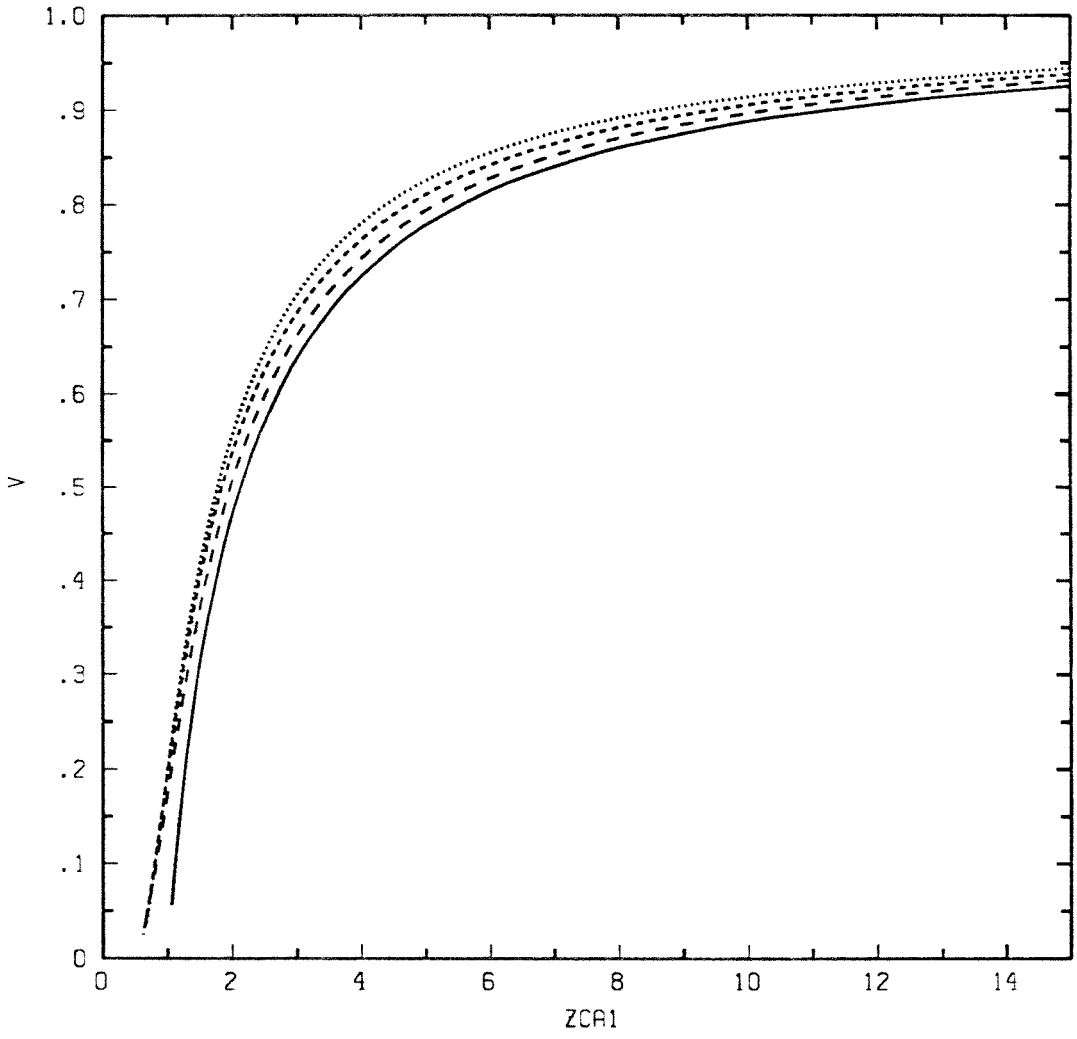
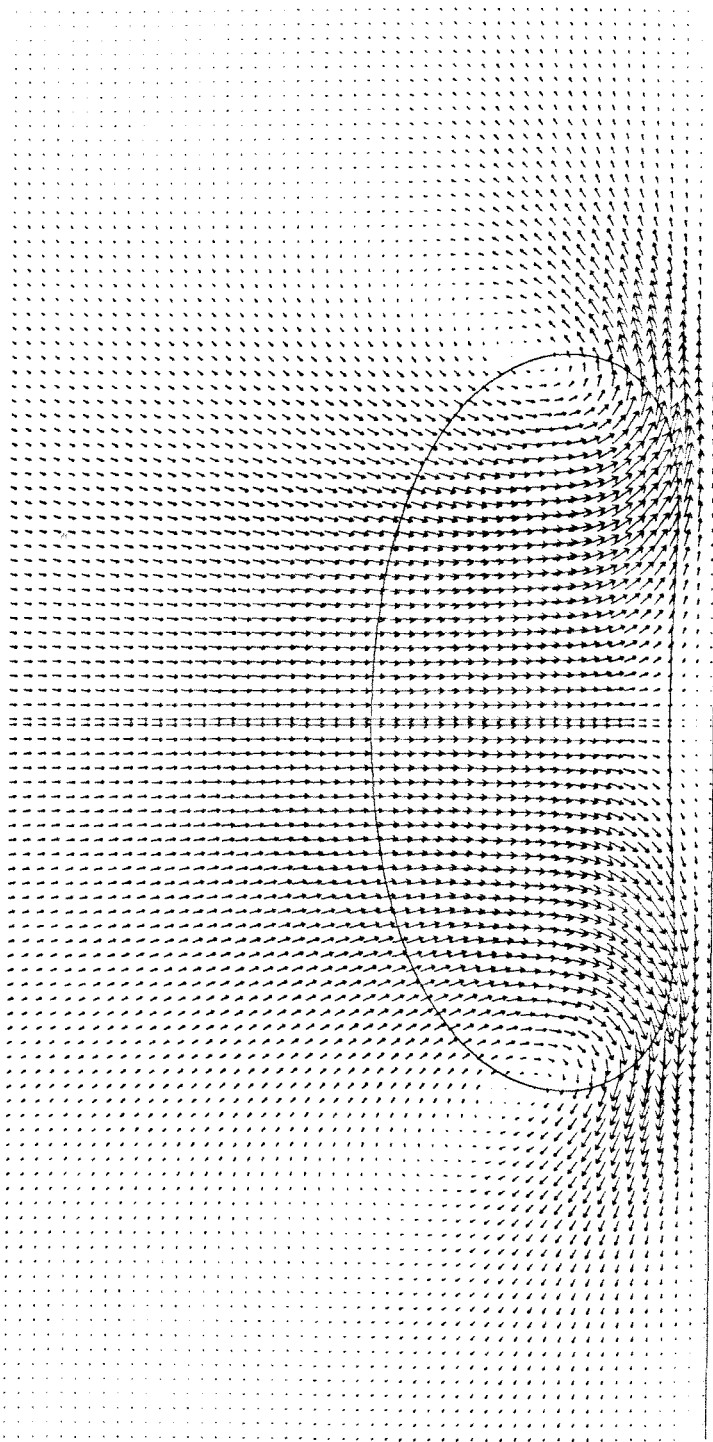
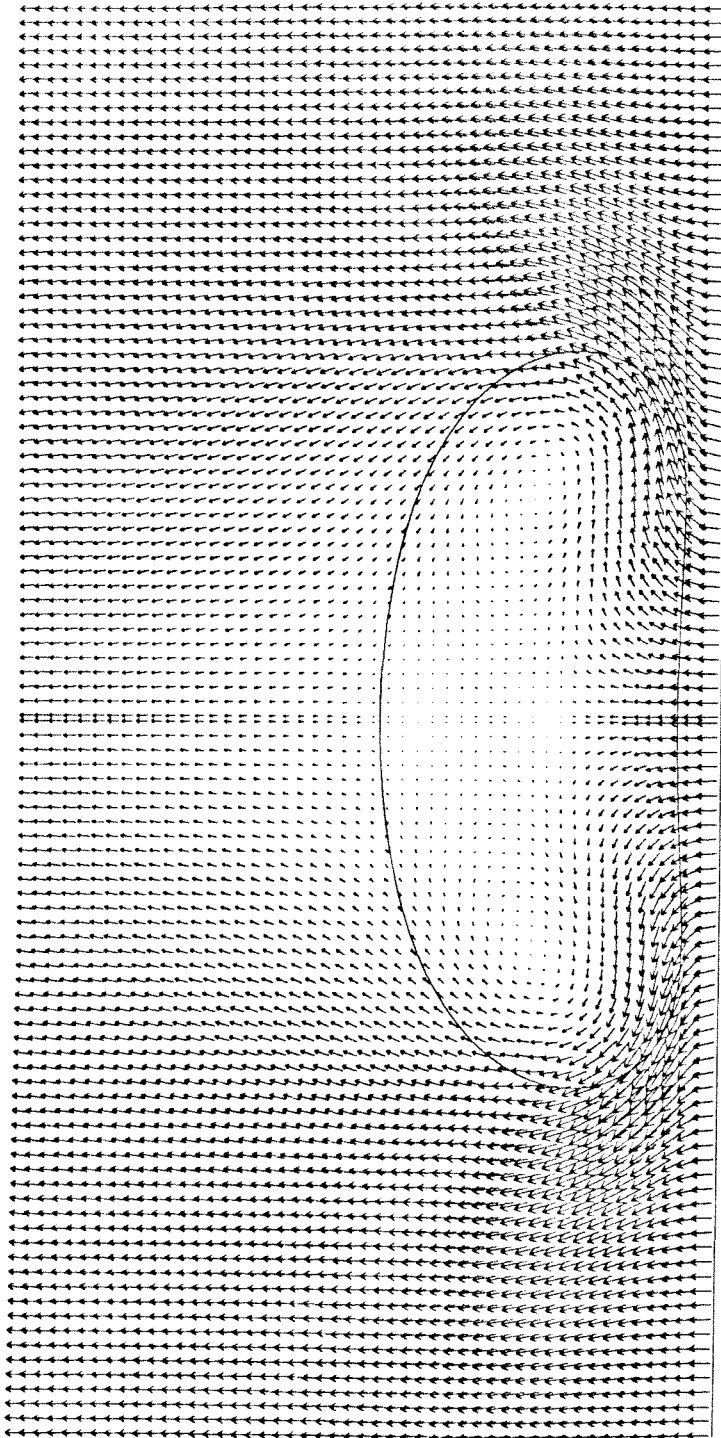


Figure 19



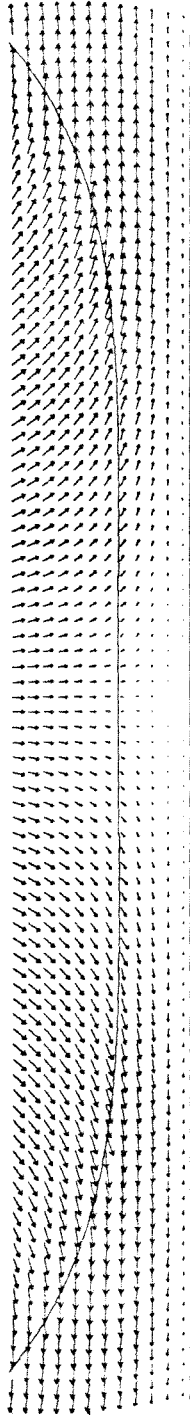
$Ca = 1, \lambda = 1$

Figure 20(a)



$Ca = 1, \lambda = 1$

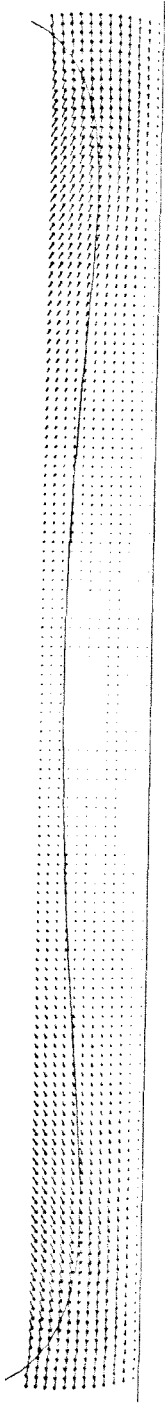
Figure 20(b)



↑

$Ca = 0.3, \lambda = 1$

Figure 21



$Ca = 3, \lambda = 1$

Figure 22(a)

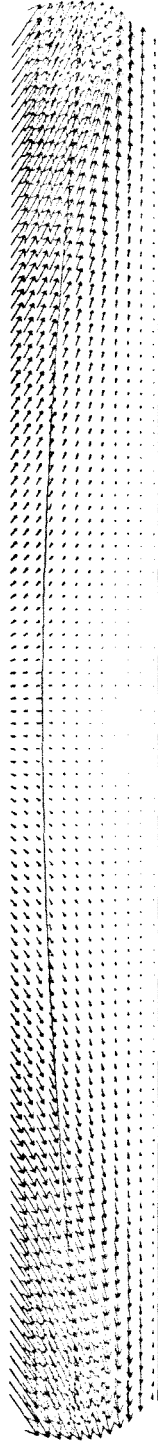


Figure 22(b)

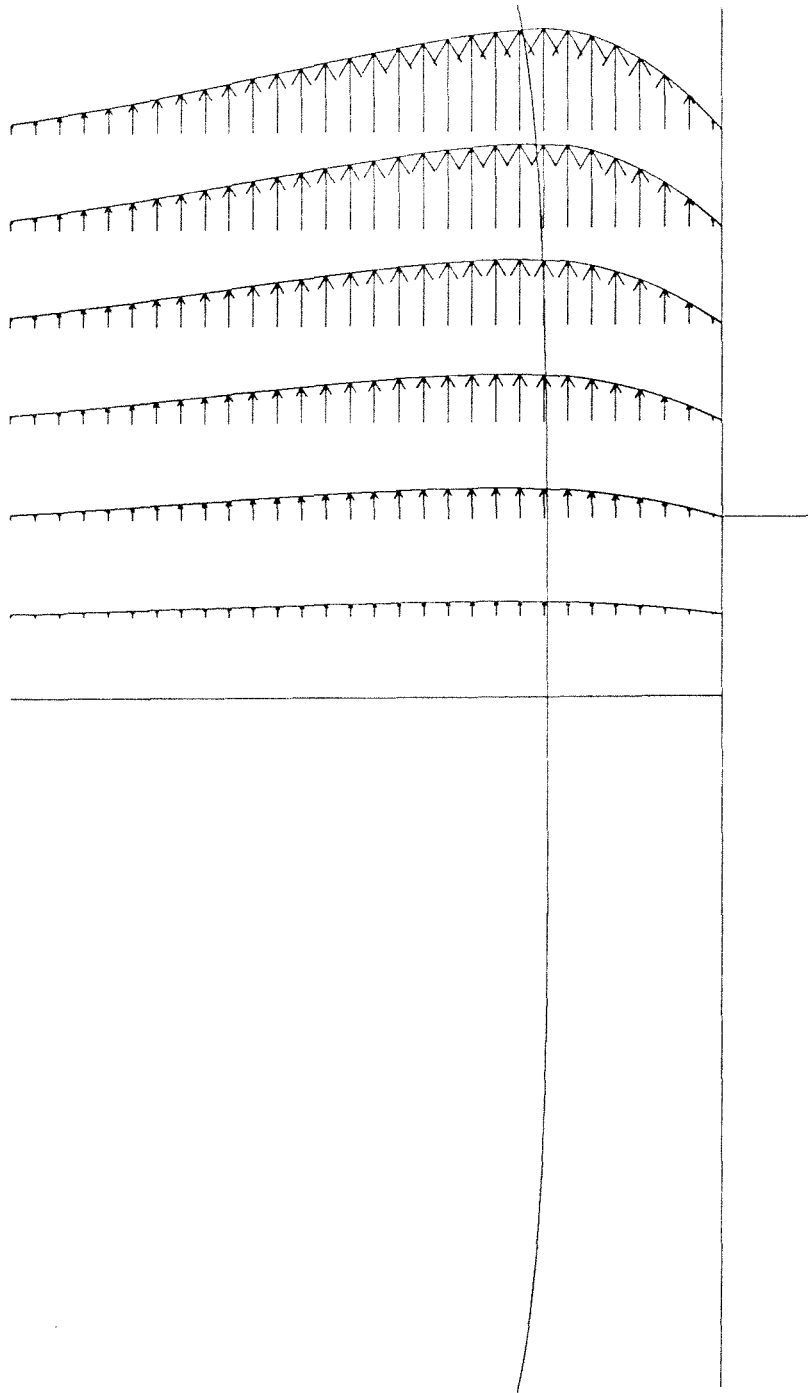


Figure 23

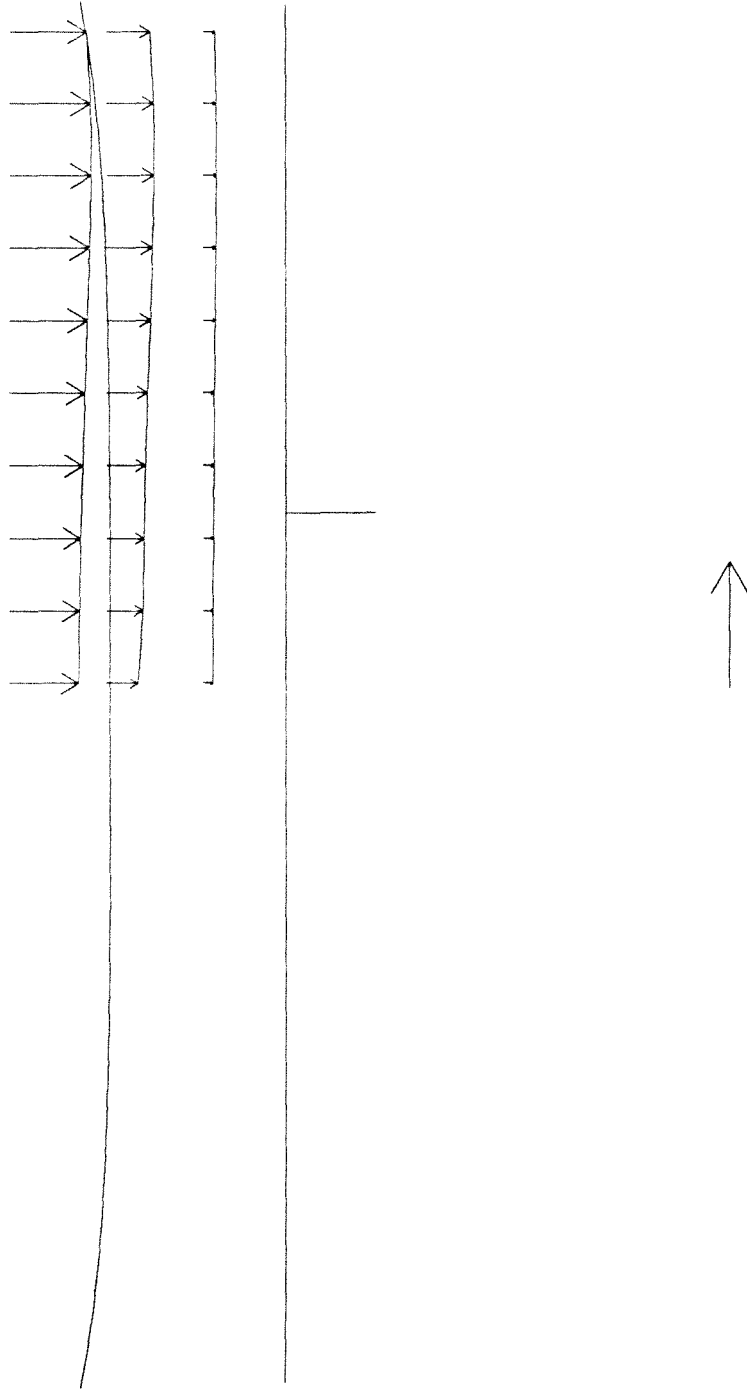


Figure 24

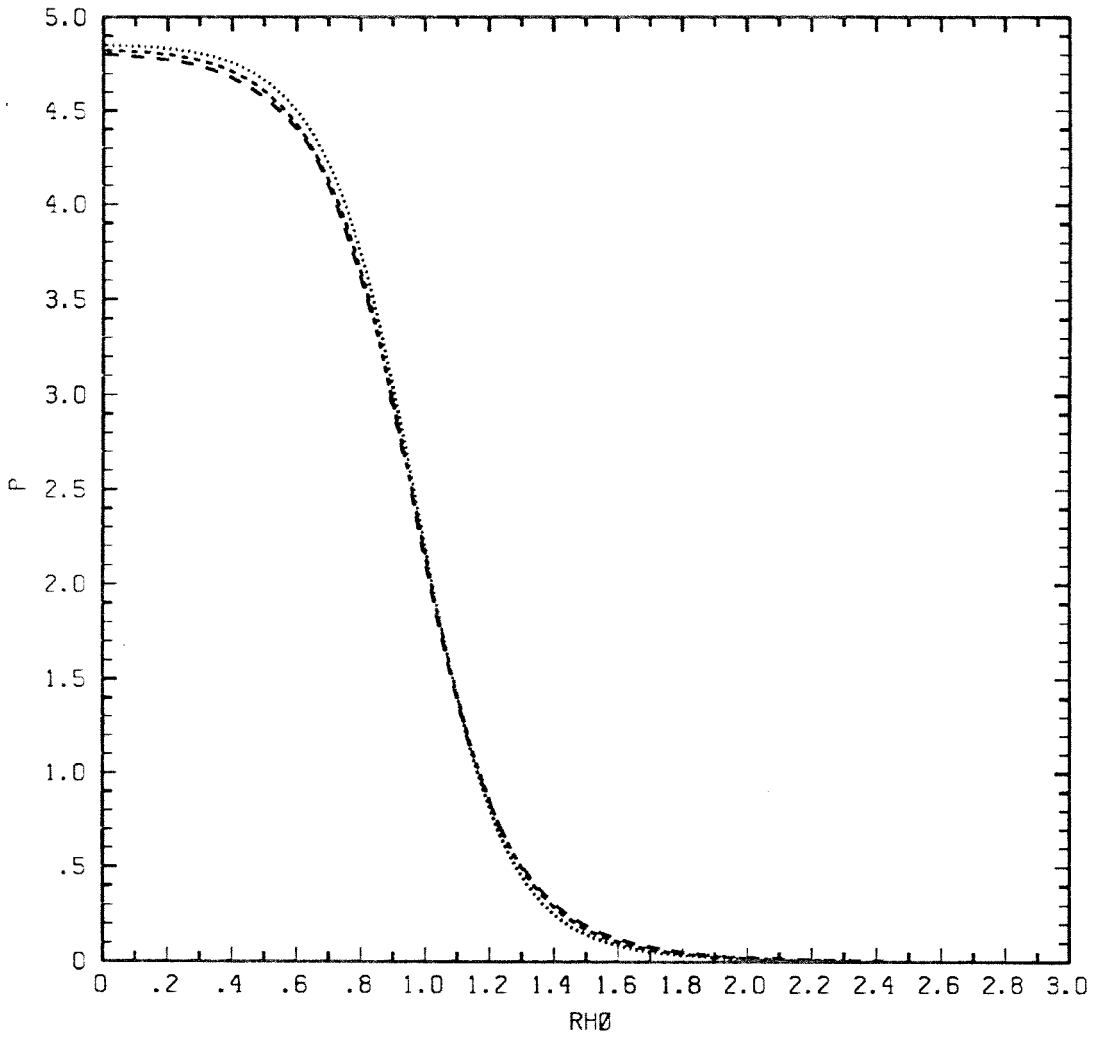


Figure 25(a)

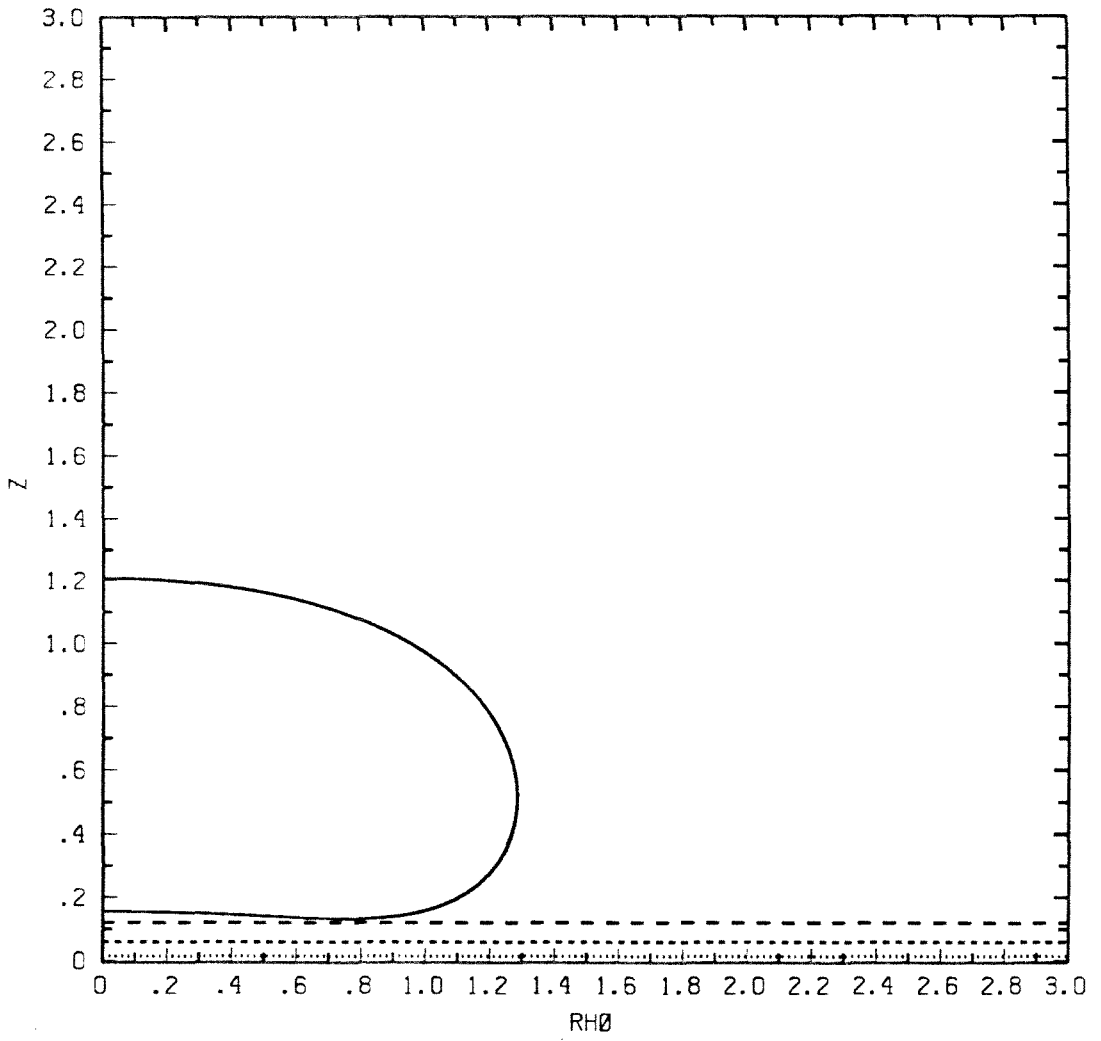


Figure 25(b)

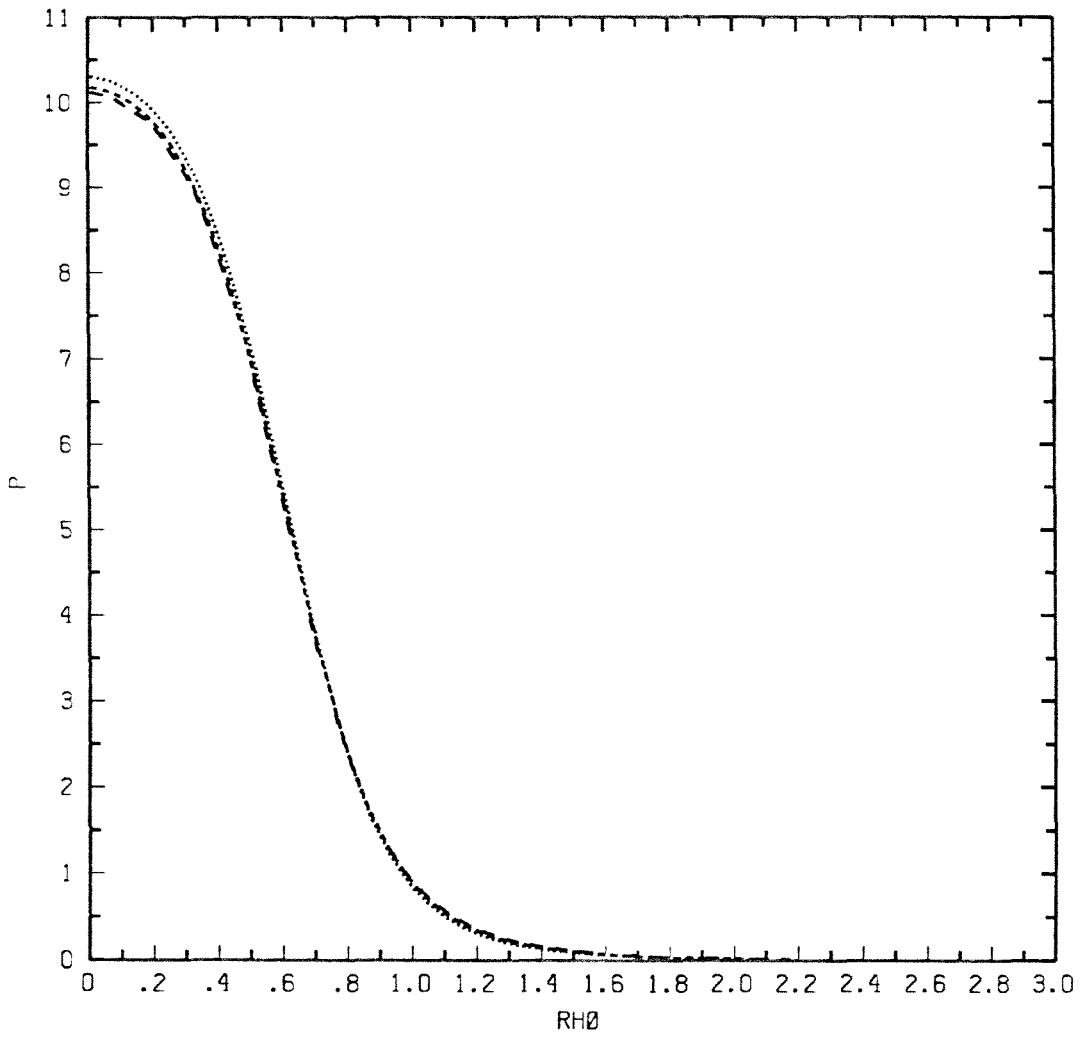


Figure 26(a)

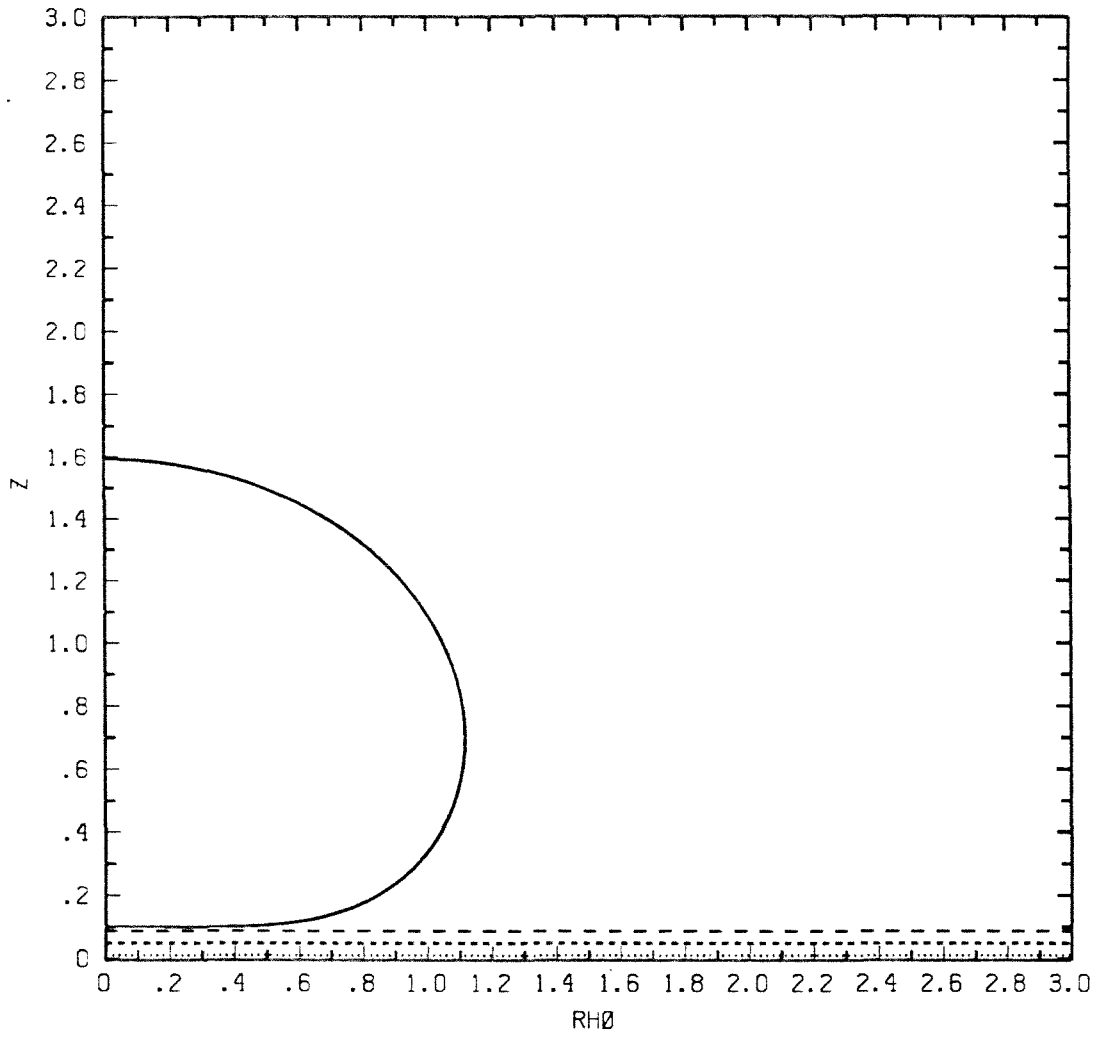


Figure 26(b)

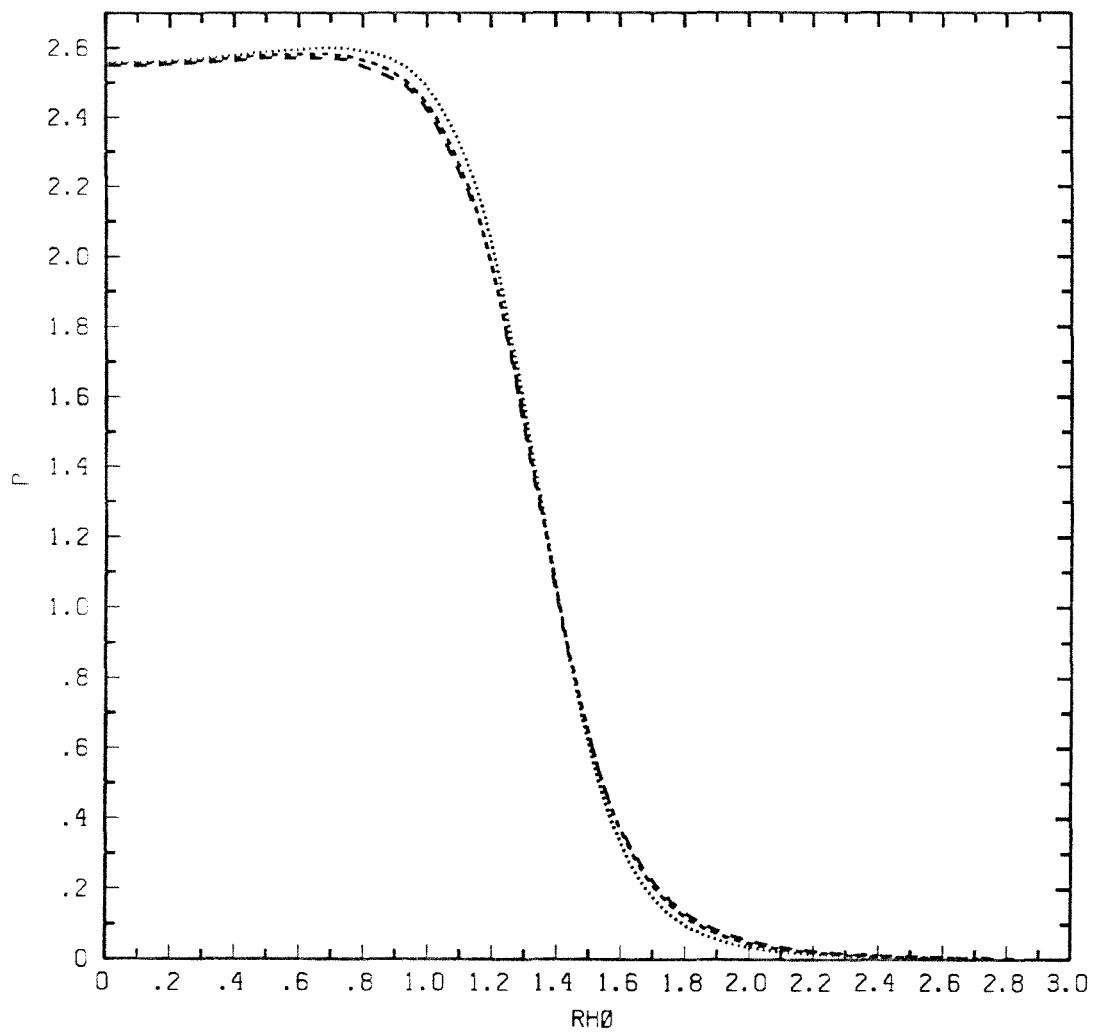


Figure 27(a)

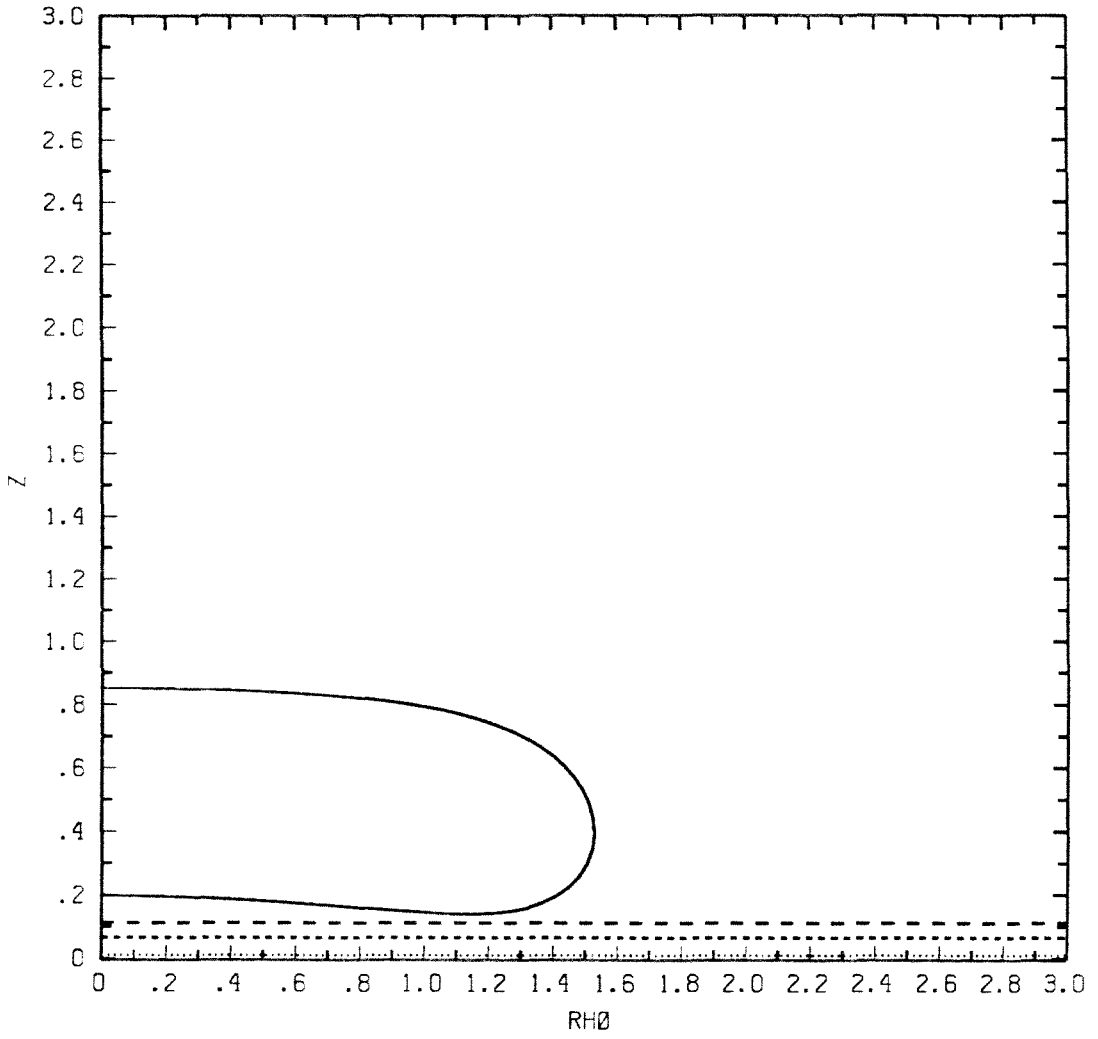


Figure 27(b)

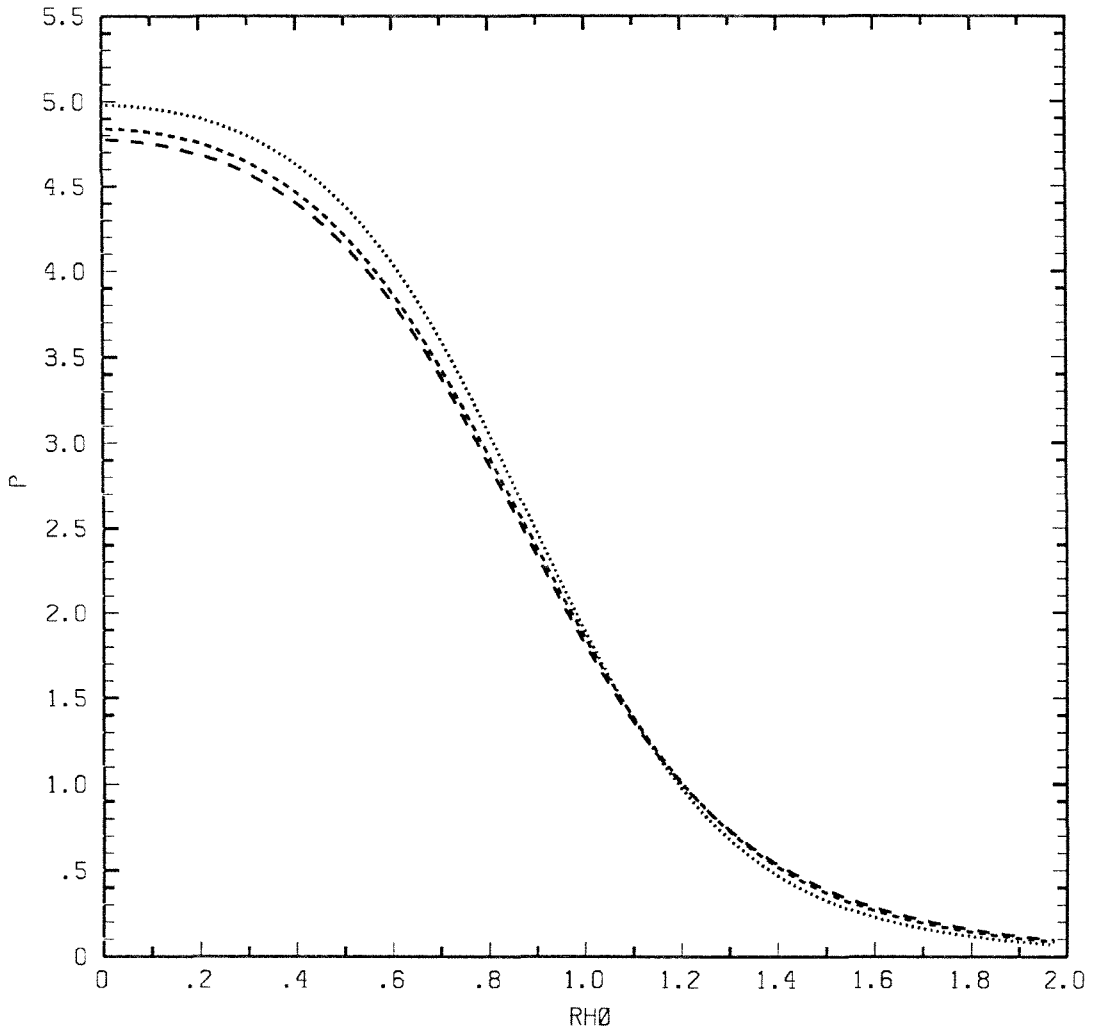


Figure 28(a)

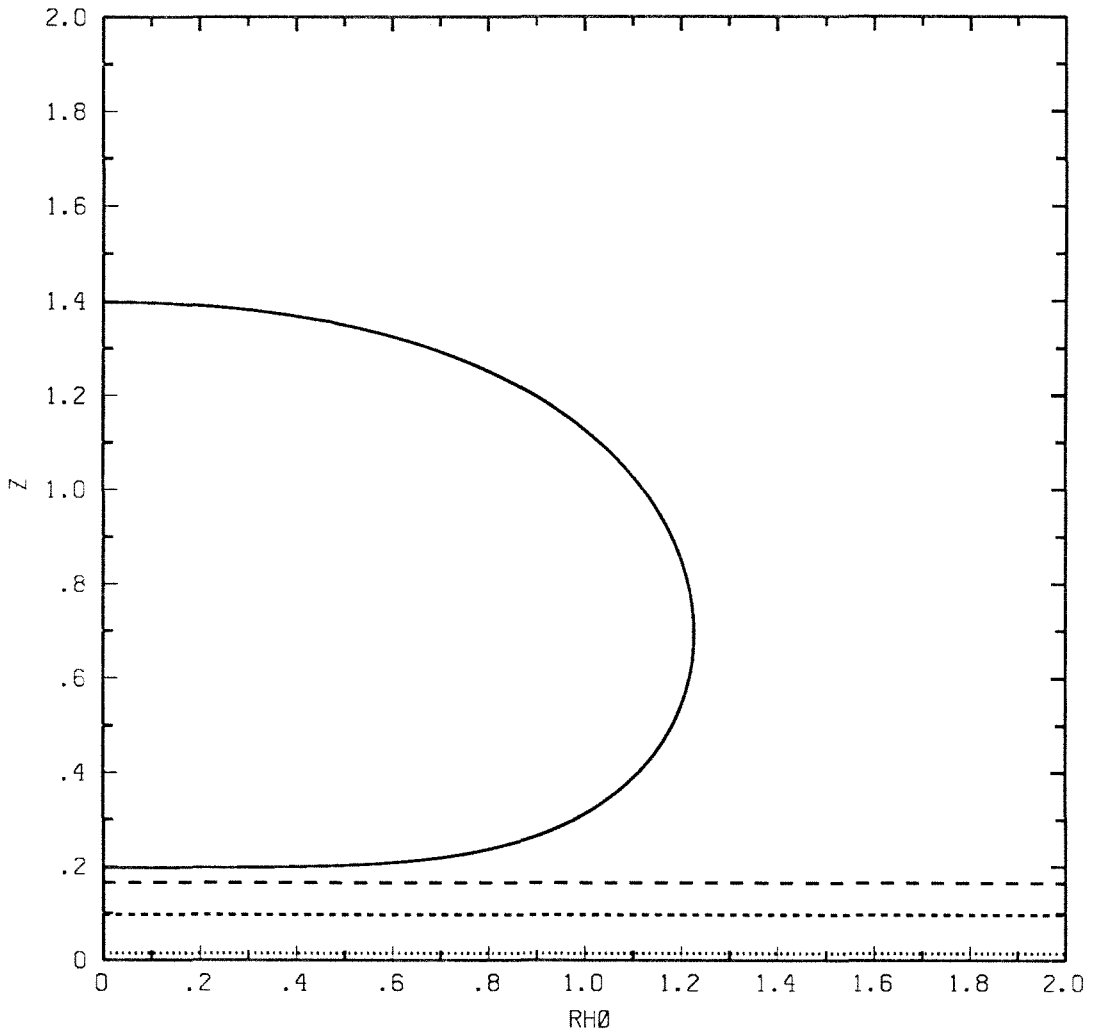


Figure 28(b)

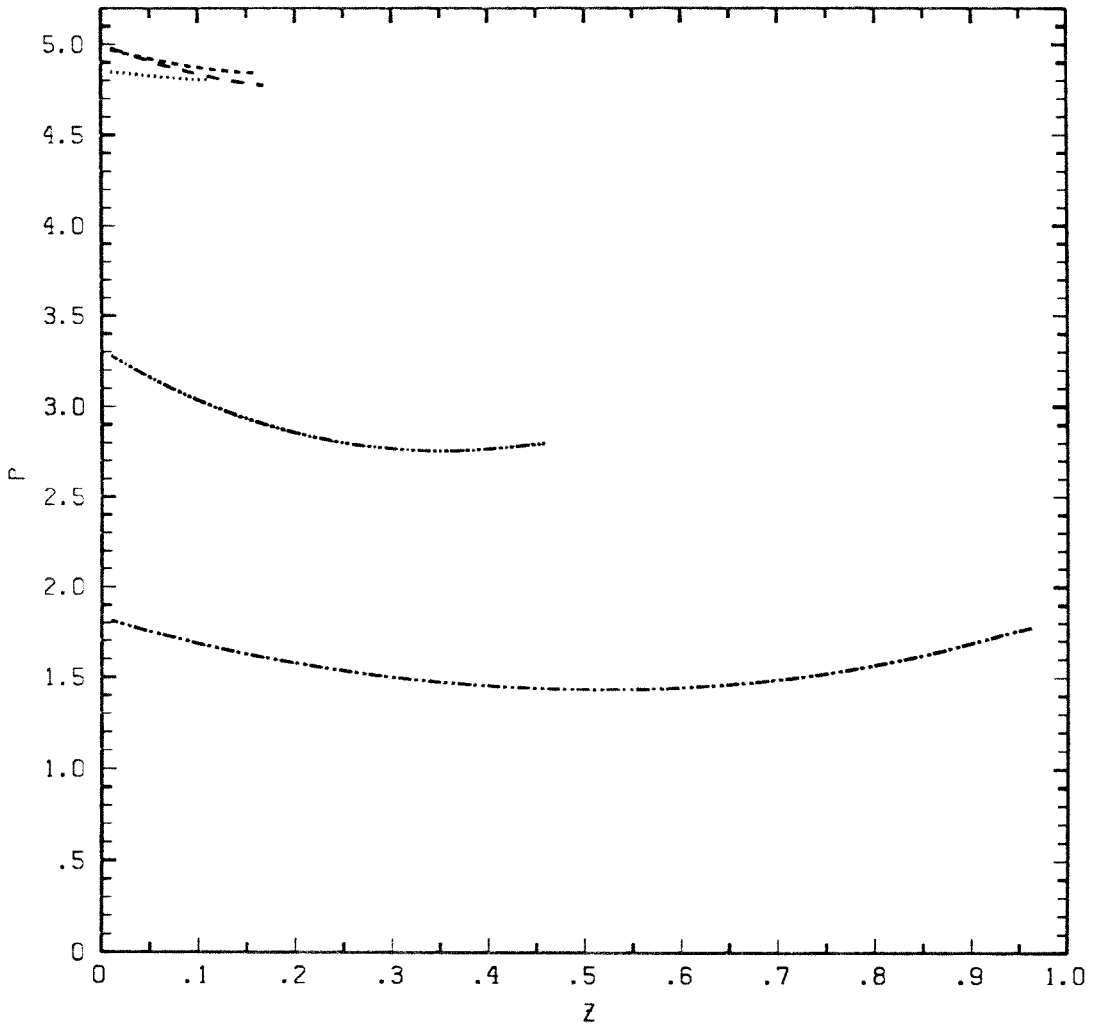


Figure 29

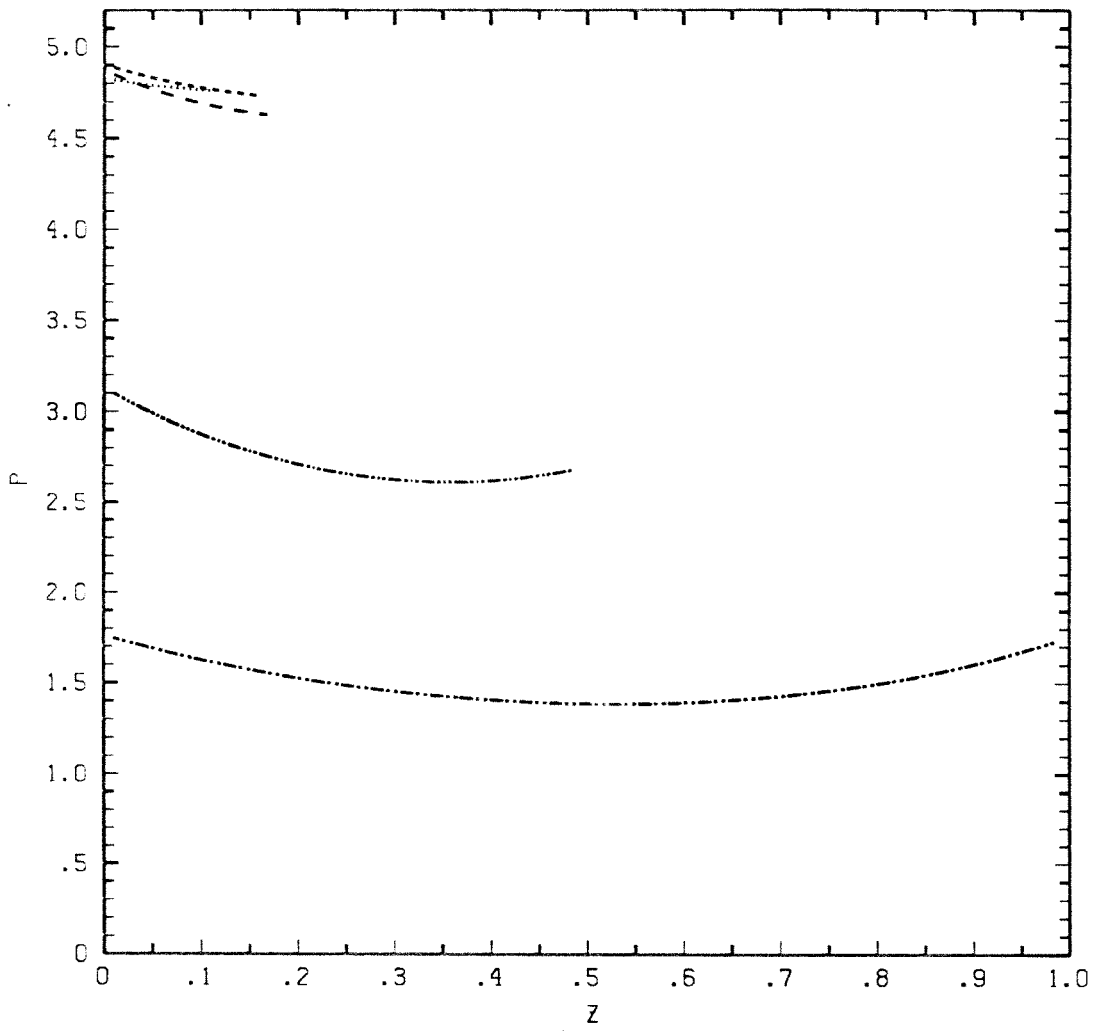


Figure 30

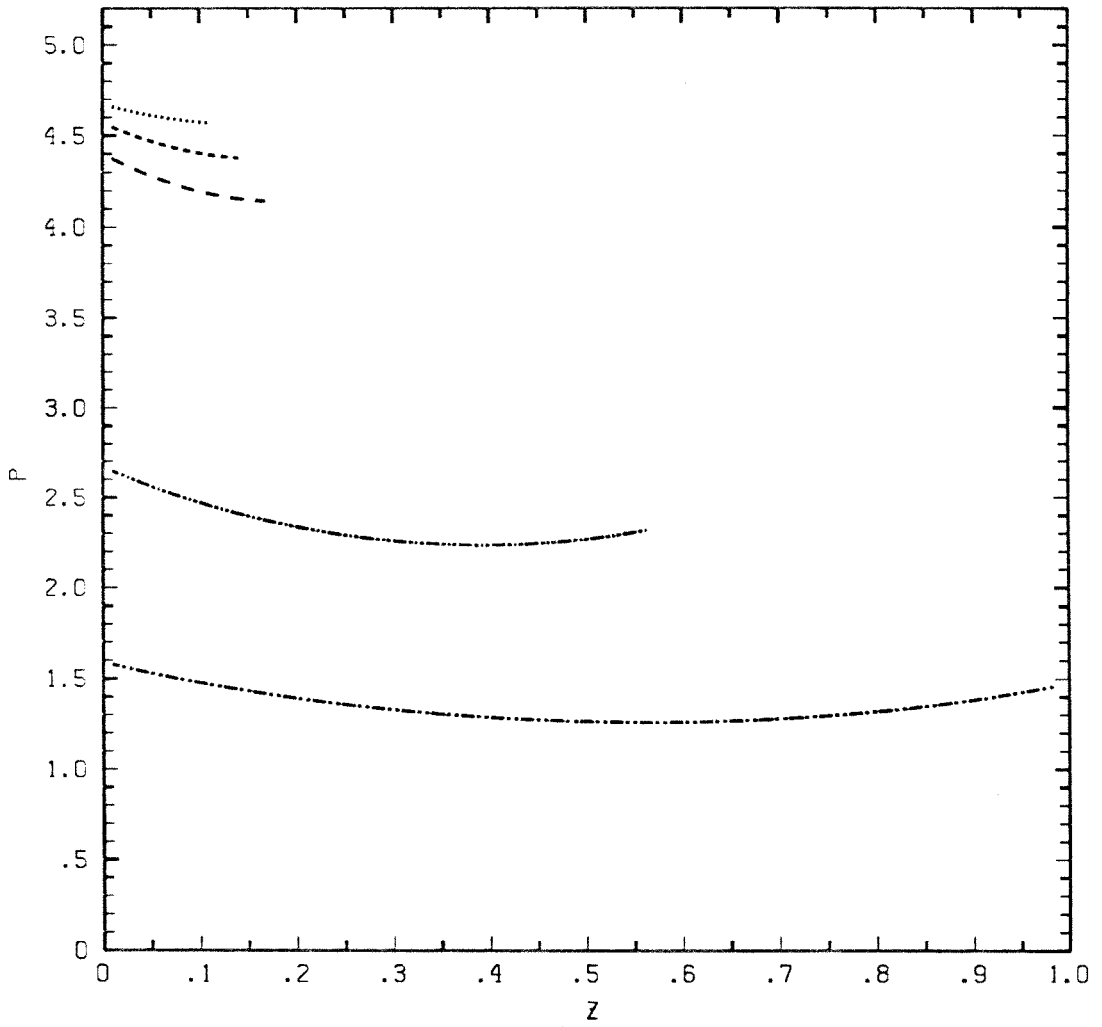


Figure 31

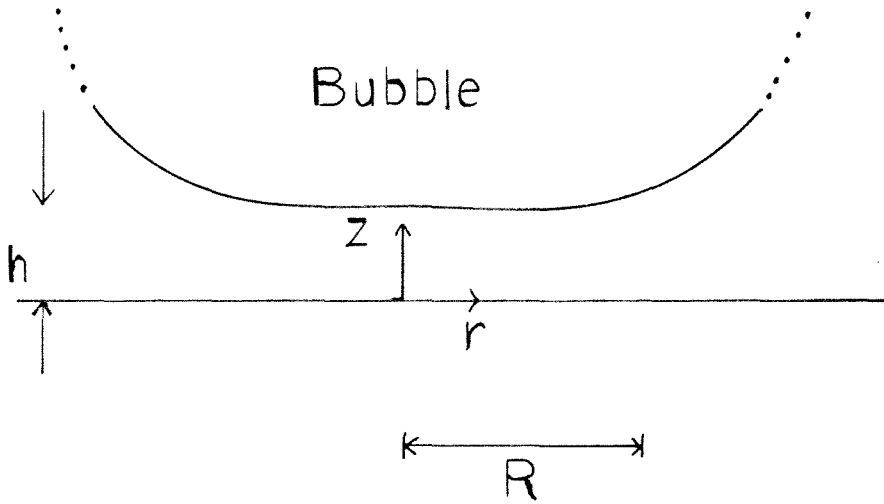


Figure B1

### Chapter III

## Thermocapillary motion of a deformable drop toward a planar wall

E.P. Ascoli and L.G. Leal

Dept. of Chemical Engineering

California Institute of Technology

Pasadena, California 91125

## Introduction

It is well documented that drops and bubbles can migrate in a fluid as a result of interfacial tension gradients (Young *et al.* (1959), Trefethan (1969)). Interfacial tension gradients can be induced at a drop or bubble surface by temperature variations, variation in surfactant concentration and variation in surface charge distribution. Interfacial gradients on a drop surface give rise to tangential stresses which, by viscous traction, result in fluid motion. Here only thermocapillary migration, i.e. motion due to temperature variations will be considered. The phenomenon of thermocapillary migration is more than a laboratory curiosity. In particular, the phenomenon has received recent attention in the context of materials processing under reduced gravity conditions. For example, thermocapillary migration is potentially an alternate mechanism to gravity for removal of gas bubbles in glass that is processed in space (Meyyappan *et al.* (1981)), Weinberg (1978)). Even in the presence of gravity, thermocapillary migration may act to eliminate gas bubbles in glass sealing and enameling. Also, thermocapillary migration may be of importance in mixing and combustion of fuel droplets.

Thermocapillary migration was first experimentally demonstrated by Young *et al.* (1959), who also theoretically determined the thermocapillary migration velocity of a spherical drop in an unbounded fluid medium. A variety of experimental and theoretical work on this subject has been done in the last 20 years and the interested reader is referred to Subramanian (1981) for a summary.

The focus in the current work is on the interaction of a thermocapillary driven drop and an infinite, no-slip, planar surface. This interaction is of importance since many of the envisioned applications of thermocapillary migration involve walls and solid surfaces. Meyyappan *et al.* (1980) theoretically considered the thermocapillary migration of a bubble in motion normal to a plane surface. Later Meyyappan *et al.* (1986) extended the analysis to include motions in an arbitrary direction with respect to the plane surface. Both analyses

assume a spherical shape and are restricted to bubbles (negligible viscosity and thermal conductivity in the enclosed phase relative to the suspending phase). The assumption of a non-deforming spherical shape is an approximation appropriate only for the restrictive case when the surface tension is large and surface tension variation across the drop or bubble is small. The current numerical work is sufficiently general to include the effects of viscosity and thermal conductivity in both phases. Further, the bubble or drop is allowed to deform in accordance with the physics of the problem.

The solution technique used here is based on the well-known boundary integral method that has been successfully used in a variety of related applications [ Youngren and Acrivos(1975, 1976), Rallison and Acrivos (1978), Lee and Leal (1982), Chi (1986), Ascoli (1987), Ascoli, Dandy and Leal (1988 a)]. In the present case, a fundamental solution (or more appropriately a Green's Function) presented by Blake (1971) will be employed. This Green's function is appropriate for systems involving an infinite, planar, no-slip boundary. Its use in the present application represents an extension of the work of Ascoli, Dandy and Leal (1988 b). These workers used the wall Green's function to determine the dynamics of a drop moving normal to a planar wall. Surface tension was assumed constant, and gravity was the driving force for motion. Variation in surface tension due to a linear temperature gradient is easily incorporated into the boundary integral formulation.

## Formulation

### (a) Equations and boundary conditions

We consider the slow motion of a deformable drop normal to a no-slip, infinite, planar surface as sketched in figure 1. The following assumptions will be made:

- (i) Fluid 1, which composes the drop, and fluid 2, the suspending fluid, are assumed to be immiscible. The physical properties of both fluids are assumed constant with the exception of interfacial tension. Thus, the fluids are assumed to be Newtonian with dynamic viscosities  $\mu_1$  and  $\mu_2$  (and kinematic viscosities  $\nu_1$  and  $\nu_2$ ), and incompressible with densities  $\rho_1$  and  $\rho_2$ . The ratio  $\mu_1/\mu_2$  will be denoted by  $\lambda$ . In addition,  $k_1$  and  $k_2$ , the respective thermal conductivities, will be assumed constant and their ratio  $k_1/k_2$  will be denoted by  $\delta$ . Finally, the respective constant thermal diffusivities will be denoted as  $\alpha_1$  and  $\alpha_2$ .
- (ii) On the drop surface, interfacial tension is assumed to depend linearly on temperature. In dimensional form this statement is equivalent to

$$\gamma(\mathbf{x}_s) = \gamma(T_w) + \frac{d\gamma}{dT}(T(\mathbf{x}_s) - T_w)$$

where  $\mathbf{x}_s$  denotes a point on the drop surface,  $\gamma$  is the dimensional surface tension,  $T$  is the dimensional temperature and  $\frac{d\gamma}{dT}$  is assumed to be negative and constant.  $T_w$  denotes the constant wall temperature, which is used here as a reference value. In terms of dimensionless parameters,  $\sigma = \gamma/\gamma(T_w)$ ,  $\omega = a|G|\frac{d\gamma}{dT}/\gamma(T_w)$ ,  $\Theta = (T - T_w)/a|G|$ , the variation in surface tension with temperature is given by

$$\sigma = 1 + \omega\Theta(\mathbf{x}_s)$$

- (iii) The motion is driven by an external temperature field, which is characterized by a constant gradient in the  $z$ -direction far away from the drop. Thus

$$T_2 \longrightarrow T_w + Gz' \quad \text{as} \quad z' \longrightarrow \infty$$

where  $T_2$  is the dimensional temperature in fluid 2 and  $z'$  is the dimensional  $z$ - coordinate. Non-dimensionalizing, this is written as

$$\Theta_2 \longrightarrow -z, \quad \text{as} \quad z \longrightarrow \infty$$

where  $\Theta_i = (T_i - T_w)/a|G|$  ( $i = 1, 2$ ) and  $z = z'/a$ .  $G$  is assumed negative. The characteristic length scale,  $a$ , is the radius of a sphere of volume equal to the drop volume.

- (iv) Gravity is assumed to be negligible. Note that the effects of gravity could be easily incorporated into the formulation and are neglected here for simplicity.
- (v) The analysis presented here is based upon the creeping motion approximation in which the inertial terms in the equations of motion are neglected entirely. The corresponding small Reynold's numbers ( $Re_1, Re_2$ ) of the system are

$$Re_1 = \frac{U a}{\nu_1} \ll 1.$$

$$Re_2 = \frac{U a}{\nu_2} \ll 1.$$

The characteristic velocity,  $U$ , (subsequently used for non-dimensionalization) is the terminal thermal migration velocity of an equal volume spherical drop in the absence of a wall and is given by ( Young *et al.* 1959)

$$U = \frac{\gamma(T_w)}{\mu_2(1 + \frac{3}{2}\lambda)} \left( \frac{|\omega|}{2 + \delta} \right)$$

- (vi) The Peclet numbers of the system are assumed small where

$$Pe_1 = \frac{aU}{\alpha_1} \ll 1$$

$$Pe_2 = \frac{aU}{\alpha_2} \ll 1$$

This assumption is equivalent to neglect of thermal convection relative to thermal diffusion.

As a result of the assumptions in the system, all motions and deformations will be axisymmetric about the line which passes through the drop center and is normal to the the planar wall, assuming that the starting drop shape is axisymmetric.

The assumptions of small Reynolds numbers reduces the momentum equations to the Stokes equations, which have been derived in dimensionless form elsewhere, and are restated below:

$$0 = -\nabla p_1 + \nabla^2 \mathbf{u}_1 \quad (1a)$$

for the drop, and

$$0 = -\nabla p_2 + \nabla^2 \mathbf{u}_2 \quad (1b)$$

for the surrounding fluid. Pressure  $p_i$  is made dimensionless with  $\frac{\mu_i U}{a}$  ( $i = 1, 2$ ).

With the assumption of constant fluid densities, the continuity equations in dimensionless form are

$$0 = \nabla \cdot \mathbf{u}_1 \quad (2a)$$

$$0 = \nabla \cdot \mathbf{u}_2. \quad (2b)$$

The thermal energy equation, for small Peclet numbers, reduces to Laplace's equation for dimensionless temperature

$$0 = \nabla^2 \Theta_1 \quad (3a)$$

$$0 = \nabla^2 \Theta_2. \quad (3b)$$

The boundary conditions in the outer fluid are

$$\Theta_2 \longrightarrow -z \quad \text{as } z \longrightarrow \infty \quad (4)$$

$$\Theta_2 = 0 \quad \text{for } \mathbf{x} \in \mathbf{P} = \left\{ \mathbf{x} \in \mathbf{R}^3 : \mathbf{x} = (x, y, z) \text{ and } z = 0 \right\} \quad (5)$$

$$\mathbf{u}_2 \longrightarrow 0 \quad \text{as } |\mathbf{x}| \longrightarrow \infty, \quad (6)$$

$$\mathbf{u}_2 = 0 \quad \text{for } \mathbf{x} \in \mathbf{P} \quad (7)$$

The boundary conditions at the drop surface,  $\mathbf{x} \in S_I$ , are:

$$\Theta_1 = \Theta_2 \stackrel{def}{=} \Theta_I \quad (8)$$

$$\delta \left( \mathbf{n} \cdot \nabla \Theta_1 \right) - \mathbf{n} \cdot \nabla \Theta_2 = 0 \quad (9)$$

$$\mathbf{u}_1 = \mathbf{u}_2 \stackrel{def}{=} \mathbf{u}_I \quad (10)$$

$$(\lambda \mathbf{n} \cdot \mathbf{T}^{(1)} - \mathbf{n} \cdot \mathbf{T}^{(2)}) = \left\{ \frac{(2 + \delta)(1 + \frac{3}{2}\lambda)}{|\omega|} \right\} \left[ -\sigma \mathbf{n} \nabla_s \cdot \mathbf{n} + \nabla_s \sigma \right] \stackrel{def}{=} \mathcal{F} \quad (11)$$

Here,  $\mathbf{n}$  is the outer normal to the drop surface,  $\nabla_s$  is the surface gradient operator and  $\mathbf{T}^{(1)}$  and  $\mathbf{T}^{(2)}$  are the respective stress tensors. Substituting the assumed form for  $\sigma$  into equation (11) gives

$$(\lambda \mathbf{n} \cdot \mathbf{T}^{(1)} - \mathbf{n} \cdot \mathbf{T}^{(2)}) = \left\{ \frac{(2 + \delta)(1 + \frac{3}{2}\lambda)}{|\omega|} \right\} \left[ -(1 + \omega \Theta_I) \mathbf{n} \nabla_s \cdot \mathbf{n} + \omega \nabla_s \Theta_I \right] \stackrel{def}{=} \mathcal{F} \quad (12)$$

The dimensionless parameters  $\omega$ ,  $\lambda$ , and  $\delta$  control the system. It is useful to define an effective capillary number as  $Ca = U\mu_2/\gamma(T_w)$ . This capillary number provides a measure of the relative importance of viscous effects to surface tension effects.  $Ca$  is not a free parameter but is determined by the system parameters  $\omega$ ,  $\lambda$  and  $\delta$ . In terms of these parameters

$$Ca = \frac{|\omega|}{(1 + \frac{3}{2}\lambda)(2 + \delta)}$$

The expression in curly braces in equation (12) is thus  $1/Ca$ .

Condition (12) provides the driving force for both the deformation and motion of the drop. Meyyappan *et al.* (1980) considered the special case of a spherical bubble and in doing so neglected the normal component of equation (12). It may be noted that if only the tangential component of equation (12) is included in the analysis, only the second term in square braces in (12) is present and the magnitude of the parameter  $\omega$  disappears from the non-dimensionalized

problem. Thus, once a spherical bubble shape is assumed, the magnitude of the parameter  $\omega$  no longer plays a role in the dimensionless problem \*.

Finally, the drop surface,  $S_I$ , is assumed to deform in accordance with the instantaneous interface velocity field to determine a new drop configuration. The kinematic condition used to deform the drop surface is

$$\frac{d\mathbf{x}_s}{dt} = \mathbf{n}(\mathbf{x}_s) \left( \mathbf{n}(\mathbf{x}_s) \cdot \mathbf{u}_I(\mathbf{x}_s) \right) \quad (13)$$

Thus, the drop surface is deformed with the normal projection of the surface velocity.

Equations (1a,b), (2a,b) with conditions (6), (7) and (12) constitute the hydrodynamic portion of the problem. Equations (3a,b) and conditions (4), (5), (8) and (9) constitute the thermal portion of the problem. The thermal and hydrodynamic problems are coupled since boundary condition (12) links stresses with temperature.

Both the thermal and hydrodynamic problems will be cast into a boundary integral formulation. Ascoli, Dandy and Leal (1988 a, b) presented the boundary integral formulation that is especially designed for the case where an infinite, no-slip, planar wall is present. There, the formulation was applied to determine the slow viscous flow of a deformable drop moving under the influence of gravity normal to a no-slip planar wall. Interfacial tension was assumed to be constant. Here interfacial tension gradients are responsible for the motion and are easily incorporated into the formulation. The final results for the transformation of equations (1a,b) and (2a,b) including conditions (6), (7) and (12) into the boundary integral form are

$$\frac{1}{2}(\mathbf{u}_I(\mathbf{x}_s))_j = \int_{S_I} \Sigma^j(\mathbf{x}_s, \xi) \cdot \mathbf{u}_I(\xi) \cdot \mathbf{n} dS_\xi - \int_{S_I} \mathbf{v}^j(\mathbf{x}_s, \xi) \cdot \mathbf{f}^{(1)}(\xi) dS_\xi \quad (14)$$

---

\* In fact,  $\omega$  plays no role for any problem which assumes a *fixed* drop shape and subsequently neglects the normal component of equation (12).

and

$$\begin{aligned}
 -\frac{1}{2}(\mathbf{u}_I(\mathbf{x}_s))_j &= -\frac{\lambda-1}{\lambda+1} \int_{S_I} \Sigma^j(\mathbf{x}_s, \xi) \cdot \mathbf{u}_I(\xi) \cdot \mathbf{n} dS_\xi \\
 &\quad + \frac{1}{(\lambda+1)} \int_{S_I} \mathbf{v}^j(\mathbf{x}, \xi) \cdot \mathcal{F} dS_\xi \quad (15) \\
 \mathbf{x}_s &\in S_I,
 \end{aligned}$$

where  $\mathbf{f}^{(i)} \stackrel{def}{=} \mathbf{n} \cdot \mathbf{T}^{(i)}$  for  $i = 1, 2$  and appropriate jump conditions have been applied. The vector  $\xi$  is the position vector on the surface,  $S_I$ , and integration is performed with respect to this variable. The vector  $\mathbf{x}_s$  corresponds to a fixed position on the surface. The kernels  $\Sigma^j$  and  $\mathbf{v}^j$  are given by

$$\begin{aligned}
 v_i^j &= \hat{v}_i^j + \hat{\hat{v}}_i^j \\
 q^j &= \hat{q}^j + \hat{\hat{q}}^j \\
 \Sigma_{ik}^j &= \hat{\Sigma}_{ik}^j + \hat{\hat{\Sigma}}_{ik}^j
 \end{aligned}$$

where

$$\begin{aligned}
 \hat{v}_i^j &= -\frac{1}{8\pi} \left\{ \frac{\delta_{ij}}{r} + \frac{r_i r_j}{r^3} \right\} \\
 \hat{q}^j &= \frac{1}{4\pi} \left\{ \frac{r_j}{r^3} \right\} \\
 \hat{\hat{\Sigma}}_{ik}^j &= \frac{3}{4\pi} \left\{ \frac{r_k r_i r_j}{r^5} \right\}
 \end{aligned}$$

and

$$\begin{aligned}
 \hat{\hat{v}}_i^j &= -\frac{1}{8\pi} \left\{ -\frac{\delta_{ij}}{R} - \frac{R_i R_j}{R^3} \right. \\
 &\quad \left. + 2x_3 \Delta_j \frac{\partial}{\partial R_j} \left[ \frac{x_3 R_i}{R^3} - \frac{\delta_{i3}}{R} - \frac{R_i R_3}{R^3} \right] \right\} \\
 &= -\frac{1}{8\pi} \left\{ -\frac{\delta_{ij}}{R} - \frac{R_i R_j}{R^3} \right. \\
 &\quad \left. + 2x_3 \Delta_j \left[ x_3 \left( \frac{\delta_{ij}}{R^3} - \frac{3R_i R_j}{R^5} \right) + \frac{\delta_{i3}}{R^3} R_j \right. \right. \\
 &\quad \left. \left. - \frac{1}{R^3} (\delta_{ij} R_3 + R_i \delta_{3j}) + \frac{3R_i R_j R_3}{R^5} \right] \right\}
 \end{aligned}$$

$$\hat{q}^j = \frac{1}{4\pi} \left[ -\frac{R_j}{R^3} - 2x_3 \Delta_j \left( \frac{\delta_{3j}}{R^3} - \frac{3R_j R_3}{R^5} \right) \right]$$

$$\hat{\Sigma}_{ik}^j = \frac{3}{4\pi} \left\{ -\frac{R_i R_j R_k}{R^5} - 2x_3 \Delta_j \left[ -\frac{x_3}{R^5} \delta_{ik} R_j \right. \right.$$

$$\left. \left. + \frac{\xi_3}{R^5} (R_i \delta_{jk} + \delta_{ij} R_k) + \frac{R_i \delta_{3j} R_k}{R^5} - \frac{5R_i R_j R_k \xi_3}{R^7} \right] \right\}.$$

where  $\mathbf{r} = (\xi_1 - x_1, \xi_2 - x_2, \xi_3 - x_3)^T$ ,  $\mathbf{R} = (\xi_1 - x_1, \xi_2 - x_2, \xi_3 + x_3)^T$ ,  $r = [(\xi_1 - x_1)^2 + (\xi_2 - x_2)^2 + (\xi_3 - x_3)^2]^{1/2}$ ,  $R = [(\xi_1 - x_1)^2 + (\xi_2 - x_2)^2 + (\xi_3 + x_3)^2]^{1/2}$ , and  $R_3 = \xi_3 + x_3$ . The quantity  $\Delta_j$  has value +1 for  $j = 1, 2$  and -1 for  $j = 3$ . This choice of kernels eliminates the need to include the wall in the domain of integration. For details of the derivation of equations (14) and (15), the reader is referred to Ascoli, Dandy and Leal (1988 a,b).

The thermal problem is recast into boundary integral form via a classical Green's function analysis for Laplace systems. The final result is

$$\Theta_I(\mathbf{x}_s) = -\left(\frac{2}{1+\delta}\right)z + \frac{2(\delta-1)}{1+\delta} \int_{S_I} \Theta_I(\xi) \mathbf{n}(\xi) \cdot \nabla \Phi(\mathbf{x}_s, \xi) dS_\xi \quad (16)$$

where

$$\Phi(x, \xi) = \frac{1}{4\pi} \left( \frac{1}{R} - \frac{1}{r} \right)$$

is the classical Green's function for the Laplace equation which vanishes identically on the planar wall. Its use in the present case again simplifies the analysis. In particular, there is no need to include the wall in the integration domain.

The drop surface was parametrized by  $(\rho(s), z(s))$  for  $\Theta \in [0, 2\pi)$ , where  $s$  is normalized arclength lying in the interval  $[0, 1]$ . The advantages of this representation are discussed in Ascoli, Dandy and Leal (1988 b). In terms of this parametrization, the components of the unit normal to the surface are

$$n_\rho = \frac{\dot{z}}{(\dot{\rho}^2 + \dot{z}^2)^{1/2}}$$

$$n_z = -\frac{\dot{\rho}}{(\dot{\rho}^2 + \dot{z}^2)^{1/2}}, \quad (17)$$

and the curvature is

$$\nabla_s \cdot \mathbf{n} = \frac{\dot{z}}{\rho(\dot{\rho}^2 + \dot{z}^2)^{1/2}} + \frac{\dot{\rho}\ddot{z} - \ddot{\rho}\dot{z}}{(\dot{\rho}^2 + \dot{z}^2)^{3/2}}.$$

where dots indicate differentiation with respect to the variable  $s$ .

Due to axisymmetry, the dependence of the integrands on  $\theta$  in this system is known and an initial integration with respect to this variable can be performed. Although the resulting integration yields quite complex expressions, the net result is the reduction of the integration domain from two dimensions to one. The results are

$$\begin{aligned} \frac{1}{2}\mathbf{u}_I(\mathbf{x}_s) = & + \int_{s_o}^{s_f} \mathbf{P}(\mathbf{x}_s, \xi) \cdot \begin{pmatrix} u_\rho \\ u_z \end{pmatrix} d\hat{s} \\ & - \int_{s_o}^{s_f} \mathbf{Q}(\mathbf{x}_s, \xi) \cdot \begin{pmatrix} f_\rho \\ f_z \end{pmatrix} d\hat{s} \end{aligned} \quad (18)$$

$$\begin{aligned} \frac{1}{2}\mathbf{u}_I(\mathbf{x}_s) = & \frac{\lambda - 1}{\lambda + 1} \int_{s_o}^{s_f} \mathbf{P}(\mathbf{x}_s, \xi) \cdot \begin{pmatrix} u_\rho \\ u_z \end{pmatrix} d\hat{s} \\ & - \frac{1}{(\lambda + 1)} \int_{s_o}^{s_f} \mathbf{Q}(\mathbf{x}_s, \xi) \cdot \begin{pmatrix} \mathcal{F}_\rho \\ \mathcal{F}_z \end{pmatrix} d\hat{s} \end{aligned} \quad (19)$$

and

$$\Theta_I(\mathbf{x}_s) = -\left(\frac{2}{1 + \delta}\right)z + \frac{2(\delta - 1)}{1 + \delta} \int_{s_o}^{s_f} \Theta_I(\xi)W(\mathbf{x}_s, \xi)d\hat{s} \quad (20)$$

where

$$d\hat{s} = ds \rho (\dot{\rho}^2 + \dot{z}^2)^{1/2} \quad \text{and} \quad \mathbf{x}_s \in S_I$$

The vector  $\mathbf{u}_I$  has been written as the column vector  $(u_\rho, u_z)^T$ ,  $\mathcal{F}$  as  $(\mathcal{F}_\rho, \mathcal{F}_z)^T$  and  $\mathbf{f}^{(1)}$  as  $(f_\rho, f_z)^T$ . Due to the parametrization, the position vector on the surface,  $\xi$ , is now written as  $\xi(s) = (\rho(s), z(s))$  for  $s \in [0, 1]$ . The form of  $W$  as well as the components of the matrices  $\mathbf{P}$  and  $\mathbf{Q}$  are listed in the appendix.

In principle, equations (18-20) are sufficient to determine temperature, velocity and stress at the surface of the drop. Equation (13) allows subsequent motion of the drop via the instantaneous shape and surface values of velocity.

(b) Implementation

System (18-20) may be discretized and solved numerically. The technique is standard and is described in detail elsewhere (Ascoli, Dandy and Leal (1988 a, b), Youngren and Acrivos (1975)). Briefly, the particle arc  $(\rho(s), z(s))$ ,  $s \in [s_o, s_f]$  is divided into  $N$  elements. This is accomplished by dividing the interval  $[s_o, s_f]$  into subintervals,  $\Delta s_j$ , with centers  $s_j$  ( $j = 1, \dots, N$ ). Each parametric value  $s_j$  corresponds to a point on the arc  $\mathbf{x}_j = (\rho(s_j), z(s_j))$  and each  $\Delta s_j$  corresponds to a segment or element of the arc. The elements are assumed to be sufficiently small that the local normal tractions  $f_\rho$ ,  $f_z$ , the velocities  $u_\rho$ ,  $u_z$  and the temperature  $\Theta_I$  may be assumed approximately constant within each element. The resulting discretized system is:

$$\frac{1}{2} \begin{pmatrix} u_\rho(\mathbf{x}_i) \\ u_z(\mathbf{x}_i) \end{pmatrix} \simeq + \sum_{j=1}^N \left\{ \left[ \int_{\Delta s_j} \mathbf{P}(\mathbf{x}_i, \xi) d\hat{s} \right] \cdot \begin{pmatrix} u_\rho(\mathbf{x}_j) \\ u_z(\mathbf{x}_j) \end{pmatrix} \right\} - \sum_{j=1}^N \left\{ \left[ \int_{\Delta s_j} \mathbf{Q}(\mathbf{x}_i, \xi) d\hat{s} \right] \cdot \begin{pmatrix} f_\rho(\mathbf{x}_j) \\ f_z(\mathbf{x}_j) \end{pmatrix} \right\} \quad (21)$$

$$\frac{1}{2} \begin{pmatrix} u_\rho(\mathbf{x}_i) \\ u_z(\mathbf{x}_i) \end{pmatrix} \simeq \frac{\lambda - 1}{\lambda + 1} \sum_{j=1}^N \left\{ \left[ \int_{\Delta s_j} \mathbf{P}(\mathbf{x}_i, \xi) d\hat{s} \right] \cdot \begin{pmatrix} u_\rho(\mathbf{x}_j) \\ u_z(\mathbf{x}_j) \end{pmatrix} \right\} + \frac{1}{\lambda + 1} \sum_{j=1}^N \left\{ \left[ \int_{\Delta s_j} \mathbf{Q}(\mathbf{x}_i, \xi) \cdot \begin{pmatrix} \mathcal{F}_\rho(\mathbf{x}_j) \\ \mathcal{F}_z(\mathbf{x}_j) \end{pmatrix} d\hat{s} \right] \right\} \quad (22)$$

$1 \leq i \leq N$

$$\Theta_I(\mathbf{x}_i) = - \left( \frac{2}{1 + \delta} \right) z_i + \frac{2(\delta - 1)}{1 + \delta} \sum_{j=1}^N \left\{ \left[ \int_{\Delta s_j} W(\mathbf{x}_i, \xi) d\hat{s} \right] \Theta_I(\mathbf{x}_j) \right\} \quad (23)$$

If a drop shape is known, each coefficient

$$\left[ \int_{\Delta s_j} \mathbf{Q}(\mathbf{x}_i, \xi) d\hat{s} \right] \quad (24)$$

$$\left[ \int_{\Delta s_j} \mathbf{P}(\mathbf{x}_i, \xi) d\hat{s} \right] \quad (25)$$

$$\left[ \int_{\Delta s_j} W(\mathbf{x}_i, \xi) d\hat{s} \right] \quad (26)$$

and the inhomogeneous term

$$\left[ \int_{\Delta s_j} \mathbf{Q}(\mathbf{x}_i, \xi) \cdot \begin{pmatrix} \mathcal{F}_\rho(\mathbf{x}_j) \\ \mathcal{F}_z(\mathbf{x}_j) \end{pmatrix} d\hat{s} \right] \quad (27)$$

for  $j \neq i$  can be easily evaluated by standard numerical integration schemes. When  $j = i$  and  $s = s_i$ , then  $\xi(s) = \mathbf{x}_i$ . In this case, the integrands in (24-27) become unbounded. Although each singularity is theoretically integrable, a direct numerical evaluation leads to obvious problems. Hence, we follow the lead of our earlier boundary integral studies, and approximately evaluate the singular contribution analytically in a small neighborhood of the singular point. The details of this singular contribution are discussed in Ascoli, Dandy and Leal (1988 a, b).

Our goal is to begin with an initial drop shape and determine all subsequent drop shapes and interfacial values of velocity and temperature. Each of the terms (24-27) requires the instantaneous shape for evaluation. In addition, (27) requires knowledge of the instantaneous temperature field. Thus equations (21-23) are coupled through both shape and temperature. Equations (21-23) are instantaneous, i.e. time does not appear explicitly. In the context of the quasi-steady assumption, time evolution enters the problem through the kinematic condition (13).

An iterative scheme has been employed here to solve the system (13) and (21-23). At time  $t$ , a starting shape is assumed to be known either as a consequence of the initial condition (i.e. a spherical drop far from the wall) or by the shape at the previous timestep,  $t - \Delta t$ . An explicit, discretized version of equation (13) is used to obtain an initial guess,  $(\rho^0(s), z^0(s))$  for shape at time  $t$ .

$$\begin{aligned} \rho^0(s, t + \Delta t) &= \rho(s, t) + n_\rho(s, t) \left[ u_\rho(s, t) n_\rho(s, t) \right. \\ &\quad \left. + u_z(s, t) n_z(s, t) \right] \Delta t \\ z^0(s, t + \Delta t) &= z(s, t) + n_z(s, t) \left[ u_\rho(s, t) n_\rho(s, t) \right. \\ &\quad \left. + u_z(s, t) n_z(s, t) \right] \Delta t \end{aligned} \quad (28)$$

This equation is applied at each of the locations  $s_j$  and  $\rho^0$  and  $z^0$  fit with cubic splines. Given  $(\rho^0(s), z^0(s))$ , equation (23) is an  $N \times N$  linear system in the unknown surface temperatures. This system may be solved directly giving an initial guess for the surface temperature field,  $\Theta_I^0(\mathbf{x}_j)$  for  $j = 1, \dots, N$ . These discrete values of surface temperature are fit with a cubic spline. Knowledge of the distribution  $\Theta_I^0(s)$  allows immediate calculation of  $u_\rho^0(\mathbf{x}_j)$  and  $u_z^0(\mathbf{x}_j)$  from the resulting  $N \times N$  linear system (22). An implicit form of equation (13) is then employed to obtain the next approximation to shape  $(\rho^1(s), z^1(s))$  at time  $t + \Delta t$ :

$$\begin{aligned} \rho^{\nu+1}(s, t + \Delta t) &= \rho(s, t) + n_\rho^{\nu+1}(s, t + \Delta t) \left[ u_\rho^\nu(s, t + \Delta t) n_\rho^{\nu+1}(s, t + \Delta t) \right. \\ &\quad \left. + u_z^\nu(s, t + \Delta t) n_z^{\nu+1}(s, t + \Delta t) \right] \Delta t \\ z^{\nu+1}(s, t + \Delta t) &= z(s, t) + n_z^{\nu+1}(s, t + \Delta t) \left[ u_\rho^\nu(s, t + \Delta t) n_\rho^{\nu+1}(s, t + \Delta t) \right. \\ &\quad \left. + u_z^\nu(s, t + \Delta t) n_z^{\nu+1}(s, t + \Delta t) \right] \Delta t \end{aligned} \tag{29}$$

The normal vector  $(n_\rho^{\nu+1}, n_z^{\nu+1})$  is defined in terms of the  $(\rho^{\nu+1}(s), z^{\nu+1}(s))$ . Thus, equation (29) is a nonlinear algebraic system for  $(\rho^{\nu+1}(s_j), z^{\nu+1}(s_j))$ ,  $j = 1, \dots, N$ . This system is solved via Newton's method (details are given in the appendix). The  $\nu + 1$  approximation to shape is then used to calculate the  $\nu + 1$  approximation to velocity and temperature. This process is continued until the solution set  $(\rho^l, z^l, u_\rho^l, u_z^l, \Theta_I^l)$  differs from the  $l - 1$  solution set by less than a prescribed tolerance at the locations  $s_j$ ,  $j = 1, \dots, N$ . This converged solution set will be denoted by  $(\rho, z, u_\rho, u_z, \Theta_I)$ . The converged values of shape and velocity satisfy the following implicit equation:

$$\begin{aligned} \rho(s, t + \Delta t) &= \rho(s, t) + n_\rho(s, t + \Delta t) \left[ u_\rho(s, t + \Delta t) n_\rho(s, t + \Delta t) \right. \\ &\quad \left. + u_z(s, t + \Delta t) n_z(s, t + \Delta t) \right] \Delta t \\ z(s, t + \Delta t) &= z(s, t) + n_z(s, t + \Delta t) \left[ u_\rho(s, t + \Delta t) n_\rho(s, t + \Delta t) \right. \\ &\quad \left. + u_z(s, t + \Delta t) n_z(s, t + \Delta t) \right] \Delta t \end{aligned} \tag{30}$$

This process is repeated for the next time step.

## Numerical Results

All calculations were begun with a spherical starting configuration at a center of mass distance of 5 undeformed radii from the wall. In this configuration, calculated surface velocities, center of mass velocities and surface temperatures were well within 1% of the theoretical values predicted by Young *et al.* (1959). Computational time increases considerably with increasing number of elements. For this reason, calculations were begun with twenty two elements. When the drop center of mass reached approximately 3 radii, additional elements were added so that the total number of elements was thirty-two. Between 4 and 25 iterations in  $\nu$  (equation (29)) were required for convergence of the velocity and temperature fields. Increased deformation corresponded to an increase in the number of iterations required. The Newton's method step, applied to equation (29) for *fixed*  $\nu$  required between two and four iterations for convergence. A single numerical run took between 4000 and 6000 cpu minutes on a Sun 3/160 workstation with a floating point accelerator.

If exactly satisfied, equation (19) guarantees that the net force exerted by the suspending fluid on the drop will be zero (this is easily seen from the definition of  $\mathcal{F}$ ). However, since the numerical solution is subject to discretization errors, the numerically calculated net force on the drop due to the suspending fluid will not be exactly zero. The normalized deviation from zero thus provides a consistency check and measure of numerical error. Equation (18) allows the surface stresses to be calculated, and subsequently the suspending fluid force on the drop to be determined. This force was normalized by the mean magnitude of local calculated surface stresses. When this normalized force deviated by 10% from zero, calculations were terminated. Typically, this normalized force was of the order of 1% or less when the center of mass of the drop was more than one undeformed radii from the wall. In the very latest stages of deformation, this normalized force increased dramatically.

Shape calculations are shown in figures 2-7. The elapsed time between

plotted shape curves is  $\frac{1}{2}$  dimensionless time unit (i.e. the time required for a spherical drop to translate  $\frac{1}{2}$  of a radii in the absence of the wall). In all cases, deformation begins by blunting of the drop at both the side nearest and the side farthest from the wall. Coincident with this blunting is an overall widening of the drop. Maximum deformation of the drop occurs at the side nearest the wall.

In the last stages of deformation shown, the side of the drop nearest the wall flattens. For the bubble cases  $\lambda = \delta = 0.01$  and  $\omega = -1, -3,$  and  $-9$  a “dimple” (i.e. a configuration where the minimum  $z$ -distance between the and the wall occurs at a value of  $\rho > 0$ ) is noticeable.

Deformation is best discussed in terms of the effective capillary number,  $Ca$ . For  $\lambda = \delta = 0.01$  and  $\omega = -0.3, -1, -3$  and  $-9$  the respective, effective capillary numbers are 0.147, 0.490, 1.47, and 4.41. Capillary number is a measure of the relative importance of viscous effects to surface tension effects. Thus, larger capillary number corresponds to increased deformation of the drop in a given flow situation. The parameter  $\omega$  is a measure of the *variation* of surface tension across the bubble or drop. Large  $|\omega|$  corresponds to large variation in surface tension and thus greater potential for deformation. Consequently,  $Ca$  increases with increasing  $|\omega|$ . Greater deformation for increasing capillary number is easily seen in figures 2-5. This trend is further demonstrated in figure 8.

For  $\lambda = \delta = 0.01$ , normalized velocity of the bubble center of mass,  $V_c$ , is plotted versus center of mass location,  $Z_c$ , in figure 9. Due to the choice of non-dimensionalization the velocity,  $V_c$ , is normalized by  $U$ , the velocity for a spherical bubble in the absence of a wall. The trends in *dimensional* velocity are easily implied from the definition of  $U$ . This figure demonstrates the *relative* trends in velocity and in particular the trends due to interaction with the wall. For  $Z_c$  in the range 1.3 to 2.5,  $V_c$  values are smaller than those predicted by Meyyappan *et al*(1980) for a spherical bubble. In this region, bubble deformation begins. Blunting of the bubble side nearest the wall and widening of the bubble corresponds to a shift in center of mass location away from the wall.

This phenomenon results in a lower  $V_c$  value. As expected, the largest deviation from the spherical bubble  $V_c$  predictions occurs for the largest  $Ca$ .

In the range  $Z_c < 1.3$ , the deformable bubbles have  $V_c$  values greater than the non-deforming spherical bubble, the largest  $V_c$  deviation occurring for the bubble with the highest  $Ca$ . In this range, stress forces at the side of the spherical bubble nearest the wall increase dramatically. These forces oppose the downward motion of the spherical bubble thus reducing  $V_c$ . For the deforming bubbles, a similar phenomenon occurs. In this case, the downward velocity of the interface region nearest the wall decreases relative to the edge and back of the bubble. As a result, the bubble flattens and broadens near the wall. Flattening and broadening of the bubble corresponds to a motion of  $Z_c$  toward the wall. This deformation results in a larger  $V_c$  value than for the spherical bubble. Once again, the degree of deformation increases with increasing  $Ca$ . Thus,  $V_c$  increases with increasing  $Ca$ .

The difference between the maximum and minimum temperatures on the bubble surface provides an indication of the interaction between temperature effects and deformation. This maximum temperature difference,  $DT_{max}$  (normalized by  $3|G|/(2 + \delta)$ , the maximum temperature across a spherical drop in the absence of the wall) is plotted in figure 10. Once again, due to the normalization, this figure provides relative trends and interaction effects due to the wall. For a spherical bubble ( $\lambda = \delta = 0$ )  $DT_{max}$  decreases with  $Z_c$  due to interactions of a non-conducting sphere with the wall (Meyyappan *et al* (1980)). In addition, deformation is observed to decrease the  $z$ -extent of the bubble.  $DT_{max}$  decreases as a consequence of this deformation.

Capillary number decreases with increasing  $\lambda$  or  $\delta$ . An increasing value of  $\delta$  corresponds to increased conduction in the drop relative to the outer fluid. This reduces the temperature difference across the drop and subsequently the driving force for motion and deformation. Similarly, increasing  $\lambda$  corresponds to increased viscous effects in the drop relative to the outer fluid. The relative

ease with which the drop fluid circulates decreases with increasing  $\lambda$ . The thermocapillary motion derives from the motion of the interface between the drop and the outer fluid. This interface motion is reduced when circulation within the drop increases in difficulty. As a consequence, the overall magnitude of the motion is damped by increased drop viscosity relative to outer fluid viscosity. This may be seen directly from the definition of  $U$ , the velocity of a spherical drop in the absence of the wall. For  $\lambda = 1$ ,  $\delta = 0.01$ ,  $\omega = -1$  and  $\lambda = 1$ ,  $\delta = 1$ ,  $\omega = -1$  the respective capillary numbers are 0.199 and 0.133. Figure 11 shows the degree of deformation for these cases relative to the case  $\lambda = 0.01$ ,  $\delta = 0.01$ ,  $\omega = -1$  ( $Ca = 0.49$ ). As expected, the degree of deformation increases with increasing  $Ca$ .

Figures 12 and 13 demonstrate the effects of increasing  $\lambda$  and  $\delta$  on  $V_c$  and  $DT_{max}$ . Increasing  $\lambda$  corresponds to increased damping of the velocity fields. Consequently, interaction between the wall and the velocity field generated by the drop will be reduced. The net result is a *normalized* center of mass velocity which is higher (closer to the value predicted in the absence of the wall). An analogous statement applies to the  $DT_{max}$  results. Note that  $\delta = 1$  corresponds to an *exactly* linear temperature field throughout fluid 1 and fluid 2. Therefore, the  $\delta = 1$  result corresponds to a reduction in  $DT_{max}$  entirely due to deformation.

## Conclusions

Thermocapillary migration of a deformable drop has been shown to depend on the viscosity ratio,  $\lambda$ , the thermal conductivity ratio,  $\delta$ , and the dimensionless rate of change of surface tension with temperature,  $\omega$ . In particular, these parameters combine to form an effective capillary number

$$Ca = \frac{|\omega|}{(1 + \frac{3}{2}\lambda)(2 + \delta)}$$

Increasing  $Ca$  corresponds to increased deformation at a particular center of mass location. In particular, deformation increases with increasing  $|\omega|$  and decreases with increasing  $\lambda$  and  $\delta$ . Equivalently, the distance at which wall interactions become significant increases with  $|\omega|$  and decreases with increasing  $\lambda$  and  $\delta$ . In all cases considered, wall interactions were found to be significant only for  $Z_c < 3$ .

## Appendix

(a) The integrands  $\mathbf{P}$ ,  $\mathbf{Q}$ , and  $W$

After integrating analytically in the axial direction, the integrands reduce to the form

$$\begin{pmatrix} P_{11} & P_{12} \\ P_{21} & P_{22} \end{pmatrix} \begin{pmatrix} u_\rho \\ u_z \end{pmatrix} \quad (A1)$$

$$\begin{pmatrix} Q_{11} & Q_{12} \\ Q_{21} & Q_{22} \end{pmatrix} \begin{pmatrix} f_\rho \\ f_z \end{pmatrix},$$

$$\begin{pmatrix} Q_{11} & Q_{12} \\ Q_{21} & Q_{22} \end{pmatrix} \begin{pmatrix} \mathcal{F}_\rho \\ \mathcal{F}_z \end{pmatrix}, \quad (A2)$$

and

$$W\Theta_I$$

The elements of the matrices  $\mathbf{P}$  and  $\mathbf{Q}$  along with the scalar  $W$  are:

$$\begin{aligned} \frac{4\pi}{3}P_{11} = & \rho\rho_\circ^2 n_\rho (C_5^{03} - \hat{C}_5^{03}) + \rho_\circ [\rho n_z (r_3 C_5^{02} - R_3 \hat{C}_5^{02}) \\ & + n_\rho (2\rho^2 + \rho_\circ^2) (C_5^{02} - \hat{C}_5^{02})] + \rho n_\rho (2\rho_\circ^2 + \rho^2) (C_5^{01} - \hat{C}_5^{01}) \\ & + n_z (\rho^2 + \rho_\circ^2) (r_3 C_5^{01} - R_3 \hat{C}_5^{01}) + \rho\rho_\circ [\rho n_\rho (C_5^{00} - \hat{C}_5^{00}) \\ & + n_z (r_3 C_5^{00} - R_3 \hat{C}_5^{00})] - 2x_3 \{-x_3 n_\rho (\rho \hat{C}_5^{01} + \rho_\circ \hat{C}_5^{00} \\ & + z \{2\rho_\circ n_\rho \hat{C}_5^{02} + (2\rho n_\rho + n_z R_3) \hat{C}_5^{01}\}) + 10x_3 z [\rho\rho_\circ^2 n_\rho \hat{C}_7^{03} \\ & + \rho_\circ \{\rho n_z R_3 + n_\rho (2\rho^2 + \rho_\circ^2)\} \hat{C}_7^{02} + \{\rho n_\rho (2\rho_\circ^2 + \rho^2) \\ & + n_z R_3 (\rho^2 + \rho_\circ^2)\} \hat{C}_7^{01} + \rho\rho_\circ (\rho n_\rho + n_z R_3) \hat{C}_7^{00}] \end{aligned} \quad (A3)$$

$$\begin{aligned} -\frac{4\pi}{3}P_{12} = & \rho\rho_\circ n_\rho (r_3 C_5^{02} - R_3 \hat{C}_5^{02}) + \rho n_z (r_3^2 C_5^{01} - R_3^2 \hat{C}_5^{01}) \\ & + n_\rho (\rho^2 + \rho_\circ^2) (r_3 C_5^{01} - R_3 \hat{C}_5^{01}) + \rho_\circ \{\rho n_\rho (r_3 C_5^{00} - R_3 \hat{C}_5^{00}) \\ & + n_z (r_3^2 C_5^{00} - R_3^2 \hat{C}_5^{00})\} - 2x_3 [-x_3 n_z (\rho \hat{C}_5^{01} + \rho_\circ \hat{C}_5^{00}) \\ & + z n_\rho R_3 \hat{C}_5^{01}] + 10x_3 z R_3 [\rho\rho_\circ n_\rho \hat{C}_7^{02} \\ & + \{\rho n_z R_3 + (\rho^2 + \rho_\circ^2) n_\rho\} \hat{C}_7^{01} + \rho_\circ (\rho n_\rho + n_z R_3) \hat{C}_7^{00}] \end{aligned} \quad (A4)$$

$$\begin{aligned}
 -\frac{4\pi}{3}P_{21} = & \rho_o^2 n_\rho (r_3 C_5^{02} - R_3 \hat{C}_5^{02}) + 2\rho\rho_o n_\rho (r_3 C_5^{01} - R_3 \hat{C}_5^{01}) \\
 & + \rho_o n_z (r_3^2 C_5^{01} - R_3^2 \hat{C}_5^{01}) + \rho^2 n_\rho (r_3 C_5^{00} - R_3 \hat{C}_5^{00}) \\
 & + \rho n_z (r_3^2 C_5^{00} - R_3^2 \hat{C}_5^{00}) + 2x_3 [-x_3 n_\rho R_3 \hat{C}_5^{00} \\
 & + z n_z (\rho_o \hat{C}_5^{01} + \rho \hat{C}_5^{00}) + \rho_o^2 n_\rho \hat{C}_5^{02} \\
 & + \rho_o (2\rho n_\rho + n_z R_3) \hat{C}_5^{01} \rho (\rho n_\rho + n_z R_3) \hat{C}_5^{00}] \\
 & - 10x_3 z R_3 [\rho_o^2 n_\rho \hat{C}_7^{02} + \rho_o (2\rho n_\rho + n_z R_3) \hat{C}_7^{01} \\
 & + \rho (\rho n_\rho + n_z R_3) \hat{C}_7^{00}]
 \end{aligned} \tag{A5}$$

$$\begin{aligned}
 \frac{4\pi}{3}P_{22} = & \rho_o n_\rho (r_3^2 C_5^{01} - R_3^2 \hat{C}_5^{01}) + \rho n_\rho (r_3^2 C_5^{00} - R_3^2 \hat{C}_5^{00}) \\
 & + n_z (r_3^3 C_5^{00} - R_3^3 \hat{C}_5^{00} + 2x_3 [-x_3 R_3 n_z \hat{C}_5^{00} \\
 & + z \{ \rho_o n_\rho \hat{C}_5^{01} + (\rho n_\rho + 2n_z R_3) \hat{C}_5^{00} \}] \\
 & + 2x_3 R_3 [\rho_o n_\rho \hat{C}_5^{01} + (\rho n_\rho + n_z R_3) \hat{C}_5^{00}] \\
 & - 10x_3 z R_3^2 [\rho_o n_\rho \hat{C}_7^{01} + (\rho n_\rho + n_z R_3) \hat{C}_7^{00}]
 \end{aligned} \tag{A6}$$

$$\begin{aligned}
 -8\pi Q_{11} = & C_1^{01} - \hat{C}_1^{01} + \rho\rho_o (C_3^{02} - \hat{C}_3^{02}) + (\rho^2 + \rho_o^2) (C_3^{01} - \hat{C}_3^{01}) \\
 & + \rho\rho_o (C_3^{00} - \hat{C}_3^{00}) - 2x_3 z [\hat{C}_3^{01} \\
 & - 3\{ (\rho^2 + \rho_o^2) \hat{C}_5^{01} + \rho\rho_o (\hat{C}_5^{02} + \hat{C}_5^{00}) \}]
 \end{aligned} \tag{A7}$$

$$\begin{aligned}
 8\pi Q_{12} = & \rho (r_3 C_3^{01} - R_3 \hat{C}_3^{01}) + \rho_o (r_3 C_3^{00} - R_3 \hat{C}_3^{00}) \\
 & + 2x_3 [\rho \hat{C}_3^{01} + \rho_o \hat{C}_3^{00} + 3z R_3 (\rho \hat{C}_5^{01} + \rho_o \hat{C}_5^{00})]
 \end{aligned} \tag{A8}$$

$$\begin{aligned}
 8\pi Q_{21} = & \rho_o (r_3 C_3^{01} - R_3 \hat{C}_3^{01}) + \rho (r_3 C_3^{00} - R_3 \hat{C}_3^{00}) \\
 & + 2x_3 [\rho_o \hat{C}_3^{01} + \rho \hat{C}_3^{00} - 3z R_3 (\rho_o \hat{C}_5^{01} + \rho \hat{C}_5^{00})]
 \end{aligned} \tag{A9}$$

$$\begin{aligned}
 -8\pi Q_{22} = & C_1^{00} - \hat{C}_1^{00} + r_3^2 C_3^{00} - R_3^2 \hat{C}_3^{00} \\
 & + 2x_3 z (\hat{C}_3^{00} - 3R_3^2 \hat{C}_5^{00}).
 \end{aligned} \tag{A10}$$

$$4\pi W = C_3^{00} (\rho n_\rho + r_3 n_z) + \rho_o n_\rho (C_3^{01} - \hat{C}_3^{01}) - \hat{C}_3^{00} (\rho n_\rho + R_3 n_z) \tag{A11}$$

The point  $(\rho, z)$  corresponds to the location of integration, and  $(\rho_o, x_3)$  is the singular point. Also,  $r_3 = z - x_3$  and  $R_3 = z + x_3$ . The symbols  $C_p^{nm}$  and  $\hat{C}_p^{nm}$

are defined by

$$C_p^{nm} \equiv \frac{2}{\gamma^{p/2}} \int_0^\pi \frac{\sin^n 2x \cos^m 2x}{[1 - k^2 \sin^2 x]^{p/2}} dx \quad (\text{A12})$$

and

$$\hat{C}_p^{nm} \equiv \frac{2}{\gamma_R^{p/2}} \int_0^\pi \frac{\sin^n 2x \cos^m 2x}{[1 - k_R^2 \sin^2 x]^{p/2}} dx, \quad (\text{A13})$$

where

$$\begin{aligned} \gamma &= (\rho + \rho_o)^2 + r_3^2 \\ k^2 &= \frac{4\rho\rho_o}{\gamma} \end{aligned}$$

and

$$\begin{aligned} \gamma_R &= (\rho + \rho_o)^2 + R_3^2 \\ k_R^2 &= \frac{4\rho\rho_o}{\gamma_R}. \end{aligned}$$

Using definitions (A12) and (A13),  $C_p^{nm}$  and  $\hat{C}_p^{nm}$  may be written in terms of elliptic integrals of the first and second kind. Expressions for  $C_p^{nm}$  and  $\hat{C}_p^{nm}$  may be found in Ascoli, Dandy and Leal (1988 a, b).

(c) Solution of Equation (29)

In practice, equation (29) is solved by first writing the unknown normal components  $(n_\rho^j, n_z^j)$  in terms of derivatives of  $(\dot{\rho}^\nu, \dot{z}^\nu)$ :

$$\begin{aligned} n_\rho^\nu &= \frac{\dot{z}^\nu}{((\dot{\rho}^\nu)^2 + (\dot{z}^\nu)^2)^{1/2}} \\ n_z^\nu &= -\frac{\dot{\rho}^\nu}{((\dot{\rho}^\nu)^2 + (\dot{z}^\nu)^2)^{1/2}}, \end{aligned}$$

Using the superscript “old” to denote the converged result at the previous timestep, this gives

$$((\dot{\rho}^\nu)^2 + (\dot{z}^\nu)^2)(z^\nu - z^{old}) + \Delta t \dot{\rho}^\nu (u_\rho^{\nu-1} \dot{z}^\nu - \dot{\rho}^\nu u_z^{\nu-1}) = 0 \quad (\text{A14})$$

These equations may be applied for  $s = s_i$ ,  $i = 2, \dots, N - 1$ .

$$((\dot{\rho}^\nu)^2 + (\dot{z}^\nu)^2)(\rho^\nu - \rho^{old}) - \Delta t \dot{z}^\nu (u_\rho^{\nu-1} \dot{z}^\nu - \dot{\rho}^\nu u_z^{\nu-1}) = 0 \quad (\text{A15})$$

The derivatives  $(\dot{\rho}^\nu, \dot{z}^\nu)$  for each node location,  $i, i = 2, \dots, N - 1$ , are given in terms of the cubic spline coefficients  $a_i^\nu$  and  $b_i^\nu$  as

$$\dot{\rho}_i^\nu = \frac{(\rho_{i+1}^\nu - \rho_i^\nu)}{h_i} - \frac{h_i}{6}(a_{i+1}^\nu + 2a_i^\nu) \quad (\text{A16})$$

$$\dot{z}_i^\nu = \frac{(z_{i+1}^\nu - z_i^\nu)}{h_i} - \frac{h_i}{6}(b_{i+1}^\nu + 2b_i^\nu) \quad (\text{A17})$$

Where  $h_i = s_i - s_{i-1}$  and for  $i = 2, \dots, N - 1$  the cubic spline coefficients satisfy

$$\left(\frac{h_{i-1}}{h_i}\right)a_{i-1}^\nu + 2\frac{h_i + h_{i+1}}{h_i}a_i^\nu + a_{i+1}^\nu - \frac{6}{h_i} \left[ \frac{(\rho_{i+1}^\nu - \rho_i^\nu)}{h_i} + \frac{(\rho_{i-1}^\nu - \rho_i^\nu)}{h_{i-1}} \right] = 0 \quad (\text{A18})$$

$$\left(\frac{h_{i-1}}{h_i}\right)b_{i-1}^\nu + 2\frac{h_i + h_{i+1}}{h_i}b_i^\nu + b_{i+1}^\nu - \frac{6}{h_i} \left[ \frac{(z_{i+1}^\nu - z_i^\nu)}{h_i} + \frac{(z_{i-1}^\nu - z_i^\nu)}{h_{i-1}} \right] = 0 \quad (\text{A19})$$

At  $i = 1$  and  $i = N$ ,  $\dot{z} = 0$  and  $\dot{\rho}$  is determined by the choice of the parametrization in  $s$  thus

$$0 = \frac{1}{h_1}(z_2^\nu - z_1^\nu) - \frac{h_1}{6}(b_2^\nu + 2b_1^\nu) \quad (\text{A20})$$

$$0 = \frac{1}{h_{N-1}}(z_N^\nu - z_{N-1}^\nu) + \frac{h_{N-1}}{6}(2b_N^\nu + b_{N-1}^\nu) \quad (\text{A21})$$

$$\dot{\rho}_1 = \frac{1}{h_1}\rho_2^\nu - \frac{h_1}{6}(a_2^\nu + 2a_1^\nu) \quad (\text{A22})$$

$$\dot{\rho}_N = -\frac{1}{h_N}\rho_{N-1}^\nu + \frac{h_{N-1}}{6}(2a_N^\nu + a_{N-1}^\nu) \quad (\text{A23})$$

In addition, at  $i = 1$  and  $i = N$ ,  $\rho = 0$  and

$$z_1^\nu = z_1^{old} + (u_z^{\nu-1})_1 \Delta t$$

$$z_N^\nu = z_N^{old} + (u_z^{\nu-1})_N \Delta t$$

There are  $4 \times N - 4$  unknowns,  $\rho_i^{\nu+1}$  and  $z_i^{\nu+1}$  for  $i = 2, \dots, N - 1$  and  $a_i^{\nu+1}$  and  $b_i^{\nu+1}$  for  $i = 1, \dots, N$ . Using (A16) and (A17), equations (A14) and (A15) provide  $2 \times N - 4$  relations. Equations (A16) and (A17) also provide  $2 \times N - 4$  relations. Equations (A20-A23) provide the final conditions necessary to determine the unknowns. Newton's method was used to solve this non-linear system.

Note that  $\dot{\rho}_1$  and  $\dot{\rho}_N$  are assumed known at this stage. These values are only known approximately. In practice, they are estimated and relaxed from the previous  $\nu$  iteration.

## References

- Ascoli, E.P., 1987 Masters Thesis, California Institute of Technology.
- (a) Ascoli, E.P., Dandy, D.S. & Leal, L.G. 1988 *Low-Reynolds number hydrodynamic interaction of a solid particle with a planar wall* submitted to *Int. J. Numer. Methods Fluids*.
- (b) Ascoli, E.P., Dandy, D.S. & Leal, L.G. 1988 *Buoyancy-driven motion of a deformable drop toward a planar wall at low Reynolds number*, manuscript in preparation.
- Blake, J.R. 1971 *Proc. Phil. Soc.* **70**, 303.
- Chi, B.K. 1986 PhD Thesis, California Institute of Technology, May 19.
- Kantorovich, L.V. & Krylov, V.I. 1963 *Approximate Methods of Higher Analysis*, Interscience.
- Ladyzhenskaya, O.A. 1963 *The Mathematical Theory of Viscous Incompressible Flow*, Gordon and Breach, New York.
- Lee, S.H. & Leal, L.G. 1982 *J. Colloid Interface Sci.* **87**, 81.
- Meyyappan, M., Wilcox, W.R. & Subramanian, R.S. 1981 *J. Colloid Interface Sci.* **83**, 199.
- Meyyappan, M. & Subramanian, R.S. 1987 *J. Colloid Interface Sci.* **115**, 207.
- Rallison, J.M. & Acrivos, A. 1978 *J. Fluid Mech.* **89**, 91.
- Subramanian, R. S. 1981 *AIChE J.* **27**, 646.
- Trefethan, L. M. 1969, *Surface Tension in Fluid Mechanics*, A color film by Encyclopedia Britannica Educational Corporation.
- Weinberg, M. C., 1978 *The Glass Industry* **59**, 22.
- Young, N.O., Goldstein, J.S. & Block, M.J. 1959 *J. Fluid Mech.* **6**, 351.
- Youngren, G.K. & Acrivos, A. 1975 *J. Fluid Mech.* **69**, 377.
- Youngren, G.K. & Acrivos, A. 1976 *J. Fluid Mech.* **76**, 433.

### Figure captions

Figure 1: Schematic of the problem.

Figure 2: Evolution of "bubble" shape.  $\lambda = \delta = 0.01$ ,  $\omega = -9$ . Elapsed time between subsequent shapes is  $\frac{1}{2}$  dimensionless time unit.

Figure 3: Evolution of "bubble" shape.  $\lambda = \delta = 0.01$ ,  $\omega = -3$ . Elapsed time between subsequent shapes is  $\frac{1}{2}$  dimensionless time unit.

Figure 4: Evolution of "bubble" shape.  $\lambda = \delta = 0.01$ ,  $\omega = -1$ . Elapsed time between subsequent shapes is  $\frac{1}{2}$  dimensionless time unit.

Figure 5: Evolution of "bubble" shape.  $\lambda = \delta = 0.01$ ,  $\omega = -0.3$ . Elapsed time between subsequent shapes is  $\frac{1}{2}$  dimensionless time unit.

Figure 6: Evolution of drop shape.  $\lambda = 1$ ,  $\delta = 0.01$ ,  $\omega = -1$ . Elapsed time between subsequent shapes is  $\frac{1}{2}$  dimensionless time unit.

Figure 7: Evolution of drop shape.  $\lambda = \delta = 1$ ,  $\omega = -1$ . Elapsed time between subsequent shapes is  $\frac{1}{2}$  dimensionless time unit.

Figure 8: Comparison of "bubble" shapes.  $\lambda = \delta = 0.01$  and  $Z_c = 1.1$ . ——— undeformed sphere; .....  $\omega = -0.3$ ; - - -  $\omega = -1$ ; - - -  $\omega = -3$ ; - - - -  $\omega = -9$ .

Figure 9:  $V_c$  versus  $Z_c$  for  $\lambda = \delta = 0.01$ . .....  $\omega = -0.3$ ; - - -  $\omega = -1$ ; - - -  $\omega = -3$ ; - - - -  $\omega = -9$ . ——— undeformed spherical bubble results given by Meyyappan *et al.* (1980);

Figure 10:  $DT_{max}$  versus  $Z_c$  for  $\lambda = \delta = 0.01$ . .....  $\omega = -0.3$ ; - - -  $\omega = -1$ ; - - -  $\omega = -3$ ; - - - -  $\omega = -9$ .

Figure 11: Comparison of shapes at  $Z_c = 1.1$ . ——— undeformed sphere; .....  $\lambda = \delta = 0.01$ ,  $\omega = -1$ ; - - -  $\lambda = 1$ ,  $\delta = 0.01$ ,  $\omega = -1$ ; - - -  $\lambda = \delta = 1$ ,  $\omega = -1$ .

Figure 12:  $V_c$  versus  $Z_c$ . .....  $\lambda = \delta = 0.01$ ,  $\omega = -1$ ; - - -  $\lambda = 1$ ,  $\delta = 0.01$ ,  $\omega = -1$ ; - - -  $\lambda = \delta = 1$ ,  $\omega = -1$ .

Figure 13:  $DT_{max}$  versus  $Z_c$  .....  $\lambda = \delta = 0.01, \omega = -1$ ; - - -  $\lambda = \delta = 1, \omega = -1$ .

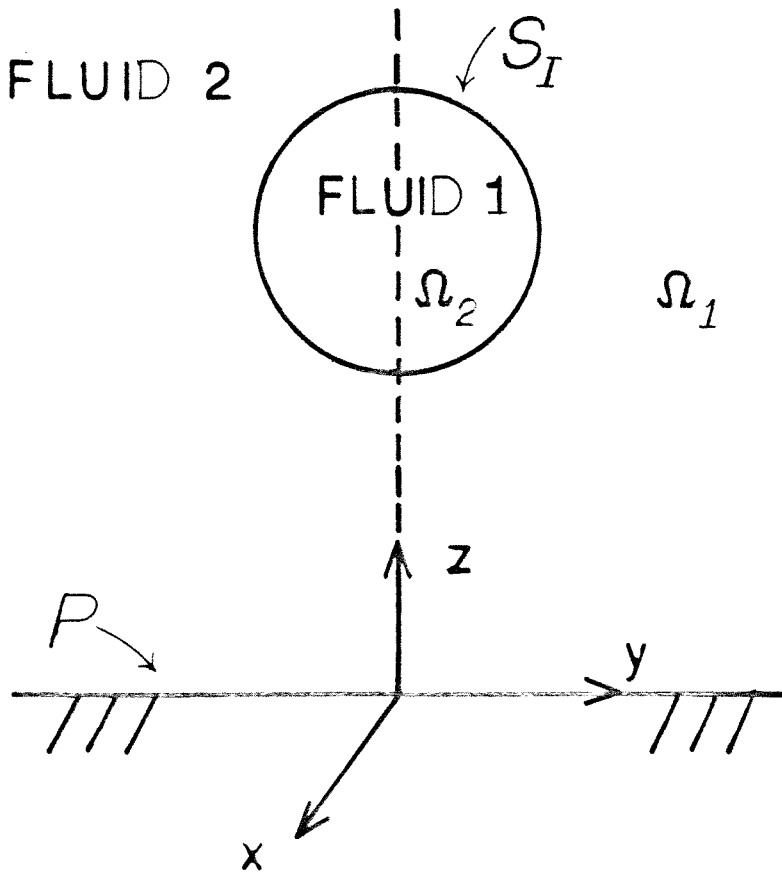


Figure 1

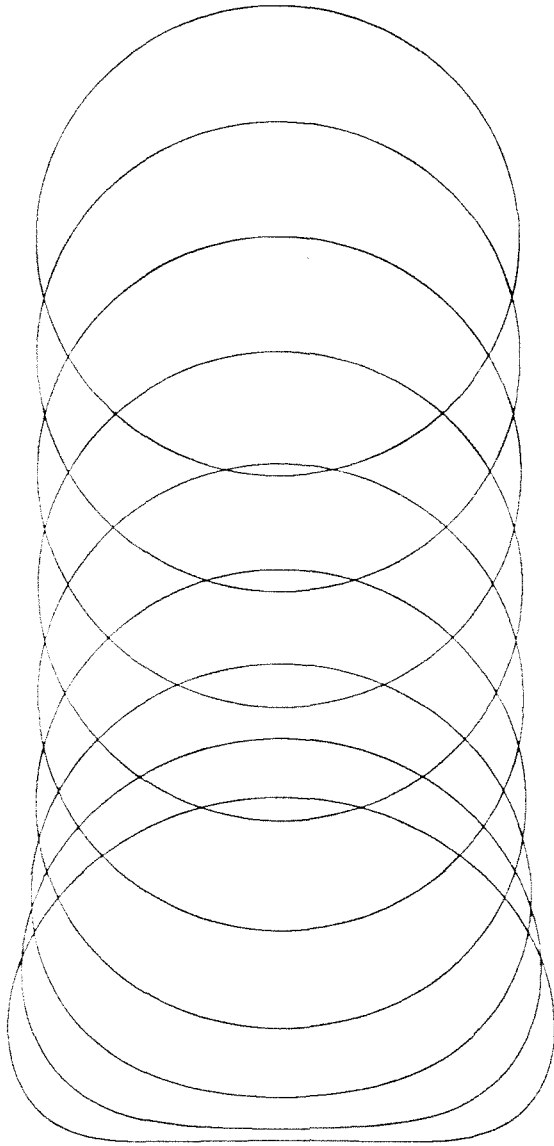


Figure 2

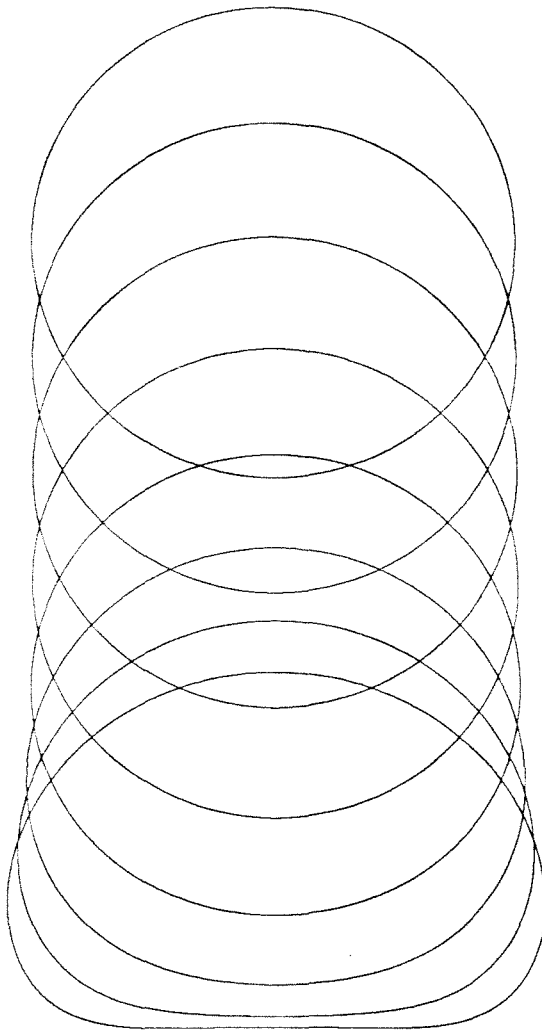
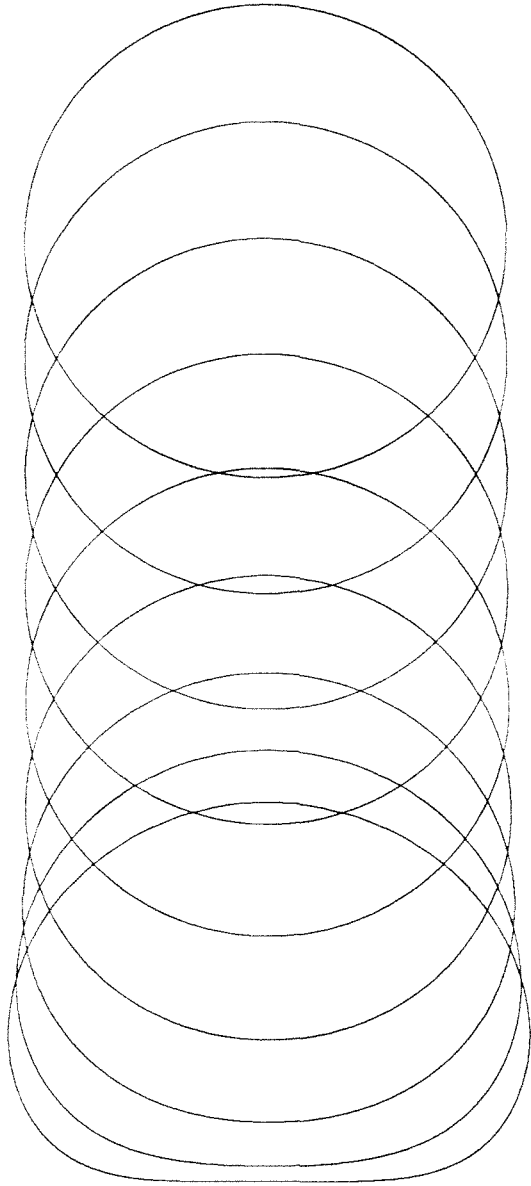


Figure 3



---

Figure 4

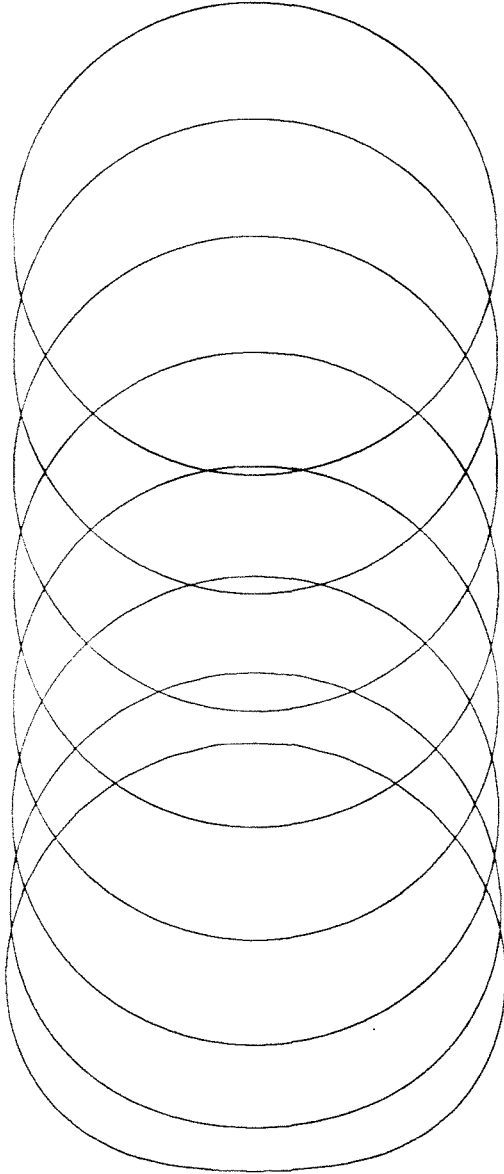


Figure 5

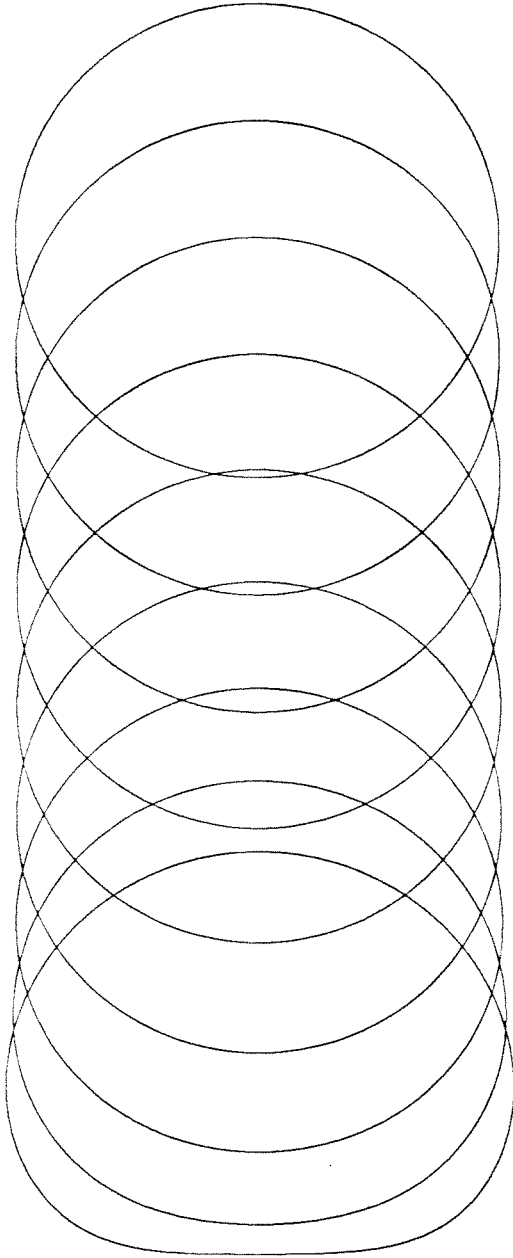


Figure 6

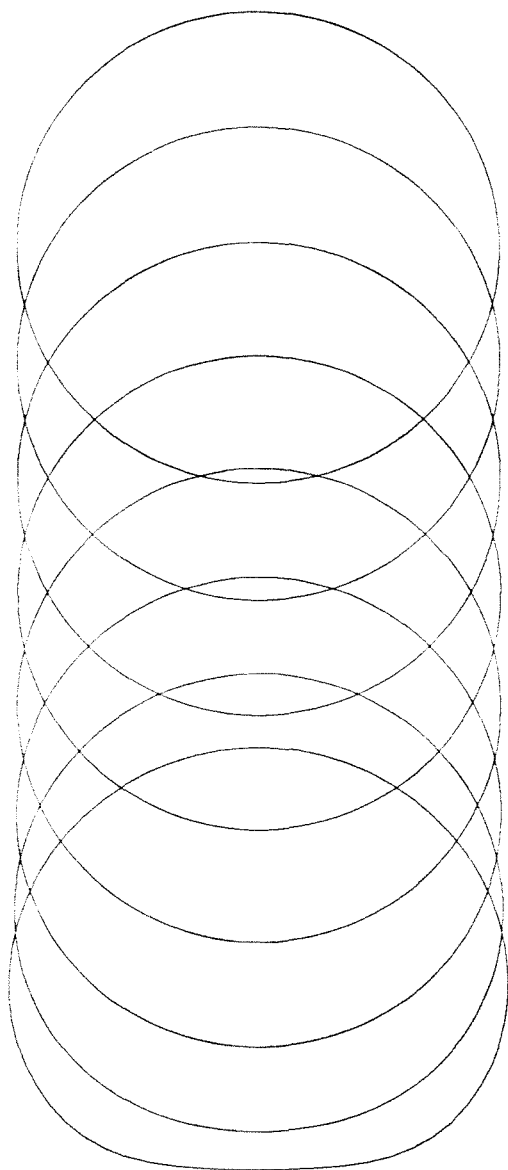


Figure 7

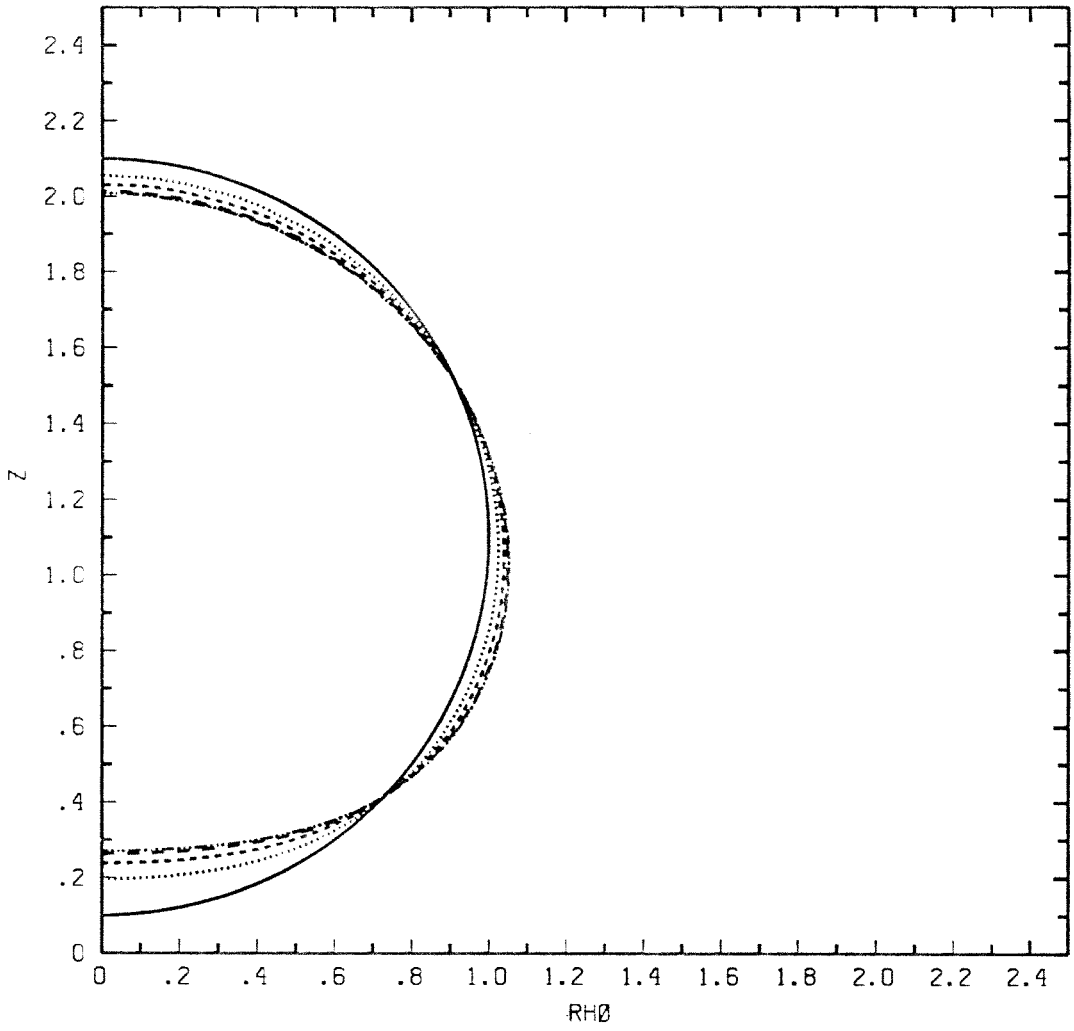


Figure 8

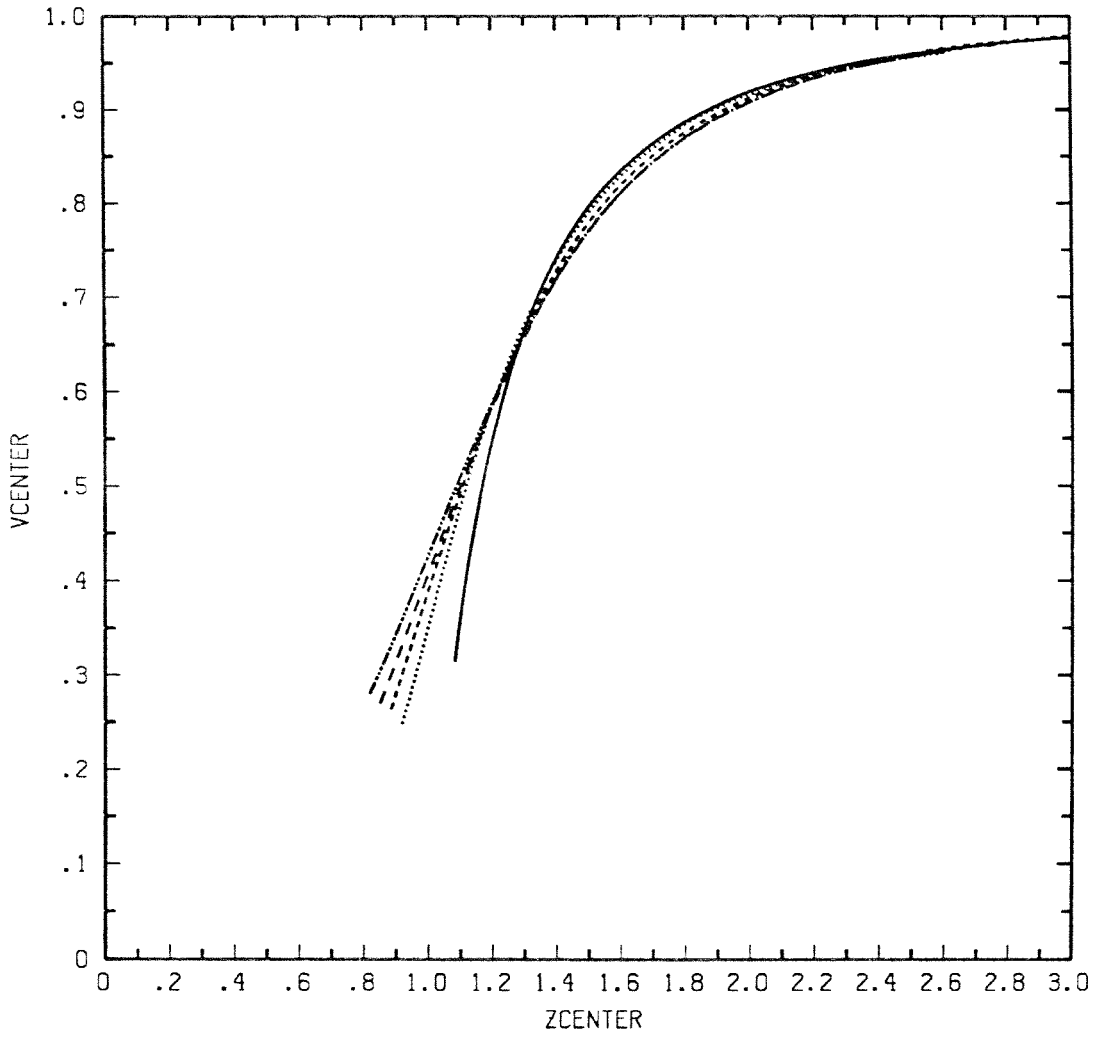


Figure 9

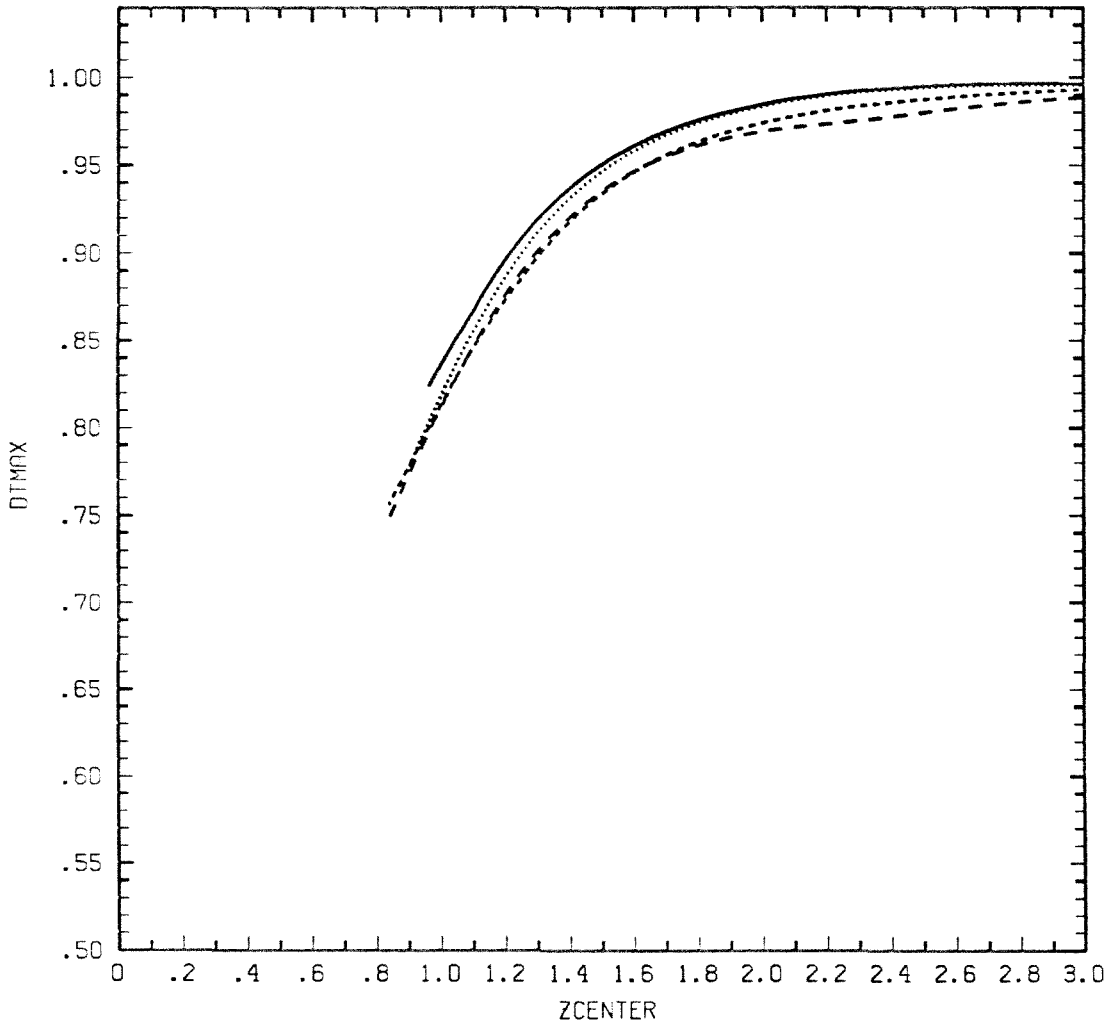


Figure 10

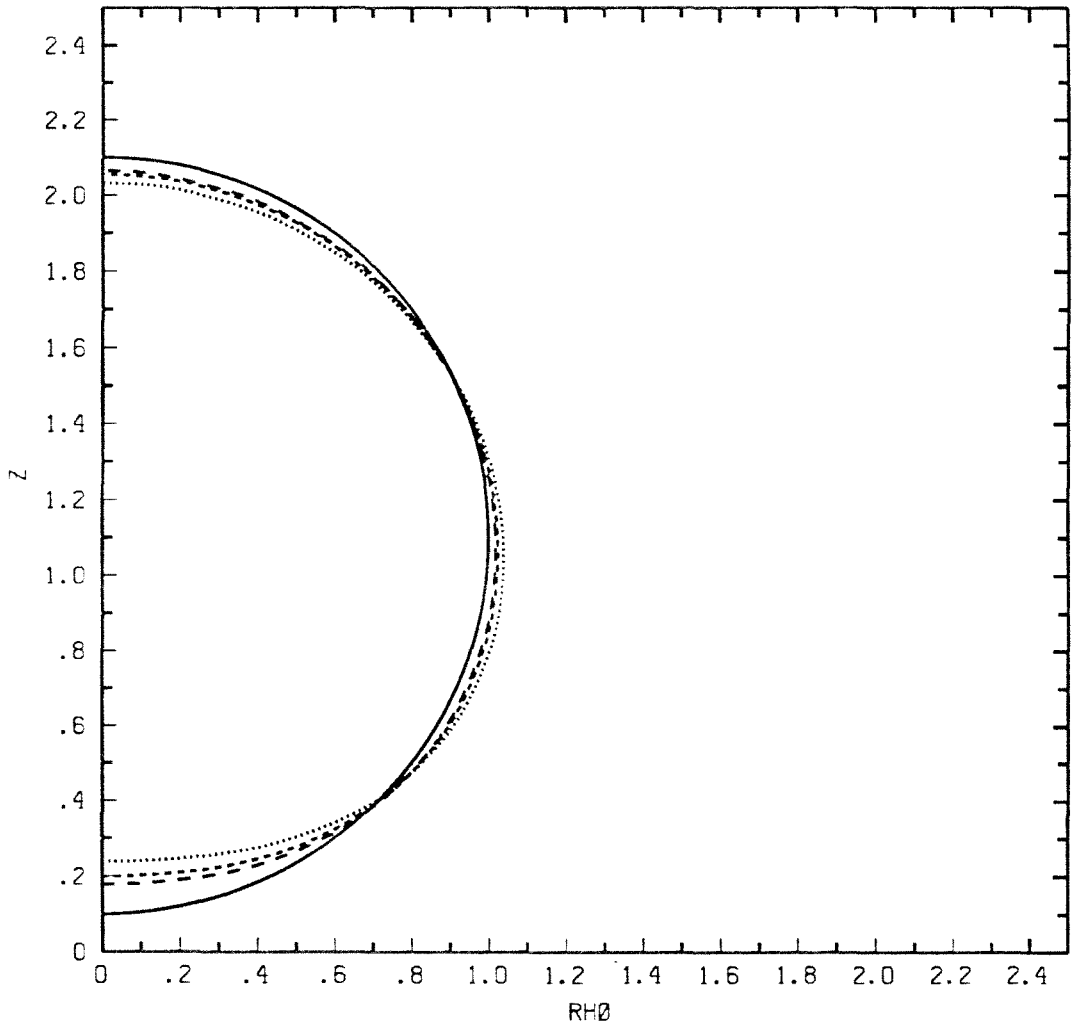


Figure 11

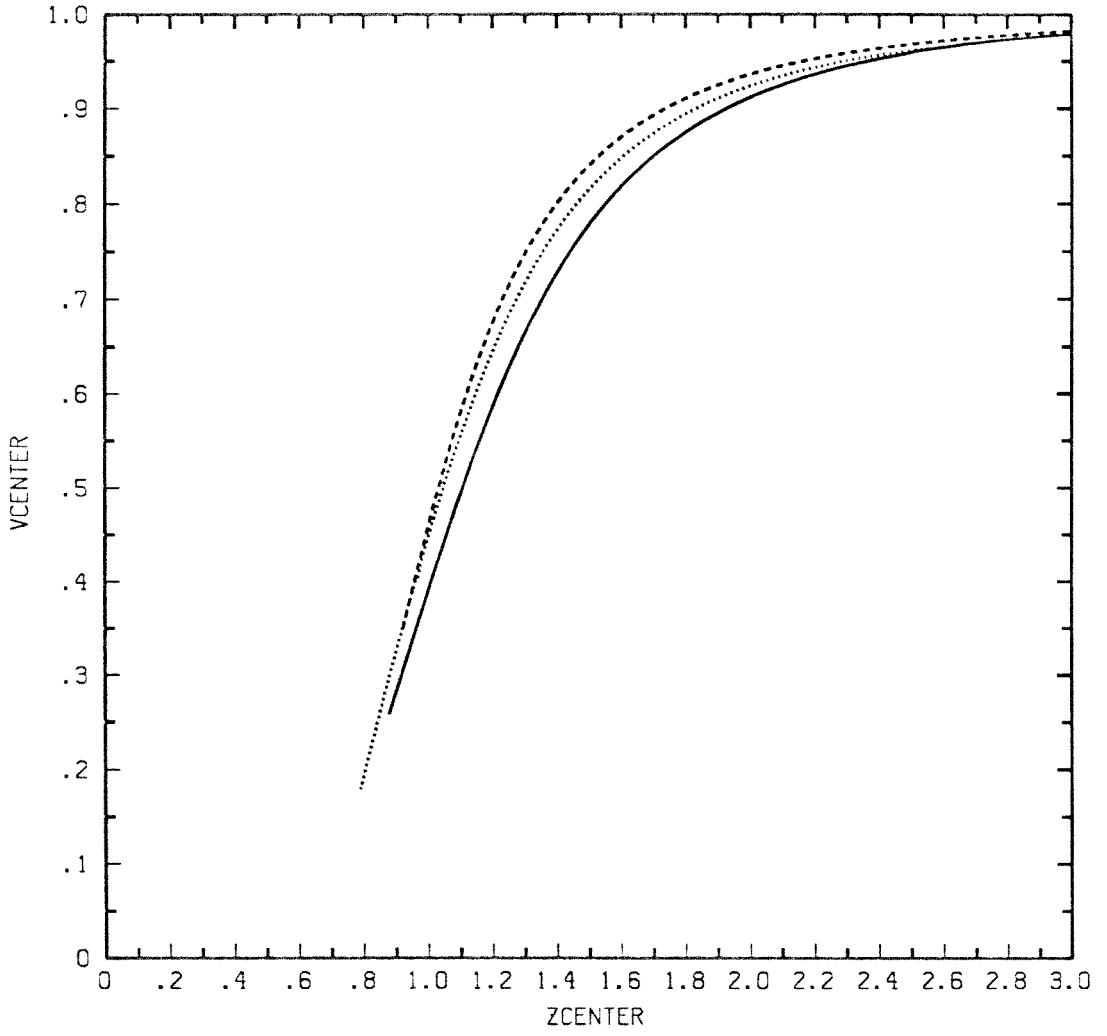


Figure 12

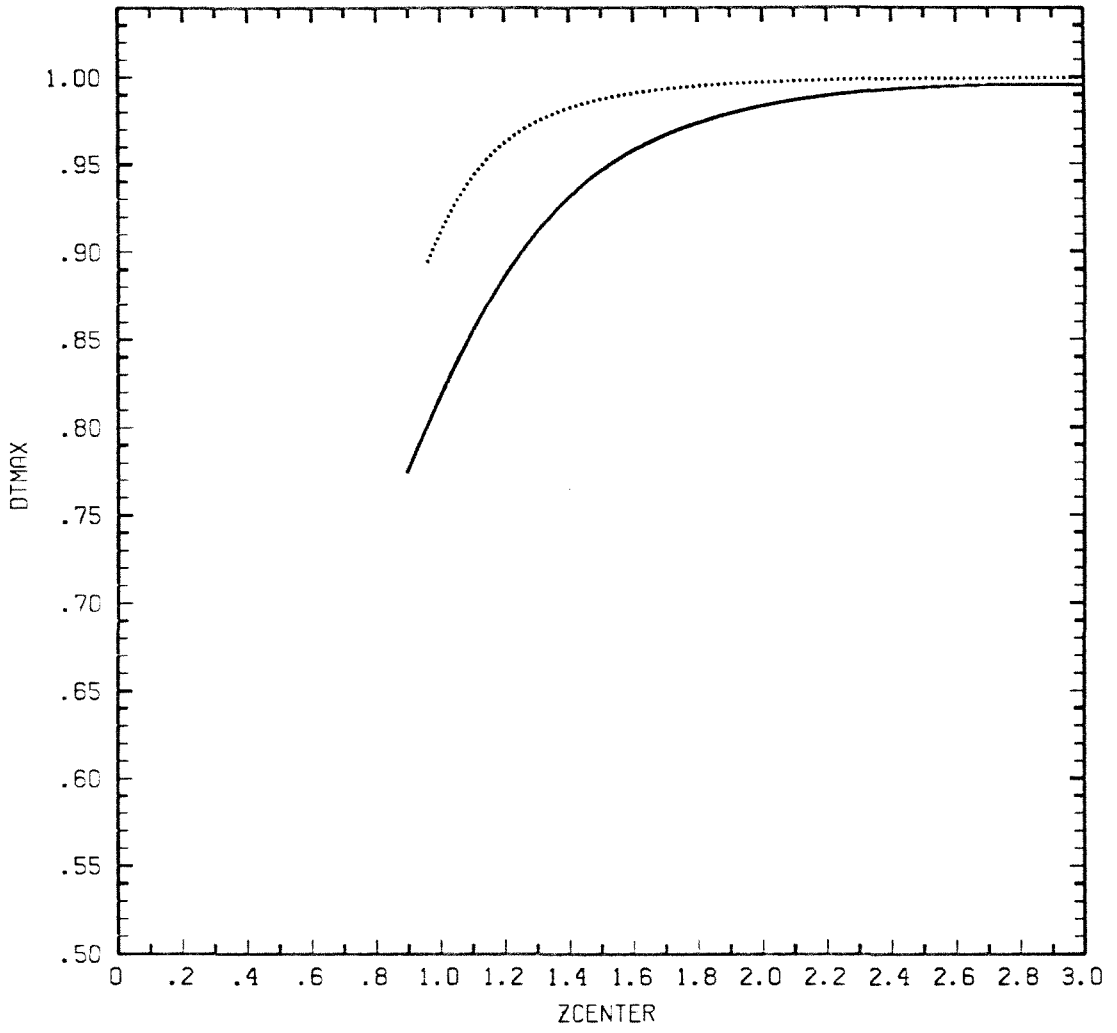


Figure 13

## Chapter IV

**A note on distortion functions for the  
strong constraint method of numerically  
generating orthogonal coordinate grids.**

E.P. Ascoli, D.S. Dandy, and L.G. Leal

Dept. of Chemical Engineering

California Institute of Technology

Pasadena, California 91125

published in

*Journal of Computational Physics*

October, 1987

### **Abstract**

In the strong constraint method of Ryskin & Leal a boundary-fitted orthogonal coordinate grid is constructed by solution of the covariant Laplace equation on a unit square. The ratio of the diagonal elements of the metric tensor is specified as input to the method, thereby providing control over spacing of the resultant coordinate grid. In this note a proof is presented for the existence for orthogonal mappings generated by the strong constraint method.

## Introduction

The emergence of large scale computing facilities in the last two decades has made it possible to solve problems that had previously been considered as intractable. In particular, the complicated partial differential equations which arise in areas such as fluid dynamics, optics, structural analysis, and quantum chemistry can now be solved efficiently using either finite difference or finite element techniques. An important advance in the application of finite difference techniques has been the development of methods to construct boundary-fitted curvilinear coordinates so that solutions can be obtained on domains of quite general shape without loss of any accuracy in the application of boundary conditions. An extensive survey of research in grid generation was done in an early paper by Thompson *et al* (1974), and more recently by Eisman (1985). There is a broad spectrum of coordinate grid types that can be created, either analytically or numerically; these grids can be orthogonal, nonorthogonal, conformal, or non-conformal.

The most common approach to numerically construct curvilinear coordinate grids is to solve an elliptic partial differential system, usually subject to Dirichlet conditions at the four boundaries. The solution of the two equations is a set of points  $x(\xi, \eta)$ ,  $y(\xi, \eta)$  which represent a discrete mapping between the physical  $(x, y)$  space and the curvilinear (computational)  $(\xi, \eta)$  space. For example, the set of points  $(x(\xi, \eta_0), y(\xi, \eta_0))$  corresponds to a coordinate line of constant  $\eta = \eta_0$  in  $(x, y)$  space. Of the elliptic PDE techniques, one that has proven to be extremely powerful in the study of free surface flow problems in fluid dynamics is a method due to Ryskin & Leal (1983) (henceforth referred to as R&L). This method was developed for the construction of boundary-fitted orthogonal curvilinear coordinate systems in 2D, with the mapping defined by the covariant Laplace equation, and constraints imposed on the components of the metric tensor to insure orthogonality and to control grid spacing. Its power for the solution of free surface flow problems is primarily due to the the method of

implementation that R&L refer to as the strong constraint method.

The strong constraint method is a one-step method of mapping a discrete set of points evenly distributed inside a unit square in a  $(\xi, \eta)$  curvilinear coordinate domain onto a discrete set of points in  $(x, y)$ . The two coordinate grids are related via the metric tensor, and to insure orthogonality of the generated grid the off-diagonal components of the metric tensor are required to be zero. The diagonal components of the metric tensor – referred to as the scale factors by R&L – are defined by

$$\begin{aligned} h_\xi &= \left[ \left( \frac{\partial x}{\partial \xi} \right)^2 + \left( \frac{\partial y}{\partial \xi} \right)^2 \right]^{\frac{1}{2}} \\ h_\eta &= \left[ \left( \frac{\partial x}{\partial \eta} \right)^2 + \left( \frac{\partial y}{\partial \eta} \right)^2 \right]^{\frac{1}{2}} \end{aligned} \tag{1a}$$

The ratio  $h_\eta(\xi, \eta)/h_\xi(\xi, \eta)$  is called the distortion function and is denoted by  $f(\xi, \eta)$ . In the strong constraint method of R&L the distortion function is allowed to vary with position in the domain, and, in fact is specified on the  $(\xi, \eta)$  domain  $[0, 1] \times [0, 1)$  as input to the method. In contrast, the ratio of the diagonal components would be unity for a conformal mapping.

The system to be solved for the mapping functions  $x(\xi, \eta)$  and  $y(\xi, \eta)$  on a unit square in  $(\xi, \eta)$  is

$$\begin{aligned} \frac{\partial}{\partial \xi} \left( f \frac{\partial x}{\partial \xi} \right) + \frac{\partial}{\partial \eta} \left( \frac{1}{f} \frac{\partial x}{\partial \eta} \right) &= 0 \\ \frac{\partial}{\partial \xi} \left( f \frac{\partial y}{\partial \xi} \right) + \frac{\partial}{\partial \eta} \left( \frac{1}{f} \frac{\partial y}{\partial \eta} \right) &= 0. \end{aligned} \tag{1b}$$

Particular to free surface problems in conjunction with the strong constraint method is the boundary condition on the above mapping system which is applied at the free surface ( $\xi = 1$ ): here  $h_\xi$  is specified. This boundary condition is of neither Neumann or Dirichlet type and it, in part, reflects the functional coupling of  $x$  and  $y$  along the free boundary.

Roughly speaking, a particular value of the distortion function  $f(\xi_0, \eta_0)$  corresponds to the ratio of the sides of an infinitesimal rectangle in the  $(x, y)$

plane which is the image of an infinitesimal square in the  $(\xi, \eta)$  plane about the point  $(\xi_0, \eta_0)$ . Thus,  $f$  is a measure of the stretching of the coordinate grid from a conformal mapping to an orthogonal one. However, since an arbitrary stretching of an orthogonal grid can produce a highly skewed, non-orthogonal grid, it is not obvious that an orthogonal mapping should exist for all choices of  $f(\xi, \eta)$ . The lack of criteria for choosing an  $f$  that will insure the existence of an orthogonal map is the most important limitation of the strong constraint method of orthogonal mapping. In the present note, we show that for a restricted class of distortion functions, the strong constraint method can be looked upon as a two-step process for which the first step is stretching of the  $(\xi, \eta)$  coordinate lines to an intermediate set of coordinates, and the second step a conformal map of the intermediate coordinates to  $(x, y)$ . As might be anticipated, a group of distortion functions which allow this interpretation are those which stretch  $\xi$  along itself independent of  $\eta$ , and  $\eta$  along itself independent of  $\xi$ , and so, in a manner analogous to classical separation of variables, a product form for  $f$ , that is,  $f(\xi, \eta) = \Phi(\xi) \Theta(\eta)$ , suggests itself. The following analysis shows that if  $f$  is of a product form, then the mapping equations, Eq. (1b), with their associated boundary conditions comprise a well-posed problem and that the existence of an orthogonal coordinate grid is guaranteed (subject, of course, to discretization error in the numerical implementation). Necessary restrictions on  $\Phi$  and  $\Theta$  will be discussed.

## Formulation

The strong constraint method splits a free boundary problem via Picard type iterations into two distinct sequences of components: (a) dynamic flow problems, and (b) coordinate grid generation problems. In terms of finite differencing, at each iteration a coordinate grid is generated for which the free surface corresponds to a coordinate line. In turn, the dynamic flow component provides updated information concerning the shape of the free boundary.

For illustrative purposes, consider the problem of flow past a deformable drop or bubble described by R&L. In terms of the natural cartesian variables  $(x, y)$  the external flow domain is of infinite extent. In R&L, as well as in this paper, a preliminary conformal transformation is performed (see Fig. 1). The fluid interface  $\Gamma$  in  $(x, y)$  space is transformed to  $\Gamma^*$  in  $(x^*, y^*)$ , so that infinity in  $(x, y)$  is transformed to the origin in  $(x^*, y^*)$ , and this simple transformation replaces the unbounded coordinates  $(x, y)$ , eliminating the need for truncation of the domain. The bounded domain  $(x^*, y^*)$  is then mapped via the grid generation method of R&L onto a unit square in which  $(\xi, \eta)$  are the working variables. Computation of the dynamic portion of the problem takes place in this unit square. The coordinate line  $\xi = 1$  corresponds to the free surface  $\Gamma^*$ , while  $\xi = 0$  corresponds to the origin in the  $(x^*, y^*)$  space. The coordinate  $\eta$  is of “angular” type ( $\xi$  is of radial type) and is required to satisfy periodic constraints, so that  $(\xi, 0)$  and  $(\xi, 1)$  correspond to the same point in  $(x^*, y^*)$ . Relative to the system  $(x^*, y^*)$  the coordinate grid generation problem may be mathematically formulated as follows: the covariant Laplace equations for the mapping functions  $x^*(\xi, \eta)$  and  $y^*(\xi, \eta)$  are

$$\begin{aligned} \frac{\partial}{\partial \xi} \left( f \frac{\partial x^*}{\partial \xi} \right) + \frac{\partial}{\partial \eta} \left( \frac{1}{f} \frac{\partial x^*}{\partial \eta} \right) &= 0 \\ \frac{\partial}{\partial \xi} \left( f \frac{\partial y^*}{\partial \xi} \right) + \frac{\partial}{\partial \eta} \left( \frac{1}{f} \frac{\partial y^*}{\partial \eta} \right) &= 0. \end{aligned} \tag{2}$$

Due to the connection between the system of Laplace equations and the Cauchy-Riemann equations in conformal mapping, it is evident that one can write an

analogous set of equations:

$$f \frac{\partial x^*}{\partial \xi} = \frac{\partial y^*}{\partial \eta} \quad \frac{\partial x^*}{\partial \eta} = -f \frac{\partial y^*}{\partial \xi}.$$

As mentioned before, the distortion function  $f$  is specified as input in the strong constraint method, along with the scale factor  $h_\xi^*(1, \eta)$  for  $\eta \in [0, 1]$ . Here,

$$h_\xi^* \equiv \left[ \left( \frac{\partial x^*}{\partial \xi} \right)^2 + \left( \frac{\partial y^*}{\partial \xi} \right)^2 \right]^{\frac{1}{2}} \quad (3a)$$

$$h_\eta^* \equiv \left[ \left( \frac{\partial x^*}{\partial \eta} \right)^2 + \left( \frac{\partial y^*}{\partial \eta} \right)^2 \right]^{\frac{1}{2}}$$

The curve defining the free surface is

$$\Gamma^* = \{x^*(1, \eta), y^*(1, \eta) : \eta \in [0, 1]\}. \quad (3b)$$

Due to periodicity,

$$(x^*(\xi, 1), y^*(\xi, 1)) = (x^*(\xi, 0), y^*(\xi, 0)) \quad \xi \in [0, 1], \quad (3c)$$

and the origin is defined by

$$(x^*(0, \eta), y^*(0, \eta)) = (0, 0) \quad \eta \in [0, 1]. \quad (3d)$$

Finally, we require that

$$y^*(1, 0) = 0. \quad (3e)$$

Conditions (3d) and (3e) are imposed to make the mapping concrete, such that Eq. (3d) fixes a particular translation of the coordinates, and Eq. (3e) fixes the “starting point” of the angular type coordinate  $\eta$ .

To reiterate, in this framework, the information provided by the dynamic problem at the most recent step is a new set of values for  $h_\xi^*(1, \eta)$ . The variable  $f$ , referred to as the distortion function in R&L is to be specified in advance by the implementer, and is incorporated into the method to provide control over grid spacing. Little guidance toward the choice of  $f$  is available. Further, R&L do not discuss the question of the existence of solutions to Eq. (2) relative to the choice of  $f$ . This note demonstrates the existence of solutions to Eq. (2) for a restricted class of  $f$ 's, specifically the case when  $f$  is of a special separable (that is, product) form in the variables  $\xi$  and  $\eta$ .

## The Proof

It must be shown that there exists a path between the unit square in the  $(\xi, \eta)$  domain and the desired domain  $\mathcal{D}$  in the  $(x^*, y^*)$  plane. This will be accomplished by breaking the path up into three steps (see Fig. 2), with the first step being a change of variables  $r = f_1(\xi)$  and  $\theta = f_2(\eta)$ , from a unit square in the  $(\xi, \eta)$  computational domain to a rectangle in a circular cylindrical-type  $(r, \theta)$  coordinate domain (maintaining the radial sense of  $\xi$  and the angular sense of  $\eta$ ). The functions  $f_1(\xi)$  and  $f_2(\eta)$  are assumed to be one-to-one and smooth \*, and are normalized and shifted for convenience so that  $f_1(0) = 0$ ,  $f_1(1) = 1$ ,  $f_2(0) = 0$ , and  $f_2(1) = 2\pi$ . Beyond these elementary restrictions  $f_1$  and  $f_2$  are arbitrary. The function  $f_1$  represents a stretching or shrinking of the coordinate  $\xi$ , independent of  $\eta$ , and likewise,  $f_2$  causes a stretching or shrinking of  $\eta$  independent of  $\xi$ . The functions  $f_1$  and  $f_2$  will be used to construct the distortion function  $f$ . In this context then, freedom in choosing  $f_1$  and  $f_2$  corresponds to control over grid spacing. As mentioned above, the coordinate variables  $r$  and  $\theta$  are circular cylindrical-type, and so the rectangle in  $(r, \theta)$  can be transformed to a unit disk in  $(u, v)$  space using the relations  $u = r \cos \theta$  and  $v = r \sin \theta$ . The motivation for carrying out these two coordinate transformations (from  $(\xi, \eta)$  to  $(r, \theta)$  to  $(u, v)$ ) arises from complex variable theory, where the Riemann mapping theorem guarantees the existence of a conformal map connecting a given, non-trivial two-dimensional domain to a unit disk. We have an analogous situation here except that for the strong constraint method the actual domain  $\mathcal{D}$  in  $(x^*, y^*)$  is not known, since the boundary  $\Gamma^*$  of  $\mathcal{D}$  is itself unknown. What is known instead is  $h_\xi^*(1, \eta)$ .

Consider a particular choice for  $f$ , namely

$$f(\xi, \eta) = \frac{f_1(\xi) f_2'(\eta)}{f_1'(\xi)}, \quad (4)$$

---

\* In theory,  $f_1$  and  $f_2$  should be  $C^\infty$  but in numerical implementation this restriction may be relaxed.

For this choice of distortion function, Eq. (2) on the unit disk reduces to

$$\begin{aligned} \frac{\partial^2 x^*}{\partial u^2} + \frac{\partial^2 x^*}{\partial v^2} &= 0 \\ \frac{\partial^2 y^*}{\partial u^2} + \frac{\partial^2 y^*}{\partial v^2} &= 0. \end{aligned} \tag{5}$$

This choice of distortion function  $f(\xi, \eta)$  is a product of the functions  $f_1(\xi)/f_1'(\xi)$  and  $f_2'(\eta)$ , and the form may appear confusing at first glance due to the term  $f_1$  in the numerator. However, this term is present because it is the necessary “length” factor required when dealing with angular and radial type coordinate systems.

The form of Eq. (5) suggests that we seek an analytic function  $F$  of the form  $F(w) \equiv F(u + iv) = x^* + iy^*$  on the closed unit disk  $u^2 + v^2 \leq 1$ . This function maps the unit disk onto the domain  $\mathcal{D}$ . Direct manipulation shows that specification of  $h_\xi^*(1, \eta)$  is equivalent to specifying  $|F'|$ , the norm of the derivative of the analytic function, on the boundary of the disk. As a result of the Cauchy-Riemann equations

$$\frac{\partial x^*}{\partial u} = \frac{\partial y^*}{\partial v} \qquad \frac{\partial x^*}{\partial v} = -\frac{\partial y^*}{\partial u},$$

Eq. (5) is identically satisfied.

Further, Eqs. (3a)-(3d) reduce to the very simple constraints

$$F(0) = 0 \tag{6a}$$

and

$$\arg\{F(1)\} = 0. \tag{6b}$$

The analytic function  $F(w)$  is required to be invertible, so in addition to the above two constraints we impose  $|F'| \neq 0$  on the closed disk.

As mentioned earlier, if  $\Gamma^*$  (or equivalently, the value of  $F$  on the boundary of the disk) is known, then the Riemann mapping theorem guarantees the existence of the conformal mapping  $F(w)$ , and therefore the existence of an orthogonal mapping between  $(\xi, \eta)$  and  $(x, y)$ . Here instead we have  $|F'|$  specified

on the boundary, and it is necessary to prove the existence of  $F(w)$ . This is carried out as follows: first, define the function

$$G(u + iv) = \log(F') = \ln |F'| + i \arg\{F'\},$$

where the  $k = 0$  branch of the log has been selected. The function  $F$  is assumed analytic on the disk, implying that  $F'$ , and therefore  $G^*$ , is also analytic on the disk. As a result, specification of  $|F'|$  on the boundary (of the disk) is equivalent to specification of  $\Re\{G\}$  on the boundary. Poisson's formula immediately gives  $\Re\{G\}$  in the interior of the disk ( $r < 1$ ):

$$\Re\{G(re^{i\theta})\} = \frac{1}{2\pi} \int_0^{2\pi} \frac{1 - r^2}{1 - 2r \cos(\theta - \alpha) + r^2} \Re\{G(e^{i\alpha})\} d\alpha. \quad (7)$$

Then,  $\Im\{G\} = \arg\{F'\}$  is determined in the disk via the Cauchy-Riemann equations for  $G$

$$\frac{\partial \Im\{G\}}{\partial v} = \frac{\partial \Re\{G\}}{\partial u} \qquad \frac{\partial \Im\{G\}}{\partial u} = - \frac{\partial \Re\{G\}}{\partial v} \quad (8)$$

and subsequent direct integration, and further,  $\arg\{F'\} = s(u, v) + c_1 = \mathcal{S}(u + iv) + c_1$ , where  $c_1$  is a real constant resulting from the integration. The total derivative  $F'(w)$  is then recovered as  $F' = |F'| \exp[i(\mathcal{S} + c_1)]$ . Analyticity of  $F'$  implies the existence of a Taylor series representation in the disk

$$F'(w) = e^{ic_1} (a_0 + a_1w + \dots) \quad (9)$$

where  $w = u + iv$ . A subsequent complex integration of  $F'(w)$  yields  $F(w)$  to within a second complex constant,  $c_2$ :

$$F(w) = c_2 + e^{ic_1} (a_0 + \frac{1}{2}a_1w + \dots)w \quad (10)$$

Application of condition (6a) yields  $c_2 = 0$ , and the real constant  $c_1$  represents the rotational orientation of the mapping and is fixed by condition (6b). Therefore, the mapping  $F(w)$  does exist subject to the constraints mentioned above.

---

\* Since  $|F'| \neq 0$  on the disk,  $G$  is well defined.

Thus, by a route involving two coordinate transformations and one conformal map, we have shown that an orthogonal mapping between  $(\xi, \eta)$  and  $(x, y)$  does exist, and that it is determined by specification of  $h_{\xi}^*(1, \eta)$  along with a special product form for the distortion function  $f$ .

## Conclusions

The purpose of the strong constraint method is to generate an orthogonal coordinate system by imposing suitable boundary conditions on the computational  $(\xi, \eta)$  domain, in conjunction with specification of the distortion function  $f(\xi, \eta)$ . The boundary conditions reflect the periodicity of the angular coordinate direction and the fact that the image of a boundary line in the  $(\xi, \eta)$  space is the origin in the  $(x^*, y^*)$  coordinate plane. In addition, along the coordinate line  $\xi = 1$  (corresponding to the free surface in physical space) the distortion function  $h_\xi^*$  is specified.

One very important consideration is the relationship between the choice of  $f$  and the existence of an orthogonal mapping. It is intuitive that an arbitrary stretching of a conformal map will yield a non-orthogonal mesh, or mapping, and further that a solution to Eq. (2) may not even exist for certain choices of  $f$ . In this note we have shown that if  $f$  is of a special product form, represented by Eq. (4), and if  $h_\xi^*$  is specified at one boundary, then an orthogonal mapping does exist between  $(\xi, \eta)$  and  $(x, y)$ .

## Acknowledgements

This work was partially supported by a grant from the National Science Foundation. The authors also wish to thank the Chevron Oil Field Research Company for partial support of this research.

## References

- P.R. Eisman, “Grid generation for fluid mechanics computations”, *Ann. Rev. Fluid Mech.* **17**, 487-522 (1985).
- G. Ryskin & L.G. Leal, “Orthogonal mapping”, *J. Comp. Phys.* **50**, 71-100 (1983).
- J.F. Thompson, F.C. Thames, & C.W. Mastin, “Automatic numerical generation of body-fitted curvilinear coordinate system for field containing any number of arbitrary two-dimensional bodies”, *J. Comp. Phys.* **15**, 299-319 (1974).

## Figure Captions

Figure 1. Schematic representation of the transformation path between the finite auxiliary domain and a unit square in the computational domain.

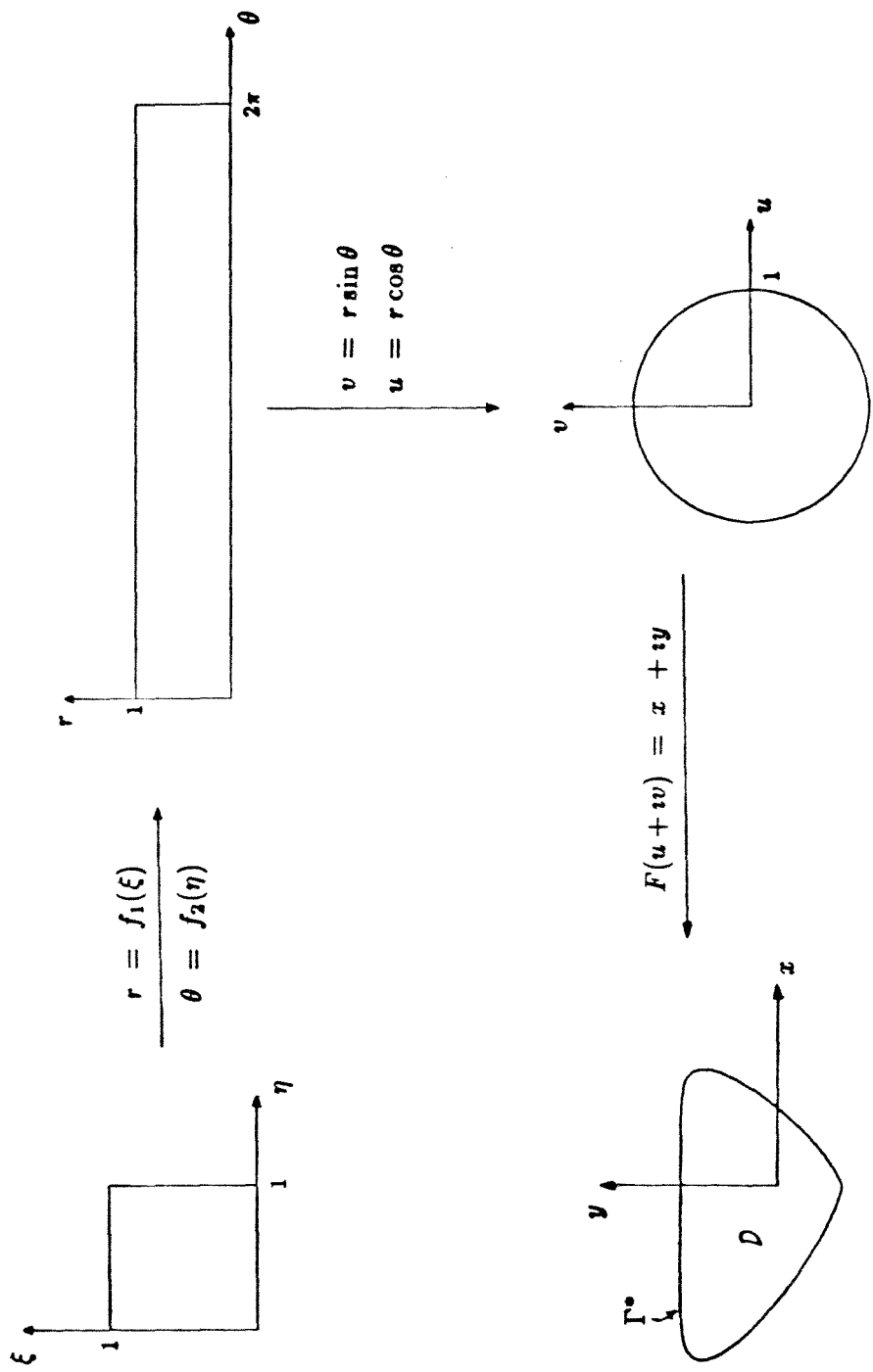


Figure 1

## Thesis Conclusions

In chapter I we developed a boundary integral technique based upon the wall Green's function. This numerical technique provided a method of calculating the hydrodynamic force on a solid particle in motion near a planar wall. The numerical results agreed exceptionally well with the exact results for the case of a sphere moving normal to the wall. The Green's function method was shown to be far superior in accuracy to the Stokeslet method, for the same number of elements. Although, for the same number of elements, the Green's function method required slightly more computation time than the Stokeslet method, for the same level of accuracy the Green's function method was as fast if not faster. For axisymmetric motion of ellipsoidal particles, far field asymptotic results agreed surprisingly well with the current numerical results. In particular, the "far-field" asymptotic theory was shown to be accurate for wall to particle center distances as small as five or six hydrodynamic radii. When the particle was extremely close to the wall, the numerical results were compared to lubrication theory. Cox's lubrication theory was found to have an extremely limited range of validity. In addition, for wall to particle gaps just outside the range of validity of Cox's theory, Reynolds' lubrication theory for a flat disk was found to provide a reasonable approximation for nearly "disk-shaped" ellipsoids.

We found in chapter II that buoyancy driven drop deformation increased with increasing capillary number. The viscosity ratio,  $\lambda$ , determined the "rate" of motion but was relatively unimportant in determining degree of deformation. Dimpling was observed numerically for all cases considered (i.e.  $Ca = 0.3, 1, 3$  for  $\lambda = 0.3, 1, 3$ ). At the instant when dimpling was first observed, the pressure in the trapped film was found to decrease in the direction normal to the planar wall. This variation in pressure was shown to be necessary for the initial formation of a dimple. Film-drainage theories employ the lubrication approximation based upon the assumption of an extremely thin film. The lubrication approximation neglects pressure variation normal to the wall. As a consequence,

we have shown that film-drainage theories employing the thin film assumption cannot capture the initial details of dimple formation.

In chapter III we examined the thermocapillary motion of a deformable drop or bubble toward a planar wall. Deformation of the drop or bubble was found to increase with increasing effective capillary number. Specifically, increasing magnitude of the parameter,  $\omega$ , the dimensionless variation of surface tension with temperature, corresponded to increased deformation. In contrast, increasing viscosity ratio,  $\lambda$ , or thermal conductivity ratio,  $\delta$ , corresponded to decreasing deformation.

Finally, in chapter IV we presented a proof of the existence of a boundary-fitted orthogonal grid for the case when the ratio of "scale factors" is of production form.